frontiers | Research Topics

Environmental change driven by climatic change, tectonism and landslide

Edited by
Hanchao Jiang, Chong Xu, Xingqi Liu, Basanta Raj Adhikari,
Xibin Tan and R. M. Yuan

Published in
Frontiers in Earth Science

ISSN 1664-8714
ISBN 978-2-83251-525-9
DOI 10.3389/978-2-83251-525-9

About Frontiers

Frontiers is more than just an open access publisher of scholarly articles: it is a pioneering approach to the world of academia, radically improving the way scholarly research is managed. The grand vision of Frontiers is a world where all people have an equal opportunity to seek, share and generate knowledge. Frontiers provides immediate and permanent online open access to all its publications, but this alone is not enough to realize our grand goals.

Frontiers journal series

The Frontiers journal series is a multi-tier and interdisciplinary set of open-access, online journals, promising a paradigm shift from the current review, selection and dissemination processes in academic publishing. All Frontiers journals are driven by researchers for researchers; therefore, they constitute a service to the scholarly community. At the same time, the *Frontiers journal series* operates on a revolutionary invention, the tiered publishing system, initially addressing specific communities of scholars, and gradually climbing up to broader public understanding, thus serving the interests of the lay society, too.

Dedication to quality

Each Frontiers article is a landmark of the highest quality, thanks to genuinely collaborative interactions between authors and review editors, who include some of the world's best academicians. Research must be certified by peers before entering a stream of knowledge that may eventually reach the public - and shape society; therefore, Frontiers only applies the most rigorous and unbiased reviews. Frontiers revolutionizes research publishing by freely delivering the most outstanding research, evaluated with no bias from both the academic and social point of view. By applying the most advanced information technologies, Frontiers is catapulting scholarly publishing into a new generation.

What are Frontiers Research Topics?

Frontiers Research Topics are very popular trademarks of the *Frontiers journals series*: they are collections of at least ten articles, all centered on a particular subject. With their unique mix of varied contributions from Original Research to Review Articles, Frontiers Research Topics unify the most influential researchers, the latest key findings and historical advances in a hot research area.

Find out more on how to host your own Frontiers Research Topic or contribute to one as an author by contacting the Frontiers editorial office: frontiersin.org/about/contact

Environmental change driven by climatic change, tectonism and landslide

Topic editors

Hanchao Jiang — Institute of Geology, China Earthquake Administration, China
Chong Xu — National Institute of Natural Hazards, Ministry of Emergency Management (China), China
Xingqi Liu — Capital Normal University, China
Basanta Raj Adhikari — Tribhuvan University (Pulchowk Campus), Nepal
Xibin Tan — Institute of Geology, China Earthquake Administration, China
R. M. Yuan — China Earthquake Administration, China

Citation

Jiang, H., Xu, C., Liu, X., Adhikari, B. R., Tan, X., Yuan, R. M., eds. (2023). *Environmental change driven by climatic change, tectonism and landslide*. Lausanne: Frontiers Media SA. doi: 10.3389/978-2-83251-525-9

Table of contents

frontiers | Frontiers in Earth Science

TYPE Editorial
PUBLISHED 02 December 2022
DOI 10.3389/feart.2022.1076801

OPEN ACCESS

EDITED AND REVIEWED BY
Candan Gokceoglu,
Hacettepe University, Turkey

*CORRESPONDENCE
Hanchao Jiang,
hcjiang@ies.ac.cn

SPECIALTY SECTION
This article was submitted to Geohazards and Georisks, a section of the journal Frontiers in Earth Science

RECEIVED 22 October 2022
ACCEPTED 23 November 2022
PUBLISHED 02 December 2022

CITATION
Jiang H, Xu C, Adhikari BR, Liu X, Tan X and Yuan R (2022), Editorial: Environmental change driven by climatic change, tectonism and landslide.
Front. Earth Sci. 10:1076801.
doi: 10.3389/feart.2022.1076801

Editorial: Environmental change driven by climatic change, tectonism and landslide

Hanchao Jiang[1]*, Chong Xu[2], Basanta Raj Adhikari[3], Xingqi Liu[4], Xibin Tan[5] and Renmao Yuan[6]

[1]State Key Laboratory of Earthquake Dynamics, Institute of Geology, China Earthquake Administration, Beijing, China, [2]National Institute of Natural Hazards, Ministry of Emergency Management of China, Beijing, China, [3]Institute of Engineering, Tribhuvan University, Lalitpur, Nepal, [4]College of Resource Environment and Tourism, Capital Normal University, Beijing, China, [5]Key Laboratory of Mountain Hazards and Earth Surface Processes, Institute of Mountain Hazards and Environment, Chinese Academy of Sciences, Chengdu, China, [6]Institute of Geology, China Earthquake Administration, Beijing, China

KEYWORDS

tectonism, sedimentation, landslide, paleoclimate, Climatic evolution, hazard assessing

Editorial on the Research Topic
Environmental change driven by climatic change, tectonism, and landslide

Introduction

Landscape evolution responds to climate change and tectonic motions, and this response is usually mediated by sediment transport and landslides (Whipple, 2004; Jerolmack and Paola, 2010). Understanding the transmission of environmental signals is crucial for predicting landscape response to climate change, and interpreting paleoclimate and tectonics from stratigraphy. Landslides and sedimentation are important surface processes, and the sediments contain important tectonic and climatic information.

Previous investigations in landslides and sediments focus mostly on climatic variations at the expense of tectonic inputs (Jiang et al., 2022). Recent investigations from tectonically active regions reveal many seismic events from modern landslides and late Pleistocene lacustrine sediments corresponding to tectonic activities (Howarth et al., 2012; Howarth et al., 2014; Jiang et al., 2014). In this context, it is of great scientific significance to consider the role and interplay of both tectonics and climate in geodynamic evolution as preserved in sedimentary records and landslide hazards.

On the other hand, for a regional scale of landslide hazard assessment, the characteristics of landslide and causative factors can be spatially different due to the

sizable study area. The stability of slopes in seismically active areas has become one of the popular Research Topic in the field of geological disaster prevention (Chen et al., 2022). Searching for the environmental context of climatic evolution and tectonism crucially depends on the interpretation of paleoclimate and tectonic archives from outcrop geology, basin sediments, river sediments, soft sediment deformation, landslides, geological hazards, and so on. Linking sedimentological processes to paleo-environmental reconstructions and models becomes increasingly important.

To present the latest achievements in this direction, we organized a Research Topic entitled *Environmental change driven by climatic change, tectonism, and landslide*. This Research Topic includes seven articles covering seismic and human impacts inferred from lake sediments, tectonic activities on the millennial- and million-year scales, and landslide hazard assessment and seismic amplification of the soil-rock slope, representing the newest progress in this discipline.

Seismic and human impacts inferred from lake sediments

The instrumental and historical earthquake records of a region are generally far too short to adequately evaluate the long-term behavior of seismogenic faults. Paleoseismology helps to fill this gap through detailed analysis of the available geological record along faults. Recently, more attention has been paid to paleoseismic records from lacustrine settings, with a greater emphasis on earthquake sedimentology (Jiang et al., 2017). Magnetic susceptibility, sedimentary structures, geochemistry, particle size, and pollen analyses are the preferred tools for identifying seismic events in lake sediment sequences (Jiang et al., 2014; Jiang et al., 2016; Jiang et al., 2017; Liang and Jiang, 2017; Wei et al., 2021). Intriguingly, different regions usually generate some new indicators for seismic activities.

Based on sedimentary characteristics (color, density, and grain size), organic matter content, and high-resolution XRF element scanning data, Liu et al. identified four seismic events from Lake Mugeco along the Xianshuihe fault zone on the southeastern margin of the Tibetan Plateau over the past 300 years, which are well correlated with four historical earthquakes. This result shows that only earthquakes with seismic intensities from VII to VIII within a 40-km radius can be recorded by lacustrine sediments in Lake Mugeco though the historical records reveal there are frequent earthquakes over Ms6. 0 along the Xianshuihe fault.

The Fuyun Fault is a typical slow-slipping fault in northwest China. Whether it left seismic imprints in nearby lake sediments remains uncertain. Fan et al. obtained two long sediment cores from Lake Yileimu and analysis of multi-proxies shows that sorting indices >3 and Si contents >700 counts per second (cps) are two effective tools to identify seismic events. Combined with analyses of sedimentary structures, magnetic susceptibility, elemental composition and carbon content, a total of 20 seismic events are identified by the Y20B core.

Besides seismic signals, lake sediments have the potential to provide excellent archives for long-term human impacts. Vegetation clearance and burning and agricultural and settlement expansion have led to increasing regional soil erosion rates (Arnaud et al., 2012). Moldovan et al. selected Lake Zaton in the Romanian Carpathians as a temporary lake for analysis of the human impact and the results show that, over the past 2,200 years, natural cycles of warm and cold periods changed the oribatid communities around the lake, with warmer cycles of rich fauna alternating with poor fauna during colder periods. However, the increased human occupation in the study area replaced the ecologically diverse fauna with eurytopic taxa in the past few centuries. This work indicates that the combined effects of climate change and long-term human impacts can have deleterious effects on invertebrate species and communities on the regional scale.

Tectonic activities on the millennial- and million-year scales

The collision of the Indian plate with the Eurasian plate led to the most complicated active structure in the southeastern margin of the Tibetan Plateau. The Gaoligong Mountain shear zone (GLGSZ) is one large-scale strike-slip fault zone with typical structural features that extend for thousands of kilometers (Allen et al., 1984; Royden et al., 2008). Wang et al. collected *in situ* samples of fresh gneiss and granite in the transects of the Gaoligong Mountain, Guyong Rock Mass, and Yinghuagu Valley for low-temperature thermochronological analysis. This work reveals that the GLGSZ experienced two rapid exhumation events at ~14.5 Ma and ~2.9 Ma. A collective comparison indicates that the deformation processes began in the northern transect and continued southwards and controlled the geomorphological features of the Gaoligong Mountains.

Relative to western China with more earthquakes, eastern China remains relatively stable with fewer earthquakes. However, in recent years, the seismic and geological survey discovered a new active fault-the Kouma Fault in the western Henan Province. Combined with trenching, drilling survey, magnetotelluric sounding and radiometric dating, He et al. conducted a detailed investigation on 12 fault outcrops on the slopes of the loess gullies and revealed two paleoseismic events of the Kouma Fault in the Middle Pleistocene and 40.9–38.8 ka B.P. This work is significant for the potential seismic source zone division, urban

and rural land planning, and the assessment and prevention of earthquake disaster risk.

Landslide hazard assessment and seismic amplification of the soil-rock slope

Earthquakes have long been recognized as one of the main triggers for landslides across the Earth (Keefer, 1984; Tian et al., 2022). The earthquake-triggered landslides threaten our society through their direct and indirect, long-term effects such as damaged infrastructure, increased debris flows and floods associated with landslide dam failures and downstream river aggradations (Zhang et al., 2021; Xu et al., 2022). Zhang et al. proposed landslide hazard assessment based on zonation in an attempt to take effective measures to address this problem. The study area is the China-Pakistan Economic Corridor and the main controlling factors for landslides were related to the site's topography, land use, and distance to an earthquake epicenter. This work shows that the accuracy of hazard assessment maps by zones was higher than that of the whole study area. Wang et al. established a centrifuge shaking table model test of anchored stabilizing piles for strengthening landslides and analyzed the dynamic response characteristics of the pile-anchor-slope under earthquake action. This work shows that the seismic amplification of the complex soil-rock slope varied strongly. The amplification of the pile-anchor cable connection is the largest, and the high-angle soil-rock interface is the smallest. Based on the obtained results, relevant suggestions for engineering design were put forward.

Concluding remarks and prospects

Landscape evolution deals with climate change, tectonism, and even human impacts, representing a complicated process. In this Research Topic, the seven articles involve multiple studying directions and accumulated much new knowledge for the development of this discipline.

The lacustrine deposition has two advantages, i.e., the innate continuity and reliability of systematic dating. Conventional paleo-seismic studies can reveal tectonic activity in localized locations or short segments, while earthquake limnology can effectively scale into basins and reconstruct seismic sequences through the recovery of sedimentary process over a large area (Jiang et al., 2014; Jiang et al., 2017). These studies make a common sense that the lacustrine deposits are the best archives of a long-term paleoseismic reconstruction and of a great importance for assessing the improvement of seismic hazards and risks in tectonically active regions.

Temporary lakes, such as Lake Zaton, can be used for paleoenvironmental studies, where natural and anthropic processes can significantly affect sediment deposition. Thus, multiple indicators of past environments can be used to assess human presence by decoupling from the rhythmic climate changes. Landslide hazard assessment based on zonation has higher accuracy than that of the whole study area, pointing to a new direction of landslide study in the future.

At the same time, these studies provide some good suggestions, for example, shallow and deep seismic explorations should be conducted in eastern China in the future to understand the tectonic activity of faults like the Kouma Fault. To study slope amplification and the seismic behavior of the pile, more available engineering cases and model test data should be obtained in the future to improve the numerical simulation.

Author contributions

All authors contributed to the critical review of the articles published in this Research Topic. HJ has provided an initial draft of this Editorial which was revised and approved by all the authors.

Funding

This study was supported by the special project of the fundamental scientific research of the Institute of Geology, China Earthquake Administration (IGCEA 1906).

Acknowledgments

We deeply thank all the authors for their submissions to this Research Topic and all the reviewers for their valuable comments and suggestions, and the Frontiers Editorial Office for their strong support in all phases of the realization of this Research Topic.

Conflict of interest

The authors declare that the research was conducted in the absence of any commercial or financial relationships that could be construed as a potential conflict of interest.

Publisher's note

References

Allen, C. R., Gillespie, A. R., Yuan, H., Sieh, K. E., Buchun, Z., and Chengnan, Z. (1984). Red River and associated faults, yunnan province, China: Quaternary geology, slip rates, and seismic hazard. *Geol. Soc. Am. Bull.* 95, 6862–7700. doi:10.1130/0016-7606(1984)95<686:RRAAFY>2.0.CO;2

Arnaud, F., Révillon, S., Debret, M., Revel, M., Chapron, E., Jacob, J., et al. (2012). Lake bourget regional erosion patterns reconstruction reveals holocene NW European alps soil evolution and paleohydrology. *Quat. Sci. Rev.* 51, 81–92. doi:10.1016/j.quascirev.2012.07.025

Chen, G. F., Zhang, G. D., Guo, F., Wang, L., Zhan, Q. H., and Huang, X. H. (2022). New arm-stretching-type anti-slide pile design and verification. *Front. Earth Sci.* 10, 846616. doi:10.3389/feart.2022.846616

Howarth, J. D., Fitzsimons, S. J., Norris, R. J., and Jacobsen, G. E. (2012). Lake sediments record cycles of sediment flux driven by large earthquakes on the alpine fault, New Zealand. *Geology* 40, 1091–1094. doi:10.1130/G33486.1

Howarth, J. D., Fitzsimons, S. J., Norris, R. J., and Jacobsen, G. E. (2014). Lake sediments record high intensity shaking that provides insight into the location and rupture length of large earthquakes on the alpine fault, New Zealand. *Earth Planet. Sci. Lett.* 403, 340–351. doi:10.1016/j.epsl.2014.07.008

Jerolmack, D. J., and Paola, C. (2010). Shredding of environmental signals by sediment transport. *Geophys. Res. Lett.* 37, L19401. doi:10.1029/2010GL044638

Jiang, H. C., Mao, X., Xu, H. Y., Yang, H. L., Ma, X. L., Zhong, N., et al. (2014). Provenance and earthquake signature of the last deglacial Xinmocun lacustrine sediments at Diexi, East Tibet. *Geomorphology* 204, 518–531. doi:10.1016/j.geomorph.2013.08.032

Jiang, H. C., Zhong, N., Li, Y. H., Xu, H. Y., Yang, H. L., and Peng, X. P. (2016). Soft sediment deformation structures in the Lixian lacustrine sediments, Eastern Tibetan Plateau and implications for postglacial seismic activity. *Sediment. Geol.* 344, 123–134. doi:10.1016/j.sedgeo.2016.06.011

Jiang, H. C., Zhong, N., Li, Y. H., Ma, X. L., Xu, H. Y., Shi, W., et al. (2017). A continuous 13.3-ka record of seismogenic dust events in lacustrine sediments in the eastern Tibetan Plateau. *Sci. Rep.* 7, 15686. doi:10.1038/s41598-017-16027-8

Jiang, H., Zhang, J., Zhang, S., Zhong, N., Wan, S., Alsop, G. I., et al. (2022). Tectonic and climatic impacts on environmental evolution in East Asia during the Palaeogene. *Geophys. Res. Lett.* 49, 2021. doi:10.1029/2021GL096832

Keefer, D. K. (1984). Landslides caused by earthquakes. *Geol. Soc. Am. Bull.* 95, 406. doi:10.1130/0016-7606(1984)95<406:lcbe>2.0.co;2;2

Liang, L. J., and Jiang, H. C. (2017). Geochemical composition of the last deglacial lacustrine sediments in East Tibet and implications for provenance, weathering and earthquake events. *Quat. Int.* 430, 41–51. doi:10.1016/j.quaint.2015.07.037

Royden, L. H., Burchfiel, B. C., and van der Hilst, R. D. (2008). The geological evolution of the Tibetan plateau. *Science* 321, 1054–1058. doi:10.1126/science.1155371

Tian, Y., Xu, C., and Yuan, R. (2022). Earthquake-triggered landslides. *Treatise Geomorphol.* 2, 583–614. doi:10.1016/B978-0-12-818234-5.00120-6

Wei, X. T., Jiang, H. C., Xu, H. Y., Fan, J. W., Shi, W., Guo, Q. Q., et al. (2021). Response of sedimentary and pollen records to the 1933 Diexi earthquake on the eastern Tibetan Plateau. *Ecol. Indic.* 129, 107887. doi:10.1016/j.ecolind.2021.107887

Whipple, K. X. (2004). Bedrock rivers and the geomorphology of active orogens. *Annu. Rev. Earth Planet. Sci.* 32, 151–185. doi:10.1146/annurev.earth.32.101802.120356

Xu, C., Gorum, T., and Tanyas, H. (2022). Editorial: Application of remote sensing and GIS in earthquake-triggered landslides. *Front. Earth Sci.* 10, 964753. doi:10.3389/feart.2022.964753

Zhang, S., Jiang, H., Fan, J., Xu, H., Shi, W., Guo, Q., et al. (2021). Accumulation of a last deglacial gravel layer at Diexi, eastern Tibetan Plateau and its possible seismic significance. *Front. Earth Sci.* 9, 797732. doi:10.3389/feart.2021.797732

frontiers in Earth Science

ORIGINAL RESEARCH
published: 27 January 2022
doi: 10.3389/feart.2022.828801

A ~28-kyr Continuous Lacustrine Paleoseismic Record of the Intraplate, Slow-Slipping Fuyun Fault in Northwest China

Jiawei Fan[1,2,3], Hongyan Xu[1], Wei Shi[1], Qiaoqiao Guo[1], Siqi Zhang[1], Xiaotong Wei[1], Minggang Cai[1], Shuaitang Huang[4], Jiangyong Wang[5] and Jule Xiao[6,7,8]*

[1]State Key Laboratory of Earthquake Dynamics, Institute of Geology, China Earthquake Administration, Beijing, China, [2]Xinjiang Pamir Intracontinental Subduction National Field Observation and Research Station, Beijing, China, [3]Urumqi Institute of Central Asia Earthquake, China Earthquake Administration, Urumqi, China, [4]Earthquake Agency of Xinjiang Uygur Autonomous Region, Urumqi, China, [5]College of Urban and Environmental Science, Northeast Normal University, Changchun, China, [6]CAS Key Laboratory of Cenozoic Geology and Environment, Institute of Geology and Geophysics, Chinese Academy of Sciences, Beijing, China, [7]CAS Center for Excellence in Life and Paleoenvironment, Beijing, China, [8]College of Earth and Planetary Sciences, University of Chinese Academy of Sciences, Beijing, China

OPEN ACCESS

Edited by:
Chong Xu,
Ministry of Emergency Management, China

Reviewed by:
Qi Yao,
China Earthquake Administration, China
Xiangli He,
China Earthquake Administration, China

***Correspondence:**
Jiawei Fan
jwfan@ies.ac.cn

Specialty section:
This article was submitted to Geohazards and Georisks, a section of the journal Frontiers in Earth Science

Received: *04 December 2021*
Accepted: *10 January 2022*
Published: *27 January 2022*

Citation:
Fan J, Xu H, Shi W, Guo Q, Zhang S, Wei X, Cai M, Huang S, Wang J and Xiao J (2022) A ~28-kyr Continuous Lacustrine Paleoseismic Record of the Intraplate, Slow-Slipping Fuyun Fault in Northwest China. Front. Earth Sci. 10:828801. doi: 10.3389/feart.2022.828801

The Fuyun Fault is a typical intraplate, slow-slipping fault, but has been repeatedly ruptured by surface wave magnitude (M_S) ≥ 8.0 earthquakes. The 11 August 1931 M_S 8.0 Fuyun earthquake resulted in more than 10,000 casualties in the sparsely populated Fuyun area. Cosmogenic ^{10}Be dating of offset landforms produced by prehistoric M_S ≥ 8.0 earthquakes yields an average recurrence interval of 9,700 ± 3,300 years, much longer than previously estimated 2,000–4,500 years, clouding our understanding of the timing and recurrence behavior of past earthquakes originating from the Fuyun Fault. Reflection seismic data reveal widely distributed subaquatic faults in Yileimu Lake, implying high sensitivity of the lake sediments to paleoearthquakes originating from the Fuyun Fault. Two new long sediment cores (Y20A: 267 cm; Y20B: 890 cm) together with previously published two short cores (Y19: 71 cm; Y20: 31.5 cm) from the depocenter and nearshore zone of Yileimu Lake are used for stratigraphic correlations and analyses of sedimentary structures, grain-size distributions, magnetic susceptibility, elemental composition and carbon content. The mass-wasting deposits with underlying soft-sediment deformation structures (SSDS) in the Y20B core indicate six siliciclastic-enriched sandy sediment fluxes from earthquake-triggered landslides of granitic rocks, and isolated SSDS record three additional earthquake-induced *in situ* deformations. Turbidite-like deposits with sorting indices >3 and Si contents >700 counts per second (cps) are comparable to those of the seismic mass-wasting deposits, and are thus interpreted as seismites from earthquake-induced re-deposition of nearshore sediments. There are a total of 20 seismic events recorded by the Y20B core. Seismic intensity calculation results, combined with historical seismic data, provide potential magnitudes of M_S ≥ 8.0, M_S ≥ 7.0, and M_S ≥ 5.5 for the earthquake-triggered mass-wasting deposits, SSDS, and turbidite-like seismites, respectively, in Yileimu Lake, generally consistent with previously published magnitude thresholds. Radiocarbon dating and stratigraphic correlations constrain the timing of these past earthquakes to

~28 cal kyr BP. This unique, long lacustrine paleoseismic record suggests a weakly periodic pattern with recurrence intervals between 2,317 and 7,830 years and an average of 5,303 years for potential $M_S \geq 8.0$ earthquakes, and reveals an unprecedented high frequency of potential $M_S \geq 7.0$ earthquakes originating from the Fuyun Fault in the last 5 kyr, demonstrating the urgent need for an improved assessment of seismic hazards and risks in the Fuyun Fault zone.

Keywords: mass-wasting deposits, soft-sediment deformations, turbidite, shaking intensity, recurrence behavior, intraplate fault

INTRODUCTION

In recent decades, the frequent occurrence of catastrophic earthquakes (e.g., the 17 August 1999 M_s 7.4 earthquake in Turkey, the 8 October 2005 M_s 7.6 earthquake in Pakistan, and the 12 May 2008 M_s 8.0 earthquake in China) produced by sudden stress release of intraplate active faults have resulted in massive casualties, property loss and ecological destruction (Vanholder et al., 2001; Sullivan and Hossain, 2010; Cui et al., 2012). The Fuyun Fault is a typical intraplate fault located at the junction of Tianshan–Altay and Mongolia–Baikal seismic zones, an area with frequent large earthquakes (Pollitz et al., 2003). A rupture along the ~170-km long Fuyun Fault produced the 11 August 1931 M_s 8.0 Fuyun earthquake with a maximum horizontal coseismic displacement of ~14 m. It resulted in more than 10,000 casualties, causing great trauma to the sparsely populated Fuyun area (Fuyun County Local Chronicles Compilation Committee, 2003). The Fuyun Fault is a slow-slipping fault but evidence indicates that it ruptured repeatedly generating prehistoric $M_s \geq 8.0$ earthquakes (Klinger et al., 2011; Xu et al., 2012). Mapping of the Fuyun Fault offsets using satellite and geomorphological data and cosmogenic ^{10}Be dating of the offset landforms yielded an average recurrence interval of 9,700 ± 3,300 years for the prehistoric earthquakes (Xu et al., 2012). However, such a long recurrence interval is in sharp contrast with the previously estimated interval of 2,000–4,500 years in Xinjiang active tectonic zones (Xu and Deng, 1996).

The short instrumental and historical earthquake records in the Fuyun area is insufficient to determine the long-term recurrence behavior of devastating earthquakes from such intraplate faults (Avşar et al., 2014; Howarth et al., 2014; Moernaut, 2020). Quaternary deposits in the Altay region are sporadic, limiting the investigation of paleoseismic trenches for the Fuyun Fault. Dendroseismological studies can provide absolute ages for past earthquakes associated with the Fuyun Fault (Lin and Lin, 1998). However, seismic intensity thresholds for tree-ring responses are poorly constrained in the fault area due to the scarcity of historical earthquake events (e.g., Fan et al., 2020a), and dendrochronological studies may be limited to a much shorter time span than the long return periods of multiple great earthquakes. Therefore, paleoseismic records with a long time span and containing information regarding earthquake size are urgently needed to gain a better understanding of seismic activities on the Fuyun Fault.

Continuously deposited lake sediments in fault-bounded basins potentially contain detailed information on the occurrence and age of paleoearthquake events (e.g., Strasser et al., 2006; Berryman et al., 2012; Hubert-Ferrari et al., 2020; Kremer et al., 2020; Moernaut, 2020; Oswald et al., 2021). Previous lacustrine paleoseismic studies have provided some intensity thresholds for earthquake-induced sedimentary and deformation processes: a Modified Mercalli Intensity (MMI) of 5–6 induced turbidite deposition in Rara Lake, western Nepal (Ghazoui et al., 2019); an intensity of 6–7 MMI produced soft-sediment deformation structures (SSDS) in Lungerer Lake, Seelisberg Lake and Baldegger Lake, central Switzerland (Monecke et al., 2004); and a violent shaking intensity of 9 MMI caused extensive landslides and triggered mass-wasting deposits in Mapourika Lake, Paringa Lake and Ellery Lake, New Zealand (Howarth et al., 2016). The intensity thresholds for earthquake-induced lacustrine sedimentary events provide a means to investigate the location and magnitude of past earthquakes and to determine the recurrence pattern of earthquake events of different intensities (Moernaut et al., 2018; Lu et al., 2020).

Yileimu Lake is bounded by the Fuyun Fault (**Figure 1A**), making this site particularly sensitive to seismic activities originating from the fault. A recent study based on a 71-cm long sediment core from Yileimu Lake provided a 450-years continuous paleoseismic record related to the Fuyun Fault (Fan et al., 2020b). Here, we present an extended history of this paleoseismic record to ~28 cal kyr BP, through high-resolution analyses of chronology and sedimentary events including mass-wasting deposits, SSDS and turbidite-like deposits in an 890-cm long sediment core from Yileimu Lake, and through careful statistical analysis of grain-size data, and elemental composition. The sedimentary events in this unique, long paleoseismic record are constrained by different shaking intensities, providing an in-depth understanding of the magnitude, frequency and recurrence behavior of past earthquakes on the Fuyun Fault since ~28 cal kyr BP.

MATERIALS AND METHODS

Study Area

The Fuyun Fault is a ~170-km long intraplate strike-slip fault in southern Altay, northern Xinjiang, which is on the border of China, Mongolia and Russia (**Figure 1A**). It consists of two segments: one is a ~50 km-long normal fault, constituting the northern segment; the other is a ~120 km-long right-lateral slip

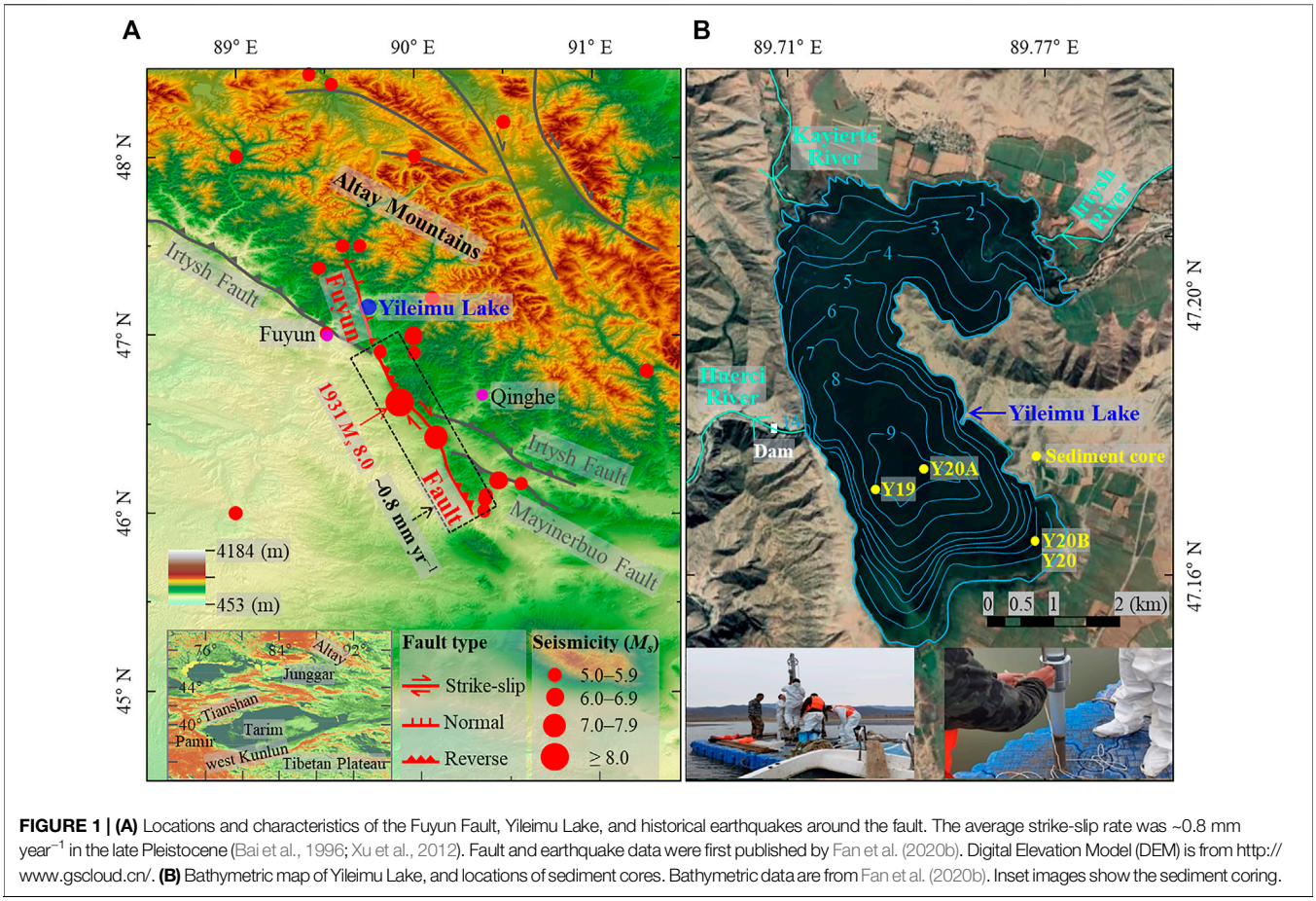

FIGURE 1 | (A) Locations and characteristics of the Fuyun Fault, Yileimu Lake, and historical earthquakes around the fault. The average strike-slip rate was ~0.8 mm year^{-1} in the late Pleistocene (Bai et al., 1996; Xu et al., 2012). Fault and earthquake data were first published by Fan et al. (2020b). Digital Elevation Model (DEM) is from http://www.gscloud.cn/. **(B)** Bathymetric map of Yileimu Lake, and locations of sediment cores. Bathymetric data are from Fan et al. (2020b). Inset images show the sediment coring.

fault with a thrust component, constituting the southern segment (**Figure 1A**) (Ding, 1985; Klinger et al., 2011; Xu et al., 2012). The southern segment of the fault is more active, in response to the southeastward movement of the Mongolia and Siberia blocks and to the far-field effect of India-Eurasia collision (Shen et al., 2003). The average strike-slip rate was ~0.8 mm year^{-1} in the late Pleistocene (Bai et al., 1996; Xu et al., 2012). Historical earthquake records cover only 120 years, but document an M_s 8.0 earthquake that ruptured the whole Fuyun Fault and triggered extensive landslides in 1931 AD (**Figure 1A**) (Fuyun County Local Chronicles Compilation Committee, 2003).

Yileimu Lake is a permanent lake formed by depression of the northern segment of the Fuyun Fault (Klinger et al., 2011). It is fed by the Kayierte and Irtysh Rivers and is discharged by the Huerci River (**Figure 1B**). The current lake level is mainly controlled by an artificial dam (20.8 m above the ground) located ~0.5 km downstream along the Huerci River (**Figure 1B**). The dam was built in 1958–1967 AD (Fuyun County Local Chronicles Compilation Committee, 2003). Yileimu Lake has a maximum water depth of ~9 m in the depocenter, and the lake floor is flat in the north and relatively steep in the south (**Figure 1B**) (Fan et al., 2021). Hills of granitic rocks with an average slope of ~35° occur along the Fuyun Fault, bounding the western margin of the lake (**Figures 1A,B**, **Supplementary Figure S1A**). The lake is surrounded by lacustrine plains along the northern, northeastern, southeastern and southern shores (**Figure 1B**). The catchment area has ~300 m of relief between the mountain peaks and lake surface, and landslides appear on the slopes to the southwest of the lake. Chemical weathering is relatively weak in the Altay Mountains, limiting the sediment sources for the lake to some extent (Fan et al., 2021).

Reflection Seismic Survey and Sediment Coring

A reflection seismic survey was conducted along nine seismic lines across Yileimu Lake in May 2021 (only three lines A, B and C in **Supplementary Figure S1A** have relatively clear seismic reflectors). Reflection seismic data were acquired using an Applied Acoustics Engineering (AAE) CSP–D2400 system in combination with a GeoAcoustics 5210A system. A Receiver Model 5210A was used to collect seismic data from an AA301 boomer seismic sound source (200 J) and a 20-unit hydrophone (100–4,000 Hz), and to collect differential Global Positioning System (DGPS) data. A band-pass filter of 200–15,000 Hz was applied and seismic data interpretation was performed using SonarWiz 7 (v7.07.04) software.

In September 2020, a 267-cm long sediment core (Y20A; 47.176°N, 89.740°E) and an 890-cm long sediment core (Y20B; 47.165°N, 89.764°E) were retrieved from the depocenter (at a

TABLE 1 | Accelerator Mass Spectrometry (AMS) ^{14}C ages for the Y20A and Y20B cores.

Laboratory number	Depth (cm)	Dating material	δ^{13}C (‰)	Conventional ^{14}C age (year BP)	Corrected ^{14}C age[a] (year BP)	Calibrated ^{14}C age (2σ) (cal year BP)
NENUR11114[b]	Core top[c]	Organic matter	–19.1	890 ± 30		–70[d]
NENUR11115[b]	45[c]	Organic matter	–14.3	8,800 ± 60[e]	3,070 ± 70	3,125–3,496
Beta–597772[f]	50[c]	Organic matter	–21.1	8,820 ± 30[e]	3,090 ± 35	3,261–3,435
NENUR11118[b]	200[c]	Organic matter	–18.2	13,600 ± 100[e]	7,870 ± 105	8,504–9,046
NENUR11120[b]	375[c]	Organic matter	–17.7	16,460 ± 150[e]	10,730 ± 155	12,224–13,135
Beta–597774[f]	450[c]	Organic matter	–19.9	24,270 ± 80		
Beta–558775[f]	650[c]	Organic matter	–20.8	20,110 ± 60[e]	14,380 ± 70	17,377–17,885
Beta–558776[f]	850[c]	Organic matter	–20.7	15,340 ± 50		
NENUR11111[b]	198[g]	Branch	–21.5	3,090 ± 35[e]	3,090 ± 35	3,261–3,435
NENUR11113[b]	264[g]	Wood	–23.6	3,180 ± 35[e]	3,180 ± 35	3,327–3,511

[a]*The reservoir-corrected ^{14}C ages. The reservoir correction factor is 5,730 years for the Y20B core (see main text for interpretation).*
[b]*NENUR: State Key Laboratory of Organic Geochemistry, Guangzhou Institute of Geochemistry, Chinese Academy of Sciences.*
[c]*Samples from the Y20B core.*
[d]*Sampling date.*
[e]*Age data used in the age–depth model of the Y20B core.*
[f]*Beta: Beta Analytic Testing Laboratory, Beta Analytic Inc, 4985 SW 74th Court Miami, Florida 33155.*
[g]*Samples from the Y20A core. The depths of 50 and 72 cm of the Y20B core correspond to the depths of 198 and 264 cm of the Y20A core, respectively (see main text for interpretation).*

water depth of 9.21 m) and nearshore zone (at a water depth of 2.00 m) of Yileimu Lake, respectively (**Figure 1B**), using a Wink S5 sonic drill system (Canada). The sediment cores had a diameter of 55 mm. The nearest offshore distances of the Y20A and Y20B cores were ~1.2 and ~0.4 km, respectively (**Figure 1B**). The Y20A and Y20B cores were split for X-ray fluorescence scanning, and then sampled at 0.5-cm intervals for physical and chemical analyses. In addition, a 31.5-cm long sediment core (Y20) was retrieved near the Y20B core, and a 71-cm long sediment core (Y19; 47.175°N, 89.729°E) was retrieved from the depocenter of the lake (**Figure 1B**), using a UWITEC gravity corer (Austria). The lithology, chronology and grain-size data from the Y19 (which was named "Y19B" in the previous study of Fan et al. 2020b) and Y20 cores were published (Fan et al., 2021) and are used for stratigraphic correlations in this study.

Accelerator Mass Spectrometry (AMS) Radiocarbon Dating

A total of eight bulk samples from organic-rich horizons of the Y20B core, plus one branch sample at 223 cm depth and one wood sample at 264 cm depth within the Y20A core, were selected for AMS ^{14}C dating. This was carried out at the Guangzhou Institute of Geochemistry, Chinese Academy of Sciences and the Beta Analytic Testing Laboratory, United States (**Table 1**). Organic matter from bulk samples was extracted through an AAA pretreatment process (washing with acid, alkali and acid) (Brock et al., 2010). Conventional ^{14}C ages were calibrated using the OxCal 7.1 calibration program (Bronk Ramsey and Lee, 2013) with IntCal20 calibration data (Reimer et al., 2020). An age–depth profile was constructed using a Bayesian Accumulation Model (Blaauw and Christen, 2011).

X-Ray Fluorescence (XRF) Scanning

One half of each of the Y20A and Y20B cores was smoothed, and then scanned on an Itrax core scanner. Radiographic images were scanned at a resolution of 0.1 cm, using an Rh tube at 60 kV voltage and 35 mA current. Relative element intensities were obtained at 30 kV voltage and 55 mA current with an exposure time of 3 s for every 0.5 cm. Principal component analysis (PCA) was conducted on the standardized proxy data (Si, K, Ti, Fe, Zr, Al, Mn, Ca, Rb, Sr) of the Y20B core, using the software SPSS (Fan et al., 2016), in order to discriminate different sedimentary facies associated with different sedimentary processes, based on their distinguishable compositional characteristics (Praet et al., 2020; Wils et al., 2021). The main factor values (PCA F1 and F2) for each sample were calculated following the method of Fan et al. (2016).

Analyses of Grain-Size Distributions and Magnetic Susceptibility (SUS)

A total of 534 samples from the Y20A core and 1780 samples from the Y20B core were used for grain-size distribution analysis, and the Y20B core was also used for analysis of magnetic susceptibility. Grain-size data were measured using a Malvern Mastersizer 3000 laser grain-size analyzer, and SUS data were measured using a Bartington MS2 susceptibility meter at the Institute of Geology, China Earthquake Administration, following the method of Fan et al. (2020b). The Mastersizer 3000 automatically outputs the volume percentage of 100 grain-size fractions. Sorting index of each grain-size distribution was calculated using the GRADISTAT program (Blott and Pye, 2001). SUS values were normalized by the sample weight.

Analysis of Total Inorganic Carbon (TIC) Content

The Y20B core was sampled at 5-cm intervals (178 samples) for analysis of TIC content, using an Elementar Rapid CS Cube analyzer at the Institute of Geology, China Earthquake Administration. Each sample was separated into two subsamples. One subsample was used for the measurement of total carbon (TC) content, and the other was pretreated with 1 M

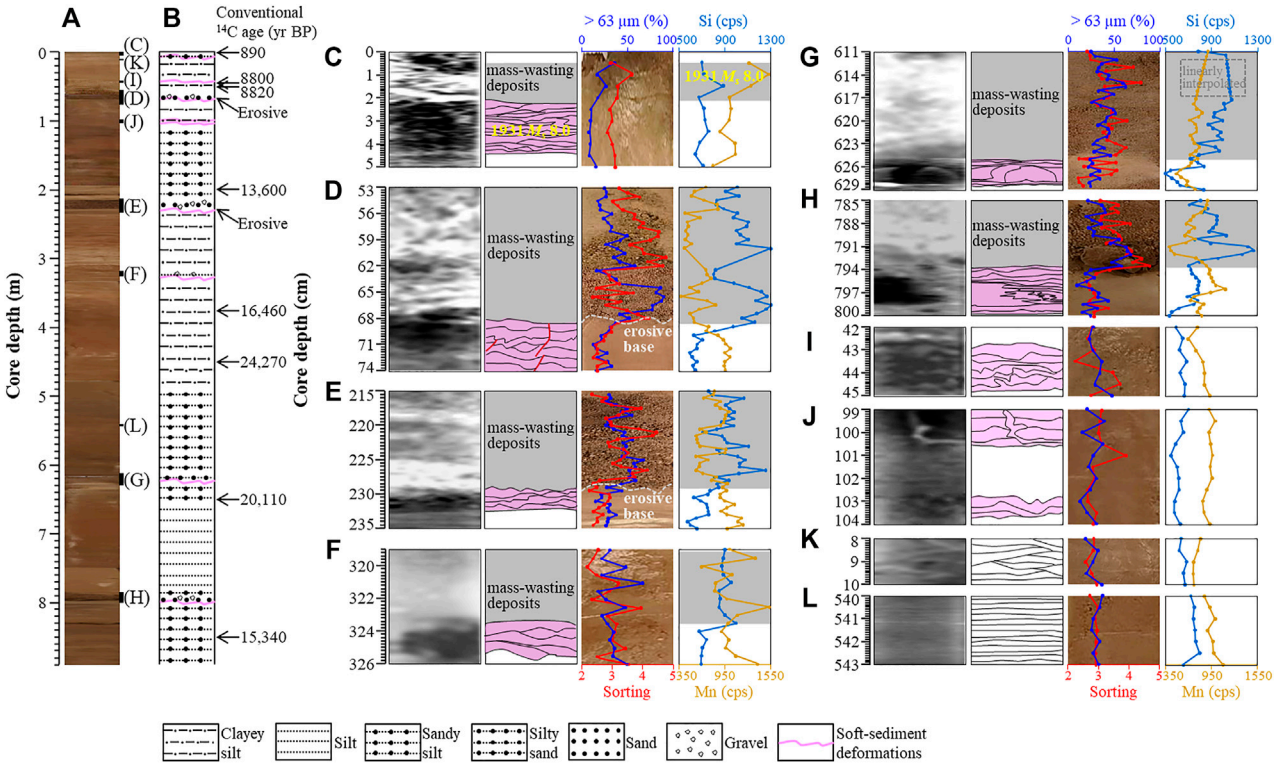

FIGURE 2 | (A) Optical image and **(B)** lithology and conventional ^{14}C ages of the Y20B core. **(C–H)** Soft-sediment deformation structures (SSDS) from radiographic images of the Y20B core, with overlying sandy deposits (mass-wasting deposits). **(C,E,F)** Linear waves. **(D)** Micro-faults. **(G)** Convolute structures. **(H)** Linear waves and clastic dykes. The mass-wasting deposits are generally characterized by high sand percentages, sorting indices and Si contents, and relatively low Mn contents. Note that the sedimentary structures are not clear in optical images, potentially due to the low sedimentation rates. Sharp erosive bases can be found at the interfaces of typical mass-wasting deposits and the underlying SSDS in **(D,E)**. The mass-wasting deposits overlying the SSDS in **(C)** are related to the 11 August 1931 M_S 8.0 Fuyun earthquake. **(I,J)** Isolated SSDS without overlying mass-wasting deposits. **(I)** Linear waves. **(J)** A clastic dyke (upper) and linear waves (lower). **(K)** Cross bedding. **(L)** Horizontal laminations (background sediments). Cps, counts per second. High sorting indices indicate poor sorting of sediments.

HCl to remove carbonates and then used for the measurement of total organic carbon (TOC) content, following the method of Fan et al. (2020b). TIC content was calculated as the difference between the TC and TOC contents.

RESULTS

Seismic Stratigraphy and Core Lithology

Seismic profiles from three lines across Yileimu Lake cover a maximum sediment depth of ~15 m (**Supplementary Figures S1A–D**). The poor penetration of seismic reflection may be related to the presence of highly reflective sediments such as coarse gravels (Wils et al., 2021). Nevertheless, several subaquatic faults are clearly imaged by reflection offsets and changes in reflector characteristics in the same horizons (**Supplementary Figures S1B–D**). In contrast to subaquatic faults, river channels are characterized by a grooved shape without lithological differences of the same horizons (**Supplementary Figure S1C**).

The Y20B core is close to a subaquatic fault in the southeast of Yileimu Lake (**Supplementary Figure S1B**). It generally consists of a continuous lacustrine sequence. The sediments can be divided into six units (**Figures 2A,B**): 890–775 cm, greyish-brown sandy silt with coarse sand and scattered gravel at 793.5–790 cm; 775–650 cm, brown silt; 650–495 cm, brown sandy silt with silty sand at 624.5–611.5 cm; 495–240 cm, brown clayey silt with silt and scattered gravel at 323.5–319 cm; 240–110 cm, greyish-brown sandy silt with sand and scattered gravel at 228–215.5 cm; 110–0 cm, greyish-brown clayey silt with sand and scattered gravel at 68.5–53 cm and sandy silt at 2–0 cm.

The Y20A core can be divided into two units (**Supplementary Figure S2**): 267–160 cm, brownish-grey silty sand with coarse gravel and abundant plant residues at 267–260 cm, plus coarse sand and scattered fine gravel at 260–254 cm; 160–0 cm, greenish-grey clayey silt with occasional black bands. The occurrence of coarse gravel at the bottom of the Y20A core hinders access to longer sediment cores in the depocenter of Yileimu Lake.

AMS Radiocarbon Ages of Sediment Cores

The conventional ^{14}C age of organic matter from the top of the Y20B core is 890 ± 30 years BP, much older than the sampling date (**Figure 2B**; **Table 1**). The age data from the upper 450 cm of the Y20B core are generally consistent with stratigraphic order (**Figure 2B**; **Table 1**). The ^{14}C ages of organic matter at the depths of 45, 50, 200, 375 and 450 cm of the Y20B core are 8,800 ± 60,

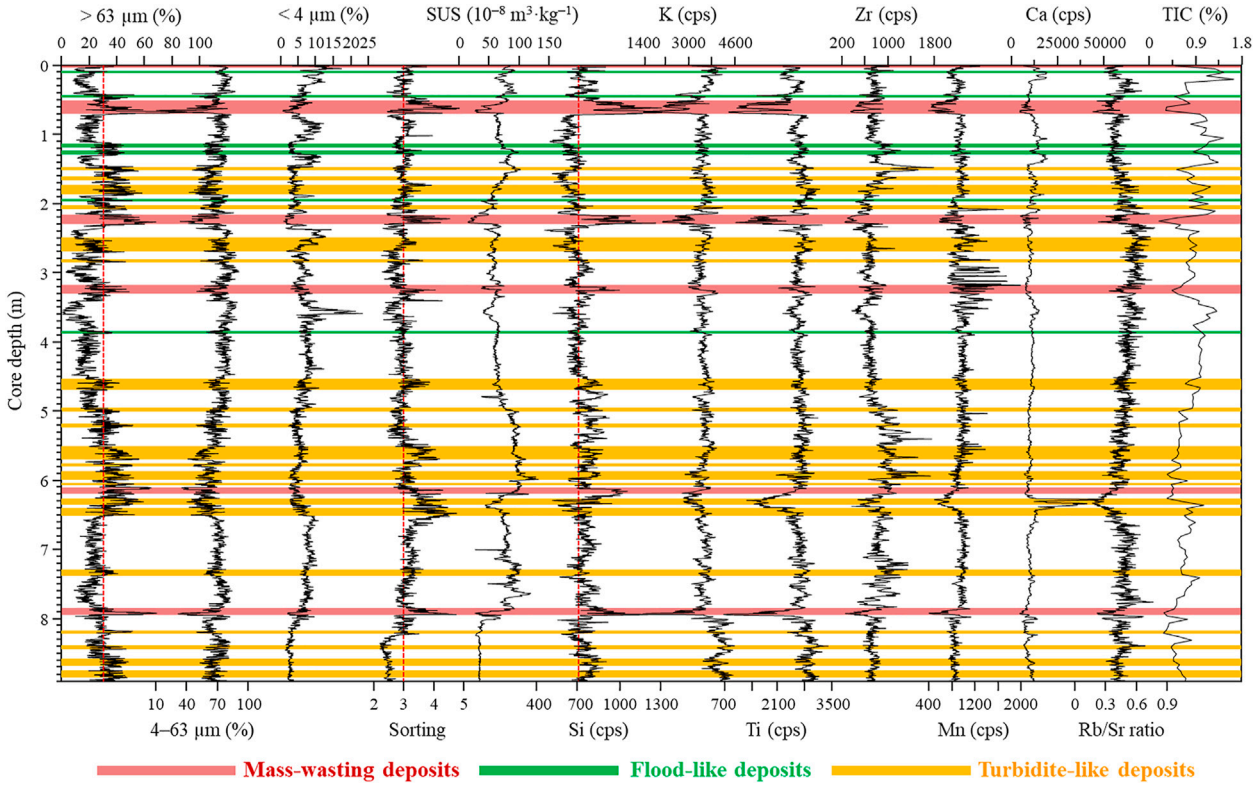

FIGURE 3 | Percentages of >63, 4–63 and <4 μm fractions, sorting index, magnetic susceptibility (SUS), major elemental contents, Rb/Sr ratio and total inorganic carbon (TIC) of the Y20B core. Red, green and yellow bars indicate the horizons of mass-wasting deposits (corresponding to **Figures 2C–H**), flood-like deposits and turbidite-like deposits, respectively. Flood-like deposits have cross bedding structures and turbidite-like deposits generally have normally graded bedding sequences.

8,820 ± 30, 13,600 ± 100, 16,460 ± 150 and 24,270 ± 80 year BP, respectively (**Figure 2B**; **Table 1**). Organic matter from the depth of 850 cm within the Y20B core has a ^{14}C age of 15,340 ± 50 years BP, much younger than the age of 20,110 ± 60 years BP found at 650 cm (**Figure 2B**; **Table 1**). The branch and wood from the depths of 198 and 264 cm of the Y20A core have conventional ^{14}C ages of 3,090 ± 35 and 3,180 ± 35 years BP, respectively (**Supplementary Figure S2**; **Table 1**).

Sedimentary Structures From XRF Radiographic Images

Sedimentary structures are obtained from painstaking searches of radiographic and optical images at 0.1-cm intervals throughout the Y20B and Y20A cores. The Y20B core contains 9 horizons of soft-sediment deformation structures (SSDS; **Figures 2C–J**), and six horizons of mass-wasting deposits overlying the SSDS (**Figures 2C–H**). The SSDS are 1–6.5 cm in thickness, and consist mainly of clayey silt (**Figures 2C,I,J**) and sandy silt (**Figures 2D–H**). They include linear waves (**Figures 2C,E,F,I,J**), micro-faults (**Figure 2D**), a liquefied diaper or convolute structures (**Figure 2G**), linear waves and clastic dykes (**Figure 2H**), and a clastic dyke (**Figure 2J**). The mass-wasting deposits are generally composed of poorly sorted medium- to coarse-sand with a massive structure and scattered gravel dispersed in (red bars in **Figure 3**). They are 2 cm (**Figure 2C**), 15.5 cm (**Figure 2D**), 14.5 cm (**Figure 2E**), 4 cm (**Figure 2F**), 13.5 cm (**Figure 2G**) and 8.5 cm (**Figure 2H**) in thickness, respectively. Except for the mass-wasting deposits at 624.5–611 cm depths, the others generally have normally graded sequences and clear lithological interfaces with the underlying SSDS (**Figures 2C–H**). There are no Bouma divisions, no horizontal or cross bedding, and no signs of bioturbation in the mass-wasting deposits. Sharp erosive bases can be found at the interfaces of typical mass-wasting deposits and the underlying SSDS (**Figures 2D,E**). The sediments consisting of sandy silt with clear cross-bedding structures and normally graded bedding sequences in the Y20B core are regarded as flood-like deposits (**Figure 2K**). The flood-like deposits are well sorted, and are less than 7 cm in thickness (green bars in **Figure 3**). In contrast, the sediments consisting of normally graded sandy silt without cross-bedding structures are regarded as turbidite-like deposits. The turbidite-like deposits have a wide range of thickness (1–19.5 cm) (yellow bars in **Figure 3**). The background sediments in the Y20B core mainly comprise laminated silt without graded sequences (e.g., **Figure 2L**). The Y20A core contains a horizon of mass-wasting deposits at 267–254 cm and a horizon of isolated SSDS layers (linear waves and convolute structures) at 171.7–168.2 cm (**Supplementary Figure S2**).

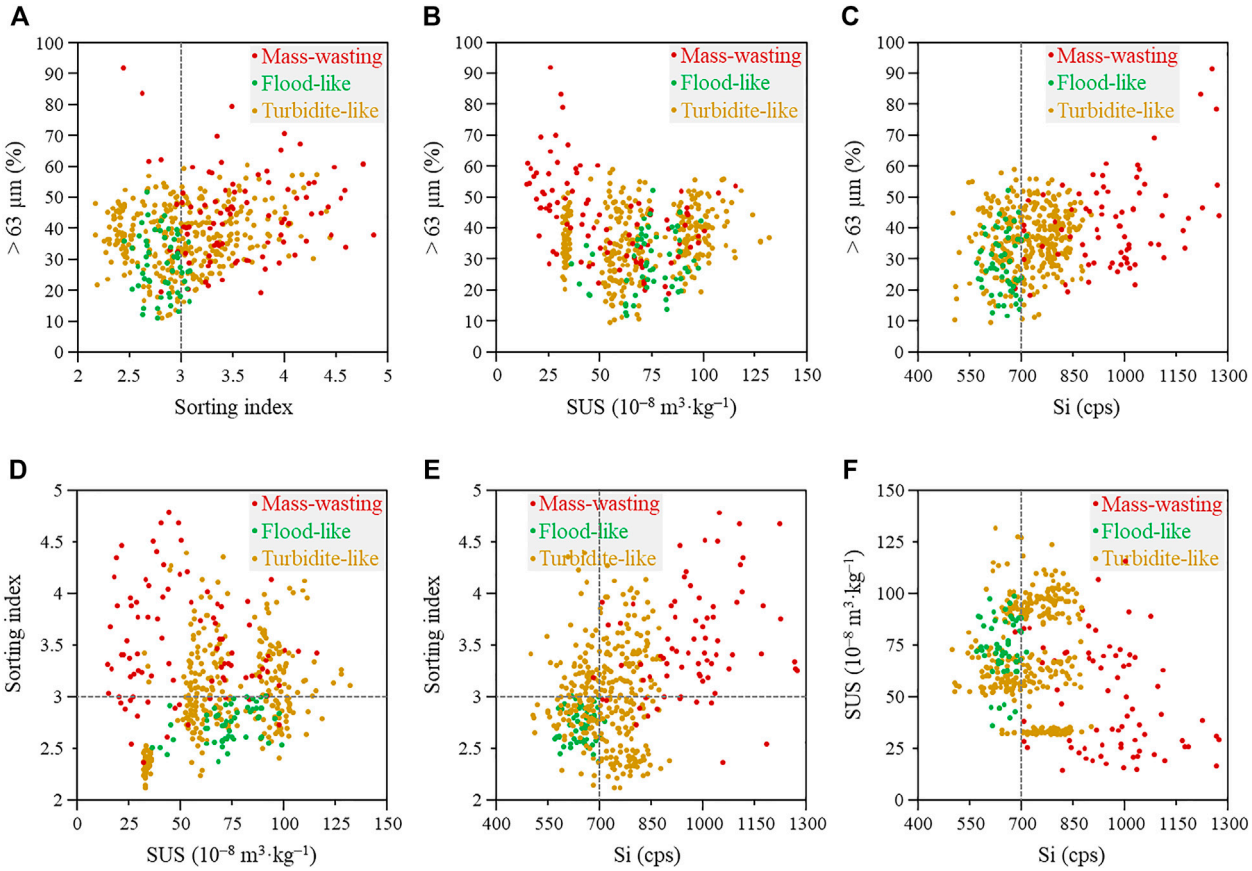

FIGURE 4 | Correlations between **(A)** percentage of >63 μm fraction and sorting index, **(B)** percentage of >63 μm fraction and SUS, **(C)** percentage of >63 μm fraction and Si content, **(D)** sorting index and SUS, **(E)** sorting index and Si content, and **(F)** SUS and Si content of the mass-wasting deposits, flood-like deposits and turbidite-like deposits from the Y20B core.

Sedimentary Proxies

There is no overall trend up the core in the variations of percentages of grain-size fractions, sorting index, SUS, major elemental contents or Rb/Sr ratio of the Y20B core (**Figure 3**). The average percentages of >63, 4–63 and <4 μm fractions are 24.7%, 69.3% and 6.0%, respectively. Sorting index and SUS have average values of 2.9 and 66.9 × 10^{-8} m^3 kg^{-1}, respectively. The average contents of Si, K, Ti, Zr, Mn and Ca are 721, 3,522, 2,617, 778, 940 and 10,696 counts per second (cps), respectively. Rb/Sr ratios and TIC contents have averages of 0.46% and 0.77%, respectively. There are a total of 32 horizons characterized by significantly high percentages of the >63 μm fraction (minimum peak value exceeds 30%). Among them, six horizons (red bars in **Figure 3**) correspond to the mass-wasting deposits (**Figures 2C–H**) and six other horizons correspond to the flood-like deposits (green bars in **Figure 3**). The remaining 20 horizons are turbidite-like deposits (yellow bars in **Figure 3**), generally characterized by abrupt increases in the percentages of >63 μm fraction at the bottom and gradual decreases upwards. The mass-wasting deposits also have remarkably high sorting indices (generally higher than 3) (high sorting indices indicate poor sorting of sediments), low SUS values (minimum valley value is only 14 × 10^{-8} m^3 kg^{-1}) and high Si contents (generally higher than 700 cps with minimum peak value exceeding 890 cps) (**Figures 2C–H**, **3**, **4**). In addition, PCA F1 and F2 account for 43.4% and 19.8% of the total variance within the elemental dataset of the Y20B core, respectively (**Figure 5A**). Three clusters can be defined: the first is dominated by Si, representing a quartz origin; the second is controlled by Ca and Sr, reflecting a plagioclase and/or carbonate origin; and the third is composed of K and other terrigenous elements (Ti, Fe, Rb, Mn, Al and Zr), with the K likely related to a K-feldspar origin (**Figure 5A**). The mass-wasting deposits have PCA F2 values generally lower than zero, and possess the minimum values of both PCA F1 (–12) and F2 (–4.9) throughout the Y20B core (**Figure 5B**). In contrast, the flood-like deposits have relatively low sorting indices (generally lower than 3), low Si contents (generally lower than 700 cps), and relatively high PCA F2 values (generally higher than zero) (**Figures 2K**, **3–5**). The turbidite-like deposits have wide ranging sorting indices (2.1–4.1) and Si contents (497–868 cps) (**Figures 3**, **4**), and have PCA F2 values generally lower than zero when their sorting index is higher than 3 (**Figure 5B**).

The Y20A core has ranges of mean grain size (Mz), percentages of >63 μm fraction, and Si content from 9.1 to

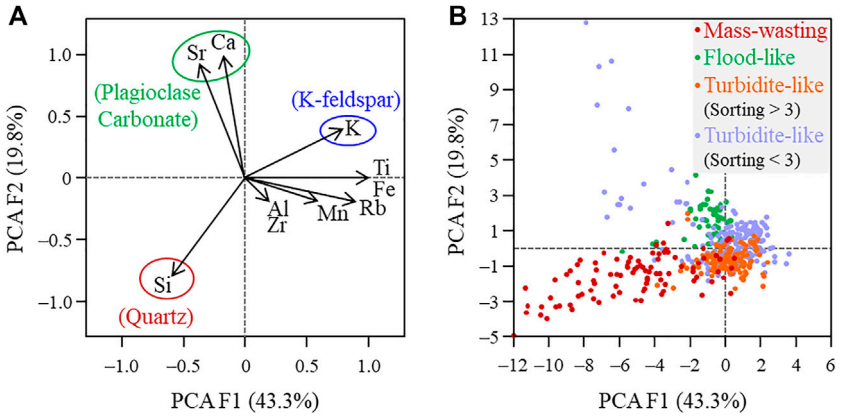

FIGURE 5 | (A) Variables factor map and **(B)** individuals factor map for principal component analysis (PCA) performed on the standardized elemental data of the Y20B core.

321.4 μm, 0%–79.8%, and 193–1376 cps, respectively (**Supplementary Figure S3**). The 260–158 cm depths of the Y20A core is characterized by relatively high values and decreasing trends of Mz, percentages of >63 μm fraction and Si content, equivalent to the 70–40 cm depths of the Y20B core (orange bar in **Supplementary Figure S3**). The peak values of Mz and Si content at 254 cm within the Y20A core correspond to those at 65.5 cm within the Y20B core (**Supplementary Figure S3**). The radiocarbon sampling depths of 198 and 264 cm within the Y20A core can be cautiously correlated with the depths of 50 and 72 cm within the Y20B core, respectively (**Supplementary Figure S3**). The upper 2 cm of the Y20B core, the upper 5 cm of the Y19 core, and the upper 2.5 cm of the Y20 core can be confidently correlated with one other (**Supplementary Figure S3**). The age at 5 cm depth within the Y19 core is 1931 AD, corresponding to the 11 August 1931 M_s 8.0 Fuyun earthquake (Fan et al., 2020b); therefore, the age at 2 cm depth within the Y20B core can also be inferred as 1931 AD (**Supplementary Figure S3**).

DISCUSSION

Sedimentary Record of Paleoearthquakes

Subaquatic faults are present in Yileimu Lake (**Supplementary Figures S1A–D**). These subaquatic faults should not be parts of the Fuyun Fault (**Figure 1A**, **Supplementary Figure S1A**). They were probably produced by seismic shaking from the Fuyun Fault, because the Fuyun Fault was the most active fault in the study area, and the lake was bounded by the Fuyun Fault (**Figure 1A**). The existence of these subaquatic faults suggests that the lake sediments are very sensitive to local seismic activities. However, there may be differences in the sedimentary response to seismicity in different areas of the lake. The Y20B core is located near a subaquatic fault in the nearshore zone of Yileimu Lake (**Figure 1B**, **Supplementary Figure S1B**), potentially representing a promising site to record past earthquakes. The Y20A core is located in the depocenter of Yileimu Lake (**Figure 1B**, **Supplementary Figure S1C**), a location characterized by a flat lake floor and lack of coarse sediments.

Soft-sediment deformation structures (SSDS) in lake sediments (deformed sediments relative to the background sediments) can be triggered by co-seismic (Sims, 1973) and non-seismic processes such as gravity (Van Daele et al., 2014) and wave loading (Migeon et al., 2017). Yileimu Lake is bounded by the Fuyun Fault which produced at least 4 prehistoric $M_s \geq 8.0$ earthquakes (Klinger et al., 2011), and the SSDS consisting of linear waves, were related to the 11 August 1931 M_s 8.0 Fuyun earthquake (**Figure 2C**) (Fan et al., 2020b). Some SSDS in the Y20B core contain high-angle micro-faults, a liquefied diaper or convolute structures, linear waves and clastic dykes, and a clastic dyke (**Figures 2D,G,H,J**), comparable to those produced by experimental and historical earthquakes (e.g., Jiang et al., 2016, 2017). Previous studies indicated that micro-faults were related to seismic-induced brittle failure of carbonate mud with a high initial lithification rate and a considerable strength and density shortly after deposition (Monecke et al., 2004 and references therein). The sedimentary layers of micro-faults at 74–68 cm depths of the Y20B core have much higher TIC (carbonate) contents than those of other types of SSDS (**Figures 2C–J**, **3**). These micro-faults can be produced by an oscillatory movement of the water column and surface sediments during seismic shaking (Migeon et al., 2017). Changes in hydrodynamic conditions should have not been responsible for micro-faults, as evidenced by the absence of micro-faults in other layers of the Y20B core, and in lake sediments which experienced significant changes in hydrodynamic conditions and hardly affected by seismic activities in North China (e.g., Fan et al., 2019). Convolute structures were complex forms of load structures and interpreted as a combination of bulk-density heterogeneities and fluidization associated with water-escape structures during seismic shaking (Suter et al., 2011 and references therein). Linear waves were considered as the results of horizontal movement with different velocities of the laminated layers at water–sediment interfaces, associated with the occurrence of shear energy induced by earthquakes (Lu et al., 2020; Wetzler et al., 2010). Clastic dykes were interpreted as the

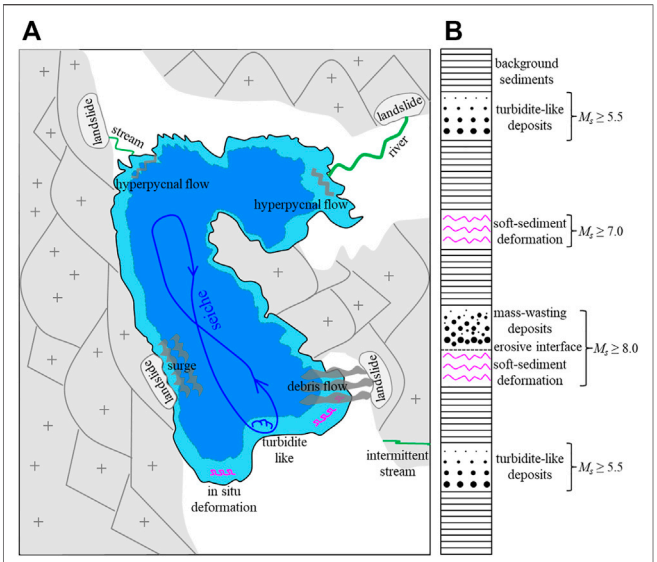

FIGURE 6 | A conceptual model showing **(A)** sedimentary processes in response to seismic shaking and **(B)** earthquake imprints on a sediment core from the nearshore zone of the lake. Mass-wasting deposits include sediments transported by debris flows and hyperpycnal flows.

infillings of hydrofractures during the upward escape of seismic-induced fluidized sediments, when water pressures in the basal layer exceeded the overlying layer (Chen et al., 2009; Moretti, 2000). Therefore, the repeated occurrence of SSDS in the sediments of Yileimu Lake is most likely seismic origin (**Figures 6A,B**). The co-occurrence of some SSDS at the corresponding depths of the Y20A and Y20B cores (**Supplementary Figures S2, S3**) provides support for seismic origin of these widely distributed SSDS in Yileimu Lake. In contrast, gravity-induced SSDS should produce a dominant and regular direction of clastic materials (Van Daele et al., 2014), and wave loading-induced SSDS should produce parallel or regular cross bedding (Beck, 2009; Migeon et al., 2017). There are a total of 9 distinct horizons of SSDS in the Y20B core (**Figures 2C–J**), with each separated by non-seismic horizontal laminations (e.g., **Figure 2J**), indicating 9 past earthquakes originating from the Fuyun Fault (E1–E5, E7, E10, E15 and E19 in **Figure 7**).

Mass-wasting deposits in sediments from small lakes in tectonically active regions were interpreted as the products of coseismic landslides and/or subaqueous slope failures (e.g., Howarth et al., 2014; Lu et al., 2017; Van Daele et al., 2017). In order to distinguish landslide-related deposits from those subaqueous origins in Yileimu Lake, mass-wasting deposits are regarded only as post-seismic deposits from landslides in the lake catchment in this study. Mass-wasting deposits were commonly seen in sediments from small lakes in tectonically active regions (e.g., Howarth et al., 2014; Oswald et al., 2021). The 6 horizons of mass-wasting deposits in the Y20B core consist of poorly sorted sand and scattered, irregularly shaped gravel, and have no Bouma divisions or signs of bioturbation (**Figures 2C–H**, **3**, **4**). The mass-wasting deposits in Yileimu Lake can be interpreted as post-seismic deposits transported by debris flows and/or hyperpycnal flows, reflecting coarse sediment fluxes from earthquake-triggered landslides from surrounding high and steep mountains (**Figures 6A,B**) (e.g., Howarth et al., 2012; Moernaut, 2020). The mass-wasting deposits overlying the SSDS in Yileimu Lake (**Figures 2C–H**) supports the seismic origin of landslides in the lake catchment and *in situ* deformations within the lake (e.g., Lu et al., 2021a). The sharp erosive bases at the interfaces of typical mass-wasting deposits and the underlying SSDS (**Figures 2D,E**) may have resulted from the horizontal movement of bottom water in the lake, induced by shear energy during seismic shaking. The mass-wasting deposits at the top of the Y20B core correspond to the 11 August 1931 M_s 8.0 Fuyun earthquake (**Figure 2C**, **Supplementary Figure S3**). The thickness of these deposits is only 1.5 cm, much thinner than the other 5 horizons of mass-wasting deposits (**Figures 2C–H**). Flood events in the 1900s AD may have expanded the size of the lake (Fan et al., 2021), possibly resulting in increasing distance between the site of the Y20B core and landslide sources, and thereby reducing the sediment flux to the core site. Increased water storage in Yileimu Lake after reservoir construction in the 1950s AD (Fan et al., 2020b) may have also reduced the sedimentation rate in the lake. These factors may therefore have reduced the thickness of the mass-wasting deposits related to the 11 August 1931 M_s 8.0 Fuyun earthquake. The flood-like deposits are well sorted and have clear cross-bedding structures (e.g., **Figures 2K**, **3**, **4**), similar to those flood deposits formed in strong hydrodynamic conditions (Benito et al., 2003).

Yileimu Lake is surrounded by hills of granitic rocks on the west and east (**Figure 1B**). The 11 August 1931 M_s 8.0 Fuyun earthquake caused extensive landslides, providing a large amount of siliciclastic-enriched clastic materials in the lake catchment, and thereby producing the Si-enriched mass-wasting deposits at the top of the Y20B core (**Figure 2C**). The other 5 horizons of mass-wasting deposits have even higher Si content than those at the top of the Y20B core (**Figures 2D–H**, **3**), potentially implying more serious landslides caused by prehistoric great earthquakes. Mn content is generally low in the mass-wasting deposits (**Figures 2C–H**, **3**), indicating oxygen-depleted sedimentary environments and rapid accumulation for these post-seismic deposits (Wils et al., 2021). TIC content is generally low and exhibits an increasing trend throughout the Y20B core, and there are no systematic correlations between the Ca and TIC contents (**Figure 3**). Therefore, a large amount of Ca (as well as Sr) should originate from plagioclase in addition to carbonates (**Figure 5A**). Rb/Sr ratio is generally low in the mass-wasting deposits (**Figure 3**), reflecting weak chemical weathering in the lake catchment (Fan et al., 2021). These data indicate that sediment sources for mass-wasting deposition in Yileimu Lake should have mainly been provided by earthquake-related landslides of weakly weathered granitic rocks. Overall, the mass-wasting deposits overlying the SSDS in the Y20B core reflect 6 past earthquakes (E1, E3, E7, E10, E15 and E19 in **Figure 7**).

Lacustrine turbidites are characterized by gradually upward decreasing grain size, and can be produced by earthquake-induced slope failures and/or slumps in tectonically active regions (e.g., Bertrand et al., 2008; Howarth et al., 2021; Moernaut et al., 2014). However, turbidites can also be formed

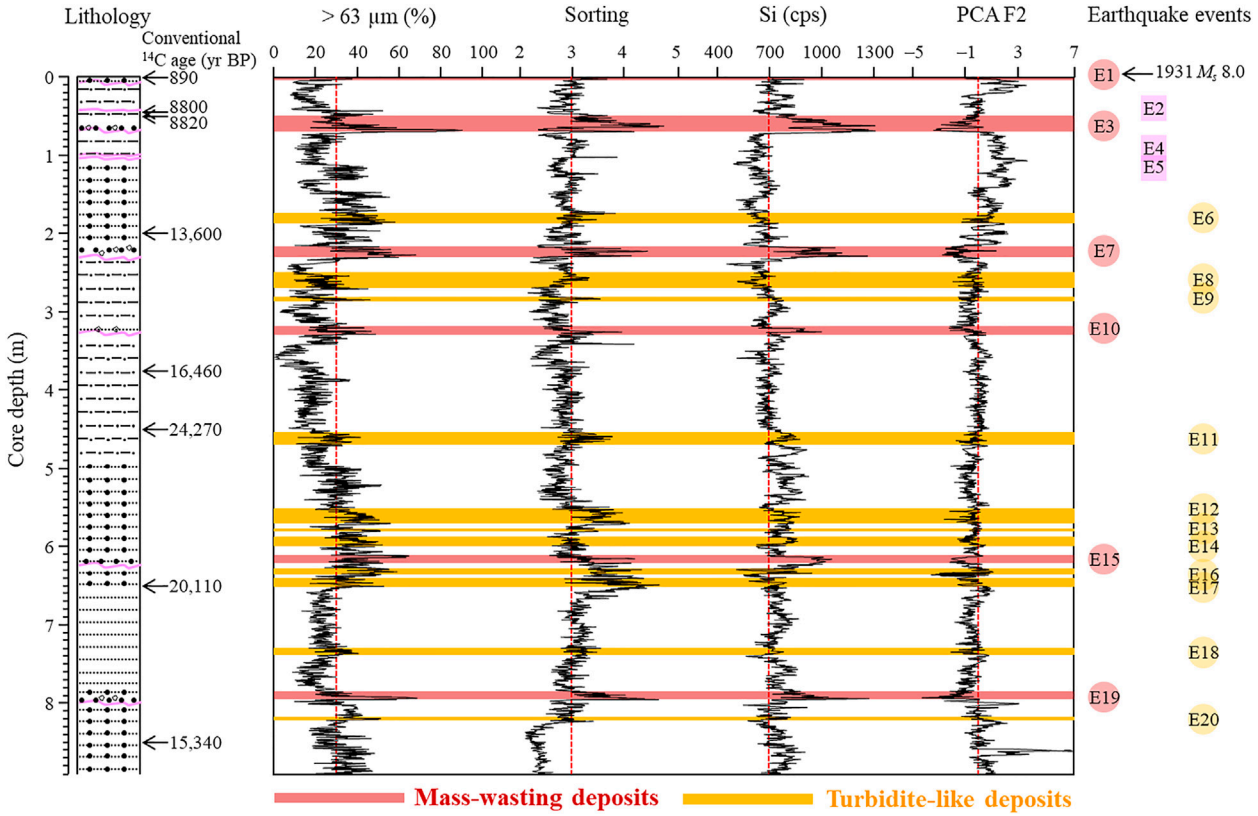

FIGURE 7 | Sedimentary record of past earthquakes inferred from the mass-wasting deposits with underlying SSDS (E1, E3, E7, E10, E15 and E19), isolated SSDS (E2, E4 and E5) and turbidite-like seismites (E6, E8–E9, E11–E14, E16–E18 and E20) from the Y20B core. Lithological legends and conventional ^{14}C ages are same as **Figure 2**.

by flood events (Beck, 2009; Migeon et al., 2017; Praet et al., 2020). Earthquake-related turbidites were commonly characterized by rapidly accumulated and poorly sorted deposits, while flood-induced turbidites were usually well sorted and contain cross-bedding structures and normally graded bedding sequences (Migeon et al., 2017; Moernaut et al., 2014) (e.g., **Figure 2K**). In this study, the deposits having similar grain-size structures to those turbidites are regarded as "turbidite-like" deposits. It is noted that earthquake-induced mass-wasting deposits have sorting indices >3, Si contents >700 cps and PCA F2 < 0 that can be distinguished from flood-like deposits (sorting indices <3, Si contents <700 cps and PCA F2 > 0) in Yileimu Lake (**Figures 3–5**). Therefore, turbidite-like deposits with sorting indices >3, Si contents >700 cps and PCA F2 < 0 are interpreted as seismites in Yileimu Lake (**Figure 7**). When compared with the mass-wasting deposits, the turbidite-like seismites have relatively lower Si contents (**Figures 3**, **4**), implying that the main sediment sources for these turbidite-like seismites were unlikely to be the Si-enriched clastic materials from extensive landslides of granitic rocks in the lake catchment. These turbidite-like seismites may have mainly been related to the re-deposition of nearshore sediments after intense shaking of the lake. Seismic shaking could cause an oscillatory movement of the water column (a seiche effect), and disturb the surface sediments at water-sediment interface (Migeon et al., 2017), resulting in successive re-deposition of sand, silt and clay, forming the turbidite-like deposits. Subaquatic slumps or slope failures within the lake should be secondary factors, because the lake floor is not very steep (**Figure 1B**) (e.g., Schnellmann et al., 2002). The turbidite-like seismites in the Y20B core indicate 11 potential earthquakes (E6, E8–E9, E11–E14, E16–E18 and E20 in **Figure 7**).

Potential Magnitudes for Paleoearthquakes

The 11 August 1931 M_s 8.0 Fuyun earthquake caused extensive landslides of granitic rocks and triggered mass-wasting deposits in the Yileimu Lake catchment (Fan et al., 2020b). Seismic intensity calculation results based on intensity prediction equations (IPEs) from Wang et al. (2000) and Dowrick and Rhoades (2005) were consistent with the published seismic intensity map of the 11 August 1931 M_s 8.0 Fuyun earthquake based on field survey by Shi et al. (2010). These data indicated that an intensity of 8.6 MMI (epicentral distance 50 km) was required for past earthquakes to trigger extensive landslides in the Yileimu Lake catchment (Fan et al., 2020b) (**Figures 8A,B**). Similarly, a minimum intensity of 9 MMI was required for earthquakes produced by the Alpine Fault to cause extensive landslides in the Ellery Lake catchment (Howarth et al., 2016). The small difference of intensity thresholds for landslides in the above two

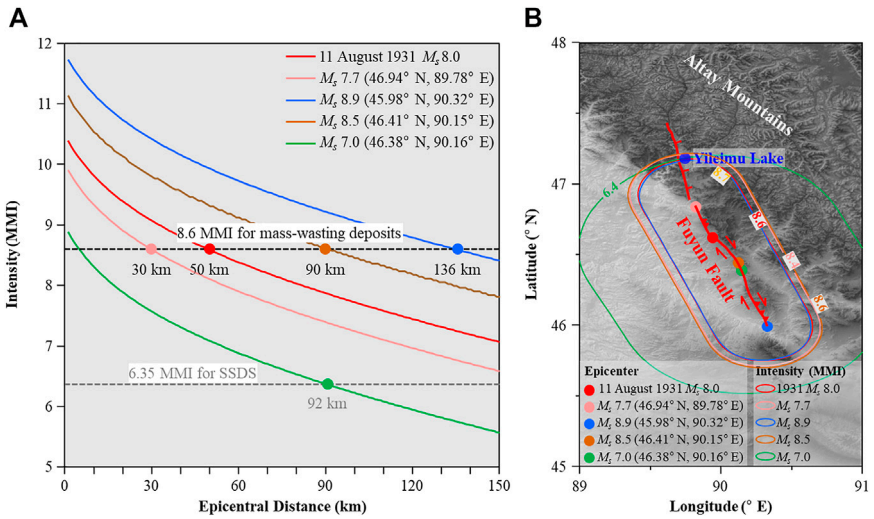

FIGURE 8 | (A) Shaking intensity variations with epicentral distance and **(B)** calibrated isoseismal modelling results for different magnitudes of earthquakes from different sites along the Fuyun Fault. The pink, red, brown, blue and green circles in **(A,B)** are in one-to-one correspondence. The intensity prediction equations (IPEs) used in **(A,B)** are from Wang et al. (2000), and Dowrick and Rhoades (2005), respectively. MMI, Modified Mercalli Intensity.

lake catchments may be related to the different slope angles and rock types. A local intensity of 8.6 MMI in Yileimu Lake could be produced by distant large earthquakes or proximal small earthquakes, making it difficult to determine the magnitudes of prehistoric earthquakes.

The Fuyun Fault is the main seismogenic fault in the study area. It generally consists of a ~50 km-long normal fault segment in the north and a ~120 km-long thrust-slip fault segment in the south (**Figures 1A**, **8B**) (Klinger et al., 2011; Xu et al., 2012). All historical $M_s \geq 7.0$ earthquakes in the study area occurred in the thrust-slip segment (**Figure 1A**). Therefore, it is the southern segment of the Fuyun Fault that seems to have the great potential to trigger large earthquakes. Based on the IPEs from Wang et al. (2000) and Dowrick and Rhoades (2005), an intensity of 8.6 MMI in Yileimu Lake could be generated by an M_s 7.7/8.9 earthquake at the north/south end of the southern fault segment (epicentral distance 30/136 km) in the geological past (**Figures 8A,B**), assuming these earthquakes had similar hypocentral depth, strike, dip and rake to those of the 11 August 1931 M_s 8.0 Fuyun earthquake (Fan et al., 2020b). In addition, characteristic dextral offsets of terraces and stream channels produced by prehistoric $M_s \geq 8.0$ earthquakes from the Fuyun Fault are mainly distributed in the central part of the southern fault segment (Klinger et al., 2011). Hence, it is likely that great earthquakes occurred mainly in the central part of the southern segment of the Fuyun Fault (epicentral distance ~90 km). Therefore, an intensity of 8.6 MMI in Yileimu Lake should be produced by prehistoric $M_s \geq 8.0$ (perhaps M_s 8.5) earthquakes from the Fuyun Fault (**Figures 6B**, **8A**,**B**).

Previous studies suggested that an intensity of 6.5 MMI was required for past earthquakes to produce *in situ* SSDS of linear waves in the Dead Sea, according to the computational fluid dynamics modelling results (Lu et al., 2020). However, these modelling results cannot be simply applied to Yileimu Lake because the lithology, sediment compaction and SSDS in the Y20B core, and the water depth of Yileimu Lake are significantly different from those in Dead Sea. In northern Xinjiang, a minimum intensity of 6.35 MMI could trigger slight SSDS (e.g., linear waves), and an intensity of 7 MMI was able to cause extensive soil liquefaction (Li et al., 2012). Therefore, a local intensity of 6.35 MMI was used as a threshold to trigger SSDS of linear waves in Yileimu Lake. An intensity of 6.35 MMI in Yileimu Lake was likely induced by an $M_s \geq 7.0$ earthquake from the central part of the southern segment of the Fuyun Fault (epicentral distance 92 km) (**Figures 8A,B**). There was no evidence for historical $M_s < 7.0$ earthquakes being able to produce SSDS in the Yileimu Lake catchment (Fan et al., 2020b). In addition, the SSDS of micro-faults (**Figure 2D**), convolute structures (**Figure 2G**) and linear waves and clastic dykes (**Figure 2H**) underlying the mass-wasting deposits in Yileimu Lake, indicates that an intensity of 8.6 MMI (potential $M_s \geq 8.0$ earthquakes) was sufficient to trigger these SSDS. Therefore, the isolated SSDS of linear waves (**Figures 2I,J**) and a clastic dyke (**Figure 2J**) should indicate prehistoric $7.0 \leq M_s < 8.0$ earthquakes (**Figure 6B**).

Turbidite seismites were triggered by a minimum shaking intensity of 5.3–5.7 MMI in Rara Lake in the central Himalaya (Ghazoui et al., 2019). In southern Altay, a historical M_s 5.8 earthquake (epicentral distance 30 km) induced turbidite-like seismites in Yileimu Lake which indicated an intensity threshold of 5.51 MMI (Fan et al., 2020b). In contrast, there was no evidence that historical $M_s < 5.5$ earthquakes could trigger turbidite-like seismites in Yileimu Lake (Fan et al., 2020b). Therefore, a minimum magnitude M_s 5.5 earthquake within a maximum distance of 25 km from Yileimu Lake appears to be required to cause turbidite-like seismites in the lake (**Figure 6B**), based on the IPEs from Wang et al. (2000) and Dowrick and Rhoades (2005). In addition, previous studies suggested a linear

correlation between shaking intensity and turbidite thickness in the south central Chilean lakes (Moernaut et al., 2014). However, distinct lake morphologies and sediment lithology may cause different sedimentary responses to past earthquakes, producing unique intensity thresholds for various turbidites in specific lakes (Moernaut et al., 2014; Lu et al., 2021a). The lack of temporal correlation between historical earthquakes and turbidite-like seismites in Yileimu Lake makes it very difficult to assess the potential magnitudes of prehistoric earthquakes. Since there were no SSDS associated with these turbidite-like seismites, a magnitude M_s < 7.0 was tentatively considered as the maximum threshold.

Timing and Recurrence Behavior of Paleoearthquakes

The ^{14}C age of organic matter from the top of the Y20B core is much older than the sampling date (**Figure 2B**; **Table 1**), possibly reflecting reservoir effects (e.g., Zhou et al., 2009). However, this ^{14}C age is not suitable for calibrating the reservoir effects of the Y20B core, because human- activities (for example, reservoir construction in Yileimu Lake, mine exploitation in Koktokay about 7 km east of Yileimu Lake, and agricultural activities such as grazing in the lacustrine plains) in recent decades (Fuyun County Local Chronicles Compilation Committee, 2003) should have significantly changed the reservoir effects in the shallow water regions of Yileimu Lake. The linearly fitted age–depth curve of the Y20B core shows an intercept of 8,052.1 year (**Supplementary Figure S4**), indicating a potential reservoir effect of thousands of years for the Y20B core. Great earthquake events such as $M_s \geq 8.0$ earthquakes could cause significant changes in the sediments of the whole lake (e.g., Howarth et al., 2014; Wils et al., 2021), allowing for stratigraphic correlations between event layers in the Y20A and Y20B cores (**Supplementary Figure S3**). The branch at 198 cm depth within the Y20A core has a ^{14}C age of 3,090 ± 35 years BP (**Supplementary Figures S2, S3**; **Table 1**). The ^{14}C age of organic matter at 50 cm depth within the Y20B core is 8,820 ± 30 years BP (**Supplementary Figures S2, S3**; **Table 1**). The depth of 198 cm within the Y20A core corresponds to the depth of 50 cm within the Y20B core (**Supplementary Figure S3**), therefore, the age difference between these two corresponding depths (5,730 years) is used as the reservoir correction factor (**Table 1**).

In addition, the linearly fitted age–depth curve of the Y20B core also shows an anomalously old ^{14}C age at 450 cm depth and an anomalously young ^{14}C age at 850 cm depth within the Y20B (**Supplementary Figure S4**; **Table 1**). The sediments at 450 cm depth within the Y20B core were deposited immediately after the earthquake event E11 (**Figure 7**) which may have produced excessive input of old carbon into the lake through remobilization of buried soils in the lake catchment. In addition, the organic matter at 850 cm depth within the Y20B core was very low, and the anomalously young ^{14}C age of organic matter at 850 cm depth within the Y20B core may have been caused by the incorporation of young carbon into the sediments, potentially sourced from near-surface groundwater. Therefore, the ^{14}C ages obtained from 450 to 850 cm depths within the Y20B core are not used. Hence, a total of 7 age data points, including the sampling date of −70 cal year BP at the core top, the ^{14}C ages of the branch and wood at 198 and 264 cm depths within the Y20A core (corresponding to 50 and 72 cm depths within the Y20B core), and the ^{14}C ages of organic matter at 45, 200, 375 and 650 cm depths within the Y20B core, are used in the Bayesian age–depth model. The four ^{14}C ages of organic matter are corrected through subtracting the reservoir correction factor, and then calibrated to the calendar ages (**Figure 9A**; **Table 1**).

The SSDS, mass-wasting deposits and turbidite-like seismites within the Y20B core record a total of 20 potential paleoearthquakes (E1–E20) originating from the Fuyun Fault (**Figure 7**). Post-seismic sediments are rapidly deposited (e.g., Howarth et al., 2014; Avşar et al., 2016; Wils et al., 2021), as evidenced by the almost same ages within the seismites (Fan et al., 2020b). Therefore, the thickness of the mass-wasting deposits and turbidite-like seismites are removed to normalize the depth of the Y20B core. In contrast, the flood-like deposits and the turbidite-like non-seismites are relatively thin and occur frequently; these sediments are not excluded in the age–depth model (Avşar et al., 2015). The Bayesian age–depth model based on the normalized core depth and 7 age data points shows an almost linear curve, indicating that there were no significant discontinuities in the Y20B core, consistent with the lithological characteristics (**Figures 2A,B**). The age–depth model indicates a ^{14}C age of 18.8 cal year BP at 2–0.5 cm depths of the Y20B core, corresponding to the 1931 M_s 8.0 Fuyun earthquake (**Figures 2**, **6**, **9A**,**B**). The Y20B core covers the past 28 kyr (**Figures 9A,B**). The sedimentation rate in the last 3 kyr (~0.15 mm/year) is slightly lower than the preceding period (~0.34 mm/year).

The sedimentary proxies, except for the TIC content, of the Y20B core spanning the past 28 kyr did not exhibit the typical climate fluctuations during the Last Glacial Maximum (LGM)–Deglaciation–Holocene periods (**Figure 3**). The catchment of Yileimu Lake is surrounded by high mountains to the northeast which are covered with perennial snow and ice 3,000 m above sea level (a.s.l.). Therefore, possible snow and ice melting during warming seasons in the geological past may have increased the transport of coarse particles into the lake, concealing the climate characteristics (cold and wet in the LGM and Deglaciation, and warm and dry in the Holocene) of the Westerlies-dominated arid Asia (e.g., Sun et al., 2013), including the Altay region, and reducing the difference in the percentages of >63 μm fraction between the seismic horizon of the E15 event and the adjacent non-seismic horizons (**Figure 7**). The TIC in the Y20B core was mainly from carbonates produced by inorganic precipitation within the lake water, because there were no carbonate rocks in the Yileimu Lake catchment. The TIC contents cannot be ignored throughout the Y20B core (**Figure 3**), implying a dominant subaquatic environment. The Bayesian age–depth model of the Y20A core indicates that the sedimentation rates in the nearshore zone of Yileimu Lake were much lower than those in the depocenter (**Supplementary Figures S2, S3**). This was probably because the depocenter of Yileimu Lake was closer to the rivers entering the lake (**Figure 1B**).

The 6 potential $M_s \geq 8.0$ earthquakes indicated by the mass-wasting deposits overlying SSDS in the Y20B core occurred 15–22, 3,132–3,535, 7,824–9,396, 10,084–11,910, 17,425–20,868 and 22,307–26,665 cal year BP, respectively, based on the Bayesian

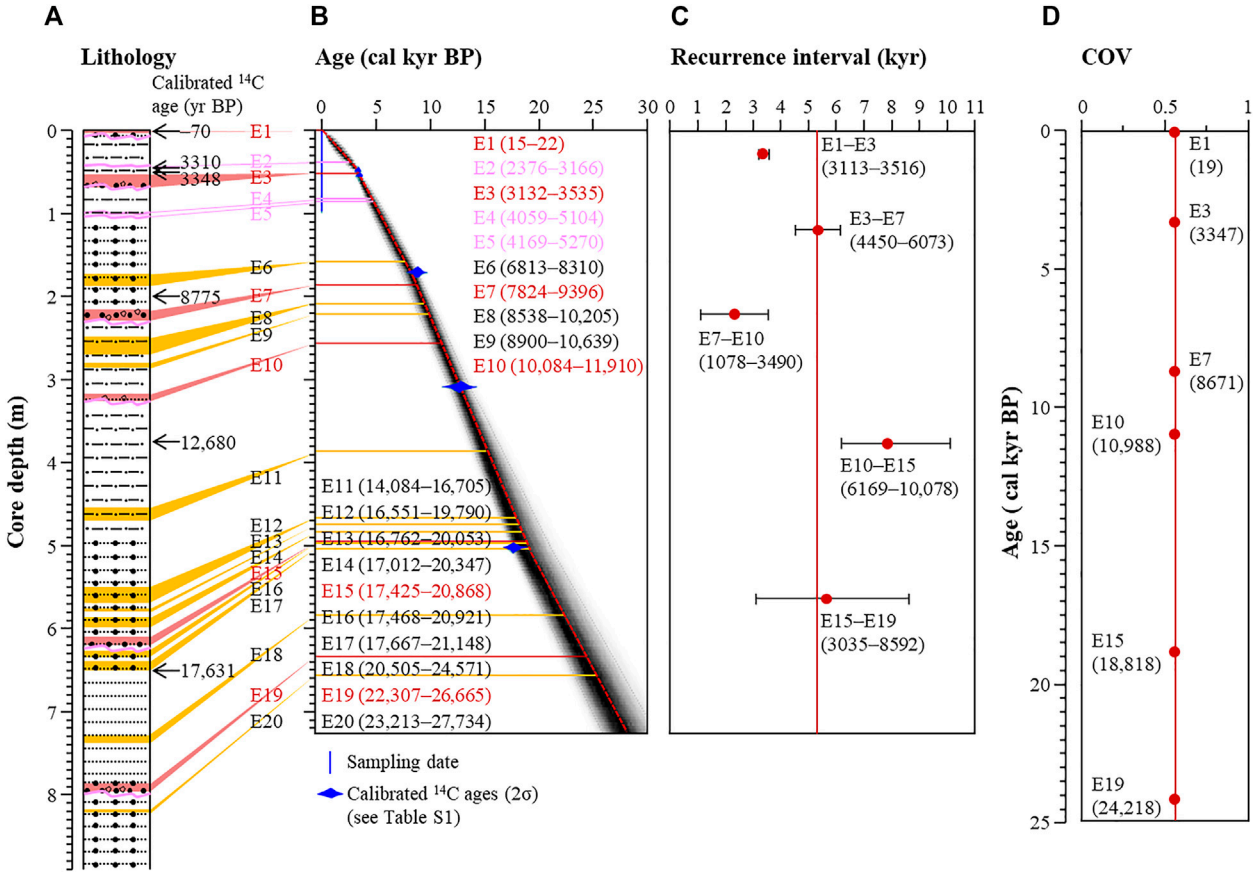

FIGURE 9 | (A) Lithology, calibrated ^{14}C ages and sedimentary record of past earthquakes from the Y20B core. Red and yellow bars indicate the horizons of mass-wasting deposits and turbidite-like seismites, respectively. Lithological legends are same as **Figure 2**. **(B)** Bayesian age–depth model of the Y20B core. Red dashed line indicates weighted mean age. The Bayesian ages (cal year BP) of earthquake events (E1–E20) are given in parentheses. **(C)** Recurrence intervals of potential $M_s \geq 8.0$ earthquakes (E1, E3, E7, E10, E15 and E19). Red circles indicate weighted mean recurrence intervals, and red line indicates average recurrence interval (5,303 years). **(D)** Coefficient of variation (COV) for potential $M_s \geq 8.0$ earthquakes. Red circles indicate weighted mean ages of earthquakes, and red line shows the COV value (0.57).

age-depth model (**Figure 9B**). The recurrence intervals for these earthquakes were between 2,317 and 7,830 years with an average of 5,303 years (**Figure 9C**), much longer than the dating uncertainties (**Figures 9B,C**), and much shorter than the previously published recurrence interval of 9,700 ± 3,300 years for prehistoric $M_s \geq 8.0$ earthquakes originating from the Fuyun Fault (Xu et al., 2012). The timing of these earthquakes was weakly periodic, with a coefficient of variation (COV) of 0.57 (**Figure 9D**) (Moernaut, 2020). The three potential $M_s \geq 7.0$ earthquakes reflected by the three isolated SSDS in the Y20B core occurred 2,376–3,166, 4,059–5,104 and 4,169–5,270 cal year BP, respectively (**Figure 9B**). The minimum recurrence interval of these earthquakes was 110 years, comparable to the previously published interval of 96 years (Fan et al., 2020b). The 11 potential $M_s \geq 5.5$ earthquakes implied by the turbidite-like seismites in the Y20B core occurred between 6,813 and 8,310 and 23,213–27,734 cal year BP, and mainly occurred before 14,084–16,705 cal year BP (**Figure 9B**).

Low sedimentation rate may hinder the identification of sediment features produced by earthquakes with relatively short recurrence intervals (Moernaut et al., 2014). However, a much higher frequency of potential $M_s \geq 7.0$ earthquakes were recorded by the SSDS in the Y20B core over the last 5 kyr, during which time the sedimentation rate of the Y20B core was even lower than the preceding period (**Figure 9B**). Future studies on multi-lake paleoseismic records from different parts of the Fuyun Fault may reveal an even more accurate recurrence pattern of past earthquakes, since small, distant earthquakes (e.g., $M_s \geq 5.5$) may not be recorded in a single lake, and individual lakes with different morphologies, lake levels, sedimentation rates, sediment sources and catchment reliefs may also have different sensitivities to past earthquakes (Moernaut et al., 2014; Hubert-Ferrari et al., 2020; Lu et al., 2021b).

CONCLUSION

Lake sediments in tectonically active regions can provide a complementary paleoseismic record. Widely distributed subaquatic faults in Yileimu Lake, imaged by reflection seismic profiles, indicate that the lake was very sensitive to

past earthquakes originating from the Fuyun Fault. The mass-wasting deposits overlying SSDS in an 890-cm long sediment core from Yileimu Lake reveals six paleoearthquakes with potential magnitudes of $M_s \geq 8.0$, and isolated SSDS reflect three additional potential $M_s \geq 7.0$ paleoearthquakes. Potentially seismic turbidite-like deposits can be distinguished from those with non-seismic origins by sorting indices >3 and Si contents >700 cps. The turbidite-like seismites record 11 potential $M_s \geq 5.5$ paleoearthquakes. Radiocarbon dating and stratigraphic correlations constrain the timing of these past earthquakes to ~28 cal kyr BP. This paleoseismic record suggests a weakly periodic pattern with recurrence intervals between 2,317 and 7,830 years and an average of 5,303 years for potential $M_s \geq 8.0$ earthquakes, and reveals an unprecedented high frequency of potential $M_s \geq 7.0$ earthquakes originating from the Fuyun Fault in the last 5 kyr. These data provide new insights into the recurrence behavior of large earthquakes from intraplate, slow-slipping faults, and highlight the urgent need for an improved assessment of seismic hazards and risks in the Fuyun Fault zone. Future studies on lake sediments with higher sedimentation rates and with wider spatial coverage may help to obtain a more complete paleoseismic record.

DATA AVAILABILITY STATEMENT

The raw data supporting the conclusions of this article will be made available by the authors, without undue reservation.

AUTHOR CONTRIBUTIONS

JF: Conceptualization, data curation, formal analysis, investigation, writing—original draft, writing—review and editing, project administration, resources, supervision. HX: Data curation, investigation, writing—review and editing. WS: data curation, investigation. QG: Data curation, investigation. SZ: Investigation. XW: Data curation. MC: Data curation. SH: Investigation. JW: Data curation. JX: Conceptualization, writing—review and editing.

FUNDING

This study is supported by the National Nonprofit Fundamental Research Grant of China, Institute of Geology, China Earthquake Administration (IGCEA2009).

ACKNOWLEDGMENTS

The authors are grateful to Yin Lu from the Institute of Geology, University of Innsbruck (Innsbruck, Austria) for insightful discussions.

SUPPLEMENTARY MATERIAL

The Supplementary Material for this article can be found online at: https://www.frontiersin.org/articles/10.3389/feart.2022.828801/full#supplementary-material

REFERENCES

Avşar, U., Hubert-Ferrari, A., Batist, M. D., and Fagel, N. (2014). A 3400 Year Lacustrine Paleoseismic Record from the North Anatolian Fault, Turkey: Implications for Bimodal Recurrence Behavior. *Geophys. Res. Lett.* 41, 377–384. doi:10.1002/2013GL058221

Avşar, U., Hubert-Ferrari, A., De Batist, M., Schmidt, S., and Fagel, N. (2015). Sedimentary Records of Past Earthquakes in Boraboy Lake during the Last Ca 600 Years (North Anatolian Fault, Turkey). *Palaeogeogr. Palaeoclimatol. Palaeoecol.* 433, 1–9. doi:10.1016/j.palaeo.2015.04.031

Avşar, U., Jónsson, S., Avşar, Ö., and Schmidt, S. (2016). Earthquake-induced Soft-Sediment Deformations and Seismically Amplified Erosion Rates Recorded in Varved Sediments of Köyceğiz Lake (SW Turkey). *J. Geophys. Res. Solid Earth* 121, 4767–4779. doi:10.1002/2016JB012820

Bai, M. X., Luo, F. Z., Yin, G. H., Xiang, Z. Y., Sheng, J., Shi, S. Z., et al. (1996). Kokotokay—Ertai Active Fault Zone in Xinjiang. *Inl. Earthq.* 10, 319–328. (in Chinese with English abstract). doi:10.16256/j.issn.1001-8956.1996.04.005

Beck, C. (2009). "Late Quaternary Lacustrine Paleo-Seismic Archives in north-western Alps: Examples of Earthquake-Origin Assessment of Sedimentary Disturbances". *Earth-Science Rev.* 96, 327–344. doi:10.1016/j.earscirev.2009.07.005

Benito, G., Sánchez-Moya, Y., and Sopeña, A. (2003). Sedimentology of High-Stage Flood Deposits of the Tagus River, Central Spain. *Sediment. Geology.* 157, 107–132. doi:10.1016/S0037-0738(02)00196-3

Berryman, K. R., Cochran, U. A., Clark, K. J., Biasi, G. P., Langridge, R. M., and Villamor, P. (2012). Major Earthquakes Occur Regularly on an Isolated Plate Boundary Fault. *Science* 336, 1690–1693. doi:10.1126/science.1218959

Bertrand, S., Charlet, F., Chapron, E., Fagel, N., and De Batist, M. (2008). Reconstruction of the Holocene Seismotectonic Activity of the Southern Andes from Seismites Recorded in Lago Icalma, Chile, 39°S. *Palaeogeogr. Palaeoclimatol. Palaeoecol.* 259, 301–322. doi:10.1016/j.palaeo.2007.10.013

Blaauw, M., and Christen, J. A. (2011). Flexible Paleoclimate Age-Depth Models Using an Autoregressive Gamma Process. *Bayesian Anal.* 6, 457–474. doi:10.1214/ba/1339616472

Blott, S. J., and Pye, K. (2001). GRADISTAT: a Grain Size Distribution and Statistics Package for the Analysis of Unconsolidated Sediments. *Earth Surf. Process. Landforms* 26, 1237–1248. doi:10.1002/esp.261

Brock, F., Higham, T., Ditchfield, P., and Ramsey, C. B. (2010). Current Pretreatment Methods for AMS Radiocarbon Dating at the Oxford Radiocarbon Accelerator Unit (Orau). *Radiocarbon* 52, 103–112. doi:10.1017/S0033822200045069

Chen, J., van Loon, A. J., Han, Z., and Chough, S. K. (2009). Funnel-shaped, Breccia-Filled Clastic Dykes in the Late Cambrian Chaomidian Formation (Shandong Province, China). *Sediment. Geology.* 221, 1–6. doi:10.1016/j.sedgeo.2009.09.006

Cui, P., Lin, Y.-m., and Chen, C. (2012). Destruction of Vegetation Due to Geo-Hazards and its Environmental Impacts in the Wenchuan Earthquake Areas. *Ecol. Eng.* 44, 61–69. doi:10.1016/j.ecoleng.2012.03.012

Ding, G. Y. (1985). *The Fuyun Earthquake Fault Zone*. Beijing: Seismological Press. (in Chinese).

Dowrick, D. J., and Rhoades, D. A. (2005). Revised Models for Attenuation of Modified Mercalli Intensity in New Zealand Earthquakes. *Bnzsee* 38, 185–214. doi:10.5459/bnzsee.38.4.185-214

Fan, J., Jiang, H., Shi, W., Guo, Q., Zhang, S., Wei, X., et al. (2021). A 450-year Warming and Wetting Climate in Southern Altay Inferred from a Yileimu Lake Sediment Core. *Quat. Int.* 592, 37–50. doi:10.1016/j.quaint.2021.04.035

Fan, J., Jiang, H., Shi, W., Guo, Q., Zhang, S., Wei, X., et al. (2020b). A 450-year Lacustrine Record of Recurrent Seismic Activities Around the Fuyun Fault, Altay Mountains, Northwest China. *Quat. Int.* 558, 75–88. doi:10.1016/j.quaint.2020.08.051

Fan, J., Wei, X., Shi, W., Guo, Q., Zhang, S., Xu, H., et al. (2020a). Response of Tree Rings to Earthquakes during the Past 350 Years at Jiuzhaigou in the Eastern Tibet. *Sci. Total Environ.* 731, 138714. doi:10.1016/j.scitotenv.2020.138714

Fan, J., Xiao, J., and Qin, X. (2019). Millennial- and Centennial-Scale Droughts at the Northern Margin of the East Asian Summer Monsoon during the Last Deglaciation: Sedimentological Evidence from Dali Lake. *Palaeogeogr. Palaeoclimatol. Palaeoecol.* 514, 361–372. doi:10.1016/j.palaeo.2018.11.001

Fan, J., Xiao, J., Wen, R., Zhang, S., Wang, X., Cui, L., et al. (2016). Droughts in the East Asian Summer Monsoon Margin during the Last 6 Kyrs: Link to the North Atlantic Cooling Events. *Quat. Sci. Rev.* 151, 88–99. doi:10.1016/j.quascirev.2016.09.001

Fuyun County Local Chronicles Compilation Committee (2003). *Annals of Fuyun County*. Urumqi: Volksverlag Xinjiang. (in Chinese).

Ghazoui, Z., Bertrand, S., Vanneste, K., Yokoyama, Y., Nomade, J., Gajurel, A. P., et al. (2019). Potentially Large post-1505 AD Earthquakes in Western Nepal Revealed by a lake Sediment Record. *Nat. Commun.* 10, 2258. doi:10.1038/s41467-019-10093-4

Howarth, J. D., Fitzsimons, S. J., Norris, R. J., and Jacobsen, G. E. (2012). Lake Sediments Record Cycles of Sediment Flux Driven by Large Earthquakes on the Alpine Fault, New Zealand. *Geology* 40, 1091–1094. doi:10.1130/G33486.1

Howarth, J. D., Fitzsimons, S. J., Norris, R. J., and Jacobsen, G. E. (2014). Lake Sediments Record High Intensity Shaking that Provides Insight into the Location and Rupture Length of Large Earthquakes on the Alpine Fault, New Zealand. *Earth Planet. Sci. Lett.* 403, 340–351. doi:10.1016/j.epsl.2014.07.008

Howarth, J. D., Fitzsimons, S. J., Norris, R. J., Langridge, R., and Vandergoes, M. J. (2016). A 2000 Yr Rupture History for the Alpine Fault Derived from Lake Ellery, South Island, New Zealand. *Geol. Soc. America Bull.* 128, 627–643. doi:10.1130/B31300.1

Howarth, J. D., Orpin, A. R., Kaneko, Y., Strachan, L. J., Nodder, S. D., Mountjoy, J. J., et al. (2021). Calibrating the marine Turbidite Palaeoseismometer Using the 2016 Kaikōura Earthquake. *Nat. Geosci.* 14, 161–167. doi:10.1038/s41561-021-00692-6

Hubert-Ferrari, A., Lamair, L., Hage, S., Schmidt, S., Çağatay, M. N., and Avşar, U. (2020). A 3800 Yr Paleoseismic Record (Lake Hazar Sediments, Eastern Turkey): Implications for the East Anatolian Fault Seismic Cycle. *Earth Planet. Sci. Lett.* 538, 116152. doi:10.1016/j.epsl.2020.116152

Jiang, H., Zhong, N., Li, Y., Ma, X., Xu, H., Shi, W., et al. (2017). A Continuous 13.3-ka Record of Seismogenic Dust Events in Lacustrine Sediments in the Eastern Tibetan Plateau. *Sci. Rep.* 7, 15686. doi:10.1038/s41598-017-16027-8

Jiang, H., Zhong, N., Li, Y., Xu, H., Yang, H., and Peng, X. (2016). Soft Sediment Deformation Structures in the Lixian Lacustrine Sediments, Eastern Tibetan Plateau and Implications for Postglacial Seismic Activity. *Sediment. Geology.* 344, 123–134. doi:10.1016/j.sedgeo.2016.06.011

Klinger, Y., Etchebes, M., Tapponnier, P., and Narteau, C. (2011). Characteristic Slip for Five Great Earthquakes along the Fuyun Fault in China. *Nat. Geosci* 4, 389–392. doi:10.1038/NGEO1158

Kremer, K., Gassner-Stamm, G., Grolimund, R., Wirth, S. B., Strasser, M., and Fäh, D. (2020). A Database of Potential Paleoseismic Evidence in Switzerland. *J. Seismol.* 24, 247–262. doi:10.1007/s10950-020-09908-5

Li, Z. Y., Cao, Z. Z., and Li, Y. R. (2012). New Prediction Formula of Sand Liquefied on Bachu-Jiashi Earthquake Survey. *Amm* 170-173, 2880–2884. doi:10.4028/www.scientific.net/AMM.170-173.2880

Lin, A., and Lin, S. j. (1998). Tree Damage and Surface Displacement: The 1931 M 8.0 Fuyun Earthquake. *J. Geology.* 106, 751–758. doi:10.1086/516058

Lu, Y., Moernaut, J., Bookman, R., Waldmann, N., Wetzler, N., Agnon, A., et al. (2021a). A New Approach to Constrain the Seismic Origin for Prehistoric Turbidites as Applied to the Dead Sea Basin. *Geophys. Res. Lett.* 48, e2020GL090947. doi:10.1029/2020GL090947

Lu, Y., Moernaut, J., Waldmann, N., Bookman, R., Ian Alsop, G., Hubert-Ferrari, A., et al. (2021b). Orbital- and Millennial-Scale Changes in Lake-Levels Facilitate Earthquake-Triggered Mass Failures in the Dead Sea Basin. *Geophys. Res. Lett.* 48, e2021GL093391. doi:10.1029/2021GL093391

Lu, Y., Waldmann, N., Alsop, G. I., and Marco, S. (2017). Interpreting Soft Sediment Deformation and Mass Transport Deposits as Seismites in the Dead Sea Depocenter. *J. Geophys. Res. Solid Earth* 122, 8305–8325. doi:10.1002/2017JB014342

Lu, Y., Wetzler, N., Waldmann, N., Agnon, A., Biasi, G. P., and Marco, S. (2020). A 220,000-Year-Long Continuous Large Earthquake Record on a Slow-Slipping Plate Boundary. *Sci. Adv.* 6, eaba4170. doi:10.1126/sciadv.aba4170

Migeon, S., Garibaldi, C., Ratzov, G., Schmidt, S., Collot, J.-Y., Zaragosi, S., et al. (2017). Earthquake-triggered Deposits in the Subduction Trench of the north Ecuador/south Colombia Margin and Their Implication for Paleoseismology. *Mar. Geology.* 384, 47–62. doi:10.1016/j.margeo.2016.09.008

Moernaut, J., Daele, M. V., Heirman, K., Fontijn, K., Strasser, M., Pino, M., et al. (2014). Lacustrine Turbidites as a Tool for Quantitative Earthquake Reconstruction: New Evidence for a Variable Rupture Mode in South central Chile. *J. Geophys. Res. Solid Earth* 119, 1607–1633. doi:10.1002/2013JB010738

Moernaut, J. (2020). Time-dependent Recurrence of strong Earthquake Shaking Near Plate Boundaries: A lake Sediment Perspective. *Earth-Science Rev.* 210, 103344. doi:10.1016/j.earscirev.2020.103344

Moernaut, J., Van Daele, M., Fontijn, K., Heirman, K., Kempf, P., Pino, M., et al. (2018). Larger Earthquakes Recur More Periodically: New Insights in the Megathrust Earthquake Cycle from Lacustrine Turbidite Records in South-central Chile. *Earth Planet. Sci. Lett.* 481, 9–19. doi:10.1016/j.epsl.2017.10.016

Monecke, K., Anselmetti, F. S., Becker, A., Sturm, M., and Giardini, D. (2004). The Record of Historic Earthquakes in lake Sediments of Central Switzerland. *Tectonophysics* 394, 21–40. doi:10.1016/j.tecto.2004.07.053

Moretti, M. (2000). Soft-sediment Deformation Structures Interpreted as Seismites in Middle-Late Pleistocene Aeolian Deposits (Apulian Foreland, Southern Italy). *Sediment. Geology.* 135, 167–179. doi:10.1016/S0037-0738(00)00070-1

Oswald, P., Strasser, M., Hammerl, C., and Moernaut, J. (2021). Seismic Control of Large Prehistoric Rockslides in the Eastern Alps. *Nat. Commun.* 12, 1059. doi:10.1038/s41467-021-21327-9

Pollitz, F., Vergnolle, M., and Calais, E. (2003). Fault Interaction and Stress Triggering of Twentieth century Earthquakes in Mongolia. *J. Geophys. Res.* 108, 2503. doi:10.1029/2002JB002375

Praet, N., Van Daele, M., Collart, T., Moernaut, J., Vandekerkhove, E., Kempf, P., et al. (2020). Turbidite Stratigraphy in Proglacial Lakes: Deciphering Trigger Mechanisms Using a Statistical Approach. *Sedimentology* 67, 2332–2359. doi:10.1111/sed.12703

Ramsey, C. B., and Lee, S. (2013). Recent and Planned Developments of the Program OxCal. *Radiocarbon* 55, 720–730. doi:10.1017/S0033822200057878

Reimer, P. J., Austin, W. E. N., Bard, E., Bayliss, A., Blackwell, P. G., Bronk Ramsey, C., et al. (2020). The IntCal20 Northern Hemisphere Radiocarbon Age Calibration Curve (0-55 Cal kBP). *Radiocarbon* 62, 725–757. doi:10.1017/RDC.2020.41

Schnellmann, M., Anselmetti, F. S., Giardini, D., McKenzie, J. A., and Ward, S. N. (2002). Prehistoric Earthquake History Revealed by Lacustrine Slump Deposits. *Geol* 30, 1131–1134. doi:10.1130/0091-7613(2002)030<1131:PEHRBL>2.0.CO;2

Shen, J., Li, Y. Z., Wang, Y. P., and Song, F. M. (2003). The Active Faults in Altai Mountains. *Earth Sci. Front.* 10, 132–141. (in Chinese with English abstract). doi:10.3321/j.issn:1005-2321.2003.z1.020

Shi, J., Shen, J., Bai, M. X., and Shi, G. L. (2010). Intensity Image Revision on Fuyun 8.0 Earthquake on Aug. 11, 1931 in Xinjiang. *Inland Earthq* 24, 37–40. (in Chinese with English abstract). doi:10.3969/j.issn.1001-8956.2010.01.007

Sims, J. D. (1973). Earthquake-induced Structures in Sediments of Van Norman Lake, San Fernando, California. *Science* 182, 161–163. doi:10.1126/science.182.4108.161

Strasser, M., Anselmetti, F. S., Fäh, D., Giardini, D., and Schnellmann, M. (2006). Magnitudes and Source Areas of Large Prehistoric Northern Alpine Earthquakes Revealed by Slope Failures in Lakes. *Geol* 34, 1005–1008. doi:10.1130/G22784A.1

Sullivan, K. M., and Hossain, S. M. M. (2010). Earthquake Mortality in Pakistan. *Disasters* 34, 176–183. doi:10.1111/j.1467-7717.2009.01121.x

Sun, A., Feng, Z., Ran, M., and Zhang, C. (2013). Pollen-recorded Bioclimatic Variations of the Last ~22,600 Years Retrieved from Achit Nuur Core in the

Western Mongolian Plateau. *Quat. Int.* 311, 36–43. doi:10.1016/j.quaint.2013.07.002

Suter, F., Martínez, J. I., and Vélez, M. I. (2011). Holocene Soft-Sediment Deformation of the Santa Fe-Sopetrán Basin, Northern Colombian Andes: Evidence for Pre-hispanic Seismic Activity? *Sediment. Geology.* 235, 188–199. doi:10.1016/j.sedgeo.2010.09.018

Van Daele, M., Cnudde, V., Duyck, P., Pino, M., Urrutia, R., and De Batist, M. (2014). Multidirectional, Synchronously-Triggered Seismo-Turbidites and Debrites Revealed by X-ray Computed Tomography (CT). *Sedimentology* 61, 861–880. doi:10.1111/sed.12070

Van Daele, M., Meyer, I., Moernaut, J., De Decker, S., Verschuren, D., and De Batist, M. (2017). A Revised Classification and Terminology for Stacked and Amalgamated Turbidites in Environments Dominated by (Hemi)pelagic Sedimentation. *Sediment. Geology.* 357, 72–82. doi:10.1016/j.sedgeo.2017.06.007

Vanholder, R., Sever, M. S., De Smet, M., Erek, E., and Lameire, N. (2001). Intervention of the Renal Disaster Relief Task Force in the 1999 Marmara, Turkey Earthquake. *Kidney Int.* 59, 783–791. doi:10.1046/j.1523-1755.2001.059002783.x

Wang, S. Y., Yu, Y. X., Gao, A. J., and Yan, X. J. (2000). Development of Attenuation Relations for Ground Motion in China. *Earthq. Res. CHN.* 16, 99–106. (in Chinese with English abstract). doi:10.3969/j.issn.1001-4683.2000.02.001

Wetzler, N., Marco, S., and Heifetz, E. (2010). Quantitative Analysis of Seismogenic Shear-Induced Turbulence in lake Sediments. *Geology* 38, 303–306. doi:10.1130/G30685.1

Wils, K., Daryono, M. R., Praet, N., Santoso, A. B., Dianto, A., Schmidt, S., et al. (2021). The Sediments of Lake Singkarak and Lake Maninjau in West Sumatra Reveal Their Earthquake, Volcanic and Rainfall History. *Sediment. Geology.* 416, 105863. doi:10.1016/j.sedgeo.2021.105863

Xu, X., and Deng, Q. (1996). Nonlinear Characteristics of Paleoseismicity in China. *J. Geophys. Res.* 101, 6209–6231. doi:10.1029/95JB01238

Xu, X. W., Sun, X. Z., Tan, X. B., Li, K., Yu, G. H., Etchebes, M., et al. (2012). Fuyun Fault: Long-Term Faulting Behavior under Low Crustal Strain Rate. *Seismol. Geol.* 34, 606–617. (in Chinese with English abstract). doi:10.3969/j.issn.0253-4967.2012.04.007

Zhou, A.-f., Chen, F.-h., Wang, Z.-l., Yang, M.-l., Qiang, M.-r., and Zhang, J.-w. (2009). Temporal Change of Radiocarbon Reservoir Effect in Sugan Lake, Northwest China during the Late Holocene. *Radiocarbon* 51, 529–535. doi:10.1017/S0033822200055909

Conflict of Interest: The authors declare that the research was conducted in the absence of any commercial or financial relationships that could be construed as a potential conflict of interest.

Publisher's Note: All claims expressed in this article are solely those of the authors and do not necessarily represent those of their affiliated organizations, or those of the publisher, the editors and the reviewers. Any product that may be evaluated in this article, or claim that may be made by its manufacturer, is not guaranteed or endorsed by the publisher.

frontiers | Frontiers in Earth Science

ORIGINAL RESEARCH
published: 13 April 2022
doi: 10.3389/feart.2022.859471

Historic Earthquakes for the Xianshuihe Fault Derived From Lake Mugeco in the Southeastern Margin of the Tibetan Plateau During the Past 300 Years

Liyuan Liu[1], Jingxuan Yang[1], Xingqi Liu[1], Xin Mao[2] and Rong Qin[1]*

[1]College of Resource Environment and Tourism, Capital Normal University, Beijing, China, [2]Institute of Hydrogeology and Environmental Geology, Chinese Academy of Geological Sciences, Shijiazhuang, China

The lacustrine deposition with continuity and chronological reliability is one of the important archives to establish paleo-seismic sequences. In this study, sediment short cores were obtained from Lake Mugeco, located in the Selaha section of the Xianshuihe fault zone on the southeastern margin of the Tibetan Plateau. The chronology is established using $^{210}Pb/^{137}Cs$ and AMS^{14}C dating results. Seismic events are identified based on sedimentary characteristics (color, density, and grain size), organic matter content, and high-resolution XRF element scanning data for the past 300 years. There are four whitish turbidites in the sediments of Lake Mugeco, which are characterized by a high content of clay fraction and detrital elements (K, Rb, Ca, Sr, Ti, and Si) and low organic matter content. These four turbidites were dated in 1944–1956 C.E., 1919–1932 C.E., 1673–1837 C.E., and 1507–1739 C.E., with dating errors, possibly corresponding to large historical earthquakes of 1955 (M_S 7.5), 1932 (M_S 6), 1786 (M_S 7 ¾), and 1725 (M_S 7) recorded in the Selaha section of the Xianshuihe fault zone. This study provides scientific evidence for further reconstructing longer-temporal seismic events in the Xianshuihe fault zone inferred from sediments of Lake Mugeco.

Keywords: lacustrine sediment, seismic event, Xianshuihe fault, Lake Mugeco, turbidite

OPEN ACCESS

Edited by:
Shiyong Yu,
Jiangsu Normal University, China

Reviewed by:
Gueorgui Ratzov,
Université Côte d'Azur, France
Pierre Sabatier,
University of Savoie-Mont Blanc, France
Fuyuan An,
Qinghai Normal University, China

****Correspondence:***
Xingqi Liu
xqliu@cnu.edu.cn

Specialty section:
This article was submitted to Quaternary Science, Geomorphology and Paleoenvironment, a section of the journal Frontiers in Earth Science

Received: *21 January 2022*
Accepted: *07 March 2022*
Published: *13 April 2022*

Citation:
Liu L, Yang J, Liu X, Mao X and Qin R (2022) Historic Earthquakes for the Xianshuihe Fault Derived From Lake Mugeco in the Southeastern Margin of the Tibetan Plateau During the Past 300 Years. Front. Earth Sci. 10:859471. doi: 10.3389/feart.2022.859471

INTRODUCTION

The Xianshuihe fault zone is regarded as one of the most tectonically active regions with high seismicity in China (Wen et al., 2008; Bai et al., 2018). Historical earthquake data and instrumental monitoring have recorded more than 20 earthquake events with a magnitude of $M_s \geq 6.5$ since 1700 C.E., over ten of which have a magnitude of above M_s 7.0 (Writing Group of Compilation of Sichuan Earthquake Data, 1980a; Writing Group of Compilation of Sichuan Earthquake Data, 1980b; Wen et al., 1989). Previous studies have discerned the paleoseismic events and inferred their recurrence periodicity and interval of strong earthquakes through techniques of trenching and dating in the Xianshuihe fault zone for the past 20,000 years (Sun et al., 2007; Liang, 2019).

Continuous lacustrine sediments can provide supplementary information to whole earthquake records in an active fault zone (Ghazoui et al., 2019; Vandekerkhove et al., 2019; Fan et al., 2020; Hubert-Ferrari et al., 2020; Gastineau et al., 2021; Wils et al., 2021). Seismic shaking can induce subaqueous slope failure and remobilization of surficial, previously deposited sediments to be

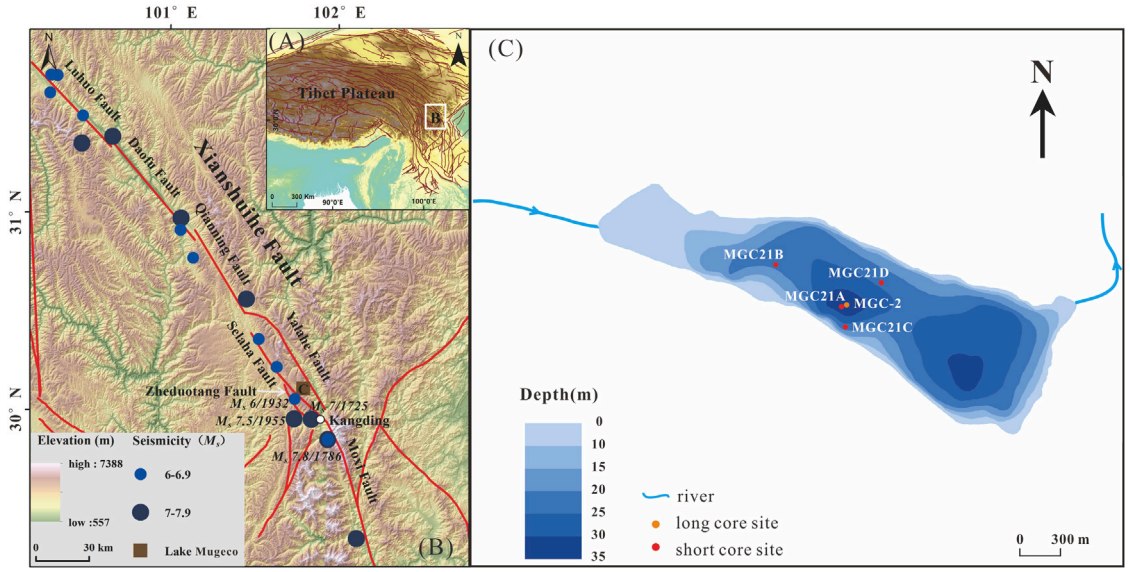

FIGURE 1 | Location of the study area. Location of the Xianshuihe fault in TP **(A)**. Seven fault segments and historical earthquakes along the fault **(B)**. Bathymetric map of Lake Mugeco and the location of sediment cores **(C)**.

transformed into the subaqueous turbidity currents and debris or mudflows flowing into the lakebed (Bryn et al., 2005; Moernaut et al., 2017; Praet et al., 2017). It may also trigger sedimentary instabilities such as onshore landslides and deltaic slope failures, resulting in mobilized masses and turbidity currents (Howarth et al., 2014; Van Daele et al., 2015). Sediment formed by these earthquake-induced turbidity currents is called seismoturbidite or homogenite (Sturm et al., 1995; Chapron et al., 1999; Shiki et al., 2000; Beck, 2009; Howarth et al., 2014; Van Daele et al., 2015; Moernaut et al., 2018; Lu et al., 2021; Polonia et al., 2021). Moreover, an earthquake can induce deformation, such as microfaults (Topal and Ozkul, 2014; Avşar et al., 2015; Jiang et al., 2016), microfolds (Monecke et al., 2004), liquefaction, and flowage (Beck, 2009; Topal and Ozkul, 2014). In addition, earthquake-induced water oscillation (i.e., seiche) can erode shallow material or resuspend sediments from the steepening parts of the lake basin and form oscillating bottom currents, influencing *in situ* soft sediment deformation and mass-transport deposits (Alsop and Marco, 2012; Lu et al., 2020). However, the aforementioned characteristics of sedimentation are not generated only by seismic events, as rainstorms and windstorms caused by climate change and spontaneous landslides due to overloading of subaqueous slopes can also result in sedimentary disturbances (Chassiot et al., 2016a; Kinder, et al., 2019; Rapuc et al., 2020; Sabatier et al., 2017; Wilhelm et al., 2012; Wilhelm et al., 2022; Wils et al., 2021). Therefore, it is crucial to correctly distinguish seismic events from other events preserved in lake sediments. Here, we first establish the chronology based on ^{210}Pb/^{137}Cs and accelerator mass spectrometry (AMS) ^{14}C dating of a short core from Lake Mugeco. Then, the sedimentary characteristics (including sediment color, density, and grain size), organic matter, and element content are employed to identify event layers preserved in several short cores from Lake Mugeco. Finally, four earthquake events different from one flood event are identified on short lake sediment cores that span a period with known historical earthquake and flood events.

STUDY AREA

The Xianshuihe fault is a giant left-lateral strike-slip fault on the southeastern margin of the Tibetan Plateau (TP) (**Figures 1A,B**). At Huiyuan Monastery, the fault is halved into NW and SE sections based on their respective structural styles (Qian et al., 1988; Wen et al., 1989). The former, with a simple geologic structure, includes the Luhuo segment, the Daofu segment, and the Qianning segment, while the latter, with complicated construction, consists of the Yalahe segment, Selaha segment, Zheduotang segment, and Moxi segment to the south of Kangding city (**Figure 1B**). It is considered that the Xianshuihe fault was formed 2–13 Ma ago and the cumulative length of slip reaches ~60 km (Roger et al., 1995; Wang et al., 1998; Wang et al., 2012; Yan and Lin, 2015). The long-term horizontal slip rate of 10–20 mm/yr estimated by different scholars is explicitly higher than others in southeastern margin of TP (Allen et al., 1991; Qiao et al., 2004; Xiong et al., 2010), so the Xianshuihe fault is regarded as a high-velocity strike-slip fault.

Lake Mugeco (30°08′N, 101°50′E) is located in Yala Town of North Kangding city, Sichuan Province, near the Selaha segment of the mid-Xianshuihe fault (**Figure 1B**). Formed by regional taphrogeny and dispersion, the lake is the largest fault lake on the Xianshuihe fault. There is a steep slope bounding the southeastern side of the basin that Lake Mugeco fills, and relatively flat terrain in the northwest. The NW-SE major

direction of the lake basin is consistent with the extensions of the Xianshuihe fault (**Figure 1C**). The batholith is dominated by medium-coarse-grained granite in the catchment. Controlled by the fault of the Selaha segment, intensive shattering spreads out and extensive fractures develop on the southwest bank of the basin (Zhou et al., 2001). Lake Mugeco lies in the transitional zone between the East Asian Summer Monsoon and the Indian Summer Monsoon region. Meteorological data from Kangding station (30°1′48″ N, 101°34′48″) show that mean annual temperature is 7.2°C and mean annual precipitation is 830 mm with most of the annual precipitation falling from May to September. Lake Mugeco and its catchment cover an area of 1.8 and 75 km^2, respectively, (Hu et al., 2015; Sun et al., 2015; 2016). The lake is at an elevation of 3780 m. The maximum water depth we measured in 2020 was 34.4 m. It is a hydrologically open lake, mainly fed by a river from the northwest. There is one outlet flowing into the Yala River on the northeast side of the lake (**Figure 1C**) (Sun et al., 2016; Ni et al., 2019).

MATERIALS AND METHODS

Sediment Coring

In July 2019, a 3.9-m-long sediment core (MGC-2) from the centre of Lake Mugeco was recovered by an Uwitec drilling platform at a depth of 30.5 m (**Figure 1C**). Then, in May 2021, four short sediment cores were obtained using a piston gravity corer at different depths varying from 23 to 30.5 m. These short cores were respectively named of MGC21A (31 cm-long), MGC21B (27 cm-long), MGC21C (25 cm-long), and MGC21D (32 cm-long) (**Figure 1C**).

Laboratory Analysis

All short sediment cores were split along the central axis with a core-cutting machine in our laboratory. Halved cores were photographed, and the lithology was described. This study focuses mainly on short-core MGC21A for dating, XRF core scanning, and analyses of grain size, total organic carbon (TOC), and total nitrogen (TN). For MGC21B, MGC21C, and MGC21D, XRF core scanning was used to get X-radiographic images and element variations.

$^{210}Pb/^{137}Cs$ and ^{14}C Dating

The subsamples of core MGC21, sampled at intervals of 0.5 cm, were vacuum freeze dried for 48 h, then ground to powder as fine as ca 150 μm with a mortar and pestle. The activities of ^{137}Cs, ^{226}Ra, and ^{210}Pb of the samples at different depth were measured by Ortec high purity germanium gamma spectrometer. Herein the excess ^{210}Pb activity ($^{210}Pb_{ex}$) was computed by subtracting the ^{226}Ra activity from the total activity of ^{210}Pb, as ^{226}Ra was assumed to be in equilibrium with supported ^{210}Pb ($^{210}Pb_{sup}$). The constant flux constant sedimentation rate (CFCS) model method is given to estimate sediment age within ca 150 years (Appleby and Oldfield, 1978; Robbins, 1978; Bruel and Sabatier, 2020). Plant remains were selected at a depth of 50 cm from the long core MGC-2 for AMS^{14}C dating at Beta Analytic Testing Laboratory, United States.

XRF Core Scanning

The surfaces of halved cores were smoothed to give a flat surface and covered with a thin Ultralene film to prevent desiccation during core scanning. The cores were scanned by the Itrax Core Scanner (Cox Analytical Instruments) equipped with an Rh X-ray tube to get optical images, X-radiographic images, and element variations. A voltage of 60 kV, a current of 35 mA, a step size of 20 μm and an exposure time of 200 ms were set to get X-radiographic images. A voltage of 30 kV, a current of 55 mA, a step size of 200 μm and an exposure time of 5 s were set to get element variations expressed as counts per second (CPS). Elements with low raw counts are excluded, as they are close to the detection limits of ITRAX and may be even measurement noise. In order to avoid the matric effect, a centered log-ratio (CLR) transformation was applied to calibrate the elements (Weltje et al., 2015). Principal component analysis (PCA) is a statistical approach that can transform a large number of variables (concentration of elements) into fewer independent variables (Sabatier et al., 2010). PCA is performed by SPSS software.

Measurement of Grain Size

Samples of core MGC21A were sliced at 0.5 cm intervals, and ~0.5 g wet samples were used for the measurement of grain size. For the removal of organic matter and carbonates, samples were pretreated with 10% H_2O_2 and with 10% HCl, and then dispersed in an ultrasonic vibrator for 15–20 min with 10% $(NaPO_3)_6$. Last, the grain-size distributions of the MGC21A core were measured using a Malvern Mastersizer 3,000 laser grain-size analyzer.

Measurement of TOC and TN

About 1 g of samples were first treated with 10% HCl to remove carbonates, rinsed with deionized water, and dried in the drying oven prior to analysis. The dried samples were ground into 100-μm-fine powder. Finally, ~3–5-mg samples were analyzed by the EURO EA 3,000 elemental analyzer to determine TOC and TN content.

RESULT

Sedimentary Characteristics

The deposits of the MGC21A core mainly consist of greyish-brown and light greyish-black clayey silt. Percentages of silt and clay range from 75.15 to 85.13% and 13.37–23.15%, with an average of 82.34 and 16.09%, respectively (**Figure 2**). The proportion of sand is less than 2.96% on average. It is found that the variation of clay is the opposite to that of silt. Also, the median diameter ranges from 9.33–11.40 μm with an average of 10.37 μm, in accordance with the variation of silt. Besides, Rad values are associated with grain size variations, which means that overall low Rad values respond to high content of clay fraction, and vice versa (**Figure 2**). There are three whitish layers presented as dark bands in the X-radiographic image at the depths of 6.5, 17, and 22 cm in the MGC21A core (shown as E1, E3, and E4 in **Figure 2**). They are also characterized by relatively high clay content and low silt content, and the median diameter and Rad values decrease correspondingly as well. At a depth of 9.5 to

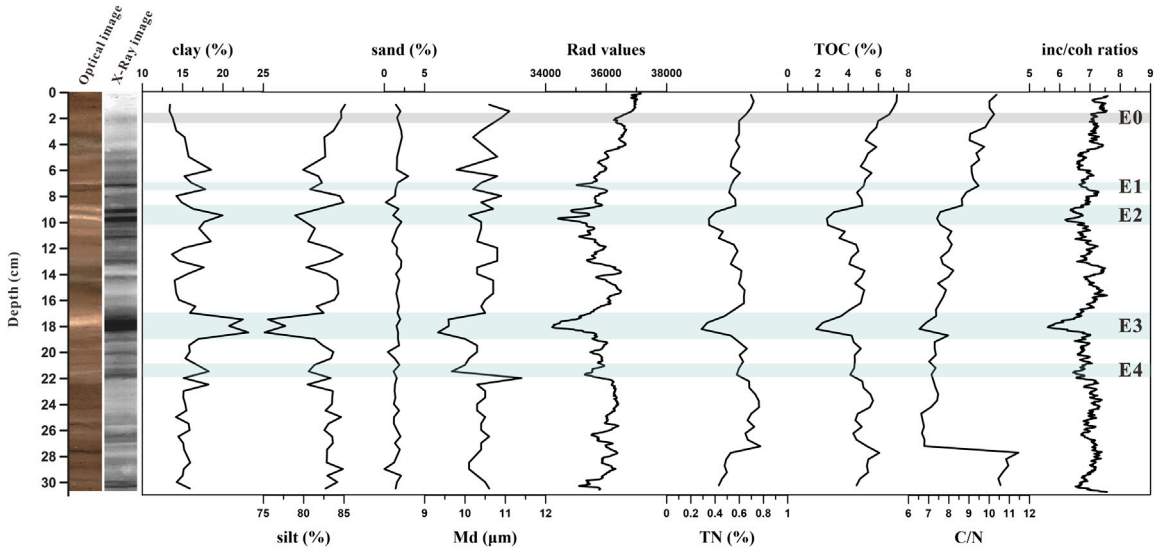

FIGURE 2 | Optical and X-radiographic images, and different proxy variations with depth in the core MGC21A. E0- flood event labeled as a light grey bar; E1, E2, E3, and E4- earthquake events labeled as light blue bars.

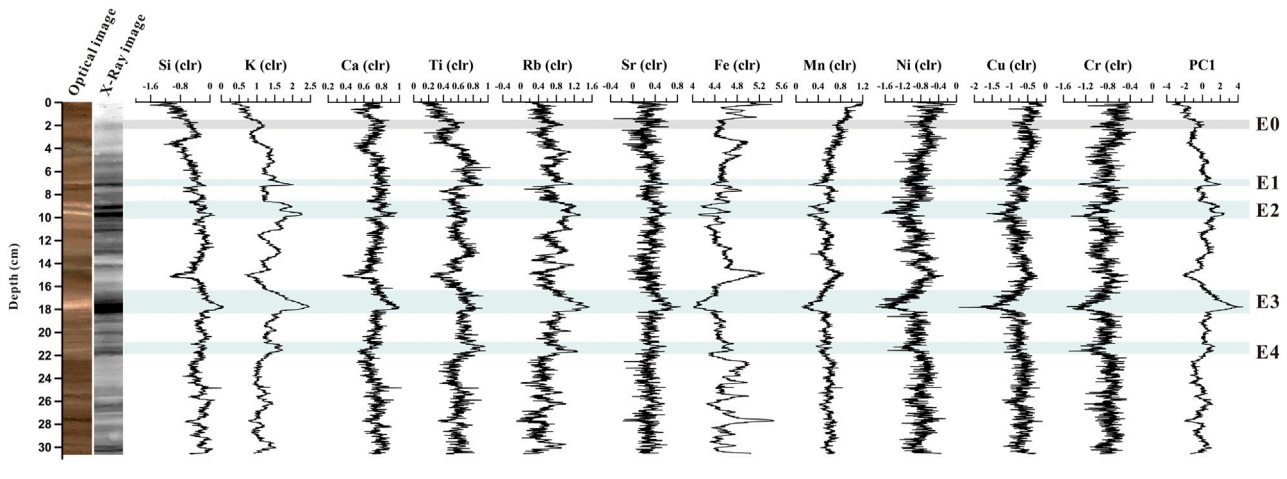

FIGURE 3 | Variations of element contents and PC1 values in the core MGC21A. E0- flood event; E1, E2, E3, and E4- earthquake events.

8.5 cm, there are two whitish layers characterized by dark bands in the X-radiographic image and low Rad values. Due to the closeness of these two layers, we named them E2 (**Figure 2**). Given that the resolution of grainsize is low, clay and silt content do not have variations, but X-radiographic images present dark and Rad values decrease in the E0 layer.

TOC, TN, C/N Ratio, and Inc/coh

In the core MGC21A, the contents of TOC and TN vary from 1.88 to 7.22% and from 0.29 to 0.78%, respectively, and their variations are consistent with each other. Carbon/nitrogen atomic (C/N) ratios are generally less than 10 (**Figure 2**). The incoherent/coherent scattering intensity ratios (inc/coh ratios) display a similar trend with TOC and TN as well (**Figure 2**). Contents of TOC, TN, and inc/coh ratios rapidly decrease in E2–E4 layers while they do not show obvious decreasing trend in E0 and E1 due to their thin layer or low resolution of TOC and TN (**Figure 2**). E2 also shows a double wiggle on variations of inc/coh ratios.

Element Variations

Variations of elements transformed by CLR in the core MGC21A are shown in **Figure 3**. PCA results show that the first two principal components together capture 65.29% of the variance (PC 1: 55.64%, PC 2: 9.65%) (**Figure 4A**). PCA 1 has positive loadings for elements of K, Rb, Ca, Sr, Ti, and Si, most of which

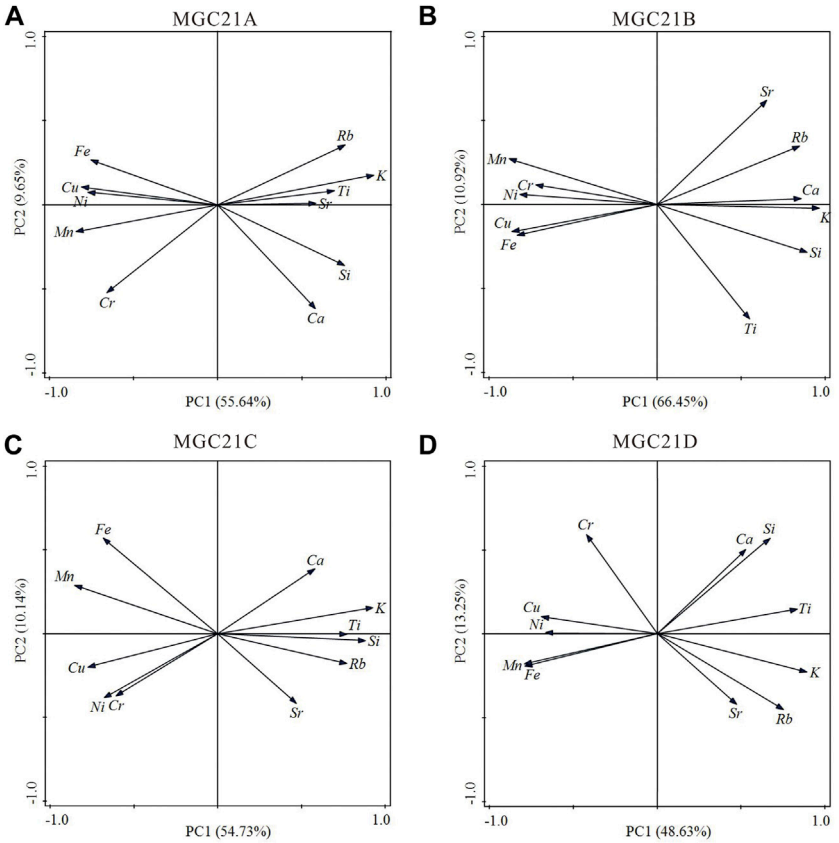

FIGURE 4 | PCA results in the cores MGC21A **(A)**, MGC21B **(B)**, MGC21C **(C)**, and MGC21D **(D)**.

belong to detrital elements. PCA 2 has positive loadings for Fe and negative loadings for Mn (**Figure 4A**), possibly reflecting the redox status of Mugeco Lake. It is discovered that the contents of K, Rb, Ca, Sr, Ti, Si, and PCA 1 values increase sharply in the base of four whitish layers and decrease upward, labeled as E0, E1, E3, and E4, especially in the E1, E3, and E4 layers (**Figure 3**). E2 also shows a double wiggle on the content of detrital elements and PC 1 values (**Figure 3**).

Generally, there are the same sedimentary characteristics in the E1, E2, E3, and E4 layers. The sediment colors in these layers turn white, and their dark X-radiographic images suggest increasing clay content (Croudace et al., 2006), decreasing median diameter, a higher density, and lower Rad values than other parts (**Figure 2**). As the sediment accumulation rate of the core is very low (0.91 mm/yr) and the highest resolution we can achieve for grainsize analysis is at a 0.5 cm interval, which spans ca. 6 years, it is impossible for grainsize data to show the graded bed with coarser sediment at the base finning upward in E0–E4 layers. However, the coarse sediment fractions are often rich in detrital elements (K, Rb, Ca, Sr, Ti, and Si), which can reflect the mm-scale changes in grain size (Avşar et al., 2014; Gastineau et al., 2021; Wilhelm et al., 2022). Sharp increasing of these detrital elements and PCA 1 values in the base of E1–E4 layers and decreasing upward well indicate coarser sediment at the base finning upward, which suggests that E1–E4 layers are characterized by turbidites. In order to avoid the one-core occasionality and to validate the universality of E0–E4 layers, three short cores (i.e., MGC21B, MGC21C, and MGC21D) in different parts of Lake Mugeco were analyzed and compared with the core MGC21A (**Figure 2**). It is found that all short cores contain five layers characterized by darker X-radiographic images, decreased Rad values, and PC 1 representing detrital element content (**Figures 4B–D**), and decreased inc/coh ratios, which can represent organic matter content (**Figure 5**).

Sediment Chronology

A logarithmic plot of $^{210}Pb_{ex}$ activity shows a general linear trend with depth (**Figure 6A**). The exponential decay pattern of $^{210}Pb_{ex}$ activity along the depth is employed to develop a chronology by applying the CFCS model (Bruel and Sabatier, 2020), indicating a low sediment accumulation rate (SAR) of 0.91 mm/yr (**Figure 6A**). The artificial isotope ^{137}Cs has been mainly released from atomic bomb tests, nuclear industrial emissions, or accidents (Foucher et al., 2021). After release, it can enter the atmosphere, and then be precipitated and preserved on land or water. The ^{137}Cs activity increases upward from the depth of 7 cm in the core of MGC21A and reaches its highest values (~160 Bq/kg) at 5 cm (**Figure 6A**), which could be related to the most intense period of nuclear

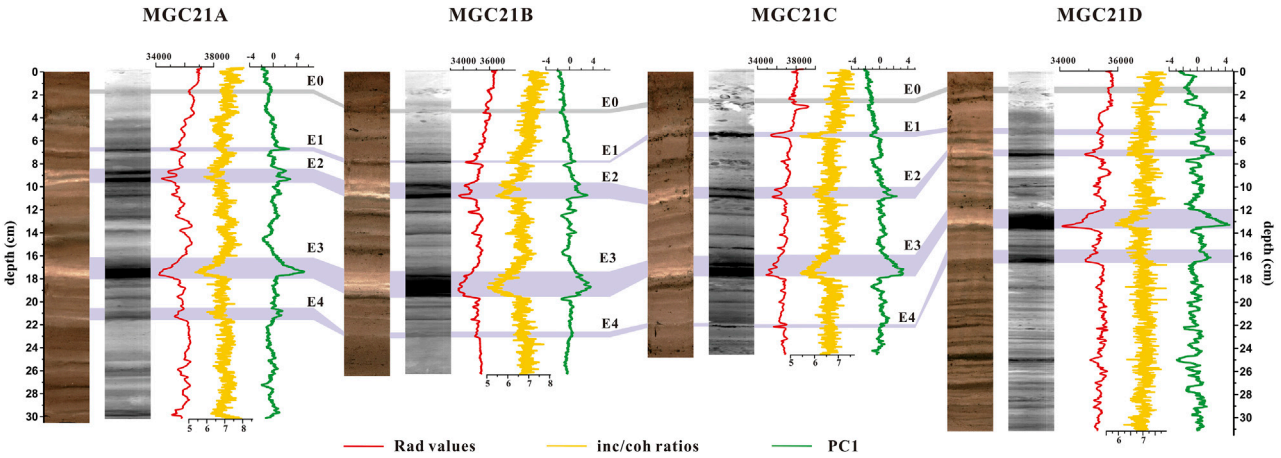

FIGURE 5 | Comparison of E0-E4 event layers characterized by Rad values, inc/coh ratios, and PC1 among the different cores in Lake Mugeco.

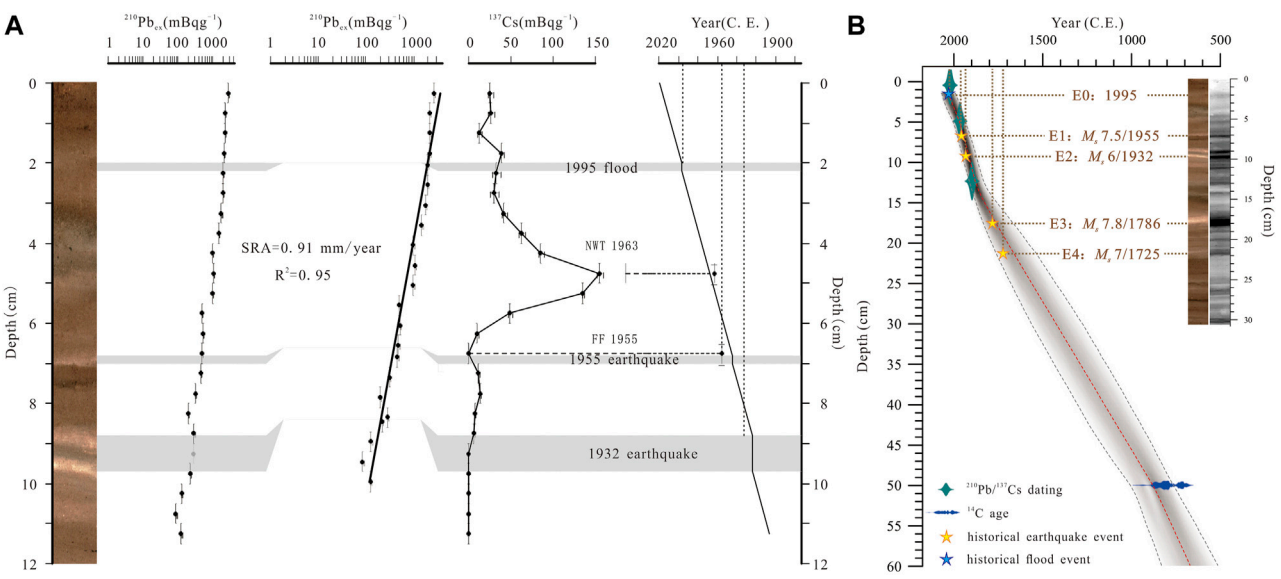

FIGURE 6 | Chronology model for cores MGC21A and MGC-2. $^{210}Pb/^{137}Cs$ dating results of the core MGC21A **(A)**. Age-depth model derived from $^{210}Pb/^{137}Cs$ dating of the core MGC21A and AMS^{14}C dating of the core MGC-2 **(B)**. E0- flood event; E1, E2, E3, and E4- earthquake events.

testfallout. And the values gradually decrease upward from a depth of 5 cm. Nuclear tests started in 1955 C.E. and reached their climax around 1963 C.E. (Foucher et al., 2021), thus the peak at 5 cm-depth is fixed at 1963 C.E. (**Figure 6A**) (Norris et al., 1994). The ^{137}Cs age of 1963 C.E. at 5 cm is consistent with the CFCS model result (**Figure 6A**). The ^{14}C age dated on the plant remains at 50 cm in the long core MGC-2 parallel to the short core MGC21A, which is 1230 ± 30 BP. Combined with the age model derived from $^{210}Pb/^{137}Cs$ and AMS^{14}C dating, the chronology is established by the Bacon 2.5.7 procedure in R software using the Bayesian method (Blaauw and Christen, 2011; Reimer et al., 2020) for the upper 50 cm sediment of Lake Mugeco (**Figure 6B**).

DISCUSSION

Seismic Events Recorded in Lake Mugeco

Previous studies indicate that turbidites can be produced by flood, landslide, deltaic collapse, or earthquake (Brocard et al., 2014; Ghazoui et al., 2019; Vandekerkhove et al., 2019; Wils et al., 2021). Flood-induced turbidities usually contain multitudes of allochthonous detrital materials and present a fining-upward unit and a better sorting in grain-size (Vandekerkhove et al., 2019; Zhang et al., 2015). Furthermore, floods and landslides have a short recurrence interval (Archer et al., 2019). It was documented that lasting heavy precipitation in June and July 1995 caused rising water levels in the Yala River and Zheduo River, which

originates from Lake Mugeco and Gongga Mountain, respectively. This heavy precipitation induced a flood occurring in 1995 in Kangding city that has encountered the most serious flood since 1776 (Xie et al., 1997). E0 at a depth of ~2.0 cm in the core of MGC21A is characterized by a dark X-radiographic image, a slight decrease in Rad and inc/coh ratios, and an increase in PC1 and elements of K, Rb, Ca, Sr, Ti, and Si. The E0 layer in other short cores also has the same characteristics. The $^{137}Cs/^{210}Pb$ dating suggests that the E0 layer is dated to 1995–1998 C.E. and was presumably triggered by the flood in 1995 (**Figure 6A**). The proxies in the E0 layer are similar to those in the E1–E4 layers (**Figure 5**), but have much little variations, which indicate that the E1–E4 layers are impossible to trigger by a flood event. Landslide-induced subaqueous deposits are generally rich in terrestrial organic matter (Avşar et al., 2014; Bussmann and Anselmetti, 2010), but with low C/N ratios in E1–E4 layers, that organic matter is endogenous (**Figure 3**). So, the E1–E4 layers are not landslide-induced deposits in Lake Mugeco. Turbidites induced by slope failure are either similar to or coarser than the background sediment as they originate in the slope areas (Moernaut et al., 2014; Van Daele et al., 2015; Wilhelm et al., 2016). E1–E4 layers with higher clay content indicate that they are unlikely to be induced by slope failure (**Figure 2**).

At the bottom of turbidite layers, there is a sharp increase in detrital element content at the base and fine-grained matter in these layers (**Figures 2**, **3**, **5**). In terms of these observations, we suggest that E1–E4 turbidite layers in Lake Mugeco are considered the result of earthquake-induced seiches (Chapron et al., 1999; Rapuc et al., 2018; Schwab et al., 2009). Beck (2009) and Aurelia et al. (2013) attributed fine-grained whitish muddy turbidites to earthquake-induced subaqueous deposits (Aurelia et al., 2013; Beck, 2009). Due to the small and narrow surface of Lake Mugeco, the seiches are prone to being triggered when an earthquake takes place (Avşar et al., 2014; Barberopoulou, 2006). Seiche waves erode surface materials from the lakeshore, and coarse grains are moved and then deposited in shoal water while separated and suspended fine grains are transported to the central lake. Meanwhile, the surficial soft sediments on the lakebed are remobilised and resuspended. Under the effect of gravity separation, fine grains are precipitated more slowly than coarse ones, and transformed into a whitish silt homogenites layer that is rich in detrital elements. From XRF core scanning, inc/coh ratios usually increase in agreement with concentrated organic matter (Woodward and Gadd, 2019), and thus Woodward et al. (2018) used inc/coh ratio as a proxy index of organic matter to reveal seismic events recorded in Lake Chappa'ai in the Southern Alps, New Zealand (Woodward et al., 2018). However, the MGC21A core shows a decrease in the inc/coh ratios, TOC and TN contents in E1–E4 layers, which means that during the formation of homogenites, suspending organic matter is oxidised and decomposed in the water column before precipitation (Schwestermann et al., 2020). Moreover, the lower C/N ratio in E1–E4 layers could indicate a lacustrine origin through mass reworked deposits related to earthquake-trigged seiches rather than a terrestrial origin characterized by higher C/N attributed to floods (**Figure 2**) (Howarth et al., 2012).

Chronology of Seismic Activities Matched With Historic Records

To further validate that the deposits in the E1, E2, E3, and E4 event layers of MGC21A were generated by earthquakes, their ages based on our chronology model were compared with the records of past earthquakes occurring in the study area. Four turbidite layers (E1-E3) are dated to 1944–1956 C.E., 1919–1932 C.E., 1673–1837C.E., and 1507–1739 C.E. respectively (**Figure 6A**). On April 14th, 1955,a M_s 7.5 earthquake happened in the Zheduotang segment (101.8°E, 30°N) to the 17 km southeast of Lake Mugeco (**Figure 1B**), its shaking intensity was measured as X at the epicentre and VII in the study area referring to the Chinese Seismic Intensity Scale (1980) (Wang et al., 1996; Yan et al., 2019). This earthquake produced a 43-km-long surface rupture to the east of the epicentre, spreading from Kangding to Wasigou, where the seismic intensity was also measured as VII. Such natural hazards as collapse, landslides, and rockfall were also triggered at Nanmenguan and Angzhou, in Luding County to the southeast (Wang et al., 1996). Based on the ^{137}Cs and ^{210}Pb chronology, the E1 layer may coincide with the M_s 7.5 earthquake in 1955 (**Figure 6A**). According to data from the National Earthquake Data Center, there was another M_s 6.0 earthquake in southwest Ganzi County, Sichuan Province (101.8°E, 30.1°N) on 3rd May, 1932. The epicentre was only about 7 km from Lake Mugeco, and the earthquake intensity exceeds VII. As there were no other earthquakes from 1919 to 1932 C.E., the E2 layer, which consists of two whitish layers, may be an amalgamated turbidite resulting from a synchronous trigger by an earthquake in 1932. There were M_s 7.8 and M_s 7.0 earthquakes with the earthquake intensity of IX at the epicentre in Dajianlu (nowadays known as Kangding) on 1st June 1786, and on 1st August, 1725, respectively (Writing Group of "Compilation of Sichuan Earthquake Data", 1980) (**Figure 1B**). Based on the chronology model (**Figure 6B**), the E3 and E4 layers are possibly related to the M_s 7.8 and M_s 7.0 earthquakes in 1786 and 1725, respectively. Generally, within dating errors, E1–E4 layers coincide with the M_s 7.5 earthquake in 1955, the M_s 6.0 earthquake of 1932, the M_s 7.8 earthquake in 1786, and the M_s 7.0 earthquake in 1725, respectively (**Figure 6**).

The sensitivity of the lacustrine sediment to seismic activity depends on the magnitude of the earthquake and the distance between the position of the lake and the epicentre. Chassiot et al. (2016b) found that maar Lake Pavin was imprinted by earthquakes with a seismic intensity of Vwithin a 15-km radius. Ghazoui et al. (2019) discovered that a minimum M_s 5.6 earthquake within a 15-km radius or more than a M_s 6.5 earthquake within an 80-km radius could be recorded by the sediment of Lake Rara (Ghazoui et al., 2019). It was shown that earthquake-triggered water oscillation (seiche) occurs when the earthquake magnitude exceeds 7.0 (Alsop & Marco, 2012; Avşar et al., 2014). Although there are lots of earthquakes with different magnitudes around Lake Mugeco, only four earthquakes of M_s 6.0–7.5 within a 40-km radius have been well-preserved in the sediment of Lake Mugeco, and the earthquake

intensity has been greater than VII in Lake Mugeco during the last 300 years. It is clear that Lake Mugeco can only record strong earthquakes with a short epicentre distance.

CONCLUSION

Lacustrine deposits are mainly composed of greyish–brown and light greyish–black silt in Lake Mugeco over the past 300 years. There are four obvious turbidite layers characterized by highly-dense whitish silt, low content of organic matter, high content of clay fraction, and detrital elements (K, Rb, Ca, Sr, Ti, and Si). The formation of these four turbidite layers is related to seiche-triggered erosion of the lakeshore and sedimentation after subaqueous surficial sediment remobilization and resuspension. Chronological results reveal that the ages of the turbidite layers are compatible with four seismic events along the Selaha segment of the Xianshuihe fault zone, i.e., M_s 7.5 earthquake in 1955, M_s 6.0 earthquake in 1932, M_s 7.8 earthquake in 1786, and M_s 7.0 earthquake in 1725. Although historical records show that there are frequent earthquakes over M_s 6.0 along the Xianshuihe fault, only earthquakes with seismic intensities from VII to VIII within a 40-km radius can be recorded by lacustrine sediments in Lake Mugeco. Our study can provide scientific evidence for a long-term paleoseismic reconstruction along the Xianshuihe fault based on lacustrine sediments of Lake Mugeco.

DATA AVAILABILITY STATEMENT

The raw data supporting the conclusions of this article will be made available by the authors without undue reservation.

AUTHOR CONTRIBUTIONS

LL and XL designed this study; RQ and XM analyzed the data; LL and JY wrote the manuscript; and LL, XL, and XM polished the paper. All authors approved the final version of the manuscript.

FUNDING

This work was financially supported by a corporative project of the National Natural Science Foundation of China (NSFC) and the German Research Foundation (DFG) (Grant No. 41861134030).

REFERENCES

Allen, C. R., Zhuoli, L., Hong, Q., Xueze, W., Huawei, Z., and Weishi, H. (1991). Field Study of a Highly Active Fault Zone: The Xianshuihe Fault of Southwestern China. *Geol. Soc. Amer. Bull.* 103 (9), 1178–1199. doi:10.1130/0016-7606(1991)103<1178:fsoaha>2.3.co;2

Alsop, G. I., and Marco, S. (2012). Tsunami and Seiche-Triggered Deformation within Offshore Sediments. *Sediment. Geology.* 261-262, 90–107. doi:10.1016/j.sedgeo.2012.03.013

Appleby, P. G., and Oldfield, F. (1978). The Calculation of lead-210 Dates Assuming a Constant Rate of Supply of Unsupported 210Pb to the Sediment. *Catena* 5 (1), 1–8. doi:10.1016/S0341-8162(78)80002-2

Archer, C., Noble, P., Rosen, M. R., Sagnotti, L., Florindo, F., Mensing, S., et al. (2019). Lakes as Paleoseismic Records in a Seismically-Active, Low-Relief Area (Rieti Basin, Central Italy). *Quat. Sci. Rev.* 211, 186–207. doi:10.1016/j.quascirev.2019.03.004

Aurelia, H.-F., Ulas, A., Meriam El, O., Gilles, L., Philippe, M., and Nathalie, F. (2013). Paleoseismic Record Obtained by Coring a Sag-Pond along the North Anatolian Fault (Turkey). *Ann. Geophys.* 55 (5), 929–953. doi:10.4401/ag-5460

Avşar, U., Hubert-Ferrari, A., De Batist, M., Lepoint, G., Schmidt, S., and Fagel, N. (2014). Seismically-triggered Organic-Rich Layers in Recent Sediments from Göllüköy Lake (North Anatolian Fault, Turkey). *Quat. Sci. Rev.* 103, 67–80. doi:10.1016/j.quascirev.2014.08.020

Avşar, U., Hubert-Ferrari, A., De Batist, M., Schmidt, S., and Fagel, N. (2015). Sedimentary Records of Past Earthquakes in Boraboy Lake during the Last Ca 600 Years (North Anatolian Fault, Turkey). *Palaeogeogr. Palaeoclimatol. Palaeoecol.* 433, 1–9. doi:10.1016/j.palaeo.2015.04.031

Bai, M., Chevalier, M.-L., Pan, J., Replumaz, A., Leloup, P. H., Métois, M., et al. (2018). Southeastward Increase of the Late Quaternary Slip-Rate of the Xianshuihe Fault, Eastern Tibet. Geodynamic and Seismic Hazard Implications. *Earth Planet. Sci. Lett.* 485, 19–31. doi:10.1016/j.epsl.2017.12.045

Barberopoulou, A. (2006). Long-Period Effects of the Denali Earthquake on Water Bodies in the Puget Lowland: Observations and Modeling. *Bull. Seismological Soc. America* 96 (2), 519–535. doi:10.1785/0120050090

Beck, C. (2009). "Late Quaternary Lacustrine Paleo-Seismic Archives in north-western Alps: Examples of Earthquake-Origin Assessment of Sedimentary Disturbances". *Earth-Science Rev.* 96 (4), 327–344. doi:10.1016/j.earscirev.2009.07.005

Blaauw, M., and Christen, J. A. (2011). Flexible Paleoclimate Age-Depth Models Using an Autoregressive Gamma Process. *Bayesian Anal.* 6 (3), 457–474. doi:10.1214/ba/1339616472

Brocard, G., Adatte, T., Magand, O., Pfeifer, H.-R., Bettini, A., Arnaud, F., et al. (2014). The Recording of Floods and Earthquakes in Lake Chichój, Guatemala during the Twentieth century. *J. Paleolimnol.* 52 (3), 155–169. doi:10.1007/s10933-014-9784-4

Bruel, R., and Sabatier, P. (2020). Serac: an R Package for ShortlivEd RAdionuclide Chronology of Recent Sediment Cores. *J. Environ. Radioactivity* 225, 106449. doi:10.1016/j.jenvrad.2020.106449

Bryn, P., Berg, K., Forsberg, C. F., Solheim, A., and Kvalstad, T. J. (2005). Explaining the Storegga Slide. *Mar. Pet. Geol.* 22 (1-2), 11–19. doi:10.1016/b978-0-08-044694-3.50005-6

Bussmann, F., and Anselmetti, F. S. (2010). Rossberg Landslide History and Flood Chronology as Recorded in Lake Lauerz Sediments (Central Switzerland). *Swiss J. Geosci.* 103 (1), 43–59. doi:10.1007/s00015-010-0001-9

Chapron, E., Beck, C., Pourchet, M., and Deconinck, J.-F. (1999). 1822 Earthquake-Triggered Homogenite in Lake Le Bourget (NW Alps). *Terra Nova* 11 (2-3), 86–92. doi:10.1046/j.1365-3121.1999.00230.x

Chassiot, L., Chapron, E., Di Giovanni, C., Albéric, P., Lajeunesse, P., Lehours, A.-C., et al. (2016a). Extreme Events in the Sedimentary Record of Maar Lake Pavin: Implications for Natural Hazards Assessment in the French Massif Central. *Quat. Sci. Rev.* 141, 9–25. doi:10.1016/j.quascirev.2016.03.020

Chassiot, L., Chapron, E., Di Giovanni, C., Lajeunesse, P., Tachikawa, K., Garcia, M., et al. (2016b). Historical Seismicity of the Mont Dore Volcanic Province (Auvergne, France) Unraveled by a Regional Lacustrine Investigation: New Insights about Lake Sensitivity to Earthquakes. *Sediment. Geology.* 339, 134–150. doi:10.1016/j.sedgeo.2016.04.007

Croudace, I. W., Rindby, A., and Rothwell, R. G. (2006). ITRAX: Description and Evaluation of a New Multi-Function X-Ray Core Scanner. *Geol. Soc. Lond. Spec. Publications* 267 (1), 51–63. doi:10.1144/GSL.SP.2006.267.01.04

Fan, J., Jiang, H., Shi, W., Guo, Q., Zhang, S., Wei, X., et al. (2020). A 450-year Lacustrine Record of Recurrent Seismic Activities Around the Fuyun Fault,

Altay Mountains, Northwest China. *Quat. Int.* 558, 75–88. doi:10.1016/j.quaint.2020.08.051

Foucher, A., Chaboche, P.-A., Sabatier, P., and Evrard, O. (2021). A Worldwide Meta-Analysis (1977-2020) of Sediment Core Dating Using Fallout Radionuclides Including ^{137}Cs and $^{210}Pb_{xs}$. *Earth Syst. Sci. Data* 13, 4951–4966. doi:10.5194/essd-13-4951-2021

Gao, S., Chen, L., Liang, M., Wang, D., Li, Y., Han, M., et al. (2021). Rupture Characteristics and Seismic Recurrence Behaviors of Xianshuihe Fault Revealed by Xinyulin Trenches, South of Kangding. *Adv. Eng. Sci.* 53, 53–61. doi:10.15961/j.jsuese.202100031

Gastineau, R., Sigoyer, J., Sabatier, P., Fabbri, S. C., Anselmetti, F. S., Develle, A. L., et al. (2021). Active Subaquatic Fault Segments in Lake Iznik along the Middle Strand of the North Anatolian Fault, NW Turkey. *Tectonics* 40 (1), e2020TC00640. doi:10.1029/2020tc006404

Ghazoui, Z., Bertrand, S., Vanneste, K., Yokoyama, Y., Nomade, J., Gajurel, A. P., et al. (2019). Potentially Large Post-1505 AD Earthquakes in Western Nepal Revealed by a Lake Sediment Record. *Nat. Commun.* 10 (1), 2258. doi:10.1038/s41467-019-10093-4

Howarth, J. D., Fitzsimons, S. J., Norris, R. J., and Jacobsen, G. E. (2012). Lake Sediments Record Cycles of Sediment Flux Driven by Large Earthquakes on the Alpine Fault, New Zealand. *Geology* 40 (12), 1091–1094. doi:10.1130/g33486.1

Howarth, J. D., Fitzsimons, S. J., Norris, R. J., and Jacobsen, G. E. (2014). Lake Sediments Record High Intensity Shaking that Provides Insight into the Location and Rupture Length of Large Earthquakes on the Alpine Fault, New Zealand. *Earth Planet. Sci. Lett.* 403, 340–351. doi:10.1016/j.epsl.2014.07.008

Hu, Z., Anderson, N. J., Yang, X., Zhang, E., Wang, R., and Jones, R. T. (2015). Climate and Tectonic Effects on Holocene Development of an Alpine Lake (Muge Co, SE Margin of Tibet). *The Holocene* 26 (5), 801–813. doi:10.1177/0959683615618263

Hubert-Ferrari, A., Lamair, L., Hage, S., Schmidt, S., Çağatay, M. N., and Avşar, U. (2020). A 3800 Yr Paleoseismic Record (Lake Hazar Sediments, Eastern Turkey): Implications for the East Anatolian Fault Seismic Cycle. *Earth Planet. Sci. Lett.* 538, 116152. doi:10.1016/j.epsl.2020.116152

Jiang, H., Zhong, N., Li, Y., Xu, H., Yang, H., and Peng, X. (2016). Soft Sediment Deformation Structures in the Lixian Lacustrine Sediments, Eastern Tibetan Plateau and Implications for Postglacial Seismic Activity. *Sediment. Geology.* 344, 123–134. doi:10.1016/j.sedgeo.2016.06.011

Kinder, M., Tylmann, W., Rzeszewski, M., and Zolitschka, B. (2019). Varves and Mass-Movement Deposits Record Distinctly Different Sedimentation Dynamics since the Late Glacial (Lake Szurpiły, Northeastern Poland). *Quat. Res.* 93, 299–313. doi:10.1017/qua.2019.61

Liang, M. (2019). *Characteristics of the Late-Quaternary Fault Activity of the Xianshuihe Fault*. PhD Thesis. Beijing: Institute of Geology, China Earthquake Administration. doi:10.27489/d.cnki.gzdds.2019.000019

Lu, Y., Wetzler, N., Waldmann, N., Agnon, A., Biasi, G. P., and Marco, S. (2020). A 220,000-Year-Long Continuous Large Earthquake Record on a Slow-Slipping Plate Boundary. *Sci. Adv.* 6 (48), eaba4170. doi:10.1126/sciadv.aba4170

Lu, Y., Moernaut, J., Bookman, R., Waldmann, N., Wetzler, N., Agnon, A., et al. (2021). A New Approach to Constrain the Seismic Origin for Prehistoric Turbidites as Applied to the Dead Sea Basin. *Geophys. Res. Lett.* 48 (3), e2020GL090947. doi:10.1029/2020gl090947

Monecke, K., Anselmetti, F. S., Becker, A., Sturm, M., and Giardini, D. (2004). The Record of Historic Earthquakes in Lake Sediments of Central Switzerland. *Tectonophysics* 394 (1-2), 21–40. doi:10.1016/j.tecto.2004.07.053

Moernaut, J., Daele, M. V., Heirman, K., Fontijn, K., Strasser, M., Pino, M., et al. (2014). Lacustrine Turbidites as a Tool for Quantitative Earthquake Reconstruction: New Evidence for a Variable Rupture Mode in South central Chile. *J. Geophys. Res. Solid Earth* 119 (3), 1607–1633. doi:10.1002/2013jb010738

Moernaut, J., Van Daele, M., Strasser, M., Clare, M. A., Heirman, K., Viel, M., et al. (2017). Lacustrine Turbidites Produced by Surficial Slope Sediment Remobilization: A Mechanism for Continuous and Sensitive Turbidite Paleoseismic Records. *Mar. Geology.* 384, 159–176. doi:10.1016/j.margeo.2015.10.009

Moernaut, J., Van Daele, M., Fontijn, K., Heirman, K., Kempf, P., Pino, M., et al. (2018). Larger Earthquakes Recur More Periodically: New Insights in the Megathrust Earthquake Cycle from Lacustrine Turbidite Records in South-central Chile. *Earth Planet. Sci. Lett.* 481, 9–19. doi:10.1016/j.epsl.2017.10.016

Ni, Z., Jones, R., Zhang, E., Chang, J., Shulmeister, J., Sun, W., et al. (2019). Contrasting Effects of Winter and Summer Climate on Holocene Montane Vegetation Belts Evolution in Southeastern Qinghai-Tibetan Plateau, China. *Palaeogeogr. Palaeoclimatol. Palaeoecol.* 533, 109232. doi:10.1016/j.palaeo.2019.06.005

Norris, R. S., Burrows, A. S., and Fieldhouse, R. W. (1994). *British, French, and Chinese Nuclear Weapons*. Boulder, Colorado: Westview Press, 333–336.

Polonia, A., Bonetti, C., Bonetti, J., Çağatay, M. N., Gallerani, A., Gasperini, L., et al. (2021). Deciphering Co-seismic Sedimentary Processes in the Mediterranean Sea Using Elemental, Organic Carbon, and Isotopic Data. *Geochem. Geophys. Geosyst.* 22 (7), e2020GC009446. doi:10.1029/2020gc009446

Praet, N., Moernaut, J., Van Daele, M., Boes, E., Haeussler, P. J., Strupler, M., et al. (2017). Paleoseismic Potential of Sublacustrine Landslide Records in a High-Seismicity Setting (South-central Alaska). *Mar. Geology.* 384, 103–119. doi:10.1016/j.margeo.2016.05.004

Qian, H., Allen, C. R., Luo, Z., Wen, X., Zhou, H., and Huang, W. (1988). The Active Characteristics of Xianshuihe Fault in the Holocence. *Earthquake Res. Chin.* 4 (02), 11–20.

Qiao, X., Wang, Q., and Du, R. (2004). Characteristics of Current Crustal Deformation of Active Blocks in the Sichuan-Yunnan Region. *Chin. J. Geophys.* 47 (05), 806–812. doi:10.1002/cjg2.568

Rapuc, W., Sabatier, P., Andrič, M., Crouzet, C., Arnaud, F., Chapron, E., et al. (2018). 6600 Years of Earthquake Record in the Julian Alps (Lake Bohinj, Slovenia). *Sedimentology* 65 (5), 1777–1799. doi:10.1111/sed.12446

Rapuc, W., Jacq, K., Develle, A.-L., Sabatier, P., Fanget, B., Perrette, Y., et al. (2020). XRF and Hyperspectral Analyses as an Automatic Way to Detect Flood Events in Sediment Cores. *Sediment. Geology.* 409, 105776. doi:10.1016/j.sedgeo.2020.105776

Reimer, P. J., Austin, W. E. N., Bard, E., Bayliss, A., Blackwell, P. G., Bronk Ramsey, C., et al. (2020). The IntCal20 Northern Hemisphere Radiocarbon Age Calibration Curve (0-55 Cal kBP). *Radiocarbon* 62 (4), 725–757. doi:10.1017/rdc.2020.41

Robbins, J. A. (1978). "Geochemical and Geophysical Applications of Radioactive lead," in *The Biogeochemistry of Lead in the Environment*. Editor J. O. Nriagu (Amsterdam: Elsevier), 285–393.

Roger, F., Calassou, S., Lancelot, J., Malavieille, J., Mattauer, M., Zhiqin, X., et al. (1995). Miocene Emplacement and Deformation of the Konga Shan Granite (Xianshuihe Fault Zone, West Sichuan, China): Geodynamic Implications. *Earth Planet. Sci. Lett.* 130 (1-4), 201–216. doi:10.1016/0012-821X(94)00252-T

Sabatier, P., Dezileau, L., Briqueu, L., Colin, C., and Siani, G. (2010). Clay Minerals and Geochemistry Record from Northwest Mediterranean Coastal Lagoon Sequence: Implications for Paleostorm Reconstruction. *Sediment. Geology.* 228 (3-4), 205–217. doi:10.1016/j.sedgeo.2010.04.012

Sabatier, P., Wilhelm, B., Ficetola, G. F., Moiroux, F., Poulenard, J., Develle, A.-L., et al. (2017). 6-kyr Record of Flood Frequency and Intensity in the Western Mediterranean Alps - Interplay of Solar and Temperature Forcing. *Quat. Sci. Rev.* 170, 121–135. doi:10.1016/j.quascirev.2017.06.019

Schwab, M. J., Werner, P., Dulski, P., McGee, E., Nowaczyk, N. R., Bertrand, S., et al. (2009). Palaeolimnology of Lake Sapanca and Identification of Historic Earthquake Signals, Northern Anatolian Fault Zone (Turkey). *Quat. Sci. Rev.* 28 (11-12), 991–1005. doi:10.1016/j.quascirev.2009.02.018

Schwestermann, T., Huang, J., Konzett, J., Kioka, A., Wefer, G., Ikehara, K., et al. (2020). Multivariate Statistical and Multiproxy Constraints on Earthquake-Triggered Sediment Remobilization Processes in the Central Japan Trench. *Geochem. Geophys. Geosyst.* 21 (6), e2019GC008861. doi:10.1029/2019GC008861

Shiki, T., Kumon, F., Inouchi, Y., Kontani, Y., Sakamoto, T., Tateishi, M., et al. (2000). Sedimentary Features of the Seismo-Turbidites, Lake Biwa, Japan. *Sediment. Geol.* 135 (1-4), 37–50. doi:10.1016/S0037-0738(00)00061-0

Sturm, M., Siegenthaler, C., and Pickrill, R. A. (1995). "Turbidites and 'homogenites,". *A Conceptual Model of Flood and Slide Deposits* (Paris: Publication IAS-16th Regional Meeting of Sedimentology), 22, p140.

Sun, Q., Chu, G., Liu, G., Li, S., and Wang, X. (2007). Calibration of Alkenone Unsaturation Index with Growth Temperature for a Lacustrine Species, Chrysotila Lamellosa (Haptophyceae). *Org. Geochem.* 38 (8), 1226–1234. doi:10.1016/j.orggeochem.2007.04.007

Sun, W., Zhang, E., Jones, R. T., Liu, E., and Shen, J. (2015). Asian Summer Monsoon Variability during the Late Glacial and Holocene Inferred from the Stable Carbon Isotope Record of Black Carbon in the Sediments of Muge Co, Southeastern Tibetan Plateau, China. *The Holocene* 25 (12), 1857–1868. doi:10.1177/0959683615605743

Sun, W., Zhang, E., Jones, R. T., Liu, E., and Shen, J. (2016). Biogeochemical Processes and Response to Climate Change Recorded in the Isotopes of Lacustrine Organic Matter, Southeastern Qinghai-Tibetan Plateau, China. *Palaeogeogr. Palaeoclimatol. Palaeoecol.* 453, 93–100. doi:10.1016/j.palaeo.2016.04.013

Topal, S., and Özkul, M. (2014). Soft-Sediment Deformation Structures Interpreted as Seismites in the Kolankaya Formation, Denizli Basin (SW Turkey). *Scientific World J.* 2014, 1–13. doi:10.1155/2014/352654

Van Daele, M., Moernaut, J., Doom, L., Boes, E., Fontijn, K., Heirman, K., et al. (2015). A Comparison of the Sedimentary Records of the 1960 and 2010 Great Chilean Earthquakes in 17 Lakes: Implications for Quantitative Lacustrine Palaeoseismology. *Sedimentology* 62 (5), 1466–1496. doi:10.1111/sed.12193

Vandekerkhove, E., Van Daele, M., Praet, N., Cnudde, V., Haeussler, P. J., De Batist, M., et al. (2019). Flood-triggered versus Earthquake-Triggered Turbidites: A Sedimentological Study in Clastic lake Sediments (Eklutna Lake, Alaska). *Sedimentology* 67 (1), 364–389. doi:10.1111/sed.12646

Wang, X., Yu, H., and Pei, X. (1996). Application and Results of Statistic Hazard Data about the 1955 M7.5 Kangding Earthquake. *Earthquake Res. Sichuan* 3, 57–64.

Wang, E., Burchfiel, B. C., Royden, L. H., Chen, L., and Chen, Z. (1998). *Late Cenozoic Xianshuihe-Xiaojiang, Red River, and Dali Fault Systems of Southwestern Sichuan and Central Yunnan, China*, 327. Colorado: The Geological Society of America, Inc. Special Paper, 108.

Wang, S., Jiang, G., Xu, T., Tian, Y., Zheng, D., and Fang, X. (2012). The Jinhe–Qinghe Fault—An Inactive Branch of the Xianshuihe–Xiaojiang Fault Zone, Eastern Tibet. *Tectonophysics* 544, 93–102. doi:10.1016/j.tecto.2012.04.004

Weltje, G. J., Bloemsma, M. R., Tjallingii, R., Heslop, D., Röhl, U., and Croudace, I. W. (2015). "Prediction of Geochemical Composition from XRF Core Scanner Data: A New Multivariate Approach Including Automatic Selection of Calibration Samples and Quantification of Uncertainties,". *Micro-XRF Studies of Sediment Cores*. Editors I. W. Croudace and R. G. Rothwell (Dordrecht: Springer Netherlands), 17, 507–534. doi:10.1007/978-94-017-9849-5_21

Wen, X., Allen, C. R., Luo, Z., Qain, H., Zhou, H., and Huang, W. (1989). Segmentation, Geometric Features, and Their Seismotectonic Implications for the Holocene Xianshuihe Fault Zone. *Acta Seismol. Sin.* 11 (4), 362–372.

Wen, X.-z., Ma, S.-l., Xu, X.-w., and He, Y.-n. (2008). Historical Pattern and Behavior of Earthquake Ruptures along the Eastern Boundary of the Sichuan-Yunnan Faulted-Block, Southwestern China. *Phys. Earth Planet. Interiors* 168 (1-2), 16–36. doi:10.1016/j.pepi.2008.04.013

Wilhelm, B., Arnaud, F., Sabatier, P., Crouzet, C., Brisset, E., Chaumillon, E., et al. (2012). 1400 Years of Extreme Precipitation Patterns over the Mediterranean French Alps and Possible Forcing Mechanisms. *Quat. Res.* 78 (1), 1–12. doi:10.1016/j.yqres.2012.03.003

Wilhelm, B., Nomade, J., Crouzet, C., Litty, C., Sabatier, P., Belle, S., et al. (2016). Quantified Sensitivity of Small lake Sediments to Record Historic Earthquakes: Implications for Paleoseismology. *J. Geophys. Res. Earth Surf.* 121 (1), 2–16. doi:10.1002/2015jf003644

Wilhelm, B., Rapuc, W., Amann, B., Anselmetti, F. S., Arnaud, F., Blanchet, J., et al. (2022). Impact of Warmer Climate Periods on Flood hazard in the European Alps. *Nat. Geosci.* 15 (2), 118–123. doi:10.1038/s41561-021-00878-y

Wils, K., Daryono, M. R., Praet, N., Santoso, A. B., Dianto, A., Schmidt, S., et al. (2021). The Sediments of Lake Singkarak and Lake Maninjau in West Sumatra Reveal Their Earthquake, Volcanic and Rainfall History. *Sediment. Geology.* 416, 105863. doi:10.1016/j.sedgeo.2021.105863

Woodward, C. A., and Gadd, P. S. (2019). The Potential Power and Pitfalls of Using the X-ray Fluorescence Molybdenum Incoherent: Coherent Scattering Ratio as a Proxy for Sediment Organic Content. *Quat. Int.* 514, 30–43. doi:10.1016/j.quaint.2018.11.031

Woodward, C. A., Slee, A., Gadd, P., Zawadzki, A., Hamze, H., Parmar, A., et al. (2018). The Role of Earthquakes and Climate in the Formation of Diamictic Sediments in a New Zealand Mountain Lake. *Quat. Int.* 470, 130–147. doi:10.1016/j.quaint.2017.10.051

Writing Group of Compilation of Sichuan Earthquake Data (1980a). *Compilation of Sichuan Earthquake Data*, Vol. 1. Chengdu: Sichuan People's Publishing House.

Writing Group of Compilation of Sichuan Earthquake Data (1980b). *Compilation of Sichuan Earthquake Data*, Vol. 2. Chengdu: Sichuan People's Publishing House.

Xie, H., Guo, D., Wang, S., and Wei, F. (1997). Flood Causes in Town Proper of Kangding in 1995. *Mt Res.* 1997 (02), 129–131. doi:10.16089/j.cnki.1008-2786.1997.02.014

Xiong, T., Yao, X., and Zhang, Y. (2010). A Review of Activity of Xianshuihe Fault Zone since the Holocene. *J. Geomechan.* 16 (02), 176–188. doi:10.3969/j.issn.1006-6616.2010.02.007

Yan, B., and Lin, A. (2015). Systematic Deflection and Offset of the Yangtze River Drainage System along the Strike-Slip Ganzi-Yushu-Xianshuihe Fault Zone, Tibetan Plateau. *J. Geodynamics* 87, 13–25. doi:10.1016/j.jog.2015.03.002

Yan, B., Wang, M., Jia, D., Cui, J., and Hu, J. (2019). Investigation and Magnitude Re-evaluation of the 1955 Zheduotang Earthquake, Eastern Tibetan Plateau, China. *Geol. J.* 55 (11), 7272–7284. doi:10.1002/gj.3628

Zhang, C., Zhou, A., Zhang, X., Wu, D., and Hao, S. (2015). Identification of Paleaoflood Events by Lacustrine Archives and Their Links to Climatic Conditions. *Prog. Geogr.* 34 (07), 898–908. doi:10.18306/dlkxjz.2015.07.011

Zhou, R., Gong, N., Ma, S., Xia, C., and Li, X. (2001). Evaluation of Possibility of Reservoir-Induced Earthquake at Mugeco Lake Hydropower Station. Des. *Hydroelectr. Power Station* 17 (02), 81–88. doi:10.3969/j.issn.1003-9805.2001.02.026

Conflict of Interest: The authors declare that the research was conducted in the absence of any commercial or financial relationships that could be construed as a potential conflict of interest.

Publisher's Note: All claims expressed in this article are solely those of the authors and do not necessarily represent those of their affiliated organizations, or those of the publisher, the editors, and the reviewers. Any product that may be evaluated in this article, or claim that may be made by its manufacturer, is not guaranteed or endorsed by the publisher.

frontiers | Frontiers in Earth Science

ORIGINAL RESEARCH
published: 26 April 2022
doi: 10.3389/feart.2022.875237

Rapid Exhumation Processes of the Gaoligong Mountain Range in the Southeastern Margin of the Qinghai–Tibet Plateau Since the Late Cenozoic

Jialong Wang[1,2], Ni Li[1], F. M. Stuart[3], L. D. Nicola[3], Huiping Zhang[4], Ying Wang[4], Jianzhang Pang[4] and Yongwei Zhao[1]*

[1]Jilin Changbaishan Volcano National Observation and Research Station, Institute of Geology, China Earthquake Administration (CEA), Beijing, China, [2]The First Monitoring and Application Center, China Earthquake Administration, Tianjin, China, [3]Isotope Geosciences Unit, SUERC, East Kilbride, United Kingdom, [4]State Key Laboratory of Earthquake Dynamics, Institute of Geology, China Earthquake Administration, Beijing, China

OPEN ACCESS

Edited by:
Chong Xu,
National Institute of Natural Hazards, China

Reviewed by:
Honghua Lu,
East China Normal University, China
Pitsanupong Kanjanapayont,
Chulalongkorn University, Thailand

***Correspondence:**
Ni Li
lini67@sina.com

Specialty section:
This article was submitted to Structural Geology and Tectonics, a section of the journal Frontiers in Earth Science

Received: *14 February 2022*
Accepted: *29 March 2022*
Published: *26 April 2022*

Citation:
Wang J, Li N, Stuart FM, Nicola LD, Zhang H, Wang Y, Pang J and Zhao Y (2022) Rapid Exhumation Processes of the Gaoligong Mountain Range in the Southeastern Margin of the Qinghai–Tibet Plateau Since the Late Cenozoic. Front. Earth Sci. 10:875237. doi: 10.3389/feart.2022.875237

Three continent-scale ductile shear zones trending N-S are distributed in the southeast margin of the Qinghai–Tibet Plateau. Their tectonic deformation and exhumation histories are of great significance to understanding the orogenic processes within the continent and the growth as well as expansion mechanism of the plateau. The Gaoligong shear zone (GLGSZ) is the westernmost zone near the boundary of the Indian subduction plate and is less well studied than the Ailaoshan–Red River shear zone (ASRRSZ) in the east. In this study, low-temperature thermochronological methods including apatite (U-Th)/He (AHe), zircon (U-Th)/He (ZHe), and apatite fission track (AFT) were used to date the vertical profile samples from the Gaoligong Mountain to understand the exhumation processes that occurred in the late Cenozoic. Our results show that the GLGSZ has experienced two stages of rapid exhumation events since the late Cenozoic: in the middle Miocene (~14.5 Ma) and early Pleistocene (~2.9 Ma). Based on our data, we divided the late Cenozoic tectonic deformation and exhumation processes in the Gaoligong Mountain area into two stages: 1) From the middle to the late Miocene, large-scale regional dextral strike-slip movements and lateral compressions controlled the ductile shear zone and continuously denuded the mountain surface; 2) in the Pleistocene, rapid river erosion and undercutting caused by fluctuations of the monsoon system, together with the continuous activity of brittle faults, drove the latest rapid exhumations. A comparison of the thermochronological data of the different areas along the Gaoligong Mountain shows that the exhumation rate in its northern transect is significantly higher and the time of the onset of exhumation is earlier than that in the southern transect. These results indicate that the deformation processes began in the north and continued southwards and controlled the geomorphological characteristics of the Gaoligong Mountain, whose elevation is higher in the northern part than in the southern part.

Keywords: southeastern tibet, gaoligong ductile shear zone, low-temperature thermochronology, exhumation, geomorphological evolution

INTRODUCTION

The collision between the Indian plate and the Eurasian plate in the Cenozoic era shortened the crust of the Asian continent by approximately 2,000–2,500 km (Dewey et al., 1989; Yin and Harrison, 2000). This created the Qinghai–Tibet Plateau, the largest and highest plateau in the world, and led to extensive intracontinental deformations in the Eurasian plate (Dewey et al., 1989; Yin and Harrison, 2000). With the uplift of the Qinghai–Tibet Plateau, the plateau materials have been continuously pushed towards the southeast, and the southeast edge of the plateau forms a landform slope with high north and low south (Clark and Royden, 2000; Liu-Zeng et al., 2008). The boundary between the Indian plate and the Eurasian plate is also the most complicated active structure causing geomorphic features of the southeastern expansion and growth of the plateau. Therefore, the Qinghai–Tibet Plateau has both thrust faults and large strike-slip faults that are oblique to the boundary of the plateau, and it is difficult to explain all observed phenomena using a single continental dynamic model. Currently, the time, velocity, and mode of migration of plateau materials to the southeast are still under debate. The hypotheses on the tectonic deformation and uplift mechanism in the southeastern margin are: 1) The lower crustal flow model that emphasises consistent plateau height and continuous deformation (Royden et al., 1997; Clark and Royden, 2000); 2) extrusion along large strike-slip faults or large shear zones as the main mechanism proposed by the continental escape model (Molnar and Tapponnier, 1978; Tapponnier et al., 1982, 2001); 3) based on the brittle block model (England and Molnar, 1990), Wang et al. (2012) suggested that the outward expansion of the plateau materials occurred in the middle and late Miocene (~10 Ma), which was caused by the delamination of the lithosphere at the bottom of the plateau and the equilibrium rebound caused by it. Wang et al. (2018) quantitatively analysed the longitudinal profile of the Nu River and considered that the accelerated river cutting and rapid rock exhumation due to the climate change in the late Miocene was of great significance to the tectonic and geomorphological evolution of the southeastern margin of the plateau. Liu et al. (2009) believed that this area was mainly dominated by tectonic uplift in the Neogene, whereas erosion dominated in the Quaternary.

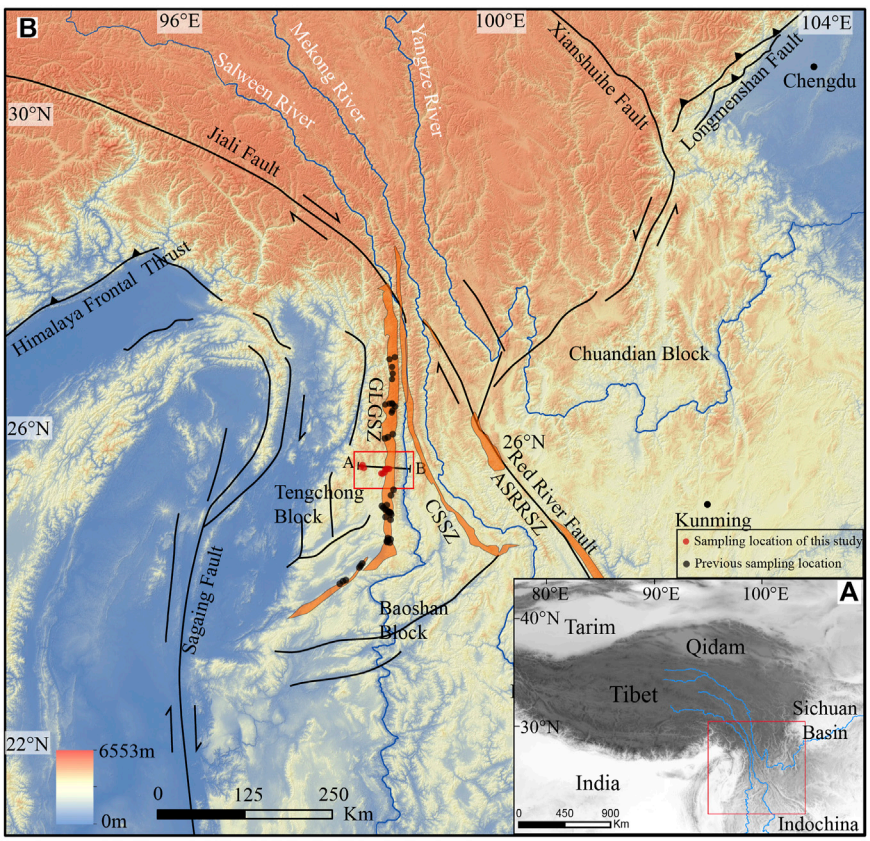

FIGURE 1 | Tectonics and regional topography of the Three Rivers Region and surrounding areas. **(A)** Simplified tectonic framework of the Tibetan Plateau. Modified from Deng et al. (2014). **(B)** Digital elevation model (DEM) of the topography and active faults in the Three Rivers Region, showing the study area (red rectangle) and sample locations in this study (red circles). DEM data is based on ~90 m Shuttle Radar Topography Mission (SRTM). Previous thermochronological ages marked by dark circles are also shown (Akciz, 2004; Wang et al., 2008; Lin et al., 2009; Song et al., 2010; Zhang et al., 2012; Liu et al., 2015; Xu et al., 2015; Tang et al., 2016; Zhang et al., 2017; Wang et al., 2018; Tang et al., 2020). GLGSZ: The Gaoligong shear zone; CSSZ: Chongshan shear zone; ASRRSZ: Ailaoshan–Red River sheer zone. Red square is the study area shown in **Figure 2**.

The Gaoligong Mountain shear zone (GLGSZ), Chongshan shear zone (CSSZ), and the Ailaoshan–Red River shear zone (ASRRSZ) are large-scale strike-slip fault zones with typical structural features that extend for thousands of kilometres across the southeastern margin of the Qinghai–Tibet Plateau (Allen et al., 1984; Clark et al., 2005, 2006; Royden et al., 2008; Wang et al., 2018; Wang et al., 2020; Shen et al., 2021; **Figure 1**). The GLGSZ is a large-scale structural zone in the southern transect of the Bangong Lake–Nu River suture zone, which was formed by the southward extrusion of blocks in the southeastern margin of the Qinghai–Tibet Plateau and consists of large-scale strike-slip faults between the blocks. The orogenic process and geomorphic evolution of these continental-scale shear zones are of great significance for revealing the deformation mechanism of the Indo-Asian Cenozoic collision inside the Asian continent (Houseman and England, 1993; Wang et al., 1998; Tapponnier et al., 2001; Liu-Zeng et al., 2008, 2018). Little research has been conducted on the GLGSZ, which is located in southwest Yunnan, owing to its relatively difficult natural environment; therefore, studies have mainly focused on geometry, kinematics, petrography, and geochronology (Ji et al., 2000; Akciz, 2004; Zhang et al., 2010; Zhang et al., 2012). Research on the exhumation, uplift, and tectonic geomorphological evolution of the GLGSZ has only started recently (Liu-Zeng et al., 2018; Liu-Zeng et al., 2018; Wang et al., 2018, 2020; Dong et al., 2021; Shen et al., 2021). These studies provide information regarding the orogenic process of the Gaoligong Mountain (Glotzbach et al., 2011).to identify the southeast migration pattern of materials in the Qinghai–Tibet Plateau and the deformation pattern of the crust in the southeast margin.

In addition, the three largest rivers in Asia, namely, the Salween River, Mekong River, and Yangtze River, originate in the Qinghai–Tibet Plateau, and flow through the nearest part of the southeast edge of the plateau by only a few tens of kilometres apart and are parallel to each other, cutting through the bedrock canyon landform of approximately 3 km (Clark et al., 2005; Liu-Zeng et al., 2008; Yang et al., 2015). Distinct geomorphic features such as high mountains and deep valleys manifest at the uplift of the Cenozoic Indo-Asian collision plateau in the southeast margin. Currently, there is little research on the timing of the geomorphic processes and on whether the erosion and undercutting process of rivers must contribute to the rapid exhumation of the large-scale structural zone in the southeastern margin of the Qinghai-Tibet Plateau. From this perspective, this study provides a quantitative assessment of the thermal history of the GLGSZ through low-temperature thermochronology. *In situ* samples of fresh gneiss and granite were collected in the transects of the Gaoligong Mountain, Guyong Rock Mass, and Yinghuagu Valley. Apatite (U-Th)/He (AHe) and zircon (U-Th)/He (ZHe) and apatite fission track (AFT) were performed, and an age-elevation vertical transect was established. A discussion on the exhumation and uplift process of the Gaoligong mountain range is provided based on the newly acquired low-temperature chronology data to outline the tectonic deformation history and landform formation of the southeast margin of the Qinghai–Tibet Plateau.

GEOLOGICAL SETTING

There are three tectonic subzones in the study area: the Gaoligong Mountain metamorphic complex belt, Tengchong Block, and Baoshan Block (**Figure 1**). The Gaoligong Group is distributed from Jiali Fault in the north to Sagaing Fault in the south, and its east and west sides are bounded by major faults manifested as the Salween River and Longchuan River, respectively. Petrological facies containing high-grade metamorphic rocks in the inner belt, which tend to be shallower from the middle to both sides, are alternately observed. Rock types are complex, including biotite plagioclase granulite, plagioclase amphibolite, eyeball-shaped striped migmatite, mixed gneiss, marble, and quartzite. Migmatization is so strong that it is impossible to distinguish between the sequences. Inner faults are extremely developed, dynamic metamorphism is strong, and tectonized rocks (fault breccia and mylonite) are common. Well-developed strata with large thicknesses are observed in the Baoshan Block, and they are distributed on both sides of the Nu River Valley and Longling–Luxi area to the east of the Gaoligong Mountain. Overall, the Baoshan Block is characterised by clastic rock, carbonate and dolomite deposits of shallow sea, coastal, and lagoon facies, and volcanic deposits. After the Jurassic period, the marine history ended and turned into continental deposits with parallel unconformity contact relationship among all systems. The stratigraphic characteristics of the Tengchong Block differ considerably from those of the Baoshan Block, with underdeveloped strata and low thickness, and the main body is coastal clastic rock deposits. The Palaeozoic strata are primarily of Silurian, Devonian, and Carboniferous origin, the Mesozoic strata are only of Triassic origin, and the Cenozoic volcanic rocks are particularly developed. This indicates that the Tengchong Block has been a terrestrial environment for a long time.

Since the Cenozoic, strike-slip faults have been the most developed tectonic structure in the study area and its surroundings. Among them, the Nabang strike-slip zone (Najman et al., 2020) on the western edge is a dextral strike-slip fault of the same scale and nature as that of the Gaoligong strike-slip zone. Dextral strike-slip faults of different scales and levels are also exposed between the two fault zones. Gaoligong strike-slip fault zone extends to the east Himalayan tectonic section in the north, turns to the south *via* Fugong and Lushui to Longling, and turns to the south *via* Ruili to the Sagaing fault in the west, with a total width of approximately 8–12 km. Gaoligong strike-slip zone in the north of Longling is distributed in the north-south direction, while in the west it turns to the north-east direction. Its altitude exceeds 3 km, and its elevation gradually decreases from north to south. It is also the watershed between the Longchuan River in the west and the Nu River in the east, and it divides the Baoshan Block and the Tengchong Block. The mountain is mainly composed of high-grade metamorphic rocks and granite (Zhong et al., 1991; Wang et al., 1998). The east of the shear zone consists of shallow metamorphic rocks of the Palaeozoic Gongyanghe Group, in which fold cleavage and cataclastic structures are developed. The deep mylonite of the Paleoproterozoic Gaoligong Mountain

Group is exposed to the west, which is composed of granite mylonite, various light-coloured veins, cataclastic rocks, and mylonite. The deformation of the mountain is strong. The Gaoligong strike-slip zone consists mainly of a dextral strike-slip as evidenced by combining the lineation and foliation of the shear zone (Socquet and Pubellier, 2005; Tang et al., 2016). Under the action of near east–west compressional shear, the right-lateral strike-slip GLGSZ was bent and connected with the Sagaing fault, and since the Miocene, the compression of the Indian plate to the Eurasian plate intensified (Yang et al., 2006, 2011). According to the results measured by the K-Ar method of muscovite and Ar/Ar method of amphibolite and biotite, it is estimated that the ductile strike-slip deformation age of Gaoligong is 32–22 Ma (Ji et al., 2000; Wang et al., 2006). The quaternary GLGSZ sides are mainly characterised by the strike-slip movement of brittle faults. In the southern section, some normal faults are observed, forming a series of graben and semi-graben basins (Wang et al., 2008), which may be related to the formation of a series of NE-trending faults in the region. The frequent earthquake events in this area in modern times (An et al., 2009. Chang et al., 2011) indicate that the faults in this area are still active. The Nabang strike-slip fault zone, which starts from the vicinity of Xima-Tongbiguan in the east and reaches the east side of the Cenozoic basin in Myanmar in the west, is an integral part of Myanmar's Magu belt (Mitchell, 1993), and is characterised by dextral strike-slip and thrust faults. The main periods of activity are 24–19 Ma and 14–11 Ma (Ji et al., 2000). The Gaoligong fault zone constitutes an important structural transformation zone for block extrusion and uplift in the southeast margin of the Qinghai–Tibet Plateau. Three large rivers in Asia, namely, the Salween, Mekong, and Yangtze Rivers, flow south along the southeast margin of the plateau, shaping deep canyon landform. In this Three Rivers region, there are many studies about evolution, bed rock profile, and clastic rocks of the river. (Ouimet et al., 2010; Yang et al., 2015; Shen et al., 2021).

SAMPLING AND METHOD

Sampling Strategy

Low-temperature thermochronology is a quantitative study of the thermal history of rocks. Information regarding the cooling process of the upper crust can be obtained by the time–temperature relationships of minerals. The geological applications of low-temperature thermochronology include absolute dating of rocks and tectonic processes, exhumation history of various geological backgrounds, long-term geomorphological evolution process, and basin analysis. AHe, fission track (FT), and ZHe are the most widely used low-temperature thermal chronological methods, and their closure temperatures ranges are 60–80°C, 100–120°C, and 180–200°C, respectively. Assuming that the paleogeothermal gradient is ~30°C/km, they record the exhumation process of rocks passing through ~6 km of the upper crust by low-temperature thermal chronological methods (Farley, 2000; Reiners, 2005; Guenthner et al., 2013). Therefore, we used low-temperature thermal chronological age data of 10 samples collected from the Gaoligong vertical transect (GLG), Guyong rock transect (GY), and Yinghuagu transect (YHG) to discuss the exhumation history of the Gaoligong Mountain by simulating the time-age process (**Figure 2**). The lithology of the shear zone mainly comprises gneiss and granite. Four samples were collected in the vertical transect of the Gaoligong Mountain, and the collection route was from Linjiapuzi in the west of the Gaoligong Mountain to Shangshan Road in the Nanzhai Public House with a horizontal distance of approximately 5 km and an elevation difference of 945 m (from 2,210 to 3,164 m, 20TC08-20TC11). No large-scale brittle fault transect was found in the geological map or in the field.

U-Th/He Analysis

At first, we tested the ages of AHe and ZHe for the above samples. Three to five mineral grains were analysed for each sample. There may be some differences between the ages of each grains, which may be related to the differences in crystal sizes (Reiners and Farley, 2001), the influence of zircon zonation (Ault and Flowers, 2012), radiation damage (Flowers et al., 2009), and experimental conditions. The AFT age was determined by laser ablation inductively coupled plasma mass spectrometry (LA-ICPMS) to directly determine the concentration of single particle ^{238}U in the sample, and then calculate the age of the sample by combining it with the spontaneous track density. Errors in the calculated spontaneous track density caused by the small number of tracks in the tested sample might exist and affect the accuracy of the estimated age. We analysed 10 samples using the Ahe method. Apatite grains were separated using the conventional heavy liquid method. Automorphic crystal grains with complete shape and no visible impurities were selected under a polarizing microscope. Only those crystal grains with a length and width of >60 μM were considered suitable for (U-Th)/He dating. Each mineral grain was wrapped in a 1 mm × 1 mm platinum bag and placed in a laser cavity. ^{4}He was degassed at 800–1000°C, and its abundance was measured using a quadrupole mass spectrometer. After degassing, the mineral particles were dissolved in concentrated HNO_3, and then the U-Th-Sm concentration of each dissolved particle was measured using mass spectrometry. Each particle was corrected by FT (Farley, 2002) to obtain the best age estimate. The error in age is caused by the analytical uncertainty of He, U, Th, and Sm measurements and the variance in the age of a single grain.

In the GLG transect, the ages of AHe were measured in the range of 3.6–4.4 Ma (**Figure 2**, **Figure 3**, **Table 1**). The ages of ZHe were in the range of 4.7–5.9 Ma (**Table 2**). Changes in age values at different elevations of the same transect may be affected by an active fault. The estimated ages of all standard samples used in the experiment are within the error range of international reports. The ages of AHe and ZHe are mostly young, and we found that there is no significant correlation between the single grain age and eU, which means that radiation damage has little effect on age. Both AHe and Zhe age-elevation maps show a steep positive correlation, which indicates that the rock mass cooled rapidly at this stage. Three samples were collected in Guyong (GY) and Yinghua Valley (YHG) transects and analysed by AHe. GY transect samples TCFT03, TCFT07, and TCFT08 were

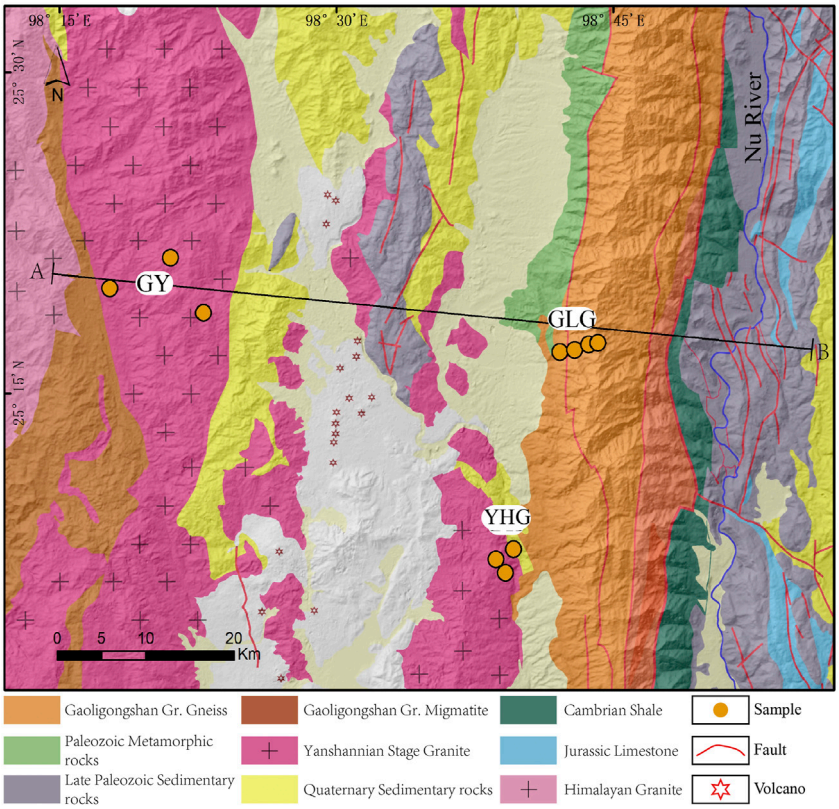

FIGURE 2 | Simplified geological map superimposed on shaded relief of the Tengchong area. Locations of samples collected for this study are shown.

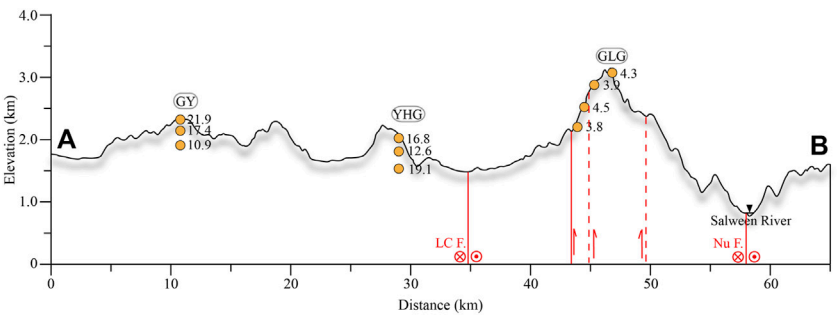

FIGURE 3 | Topographic cross section of Tengchong area **(Figure 1**: **A,B)**. The numbers in the figure represent the ages of AHe. GY, Guyong transect; YHG, Yinghua Valley transect; GLG, Gaoligong transect; Nu F, Nujiang fault; LC F, Longchuangjiang fault.

collected at elevations of 1,760 m, 2,273 m, and 2,147 m and indicate ages of 10.9 ± 0.8 Ma, 21.9 ± 4.3 Ma, and 17.4 ± 1.7 Ma (**Figure 3**) (**Table 3**), respectively. YHG profile samples 19 TC 05, 19 TC 04, and 19 TC 03 were collected at elevations of 1,430 m, 1,744 m, and 2,052 m and indicate ages of 19.1 ± 16.4 Ma, 12.6 ± 1.0 Ma, and 16.8 ± 1.6 Ma (**Figure 3**) (**Table 3**), respectively. We abandoned two estimates that had significant errors (**Tables 1**, **3**). Generally, the age of vertical profile samples increases gradually with the increase in elevation, or the change is small and concentrated in a certain time scale. The relationship between the elevation above sea level and the age estimate based on low-temperature chronology represents the average exhumation rate of this time scale. In this study, by combining AHe and ZHe age data of the GLG transect, the long-term exhumation rate was estimated using the relationship between age and elevation (**Figure 4**). The average ages of AHe and ZHe in this transect are closely related to altitude (**Figure 4**), and therefore the least square method was used to fit

TABLE 1 | Results of the apatite single particle (U-Th)/He analysis in the Gaoligong ductile shear zone (GLGSZ).

Sample ID	U (ppm)	Th (ppm)	He (ppm)	eU (mol)	Length (μM)	Width (μM)	FT	Cor date (Ma)	±σ (Ma)	Mean date (Ma)	±σ (Ma)	Latitude	Longitude	Elevation (m)	Rock type
20TC08-1	10.35	22.21	4.08E–03	1.08E–13	148.4	91.1	0.69			3.63	1.09	25.284	98.703	2,210	gneiss
20TC08-2	4.68	7.84	4.92E–04	1.30E–13	197.5	107.7	0.79	4.40	0.10						
20TC08-3	5.07	23.34	3.73E–04	8.55E–14	162.5	81.8	0.70	2.34	0.07						
20TC08-4	4.07	8.33	3.02E–04	1.02E–13	170.9	106.6	0.74	3.13	0.09						
20TC08-5	23.55	33.81	2.41E–03	4.78E–13	193.4	118.1	0.76	4.67	0.08						
20TC09-1	20.04	18.18	1.35E–03	1.07E–13	113.6	66.5	0.62	4.18	0.10	4.52	0.30	25.286	98.716	2,590	gneiss
20TC09-2	15.51	18.89	1.18E–03	8.17E–14	109.9	65.7	0.61	4.49	0.12						
20TC09-3	18.32	64.82	2.14E–03	1.03E–13	130.4	55.5	0.60	4.92	0.10						
20TC09-4	64.14	39.65	4.91E–03	3.62E–13	120.3	68.8	0.69	4.49	0.07						
20TC09-5	0.04	0.23	3.51E–01	2.42E–16	127.3	54.6	0.53	50,181.83	2,393.56						
20TC10-1	49.31	32.51	3.76E–03	1.11E–12	205.9	104.2	0.75	4.06	0.06	4.03	0.30	25.29	98.728	2,805	Granite
20TC10-2	38.46	18.90	2.60E–03	4.07E–13	169.6	98.4	0.72	3.89	0.06						
20TC10-3	30.25	15.48	1.90E–03	3.09E–13	164.5	79.8	0.69	3.78	0.07						
20TC10-4	43.61	31.42	2.96E–03	8.99E–13	205.0	80.1	0.69	3.89	0.05						
20TC10-5	39.11	44.48	3.37E–03	8.31E–13	175.0	77.5	0.69	4.54	0.06						
20TC11-1	35.74	44.36	2.84E–03	3.42E–13	163.6	72.3	0.66	4.34	0.07	4.42	0.43	25.291	98.737	3164	Granite
20TC11-4	31.15	29.33	2.29E–03	2.18E–13	138.9	68.8	0.69	4.04	0.07						
20TC11-5	30.36	22.83	2.44E–03	1.96E–13	111.8	75.3	0.65	4.88	0.08						

eU: effective uranium concentration, a parameter that weights the decay of the two parents for their alpha productivity, by (U) + 0.235 × (Th) (Flowers et al., 2009). FT is the alpha-ejection correction after Farley et al. (1996). Errors on the (U-Th)/He dates (1σ) are based on analytical uncertainty in U,Th, and He measurements. Standard deviation for the replicate analyses. Dates that were excluded from the mean calculation.

TABLE 2 | Results of the zircon single particle (U-Th)/He analysis in the Gaoligong ductile shear zone (GLGSZ).

Sample ID	U (ppm)	Th (ppm)	He (ppm)	eU (mol)	Length (μM)	Width (μM)	FT	Cor date (Ma)	±σ (Ma)	Mean date (Ma)	±σ (Ma)	Latitude	Longitude	Elevation (m)	Rock type
20TC08-1	426.30	57.92	4.44E–02	1.81E–11	254.5	107.8	0.83	5.66	0.12	5.99	0.63	25.284	98.703	2,210	gneiss
20TC08-2	779.67	118.62	9.21E–02	2.51E–11	226.6	98.9	0.81	6.52	0.15						
20TC08-3	118.36	40.80	1.24E–02	7.00E–12	304.5	109.6	0.84	5.40	0.11						
20TC08-4	419.75	60.68	4.15E–02	1.01E–11	202.8	89.2	0.80	5.58	0.13						
20TC08-5	149.59	84.77	2.00E–02	5.32E–12	251.0	88.0	0.80	6.81	0.14						
20TC09-1	479.74	83.00	5.54E–02	5.27E–12	159.6	79.5	0.73	7.02	0.15	5.67	1.05	25.286	98.716	2590	gneiss
20TC09-2	298.60	127.71	2.28E–02	5.47E–12	169.0	87.5	0.78	4.14	0.09						
20TC09-3	152.46	52.50	1.57E–02	3.38E–12	191.7	98.5	0.79	5.64	0.13						
20TC09-4	157.85	153.13	1.99E–02	4.03EV12	203.1	87.8	0.78	6.10	0.12						
20TC09-5	163.33	104.28	1.76E–02	4.39E–12	186.2	108.0	0.80	5.45	0.11						
20TC10-1	353.75	282.55	3.14E–02	9.82E–12	216.9	87.6	0.79	4.40	0.09	4.7	0.31	25.29	98.728	2805	Granite
20TC10-2	475.16	418.41	4.39E–02	6.58E–12	157.9	82.8	0.74	4.81	0.09						
20TC10-3	207.34	149.77	2.15E–02	8.37E–12	253.5	103.2	0.81	5.08	0.10						
20TC10-5	512.54	420.11	4.04E–02	3.43E–12	117.2	72.1	0.68	4.50	0.09						
20TC11-1	447.23	403.74	5.54E–02	1.01E–11	196.3	86.8	0.77	6.13	0.13	5.98	0.36	25.291	98.737	3164	Granite
20TC11-2	507.04	338.81	5.75E–02	8.48E–12	184.9	79.4	0.75	6.04	0.12						
20TC11-3	404.44	250.18	4.30E–02	1.23E–11	237.5	93.7	0.79	5.44	0.11						
20TC11-4	427.71	371.01	5.05E–02	1.02E–11	202.9	78.5	0.78	5.86	0.12						
20TC11-5	693.55	435.46	8.57E–02	1.49E–11	189.9	83.2	0.78	6.43	0.13						

eU: effective uranium concentration, a parameter that weights the decay of the two parents for their alpha productivity, by (U) + 0.235 × (Th) (Flowers et al., 2009). bFT is the alpha-ejection correction after Farley et al. (1996). cErrors on the (U-Th)/He dates (1σ) are based on analytical uncertainty in U, Th, and He measurements. Standard deviation for the replicate analyse.

TABLE 3 | Results of the apatite single particle (U-Th)/He analysis in the GY and YHG transects.

Sample ID	U (ng)	Th (ng)	He (cc)	Width (μM)	Length (μM)	Raw date (Ma)	FT	Cor date (Ma)	±σ (Ma)	Mean date (Ma)	±σ (Ma)	Latitude	Longitude	Elevation (m)	Rock type
TCFT03-1	0.11	0.59	2.50E−10	90	260	8.2	0.73	11.20	0.20	10.93	0.83	25.332	98.297	1760	Granite
TCFT03-2	0.14	0.88	3.64E−10	100	240	8.7	0.75	11.60	0.20						
TCFT03-3	0.07	0.53	1.54E−10	90	180	6.6	0.66	10.00	0.20						
TCFT07-1	0.06	0.06	2.70E−10	110	190	32.0	0.75	42.70	1.40	21.95	4.31	25.365	98.351	2,273	Granite
TCFT07-2	0.01	0.12	6.70E−11	90	130	13.3	0.70	18.90	0.50						
TCFT07-3	0.02	0.18	1.30E−10	80	130	16.6	0.67	25.00	0.60						
TCFT08-1	0.01	0.17	8.60E−11	90	180	13.3	0.72	18.60	0.40	17.40	1.70	25.314	98.381	2,147	Granite
TCFT08-2	0.01	0.00	-8.70E−12	60	150	11.5	0.60	19.20	-8.2						
TCFT08-3	0.08	0.60	3.70E−10	200	230	13.8	0.85	16.20	0.30						
19TC03-1	0.14	2.06	8.46E−10	70	150	11.1	0.68	16.50	0.40	16.80	1.67	25.123	98.645	2052	Granite
19TC03-2	0.06	3.19	1.12E−09	70	130	11.5	0.68	16.80	2.80						
19TC03-3	0.02	1.68	6.30E−10	80	150	12.5	0.65	19.30	1.00						
19TC03-4	0.18	2.10	7.78E−10	70	150	9.5	0.65	14.60	0.30						
19TC03-5	0.17	1.25	5.67E−10	70	150	10.1	0.60	16.80	0.30						
19TC04-1	0.09	0.79	2.21E−10	50	140	6.6	0.54	12.20	0.20	12.63	1.02	25.112	98.654	1744	Granite
19TC04-2	0.23	1.66	5.49E−10	65	120	7.3	0.62	11.90	0.20						
19TC04-3	0.06	0.56	1.73E−10	50	120	7.3	0.53	13.80	0.20						
19TC05-1	0.03	0.23	1.55E−10	60	110	14.8	0.59	25.20	0.50	19.10	16.42	25.13	98.66	1430	Gneiss
19TC05-2	0.02	0.16	1.28E−10	60	100	18.3	0.58	31.60	0.70						
19TC05-3	0.03	0.23	2.83E−12	60	120	0.3	0.59	0.50	0.00						

FT is the alpha-ejection correction after Farley et al. (1996). Errors on the (U-Th)/He dates (1σ) are based on analytical uncertainty in U,Th, and He measurements. Standard deviation for the replicate analyses. Dates that were excluded from the mean calculation.

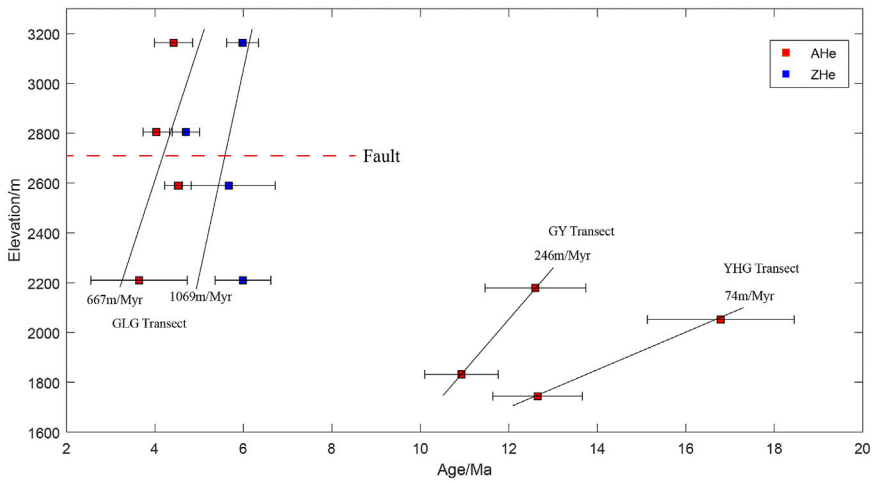

FIGURE 4 | Age–elevation relationship diagram of low-temperature thermochronological data of Ahe and Zhe.

the relationship between age and altitude (Glotzbach et al., 2011). Results show that the exhumation rate of the YHG transect that is located in the footwall of the Gaoligong shear zone is the lowest, with approximately 74 m/Ma at 18–12 Ma. At 6–2 Ma, the exhumation rate at GLG transect is 667–1,069 m/Ma, which is 9–14 times that of the former. This finding reveals the significant difference between the Ailaoshan mountain and the Gaoligong Mountain. The GY transect is located in the west of the Tengchong Basin, which may be affected by the Nabang fault, resulting in a high exhumation rate.

Fission Track Analysis

Apatite fission track (AFT) analyses of samples of GLG transect were conducted at the Neotectonic Geochronology Laboratory at the Institute of Geology, China Earthquake Administration. Apatite fission track ages were obtained using the LA-ICPMS

TABLE 4 | Results of the fission track analysis of apatite in the Gaoligong ductile shear zone(GLGSZ).

Sample ID (TC)	Latitude	Longitude	Elevation (m)	ρs	Ns ($\times10^5 cm^{-2}$)	Nc	P(X^2) (%)	Age (Ma)	±σ (Ma)	Dpar (μm±SD)
2008	25.284	98.703	2210	0.269	85	35	100	7.46	0.81	1.54 ± 0.25
2009	25.286	98.716	2590	0.852	87	29	58	8.19	0.94	1.82 ± 0.3
2010	25.29	98.728	2805	0.897	229	30	59	3.26	0.22	1.7 ± 0.25
2011	25.291	98.737	3164	1.186	208	30	74	4.25	0.3	1.6 ± 0.15

Rho-S, spontaneous track density; Ni, total number of induced tracks; Rho-I, induced track density; Nd, number of tracks counted on dosimeter; Rho-D, effective fission-track densities for the fluence monitor; P (χ^2) (%), probability of obtaining Chi-square value (χ^2); Age, ±1σ; ζ value is 370.1 ± 11.2; all samples pass the Chi-squared test, and therefore, reported ages are all pooled ages; Dpar, average etch pit diameter of fission tracks.

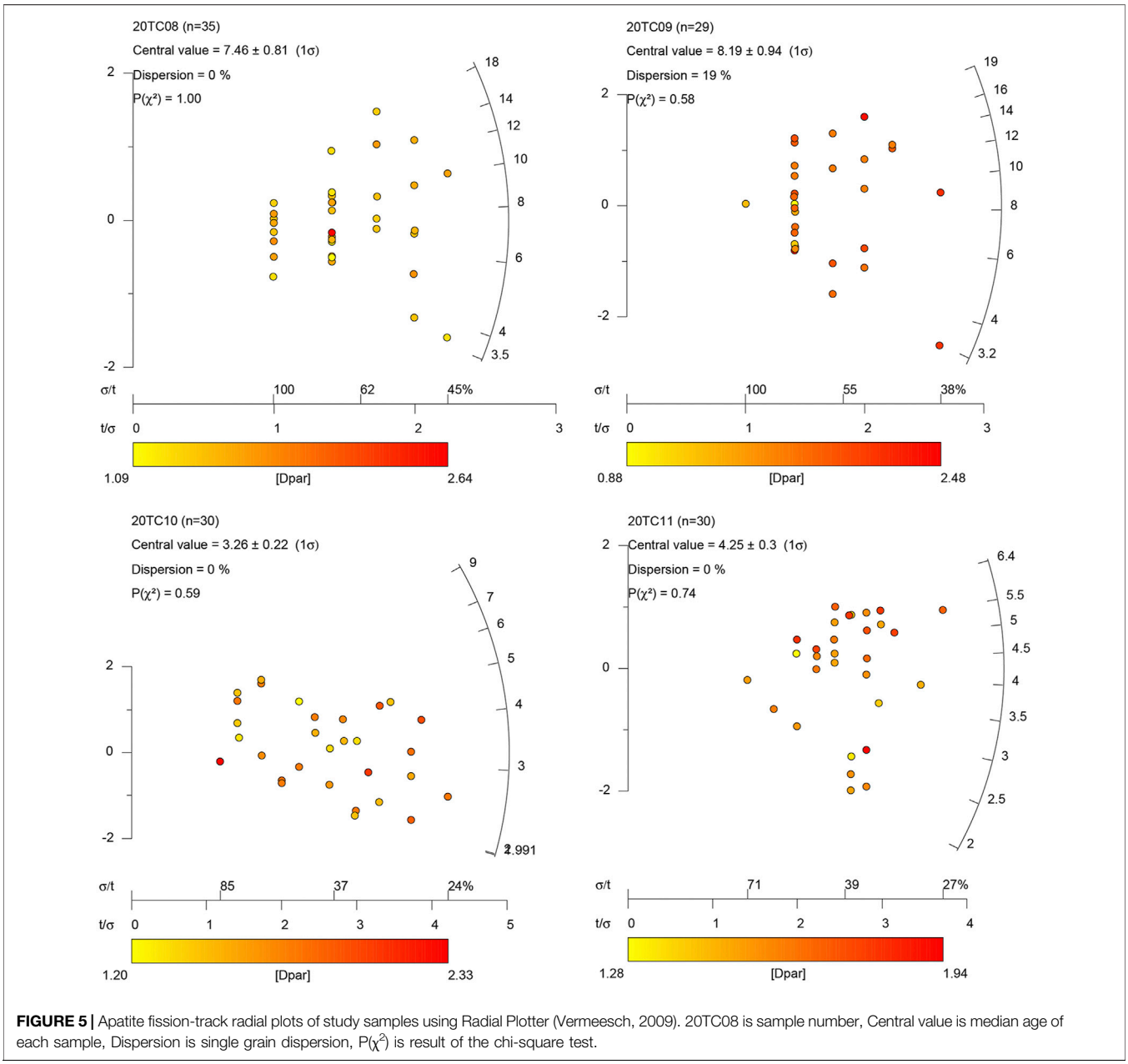

FIGURE 5 | Apatite fission-track radial plots of study samples using Radial Plotter (Vermeesch, 2009). 20TC08 is sample number, Central value is median age of each sample, Dispersion is single grain dispersion, P(χ^2) is result of the chi-square test.

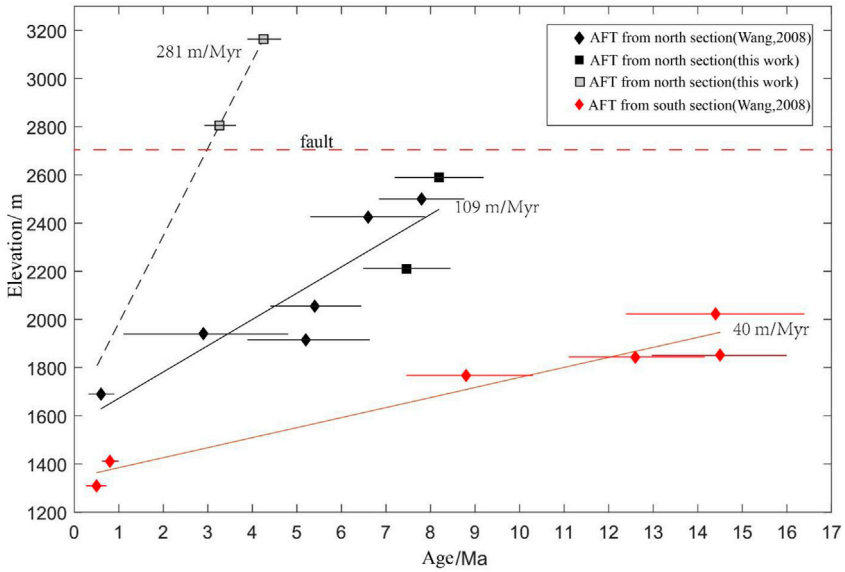

FIGURE 6 | Age–elevation relationship diagram of AFT data in different transects of the Gaoligong shear zone.

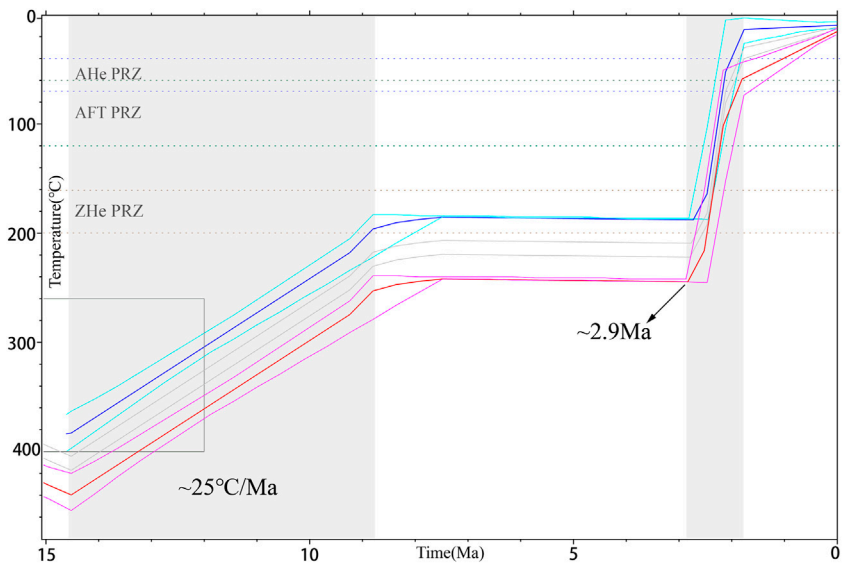

FIGURE 7 | Thermal modelling of the GLG transect using QTQt (Gallagher, 2012). The grey box indicates the initial constraint. For the uppermost thermal history, the thin blue lines depict 95% confidence intervals, reflecting the uncertainty in the inferred thermal history alone. For the lowermost thermal history, the thin red lines show 95% confidence intervals, reflecting combined uncertainties in the inferred thermal history and temperature offset. The provided AHe ages are uncorrected for the comparison of observed and predicted data.

method (Hasebe et al., 2004; Lisker et al., 2009; Hasebe et al., 2013) and calculated by the zeta calibration method (Pang et al., 2017). Age-calibration standard is Durango apatite (31.4 ± 0.5 Ma). The National Bureau of Standards trace element glass NIST612 were used as an external standard to measure the signal intensity the test. Uranium measurement was carried out under the LA-ICPMS equipment. Spontaneous fission tracks in apatite were etched in 5.5N HNO3 at 21°C for 20 s. Fission tracks and track-length measurements were counted on a Zeiss Axioplan2 microscope, using a dry objective with magnification of 1000. All analyses were performed by J. Z Pang whose lab had a weighted mean zeta of Apatite-Zeta NIST612=1940 ± 50 while using the above methods and standards. Apatite fission track data are listed in supplement **Table 4**.

In the GLG transect, The AFT ages were from 3.2 to 8.1 Ma (**Figure 5** and **Table 4**). All ages have passed the P(χ^2) test, and the

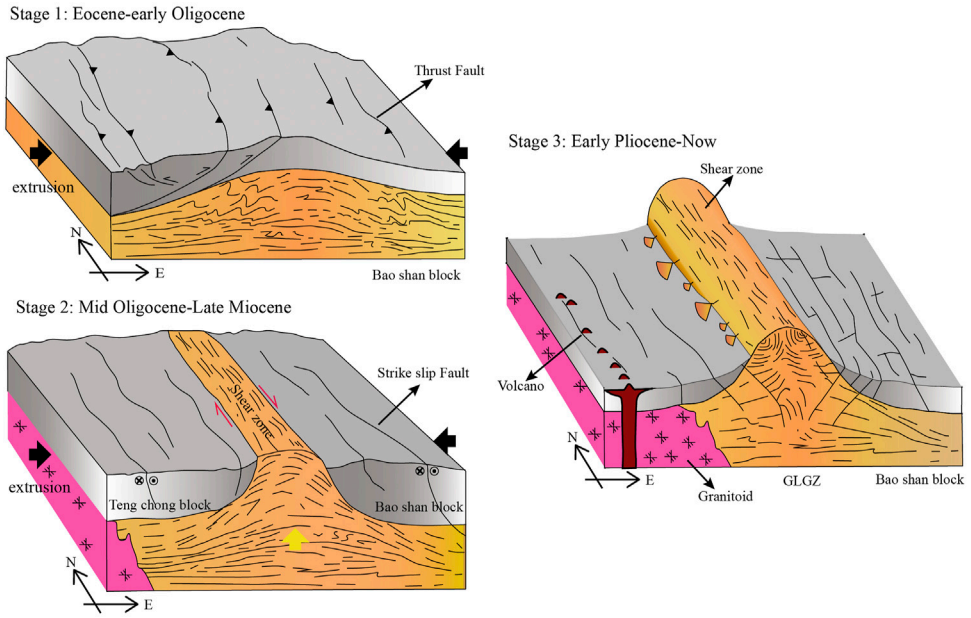

FIGURE 8 | A simplified conceptual model illustrating the tectonic evolution and uplift and exhumation process of the Gaoligong shear zone (GLGSZ). During the Eocene–Early Oligocene, the crust might have been shortened and thickened in the southeastern margin of the Qinghai–Tibet Plateau, resulting in the weakening of the rheology of the middle and lower crust. Right-lateral ductile shear occurred from the Middle Oligocene to Late Miocene. During this time, the GLGSZ acted as a channel for vertical extrusion of low-viscosity crustal materials in the deep. Since the early Pleistocene, the Gaoligong Mountain has been further uplifted and exposed, the middle and upper crust has been dominated by brittle deformation, the plates have been staggered by active faults, and magmatic activity has been enhanced.

discrete value is low, indicating a single age group. Owing to the small number of tracks in all samples, only one sample, 20TC10, had a track length, and its average track length was 12.18–16.02 μm. The Dpar values of all samples were between 1.3 and 2.1 μm. Together with the AFT data of Wang et al. (2018) (**Figure 4A**), we found that the exhumation rate of the south section of GLGSZ is ~40 m/Ma and the exhumation rate of the north section is ~109 m/Ma. We collected some samples at the top of the north section (altitude >2,800 m), and the exhumation rate is approximately 281 m/Ma. Therefore, since the Miocene, the exhumation rate in the north section of GLGSZ has become significantly faster than that in the south section, and the exhumation rate at the top of the north section is faster than that at the bottom (**Figure 6**). The two samples at the top of the vertical transect are abnormally young, and it may be related to the activity of the fault at elevations of about 2,700 m (**Figure 6**).

Modeling

In order to study the history of thermal evolution of the GLG, we used the QTQt program, which uses the Markov chain Monte Carlo method. To simulate the thermal history (Gallagher et al., 2005; Gallagher, 2012) of the GLG, we inverted the thermochronological ages of different elevations. In this study, AHe, ZHe, and AFT data of the GLG profile were also modelled using the QTQt program. According to the published $^{40}Ar/^{39}Ar$ ages of granite and mylonite-biotite, we set the initial temperature of the GLG transect at 330 ± 70°C and the corresponding age at 17 ± 5 Ma (Akciz, 2004; Lin et al., 2009; Zhang et al., 2010; Zhang et al., 2012). The simulation was carried out for 400,000 iterations, of which 200,000 each were used for burn-in inversion and joint simulation of three types of data. Using a higher number of iterations did not significantly improve the simulation results.

The inversion simulation of the GLG profile revealed two stages of rapid cooling (**Figure 7**). The first stage occurred between 14.5 and 8.8 Ma, and some samples even reached the partial retention zone (PRZ) of zircon, and then experienced a slow cooling process lasting approximately 6 Ma. Subsequently, the cooling rate began to increase at ~2.9 Ma, and all the samples were denuded to the near surface. The rate of the second cooling was much higher than that of the first. According to the thermal history model, the two cooling temperatures are similar. The estimation of the exhumation quantity depends on the low-temperature gradient, but this parameter is often unknown. Here, we assume that the range of the low-temperature gradient is 30–40°C/km, which is similar to related research conducted in nearby areas (Clark et al., 2005; Wang et al., 2018), and conclude that the shear zone may have experienced 5–6 km of exhumation at this stage. In summary, the inversion results of the GLG profile show that the GLGSZ experienced two rapid exhumation stages in the Miocene and Pliocene.

DISCUSSION

History of Exhumation of the Gaoligong Shear Zone

The GLGSZ divides the Baoshan and Tengchong Blocks and is mainly composed of high-grade metamorphic rocks and intrusive

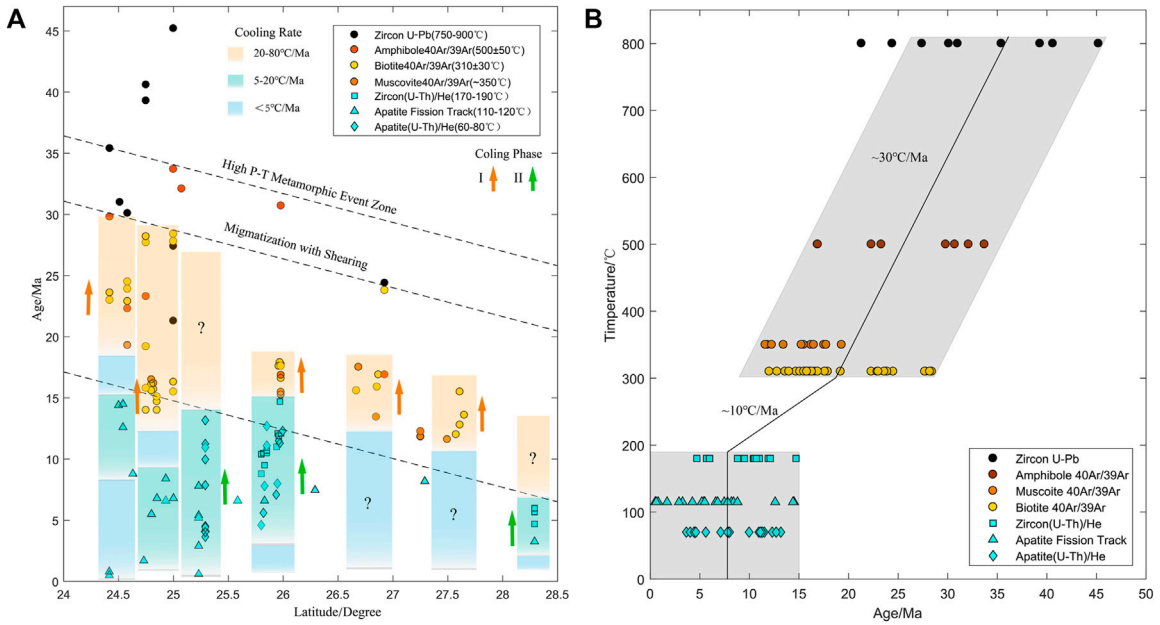

FIGURE 9 | Summary of thermochronological data for the Gaoligong shear zone (GLGSZ). Ages are compiled from Wang et al. (2008, 2018), Akciz et al. (2008), Gilley et al. (2003), Lin et al. (2009), Zhang et al. (2012, 2017), Xu et al. (2015), Ji et al. (2000), Ding (1991), Tang et al. (2016, 2020), and this study. A synthesis of these data suggests differential thermal histories along the latitude. **(A)** The GLGSZ experienced prominent and rapid cooling from a high temperature of >500–190°C at a rate of 20–80°C/Ma during 30–15 Ma at 25° north latitude. A lower-magnitude accelerated cooling event took place during 15–0 Ma at 24.5°–26° north latitude. **(B)** Age-temperature relationship of different thermochronological data of the GLGSZ.

granite. The foliation and mineral lineation parallel to the mountain's strike show significant stretching and the movement direction of the dextral shear (Socquet and Pubellier, 2005; Qi et al., 2012). The U/Pb age of high-temperature metamorphic zircon in the Gaoligong right strike-slip shear zone is 52–46 Ma (Xu et al., 2015), which indicates that the initial time of the India–Asia oblique collision outside the East Indian tectonic segment may be around 50 Ma. ^{40}Ar-^{39}Ar dating shows that the right strike slip of the Gaoligong shear zone started at 32 Ma, and its main activities were in three stages during 27–29 Ma, 18–17 Ma, and 14 Ma (Wang et al., 2008). The mylonite of the Gaoligong Group thrusted on to the Eocene strata (Qi et al., 2012), which also indicated that the GLGSZ was uplifted after the Eocene. The data of zircon U-Pb and mica K-Ar show that the GLGSZ has rapidly cooled 18 Ma ago (Lin et al., 2009). Ji et al. (2000) measured the main active ages of the Gaoligong strike-slip fault zone, and their active ages were estimated at 24–19 Ma and 14–11 Ma, respectively. In the Middle Miocene (~18 Ma), the GLGSZ was connected with the Jiali fault zone and began to cooperate with a dextral strike-slip movement (Lin et al., 2009). The dextral shear process of the GLGSZ caused partial melting of the crust, resulting in the intrusion of many light-coloured granites with U-Pb ages of ~24–21 Ma (Song et al., 2010). The ^{40}Ar/^{39}Ar dating of muscovite and biotite recorded rapid exhumation of the GLGSZ at 18–11 Ma (Akciz, 2004; Wang et al., 2006; Lin et al., 2009; Zhang et al., 2012). Mylonitization of rocks occurred at 20–12 Ma (Zhong et al., 1991; Wang et al., 1998), which is the same period as when rapid exhumation and dextral ductile shear of the GLGSZ occurred. Therefore, in the early Eocene, the outer side of the East Indian tectonic node began to collide with the Lhasa plate, and dynamic metamorphism formed high-grade metamorphic rocks with significant directional minerals and intrusion of magma. The GLGSZ actively responded to the continuous compression of the northeast corner of the Indian plate and moved synchronously with the Eastern Himalayan syntaxis (EHS). The early–middle Miocene EHS activity dominated the evolution of large strike-slip fault zones in this area. The GLGSZ experienced dextral shear, rapid exhumation, mylonitization, and magmatic intrusion of the mountain at the same time. In the early Miocene, the time of activity of the GLGSZ coincided with that of the Honghe River–Ailao Mountain ductile shear zone in the east, and it was connected with the Jiali fault and began to cooperate with the dextral strike-slip movement. In the middle Miocene, the expansion of the Andaman Sea and the dextral strike-slip movement of the Shijie fault were consistent. From the Jiali fault to Gaoligong ductile shear zone and then to the Sagaing fault, a huge western boundary of the Indosinian block was formed. After experiencing the complex tectonic movement in the Miocene, the basic geomorphic pattern of the southeastern margin of the Qinghai–Tibet Plateau was laid.

Possible Contribution of the Quaternary Glaciation to the Rapid Exhumation of the GLGSZ

Low-temperature thermal chronological data of AHe, ZHe, and AFT showed that the GLGSZ stopped rapid cooling at ~10 Ma, which is also in good agreement with our modeling results.

However, ZHe data of the Chongshan Mountain ductile shear zone shows that its rapid cooling also stopped at ~10 Ma (Wang et al., 2018), which indicates that the large-scale ductile shear zone in the southeastern margin of the Qinghai–Tibet Plateau almost moved in concert in the Miocene. The rapid uplift of the surface in western Sichuan occurred during 8–1 Ma (Kirby et al., 2002; Clark et al., 2005), but it may be later than 5 Ma in the Three Rivers Region (Schoenbohm et al., 2006). The simulation of thermal history using comprehensive data shows that the latest rapid cooling event of the GLGSZ began at 2.9 Ma, which was difficult to discern in past research because of the influence of the precision of testing instruments and equipment and the quality of samples. This cooling event lasted for ~1 Ma, and the cooling rate was faster than that in the Miocene. Assuming that the low temperature gradient was 30–40°C/Km, the stratum exhumation thickness of this event reached 5–6 km at 2.9 Ma. This period is very close to the period of the global Quaternary glaciation. Glacial landforms such as U-shaped valleys are widely distributed in the study area, which is one of the most extensive glacier areas in the southeastern margin of the Qinghai–Tibet Plateau (Fu et al., 2013). The study area is located in the upper reaches of the Three River Basin, and this rapid cooling event is related to the rapid downcutting by the river (Yang et al., 2015). This period was also a period of intense activity of volcanoes and active faults, which may also have accelerated the cooling process of the GLGSZ. Yang et al. (2015) tested seven blocks of AHe samples near EHS and believed that the erosion in this area significantly accelerated at ~2 Ma. Therefore, as the global climate in the early Pleistocene entered the ice age, the ice erosion in the study area intensified, and the glacier landform developed widely. Affected by the uplift of mountains and climate, water vapor from the Pacific Ocean and the Indian Ocean was blocked to form rainfall, which accelerated the erosion of landforms and the undercutting of rivers. In addition, brittle faults and volcanic activities were also significantly intensified. The Baoshan Block located in the east of the GLGSZ is fragmented by fault depression. The Tengchong Block located in the west of the GLGSZ is mainly composed of granite and basalt. Hundreds of volcanic cones are scattered inside the basin, and volcanic activities are mainly concentrated in the Pleistocene (Li et al., 2019). At an altitude of 2,200 m, the average exhumation rate of the GLGSZ is 3–4 times that of the Tengchong Block. Then, under the combined action of climate, river erosion, fault activity, and overall uplift of the crust, the study area underwent rapid cooling in the early Pleistocene (**Figure 8**).

Dynamic Model of Growth and Propagation of the Plateau

In terms of the genesis of the unique geomorphological features in the southeastern margin of the Qinghai–Tibet Plateau and its geodynamic model, our results comparatively support the lower crustal flow model. The key geological and geomorphological supporting evidence in this model is that there is a "plane-like structure" in the southeast edge of the plateau that stretches for thousands of kilometres in the region before uplift, from the boundary line of the internal/external water system in the plateau to the low altitude of the South China Sea. This remains in the deep valley highland (Clark et al., 2006). Recent geophysical research results explain that there are two uniform low-velocity zones in the middle and lower crust at the EHS (Yao et al., 2010; Sun et al., 2014; Bao et al., 2015). The low-speed zone on the west side is located below the GLGSZ and CSSZ (Bao et al., 2015). Although these results cannot accurately define the uplift process of the plateau during the Quaternary period, inferences can be drawn based on other factors. The uplift process is caused by different exhumation rates in the north and south of the GLGSZ, gravity creep flow rising from the middle of the plateau to its edge, occurrence of tilting uplift in the southeast direction, and upward pushing force generated by the continuous thickening of the middle and lower crust providing the main source of material and power in the southeast edge, and spontaneous river attack and accelerated exhumation since Pliocene leading to unloading and acceleration of erosion to break the balance of the crust. In addition, Wang et al. (2018) suggested that the GLGSZ is high in the north and low in the south, which is the result of gravity collapse, but the present study does not support this conclusion. According to data presented in **Figure 9**, the exhumation rate in the north of the GLGSZ is higher than that in the south, and hence, the closer to the north, the higher the corresponding altitude. Yang et al. (2015) estimated the erosion rate in this area through the longitudinal profile of the river. Similarly, the erosion rate in the north is higher than that in the south, and no re-heating process was evident based on our thermal chronological data. If the rapid exhumation of the GLGSZ in the Pliocene is related to the influx of lower crust materials, then our low-temperature thermochronology data recorded the events of this process accurately. This can also explain the special topography of the GLGSZ, which is high in the north and low in the south, and the spatiotemporal variations show that the uplift gradually reduces from north to south.

CONCLUSION

In this study, the history of thermal evolution of the ductile strike-slip shear zone in the Gaoligong Mountain in the southeast margin of the Qinghai–Tibet Plateau was analysed using AHe, ZHe, and AFT to reveal the rapid cooling process in two stages of the early Miocene–middle Miocene (~14.5 Ma) and early Pleistocene (~2.9 Ma). In the Eocene, the northeast corner of the Indian plate collided obliquely with the Eurasian plate in the eastern structure, and the lithosphere of the eastern syntaxis in the region thickened and started the dextral strike-slip movement synchronously. During the early Miocene–middle Miocene period, influenced by the plateau uplift and structural adjustment of the EHS, the GLGSZ continued the dextral shear movement, and was rapidly exposed. In the early Pleistocene, under the combined action of rapid incised erosion of rivers and continuous activity of brittle faults, the GLGSZ was rapidly denuded again, and at this time, the exhumation rate significantly increased, and the rocks were denuded to the surface. The

exhumation and erosion rates of the GLGSZ were different at different latitudes, and this tilting type of the uplift has formed a special landform that is high in the north and low in the south.

DATA AVAILABILITY STATEMENT

The original contributions presented in the study are included in the article/Supplementary Material, further inquiries can be directed to the corresponding author.

AUTHOR CONTRIBUTIONS

JW gathered and prepared all data, performed all calculations, and created all figures. He developed the model and modelling procedure with the guidance of HZ. FS and NL contributed to the discussion of results and participated in the writing of the paper. YW, LN, and JP prepared the samples and conducted the experiments. JW and YZ conducted the field work.

FUNDING

This work was supported by the Institute of Geology, China Earthquake Administration (IGCEA 2003) and Jilin Changbaishan Volcano National Observation and Research Station, IGCEA (NORSCBS21-06).

ACKNOWLEDGMENTS

I would like to thank China Scholarship Council for sponsoring me during my studies at the University of Glasgow.

REFERENCES

Akciz, O. S. (2004). *Structure and Geochronological Constraints on the Ductile Deformation Observed along the Gaoligong Shan and Chong Shan Shear Zones*. Yunnan (China)[Boston(MA)]: Massachusetts Institute of Technology. [dissertation thesis].

Akciz, S., BurchfielCrowley, B. C. J. L., Crowley, J. L., Jiyun, Y., and Liangzhong, C. (2008). Geometry, Kinematics, and Regional Significance of the Chong Shan Shear Zone, Eastern Himalayan Syntaxis, Yunnan, China. *Geosphere* 4, 292–314. doi:10.1130/GES00111.1

Allen, C. R., Gillespie, A. R., Yuan, H., Sieh, K. E., Buchun, Z., and Chengnan, Z. (1984). Red River and Associated Faults, Yunnan Province, China: Quaternary Geology, Slip Rates, and Seismic hazard. *Geol. Soc. America Bull.* 95, 6862–7700. doi:10.1130/0016-7606(1984)952.0.CO10.1130/0016-7606(1984)95<686:rraafy>2.0.co;2

Ault, A. K., and Flowers, R. M. (2012). Is Apatite U-Th Zonation Information Necessary for Accurate Interpretation of Apatite (U-Th)/He Thermochronometry Data? *Geochimica et Cosmochimica Acta* 79, 60–78. doi:10.1016/j.gca.2011.11.037

Bao, X., Sun, X., Xu, M., Eaton, D. W., Song, X., Wang, L., et al. (2015). Two Crustal Low-Velocity Channels beneath SE Tibet Revealed by Joint Inversion of Rayleigh Wave Dispersion and Receiver Functions. *Earth Planet. Sci. Lett.* 415, 16–24. doi:10.1016/j.epsl.2015.01.020

Chang, Z., Chen, G., and Yu, J. (2011). Geological Evidence of Activity along the Dayingjaing Fault since Late Pleistocene. *Seismology Geology*. 33, 877–888. (in Chinese with English abstract).doi:10.3969/j.issn.0253-4967.2011.04.012

Clark, M. K., House, M. A., Royden, L. H., Whipple, K. X., Burchfiel, B. C., Zhang, X., et al. (2005). Late Cenozoic Uplift of southeastern Tibet. *Geol* 33, 525–528. doi:10.1111/1755-6724.12148_210.1130/g21265.1

Clark, M. K., Royden, L. H., Whipple, K. X., Burchfiel, B. C., Zhang, X., and Tang, W. (2006). Use of a Regional, Relict Landscape to Measure Vertical Deformation of the Eastern Tibetan Plateau. *J. Geophys. Res.* 111, a–n. doi:10.1029/2005jf000294

Dewey, J. F., Cande, S. C., and Pitman, W. C. I. (1989). Tectonic Evolution of the India/Eurasia Collision Zone. *Eclogae Geologicae Helv.* 82, 717–734. doi:10.111/j.1365-3091.1989.tb00830.x

Ding, L. (1991). *The Characteristics of Deformation and Tectonic Implications in South Gaoligong, Western Yunnan, China*. [master thesis]. Beijing]:: Institure of Geology, Chinese Academy of Science. doi:10.1111/j.1365-3091.1989.tb00830.x

Dong, Y., Cao, S., Neubauer, F., Wang, H., Li, W., and Genser, J. (2021). Exhumation of the Crustal-Scale Gaoligong Strike-Slip Shear belt in SE Asia. *J. Geol. Soc.* doi:10.6084/m9.figshare.c.5598365.v110.1144/jgs2021-038

England, P., and Molnar, P. (1990). Surface Uplift, Uplift of Rocks, and Exhumation of Rocks. *Geol* 18, 1173–1177. doi:10.1130/0091-7613(1990)018<1173:suuora>2.3.co;2

Farley, K. A. (2000). Helium Diffusion from Apatite: General Behavior as Illustrated by Durango Fluorapatite. *J. Geophys. Res.* 105, 2903–2914. doi:10.1029/1999jb900348

Farley, K. A. (2002). (U-Th)/He Dating: Techniques, Calibrations, and Applications. *Rev. Mineralogy Geochem.* 47, 819–844. doi:10.2138/rmg.2002.47.18

Flowers, R. M., Ketcham, R. A., Shuster, D. L., and Farley, K. A. (2009). Apatite (U-Th)/He Thermochronometry Using a Radiation Damage Accumulation and Annealing Model. *Geochimica et Cosmochimica Acta* 73, 2347–2365. doi:10.1016/j.gca.2009.01.015

Fu, P., Harbor, J. M., Stroeven, A. P., Hättestrand, C., Heyman, J., and Zhou, L. (2013). Glacial Geomorphology and Paleoglaciation Patterns in Shaluli Shan, the southeastern Tibetan Plateau - Evidence for Polythermal Ice Cap Glaciation. *Geomorphology* 182, 66–78. doi:10.1016/j.geomorph.2012.10.030

Gallagher, K., Stephenson, J., Brown, R., Holmes, C., and Fitzgerald, P. (2005). Low Temperature Thermochronology and Modeling Strategies for Multiple Samples 1: Vertical Profiles. *Earth Planet. Sci. Lett.* 237, 193–208. doi:10.1016/j.epsl.2005.06.025

Gallagher, K. (2012). Transdimensional Inverse thermal History Modeling for Quantitative Thermochronology. *J. Geophys. Res.* 117, a–n. doi:10.1029/2011JB008825

Gilley, L. D., Harrison, T. M., Leloup, P. H., Ryerson, F. J., Lovera, O. M., and Wang, J.-H. (2003). Direct Dating of Left-Lateral Deformation along the Red River Shear Zone, China and Vietnam. *J. Geophys. Res.* 108, 14–21. doi:10.1029/2001JB001726

Glotzbach, C., van der Beek, P. A., and Spiegel, C. (2011). Episodic Exhumation and Relief Growth in the Mont Blanc Massif, Western Alps from Numerical Modelling of Thermochronology Data. *Earth Planet. Sci. Lett.* 304, 417–430. doi:10.1016/j.epsl.2011.02.020

Guenthner, W. R., Reiners, P. W., Ketcham, R. A., Nasdala, L., and Giester, G. (2013). Helium Diffusion in Natural Zircon: Radiation Damage, Anisotropy, and the Interpretation of Zircon (U-Th)/He Thermochronology. *Am. J. Sci.* 313, 145–198. doi:10.2475/03.2013.01

Hasebe, N., Barbarand, J., Jarvis, K., Carter, A., and Hurford, A. J. (2004). Apatite Fission-Track Chronometry Using Laser Ablation ICP-MS. *Chem. Geology.* 207, 135–145. doi:10.1016/j.chemgeo.2004.01.007

Hasebe, N., Tamura, A., and Arai, S. (2013). Zeta Equivalent Fission-Track Dating Using LA-ICP-MS and Examples with Simultaneous U-Pb Dating. *Isl. Arc* 22, 280–291. doi:10.1111/iar.12040

Houseman, G., and England, P. (1993). Crustal Thickening versus Lateral Expulsion in the Indian-Asian continental Collision. *J. Geophys. Res.* 98 (12), 12233–12249. doi:10.1029/93JB00443

Ji, J. Q., Zhong, D. L., Sang, H. Q., Qiu, J., and Hu, S. L. (2000). Dating of Two Metamorphic Events on the basalt Granulite from the Nabang Area on the Border of China and Burma. *Acta Petrologica Sinica* 16, 227–232. doi:10.2118/64226-PA

Kirby, E., Reiners, P. W., Krol, M. A., Whipple, K. X., Hodges, K. V., Farley, K. A., et al. (2002). Late Cenozoic Evolution of the Eastern Margin of the Tibetan Plateau: Inferences from40Ar/39Ar and (U-Th)/He Thermochronology. *Tectonics* 21, 1. doi:10.1029/2000TC001246

Kristen Clark, M., and Handy Royden, L. (2000). Topographic Ooze: Building the Eastern Margin of Tibet by Lower Crustal Flow. *Geology* 28, 703–706. doi:10.1130/0091-7613(2000)028<0703:tobtem>2.3.co;2

Li, H.-A., Dai, J.-G., Xu, S.-Y., Liu, B.-R., Han, X., Wang, Y.-N., et al. (2019). The Formation and Expansion of the Eastern Proto-Tibetan Plateau: Insights from Low-Temperature Thermochronology. *J. Asian Earth Sci.* 183, 103975. doi:10.1016/j.jseaes.2019.103975

Li, N., Zhao, Y.-W., Zhang, L.-Y., and Wang, J.-L. (2020). The Quaternary Eruptive Sequence of the Tengchong Volcanic Group, Southwestern China. *Lithos* 354-355, 105173. doi:10.1016/j.lithos.2019.105173

Lin, T.-H., Lo, C.-H., Chung, S.-L., Hsu, F.-J. Yeh., Yeh, M.-W., Lee, T.-Y., et al. (2009). 40Ar/39Ar Dating of the Jiali and Gaoligong Shear Zones: Implications for Crustal Deformation Around the Eastern Himalayan Syntaxis. *J. Asian Earth Sci.* 34, 674–685. doi:10.1016/j.jseaes.2008.10.009

Lisker, F., Ventura, B., and Glasmacher, U. A. (2009). Apatite Thermochronology in Modern Geology. *Geol. Soc. Lond. Spec. Publications* 324, 1–23. doi:10.1144/SP324.1

Liu, J., Zeng, L., Ding, L., Tapponnier, P., Gaudemer, Y., Wen, L., et al. (2009). Tectonic Geomorphology|active Tectonics and Lower Crustal Channel Flow Hypothesis of the southeastern Tibetan Plateau. *Chin. J. Geology.* 44, 1227–1255. doi:10.3321/j.issn:0563-5020.2009.04.014

Liu-Zeng, J., Tapponnier, P., Gaudemer, Y., and Ding, L. (2008). Quantifying Landscape Differences across the Tibetan Plateau: Implications for Topographic Relief Evolution. *J. Geophys. Res.* 113, F04018. doi:10.1029/2007JF000897

Liu-Zeng, J., Zhang, J., McPhillips, D., Reiners, P., Wang, W., Pik, R., et al. (2018). Multiple Episodes of Fast Exhumation since Cretaceous in Southeast Tibet, Revealed by Low-Temperature Thermochronology. *Earth Planet. Sci. Lett.* 490, 62–76. doi:10.1016/j.epsl.2018.03.011

Mitchell, A. H. G. (1993). Cretaceous-Cenozoic Tectonic Events in the Western Myanmar (Burma)-Assam Region. *J. Geol. Soc.* 150, 1089–1102. doi:10.1144/gsjgs.150.6.1089

Molnar, P., and England, P. (1990). Late Cenozoic Uplift of Mountain Ranges and Global Climate Change: Chicken or Egg? *Nature* 346, 29–34. doi:10.1038/346029a0

Molnar, P., and Tapponnier, P. (1978). Active Tectonics of Tibet. *J. Geophys. Res.* 83, 5361–5376. doi:10.1029/JB083IB11p05361

Naiman, Y., Sobel, E. R., Millar, I., Stockli, D. F., Govin, G., Lisker, F., et al. (2020). The Exhumation of the Indo-Burman Ranges, Myanmar. *Earth Planet. Sci. Lett.* 530, 115948. doi:10.1016/j.epsl.2019.115948

Ouimet, W., Whipple, K., Royden, L., Reiners, P., Hodges, K., and Pringle, M. (2010). Regional Incision of the Eastern Margin of the Tibetan Plateau. *Lithosphere* 2, 50–63. doi:10.1130/l57.1

Qi, X., Zhao, Y., Zhu, L., and Li, Z. (2012). Discovery of High-Pressure Pelitic Granulite in Ailaoshan Orogenic belt, southeastern Tibet and its Tectonic Implications. *Acta Petrologica Sinica* 28, 1846.

Reiners, P. W., and Farley, K. A. (2001). Influence of crystal Size on Apatite (U-Th)/He Thermochronology: An Example from the Bighorn Mountains, Wyoming. *Earth Planet. Sci. Lett.* 188, 413–420. doi:10.1016/S0012-821X(01)00341-7

Reiners, P. W. (2005). Zircon (U-Th)/He Thermochronometry. *Rev. Mineralogy Geochem.* 58, 151–179. doi:10.2138/rmg.2005.58.6

Royden, L. H., Burchfiel, B. C., King, R. W., Wang, E., Chen, Z., Shen, F., et al. (1997). Surface Deformation and Lower Crustal Flow in Eastern Tibet. *Science* 276, 788–790. doi:10.1126/science.276.5313.788

Royden, L. H., Burchfiel, B. C., and van der Hilst, R. D. (2008). The Geological Evolution of the Tibetan Plateau. *Science* 321, 1054–1058. doi:10.1126/science.1155371

Shen, X., Tian, Y., Wang, Y., Wu, L., Jia, Y., Tang, X., et al. (2021). Enhanced Quaternary Exhumation in the Central Three Rivers Region, Southeastern Tibet. *Front. Earth Sci.* 9, 741491. doi:10.3389/feart.2021.741491

Socquet, A., and Pubellier, M. (2005). Cenozoic Deformation in Western Yunnan (China-Myanmar Border). *J. Asian Earth Sci.* 24, 495–515. doi:10.1016/j.jseaes.2004.03.006

Song, S., Niu, Y., Wei, C., Ji, J., and Su, L. (2010). Metamorphism, Anatexis, Zircon Ages and Tectonic Evolution of the Gongshan Block in the Northern Indochina Continent-An Eastern Extension of the Lhasa Block. *Lithos* 120, 327–346. doi:10.1016/j.lithos.2010.08.021

Sun, X., Bao, X., Xu, M., Eaton, D. W., Song, X., Wang, L., et al. (2014). Crustal Structure beneath SE Tibet from Joint Analysis of Receiver Functions and Rayleigh Wave Dispersion. *Geophys. Res. Lett.* 41, 1479–1484. doi:10.1002/2014GL059269

Tang, Y., Wang, D. B., Liao, S. Y., Wang, B. D., Yin, F. G., and Wang, L. Q. (2016). Geochronological Characterization and Regional Tectonic Implication of the Leucogranites in the Southern Segment of Gaoligong Metamorphic Zone, Western Yunnan. *Acta Petrologica Sinica* 32, 2347–2366. doi:10.1007/s10114-016-4736-8

Tang, Y., Wang, D., Liao, S., Wang, B., and Yin, F. (2020). Fabrics and 40Ar/39Ar Ages of Metamorphic Rocks in the Gaoligong Tectonic belt: Implications for Cenozoic Metamorphism and Deformation in the SE Tibetan Plateau. *J. Asian Earth Sci.* 192, 104270. doi:10.1016/j.jseaes.2020.104270

Tapponnier, P., Peltzer, G., Le Dain, A. Y., Armijo, R., and Cobbold, P. (1982). Propagating Extrusion Tectonics in Asia: New Insights from Simple Experiments with Plasticine. *Geol* 10, 611–616. doi:10.1130/0091-7613(1982)10<611:petian>2.0.co;2

Tapponnier, P., Zhiqin, X., Roger, F., Meyer, B., Arnaud, N., Wittlinger, G., et al. (2001). Oblique Stepwise Rise and Growth of the Tibet Plateau. *Science* 294, 1671–1677. doi:10.1126/science.105978

Wang, C., Liang, C., Deng, K., Huang, Y., and Zhou, L. (2018). Spatiotemporal Distribution of Microearthquakes and Implications Around the Seismic Gap between the Wenchuan and Lushan Earthquakes. *Tectonics* 37, 2695–2709. doi:10.1029/2018TC005000

Wang, C., Zhao, X., Liu, Z., Lippert, P. C., Graham, S. A., Coe, R. S., et al. (2008). Constraints on the Early Uplift History of the Tibetan Plateau. *Proc. Natl. Acad. Sci. U.S.A.* 105 (13), 4987–4992. doi:10.1073/pnas.0703595105

Wang, E., Burchfiel, B. C., Royden, L. H., Chen, L. Z., Chen, J. S., Li, W. X., et al. (1998). *Late Cenozoic Xianshuihe-Xiaojiang, Red River, and Dali Fault Systems of Southwestern Sichuan and Central Yunnan*. ChinaBoulder: Geological Society of America Publications.

Wang, E., KirbyFurlong, E. K. P., Furlong, K. P., van Soest, M., Xu, G., Shi, X., et al. (2012). Two-phase Growth of High Topography in Eastern Tibet during the Cenozoic. *Nat. Geosci* 5, 640–645. doi:10.1038/ngeo1538

Wang, G., Wan, J., Wang, E., Zheng, D., and Li, F. (2008). Late Cenozoic to Recent Transtensional Deformation across the Southern Part of the Gaoligong Shear Zone between the Indian Plate and SE Margin of the Tibetan Plateau and its Tectonic Origin. *Tectonophysics* 460, 1–20. doi:10.1016/j.tecto.2008.04.007

Wang, G., Wan, J., and Zhao, W, E. (2006). Late Cenozoic Tectonics-Gravity Collapse and its Causes in the Southern Gaoligong Mountains. *Acta Geologica Sinica* 9, 1262–1273. (in Chinese). doi:10.3321/j.issn:0001-5717.2006.09.004

Wang, Y., Fan, W., Zhang, Y., Peng, T., Chen, X., and Xu, Y. (2006). Kinematics and 40Ar/39Ar Geochronology of the Gaoligong and Chongshan Shear Systems, Western Yunnan, China: Implications for Early Oligocene Tectonic Extrusion of SE Asia. *Tectonophysics* 418 (3-4), 235–254. doi:10.1016/j.tecto.2006.02.005

Wang, Y., Fan, W., Zhang, Y., Peng, T., Chen, X., and Xu, Y. (2006). Kinematics and 40Ar/39Ar Geochronology of the Gaoligong and Chongshan Shear Systems, Western Yunnan, China: Implications for Early Oligocene Tectonic Extrusion of SE Asia. *Tectonophysics* 418, 235–254. doi:10.1016/j.tecto.2006.02.005

Wang, Y., Wang, Y., Schoenbohm, L. M., Zhang, P., Zhang, B., Sobel, E. R., et al. (2020). Cenozoic Exhumation of the Ailaoshan-Red River Shear Zone: New Insights from Low-temperature Thermochronology. *Tectonics* 39, e2020TC006151. doi:10.1029/2020tc006151

Xu, Z., Wang, Q., Cai, Z., Dong, H., Li, H., Chen, X., et al. (2015). Kinematics of the Tengchong Terrane in SE Tibet from the Late Eocene to Early Miocene: Insights from Coeval Mid-crustal Detachments and Strike-Slip Shear Zones. *Tectonophysics* 665, 127–148. doi:10.1016/j.tecto.2015.09.033

Yang, Q., Xu, Y., and Huang, X. (2006). Geochronology and Geochemistry of Granites in the Gaoligong Tectonic belt, Western Yunnan: Tectonic Implications. *Acta Petrologica Sinica* 22, 817. doi:10.3321/j.issn:1000-0569.2006.04.006

Yang, Q., and Xu, Y. (2011). The Emplacement of Granites in Nujiang-Gaoligong belt, Western Yunnan, and Response to the Evolvement of Neo-Tethys. *J. Jilin Univ. (Earth Sci. Edition)* 41, 1353–1361. doi:10.3969/j.issn.1671-5888.2011.05.009

Yang, R., Willett, S. D., and Goren, L. (2015). *In Situ* low-relief Landscape Formation as a Result of River Network Disruption. *Nature* 520, 526–529. doi:10.1038/nature14354

Yao, H., van der Hilst, R. D., and Montagner, J.-P. (2010). Heterogeneity and Anisotropy of the Lithosphere of SE Tibet from Surface Wave Array Tomography. *J. Geophys. Res.* 115, B12307. doi:10.1029/2009JB007142

Yin, A., and Harrison, T. M. (2000). Geologic Evolution of the Himalayan-Tibetan Orogen. *Annu. Rev. Earth Planet. Sci.* 28, 211–280. doi:10.1146/annurev.earth.28.1.211

Zhang, B., Chai, Z., Yin, C. Y., Huang, W. T., Wang, Y., Zhang, J. J., et al. (2017). Intra-continental Transpression and Gneiss Doming in an Obliquely Convergent Regime in SE Asia. *J. Struct. Geology.* 97, 48–70. doi:10.1016/j.jsg.2017.02.010

Zhang, B., Zhang, J., and Zhong, D. (2010). Structure, Kinematics and Ages of Transpression during Strain-Partitioning in the Chongshan Shear Zone, Western Yunnan, China. *J. Struct. Geology.* 32, 445–463. doi:10.1016/j.jsg.2010.02.001

Zhang, B., Zhang, J., Zhong, D., Yang, L., Yue, Y., and Yan, S. (2012). Polystage Deformation of the Gaoligong Metamorphic Zone: Structures, 40Ar/39Ar Mica Ages, and Tectonic Implications. *J. Struct. Geology.* 37, 1–18. doi:10.1016/j.jsg.2012.02.007

Conflict of Interest: The authors declare that the research was conducted in the absence of any commercial or financial relationships that could be construed as a potential conflict of interest.

frontiers | Frontiers in Earth Science

ORIGINAL RESEARCH
published: 27 April 2022
doi: 10.3389/feart.2022.856685

Small Human Population Drastic Impact, as Inferred From Multi-Proxies of a Temporary Carpathian Lake

Oana Teodora Moldovan[1,2,3†], Ladislav Miko[4†], Cristian Panaiotu[5†], Relu-Dumitru Roban[5†], Michał Gąsiorowski[6], Helena Hercman[6], Răzvan Orza[5], Marius Kenesz[1,2], Ionuț Cornel Mirea[7,2], Alexandru Petculescu[7,2], Marius Robu[7,8] and Silviu Constantin[7,2,3†]*

[1]Cluj-Napoca Department, Emil Racovita Institute of Speleology, Romanian Academy, Cluj-Napoca, Romania, [2]Romanian Institute of Science and Technology, Cluj-Napoca, Romania, [3]Centro Nacional de Investigación Sobre la Evolución Humana, CENIEH, Burgos, Spain, [4]Institute for Environmental Studies, Charles University Prague, Prague, Czechia, [5]Faculty of Geology and Geophysics, University of Bucharest, Bucharest, Romania, [6]Institute of Geological Sciences, Polish Academy of Sciences, Warsaw, Poland, [7]Department of Geospeleology and Paleontology, Emil Racovita Institute of Speleology, Romanian Academy, Bucharest, Romania, [8]Department of Biosciences, Centre for Ecological and Evolutionary Synthesis, University of Oslo, Oslo, Norway

Over the last thousands of years, human impact led to significant changes in the landscape, with impacts on the environment and the functioning of the ecosystems. We assumed that even small human settlements developed around water bodies might have a substantial impact that surpasses the natural cycles of climate change in an area, especially linked to forest cutting. We have chosen a temporary lake in the Romanian Carpathians as temporary lakes are overlooked in paleoclimatic studies, although they have potential as hotspots for paleoenvironmental research studies. Zăton Lake has exposed riverbank sediments dated with radioactive lead and optical stimulated luminescence techniques, analyzed for sediments and paleomagnetism, and sampled for fossil Oribatida mites. The results show that for the last 2,200 years, natural cycles of warm and cold periods changed the oribatid communities around the lake, with warmer cycles of rich fauna alternating with poor fauna during colder periods. However, in the last few centuries, the increased human occupation in the area replaced the ecologically diverse fauna with eurytopic taxa, more similar to the colder periods of the environmental evolution around the lake. Even if the human occupation around the lake was negligible, probably a few hundred to ~2,500 people as in the present, the impact on the area is drastic, with ecologically nonspecific species becoming dominant. In conclusion, even small and temporary water bodies can contain unique and valuable information on past histories of climate change and human impacts. At regional scales, the combined effects of climate change and long-term human impacts in local areas can have deleterious effects on invertebrate species and communities.

Keywords: Oribatida, climate change, human impact, paleoenvironments, indicator species

OPEN ACCESS

Edited by:
Xibin Tan,
China Earthquake Administration, China

Reviewed by:
Jiawei Fan,
China Earthquake Administration, China
Hu Wang,
Southwest Jiaotong University, China

****Correspondence:***
Oana Teodora Moldovan
oanamol35@gmail.com

[†]These authors have contributed equally to this work

Specialty section:
This article was submitted to Quaternary Science, Geomorphology and Paleoenvironment, a section of the journal Frontiers in Earth Science

Received: *17 January 2022*
Accepted: *28 March 2022*
Published: *27 April 2022*

Citation:
Moldovan OT, Miko L, Panaiotu C, Roban R-D, Gąsiorowski M, Hercman H, Orza R, Kenesz M, Mirea IC, Petculescu A, Robu M and Constantin S (2022) Small Human Population Drastic Impact, as Inferred From Multi-Proxies of a Temporary Carpathian Lake. Front. Earth Sci. 10:856685. doi: 10.3389/feart.2022.856685

INTRODUCTION

Human land use during the Holocene has led to some drastic changes in soil stability and productivity, the functioning of river ecosystems, and lateral transfer of sediments and carbon, with possible effects also on the local climate (Montgomery, 2007; Borrelli et al., 2017; Wang et al., 2017). Vegetation clearance and burning and agricultural and settlement expansion have led to increasing regional soil erosion rates (Arnaud et al., 2012; Roberts et al., 2018). Jenny et al. (2019) have found that a significant portion of the Earth's surface had already shifted to human-driven soil erosion 4,000 years ago, following land deforestation. Land-use changes also impact the aquatic ecosystems that provide unique communities and numerous services. Their vulnerability is also enhanced because most of the world's human populations develop around water bodies (Williamson et al., 2008). Lake sediments have the potential of providing excellent archives for long-term human impacts, although only recently, research on lake sediments switched from generating climate records to detecting human impacts caused by the exploitation of both land and water (Dubois et al., 2018). For many European lakes, the pristine conditions pre-date the forest clearance and introduction of agriculture between the Neolithic and Bronze Age with an intensification caused by industrialization and population growth in the 19th century (Bennion et al., 2010). The paleolimnological analysis in northwestern Europe considered human impact minimal before the pre-industrial period (1800–1850 A.D.), a period which is a reference for the lack of impacts (Bennion et al., 2010; Rose et al., 2011; Battarbee et al., 2012; Bennion et al., 2012; Bennion et al., 2012). However, more recently, research has shown that significant metal pollutions from 600 BCE onward occurred in the Balkans, with gradually increasing values in metals of anthropogenic origin until a peak at ~1,620 CE (Longman et al., 2018). This pollution includes a prominent, likely medieval lead peak and extended periods of metal production in the region after the Roman occupation. These early peaks were followed by recent (1850–present) enrichment in all elements.

Nevertheless, the separation of human impacts from other natural causes, such as climate change or other environmental signals, varies significantly between sites and can be subject to false interpretation (Bennion et al., 2010). For example, climate change impacts on freshwaters can be similar to the effects of eutrophication (Jeppesen et al., 2014). The use of lake proxies to cover at least some of the important climate changes that preceded the industrial impacts of the 19th century can overcome such erroneous interpretation and other constraints of paleolimnological studies given by a poor dating control and low preservation of the appropriate proxies. By studying sediments from caves using a multi-proxy approach, we found that these can provide paleoclimatic and paleoenvironmental archives for periods poorly covered by the surface sediments and offer biological proxies in a good state of preservation (Moldovan et al., 2011, 2016).

Temporary lakes are a neglected category of water bodies because they are not stable water and food sources. They are also neglected by studies on climate change and human impact, even if they have been recognized important in carbon processing (Morris et al., 2013; Catalan et al., 2014; Bartolotti et al., 2016). Temporary lakes develop in shallow depressions with varying surfaces and experience dry periods of various lengths, with occasionally predictable onset and duration.

Zăton Lake (Southern Carpathians, Romania) has exposed riverbank sediments during periods of low water and a small and stable human population in the surrounding basin that dates to at least the 14th century. A preliminary investigation on short sequences of sediments deposited in the meanders of Bulba Cave (Southwestern Carpathians) provided calibrated radiocarbon ages from 1671 to 1995 A.D. (unpublished data). As the cave belongs to the karstic system connected to Zăton Lake, we decided to concentrate our attention on the latter to understand the evolution of the subterranean system. Zăton Lake is temporary, with alternating regimes of water accumulation and slow drainage, and it is a source of sediments for the cave system. The scope of this article was to study the temporal dynamics and resilience of Zăton Lake by the combined effects of human impacts and climatic changes using sediments and fossil mites (Acari: Oribatida) as paleoenvironmental indicators. We have chosen this simple system for our investigation with few known environmental data to verify the assumption that human impacts prevail over climate change, at least in small systems with low resilience. The stratigraphic and quantitative studies on oribatid mites are fewer than those on insects and mollusks due to their more recent recognition as paleoecological indicators and the much lower number of specialists (Solhøy & Solhøy 2000). Nevertheless, recent studies have shown their presence even in very old karstic sediments and their important paleoenvironmental information when cross-correlated with coeval proxies (Moldovan et al., 2011, 2016).

There are studies showing changes in the lake sediments worldwide caused by nutrient enrichment starting with the Bronze Age but mostly of increased acidification after the 19th century and decreased total organic carbonic carbon over the last 200 years (Bennion et al., 2010). Renberg (1990) showed that natural acidification over the early and middle Holocene was followed by a period of elevated pH associated with forest clearance and early agriculture during the Bronze Age and two phases of recent acidification associated with re-acidification caused by land abandonment, forest regeneration, and acid deposition. In a high-altitude lake (above 2000 m a.s.l.) in the Southern Carpathians, Vincze et al. (2017) found evidence of human impact only after 4,200 cal yr B.P., during the Bronze Age. At a lower altitude, in a northern lake in Romania, Peters et al. (2020) found the first anthropogenic impacts after 5,000 cal yr B.P., slightly stronger between 2,300 cal yr B.P. and the 12th century A.D., with large scale forest clearings in the lowlands, foothills, and intensified agriculture. The impact intensified during the Iron Age and the Medieval Period, around 2,600 cal yr B.P. For the last 100–150 years, several natural and anthropogenic drivers of the changes observed in lake sediments or peat bogs were mentioned for sites in Romania (Feurdean et al., 2013, 2015; Haliuc et al., 2019, 2020) in northern, northeastern, and northwestern Romania.

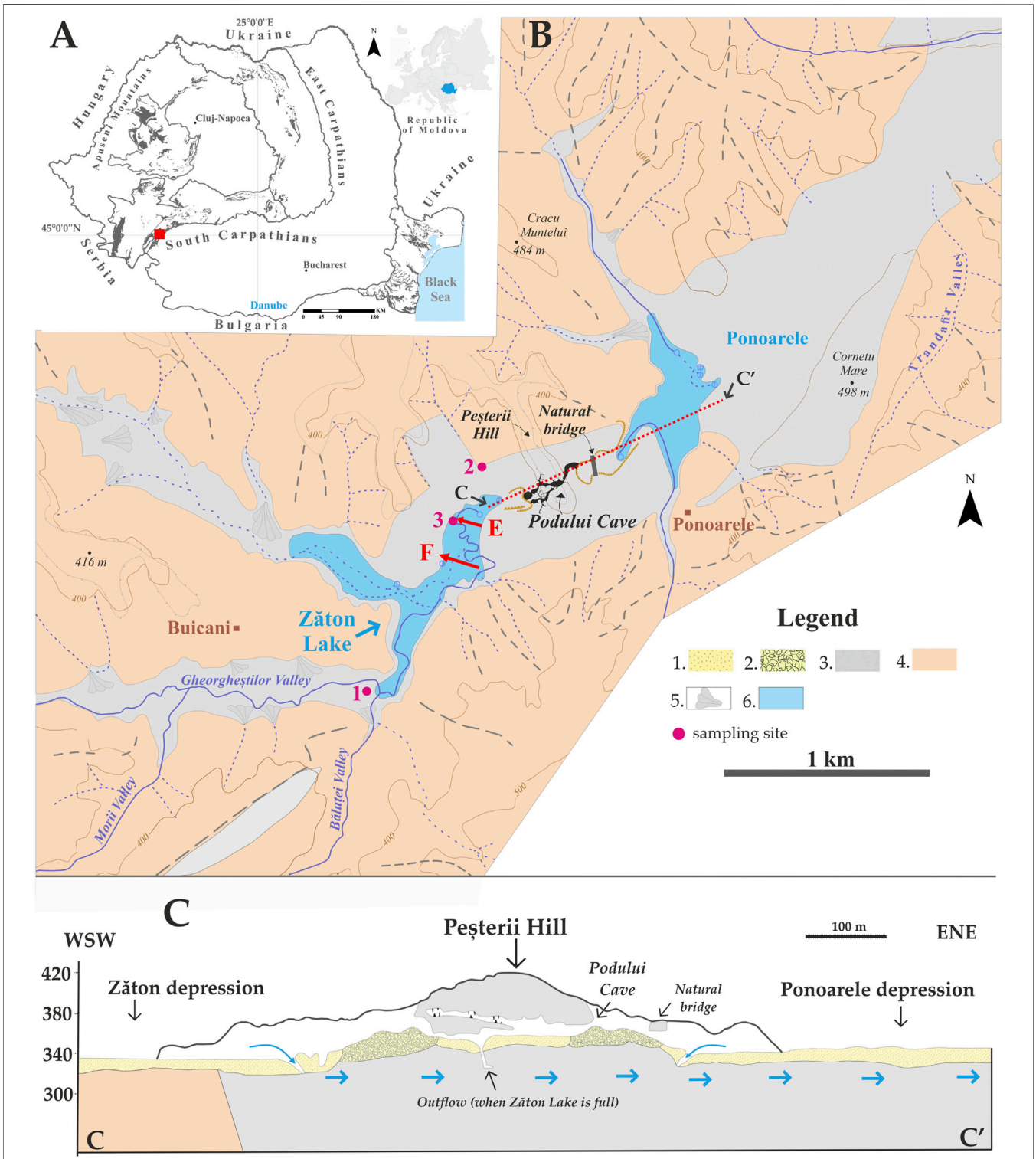

FIGURE 1 | (A) Location of the Zăton Basin in the S.W. part of the Romanian Carpathians. **(B)** Zăton Lake and the connected cave system. **(C)** Schematic representation of the long section of the cave system and its functioning when Zăton depression fills with water. The E and F positions of the two geophysical profiles are marked with red arrows. 1 = quaternary sediments; 2 = scree debris; 3 = limestone; 4 = impervious rocks; 5 = talus fan; and 6 = lake. **(B,C)** Modified from Goran, 1978.

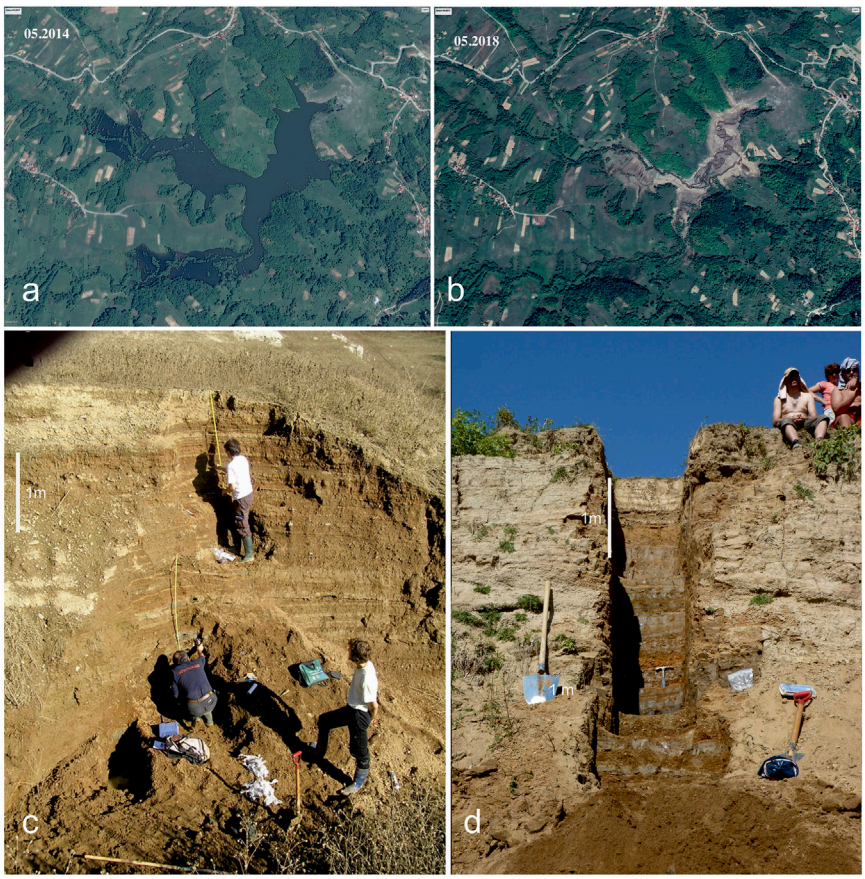

FIGURE 2 | Google Earth images of Zăton Lake taken in May 2014 **(A)** and May 2018 **(B)**, with and without water, respectively. The pictures shown as follows were taken in November 2010 of the Zaton2 profile **(C)** and in June 2013 of the Zaton3 profile **(D)**.

MATERIAL AND METHODS

Study Area

Located in the northeastern part of the Mehedinți Plateau, in the Southern Carpathians (44°58′24.6″N, 22°45′20.8″E; **Figure 1**), the Zăton basin (19.5 km^2) is the largest temporary karst lake in Romania. Its watershed lies at elevations ranging between 810 and 327 m a.s.l. The lower point corresponds to a sink located at the limit between the impervious and karstic deposits. It is a temporary lake formed in a semi-closed depression, flooded during periods with high precipitation or snow melting, and formed at the contact between impervious and karstic deposits. Its slopes are used for agriculture and cattle farming. The lake can extend more than 2.5 km, while its depth may exceed 20 m. Granitic and metamorphic formations of the Danubian Unit and impervious sedimentary deposits (Upper Cretaceous; Miocene), especially including shales and siliciclastic rocks, form the lake bed.

The lake is supplied by the Valea Mare and Valea Gheorgheştilor streams and small tributaries. During the dry season, the lake dries down, and the scarce stream waters sink into one or more swallet holes on contact with a stripe of massive limestone of the Upper Jurassic–Lower Cretaceous. The waters drain through karst conduits in the lower level of the Podului Cave (~750 m long) toward the west to further reach the passages of Bulba Cave (>5 km-long). The sink and karst conduits cannot drain all the flow during the wet season, and a reservoir forms upstream.

The water accumulation strongly depends on the amount of precipitation and the drainage capacity of the karst conduits, with years when the lake does not form at all. Maximum water levels are usually recorded during the spring and late autumn. The main stream has a meandering course incised within the terrace deposits at low water levels. Short tributaries have steeper and more rugged profiles, typical for ravines (**Figure 2**).

The climate is temperate continental with a mean annual temperature of 9.1°C, a mean summer temperature of 19.2°C, and a mean winter temperature of −1.1°C. Annual mean precipitations are 670 mm (Fick and Hijmans, 2017). Southwestern Romania is located in a transition zone with a regional climate dominated by the influence of the Carpathian mountain topography and westerly driven circulation patterns (Micu et al., 2015). Most studies display substantial inter-site variability to indicate the complexity of climate in the Romanian

Carpathians in southeastern Europe (Roberts et al., 2012; Longman et al., 2017).

The vegetation around the lake is represented by scarce patches of forest and shrubs with rocky surfaces covered with grass and agricultural fields. The forest is represented mainly by deciduous trees with some planted coniferous.

Analyzed Sections

Three profiles (**Figures 1**, **2**) were sampled in the Zăton basin. Zaton1 was a ~4 m-long core drilled on a small terrace located between Valea Mare and Valea Gheorgheștilor. The borehole intercepted the local aquifer, and part of the samples (mainly sands) were lost and highly disturbed. The retrieved samples were very recent sediments; hence, Zaton1 was used as a reference for modern sediments, but it will not be used in this study.

Zaton2 was a trench excavated within a natural outcrop on a left-hand side tributary of the main stream, immediately upstream of the sink of the lake. It is mainly composed of coarse sediments and has a thickness of ~4 m.

Zaton3 was another trench excavated within a meander inner bank of the main stream. This 4.8 m-thick section includes various sediments ranging from clays through gravels. Both Zaton2 and Zaton3 were sampled during the dry season at low water levels.

Sedimentary Facies Analysis

In the field, Zaton2 and Zaton3 sections were described (**Figures 2C,D**), following the principles of facies analysis (Walker and James, 1992; Miall, 1985, 1996). These included the separation and description of the facies, interpretation of sedimentary processes, and separation and interpretation of facies associations in terms of the geometry of the fluvial and lake sedimentary architecture.

Geophysical Measurements

Resistivity methods calculate the electrical apparent resistivity distribution in the subsoil (Daily and Lytle, 1983). Integrated resistivity and ground-penetrating radar (GPR) surveys have been widely used to highlight, at different scales, the heterogeneity and morphology of fluvial deposits (Kostic and Aigner, 2007; Wozniak et al., 2018; Yogeswar et al., 2019), a key factor for groundwater flow modeling in valley-fill deposits. The GPR method is a high-resolution technique that uses high-frequency electromagnetic pulses to map shallow subsurface contrasts in dielectric properties (Jeffy et al., 2019). Both methods allow a noninvasive investigation of the sedimentary units in the near subsurface.

Vertical electrical soundings undertaken in profiles E and F (**Figure 1B**) were performed to characterize the resistivity variation within the Zăton infill deposits. For both profiles, the maximum depth of investigation was about 26.67 m. An ABEM SAS 1000 resistivity-meter with a Schlumberger type array was used for data recording. Along with profile E, a GPR profile was recorded using a GSSI Sir 3,000 system with a 200-Mhz antenna. The acquisition parameters for the resistivity survey were carefully established to increase the signal/noise ratio. The error limit between the repeated measurements was set to 0.2%, and for each measurement, a number between minimum 1 and maximum 4 repetitions was automatically performed in case the error limit was not reached. The GPR acquisition parameters were chosen after performing several tests on site. A total of 1024 samples/scans were used to increase the vertical resolution and a time window of 50 ns. The chosen value for the dielectric constant was 8, and the number of scans/units was set to 60. The calibration of the wheel was realized at a distance of 20 m.

In order to emphasize the resistivity distribution in the subsurface, the acquired resistivity data were inverted by using Res2DInv (Loke and Dahlin, 2002). The inversion routines are based on the smoothness-constrained least-squares method (Silvester and Ferrari, 1990; Loke and Barker, 1995), and the forward resistivity calculations were executed by applying an iterative algorithm based on the finite element method.

GPR data were processed with RADAN 6.6 (radar data analysis) provided by GSSI, and after the time-zero offset correction, the usage of a horizontal high pass filter (background removal) was involved in order to remove the low-frequency features. The multiple reflections caused by radar energy reverberations were attenuated using a deconvolution filter. The penetration depth was limited to 3m, but features below the saturated zone could not be detected.

Paleomagnetism of the Zaton3 Section

Paleomagnetic analysis was possible only on the Zaton3 profile due to its fine sediments in opposition to the coarser sediments of Zaton2.

For rock-magnetism, samples were collected in plastic cylinders (~11 cm^3) specially designed to avoid the rotation of the sample during sampling or measurements. The cylinders were oriented using a magnetic compass corrected for the local declination, excavated, capped, and packaged to avoid the loss of humidity during the transport. We sampled only undisturbed horizontal fine sediments (clay or silt), which allowed us to press the cylinders into the clean face of the outcrop. In the laboratory, the samples were kept in a refrigerator to preserve the original humidity as much as possible.

In the Paleomagnetic Laboratory of the University of Bucharest, we analyzed the structure of natural remanent magnetization by alternating field (AF) demagnetization. AF demagnetization was performed using an LDA-3A–A.F. demagnetizer (AGICO) in several steps up to a maximum of 100 mT. After each demagnetization step, remanent magnetization was measured using a JR6 spinner magnetometer (AGICO). Demagnetization results were analyzed on orthogonal demagnetization diagrams (Zijderveld, 1967), and magnetization components were isolated by principal component analysis (Kirschvink, 1980) by Remasoft 3.0 software (Chadima and Hrouda, 2006). The line fits were based on the following restraints: (1) a minimum of 4 demagnetization steps; (2) the line fit was anchored to the origin; and (3) the maximum angular deviation was $<10^{\circ}$. From 30 samples, 26 samples gave results that fit these criteria. The typical results are presented in the **Supplementary Material**.

Dating of the Profiles

Optically stimulated luminescence (OSL) and ^{210}Pb methods were used for age determination of the sediments of Zaton2 and Zaton3, respectively. ^{210}Pb isotope with a half-life of 22.2 years was used to estimate sediment rates for the last 100 years on the Zaton2 section. The OSL method was used for sediments that were presumed to be older than 100 years.

For ^{210}Pb, samples taken from section Zaton2 were sealed in plastic bags and stored for at least 28 days prior to measurements. The measurements were performed at the Institute of Geological Sciences, Polish Academy of Sciences, Warsaw, Poland. The activity of unsupported (allogenic) ^{210}Pb was calculated by extraction of the supported ^{210}Pb activity from the total activity of ^{210}Pb. The constant rate of supply (CRS) model was applied to age calculation (Appleby, 2001). An age-depth function was calculated using the randomization method and was fitted using the LOESS procedure (Clevland and Devlin, 1988).

Sediment samples for OSL dating were collected by hammering 25 cm-long, opaque plastic tubes (20 cm) into the sediment sections under no-light conditions. The measurement protocol was the single aliquot regeneration (SAR) applied on quartz (Murray and Wintle, 2003; Wintle and Murray, 2006). The OSL dating was performed at the Dating and Luminescence Dosimetry Laboratory, Babes-Bolyai University, Cluj-Napoca, Romania.

Fauna Sampling

For fossil invertebrates, a total of 22 samples were taken from Zaton2 and 15 samples from Zaton3 sections and analyzed. The selection of samples was made according to the succession of sedimentary layers by sampling each possible layer. Approximately 1 kg of sediment was taken from each sampling point and placed in sealed and labeled plastic bags. In the laboratory, the samples were kept in 10% KOH for 30 min and washed successively through sieves of 250 μm, 125 μm, and 40 μm with filtered water. Sub-samples for each sieve dimension were examined separately under an Olympus SZX2 stereomicroscope in 90° alcohol, and each specimen was identified under an Olympus BX51 microscope. Identification of the species was carried out following the specific methods for Oribatida mites (Weigmann, 2006).

For the ecological characterization of the identified oribatids, the following references were used: Weigmann and Kratz (1982), Lytle (1983), Schatz (1983), and Miko (2016).

Mites have been used in paleoclimatic and paleoenvironmental studies, especially in the last decades (Krivolutsky and Druk, 1986; Erickson, 1988; Elias, 1994; Coetzee and Brink, 2003; Erickson et al., 2003; Krivolutsky and Sidorchuk, 2003; Solhøy, 2001; Erickson and Platt, 2007; Moldovan et al., 2011, 2016). The choice of oribatid mites for paleoenvironmental studies has several rationalities: (i) abundant in karstic sites, such as the Zăton Lake basin; (ii) narrow ecological niches reflecting the paleoenvironments thoroughly; (iii) flightless, reflecting the structure of past *in situ* communities; (iv) trophically diverse and, thus, have a high species diversity; and (v) very sensitive to habitat evolution and various kinds of disturbance, including chemical pollution by metals or synthetic products, land use, management, and fires (Van Straalen, 1998; Behan-Pelletier, 1999; Behan-Pelletier & Newton, 1999; Solhøy & Solhøy, 2000; Fountain & Hopkin, 2001; Henig-Sever et al., 2001; Lindo & Visser, 2004; Migliorini et al., 2005; Migliorini, 2009; Erdmann et al., 2007).

RESULTS

Sediment Thickness and Distribution

The thickness of the sedimentary filling and its boundary with the bedrock were estimated using the inverted resistivity sections, which are displayed and described in **Supplementary Figure S1**.

Facies and Facies Associations, Processes, and Environmental Evaluation

Following the principles of facies analysis, lithological logs were drawn for Zaton2 and Zaton3 sections, allowing for the description of five sedimentary facies and two types of facies associations (**Figure 3**) based on grain-size characteristics (**Supplementary Material**), sedimentary textures/structures, and thickness.

Massive or crudely stratified gravel (Gm) is characteristic of the Zaton2 profile but was also found in the lower part of the Zaton3 section. It comprises a layer of decimeter and centimeter thickness of poorly sorted gravel. The largest clasts reach 7–10 cm. The shape of the clasts is mainly sub-angular or sub-rounded. The internal structure is massive, sometimes with normal grading or horizontal parallel stratification. Imbrication of larger clasts has rarely been observed. Occasional changes from clast-supported to matrix-supported have been encountered. The matrix consists of sand or, sometimes, mud. This facies suggests a bed load of higher density tractive stream flows. They are typical for alluvial bars (Miall, 1985, 1996) but also for the distal parts of the alluvial fans.

Horizontally stratified sand and gravelly sand (Sh) were abundant in the section of Zaton2. In Zaton3, it was encountered as decimetric layers toward the top. It includes sand, sometimes with granular gravels (2–4 mm). The clasts rarely exceed 1 cm in diameter. It shows an organized character, laminated or stratified parallel to the general stratification of the sedimentary filling of the basin. This facies suggests the bottom load of tractive currents, characteristic of sandy river bars (Miall, 1985). Planar stratified gravelly sand (Sp) was found only once in the upper part of the Zaton3 section. It has a thickness of 20 cm. It consists of coarse, poorly sorted sand and coarse clasts of gravel. The internal structure was organized and tabularly oblique stratified. In a lower flow regime, it is a tractive facies specific to river bars. Small scale massive and laminated sand (Sl): this facies subordinated as the frequency was met in the median part of the basin Zaton3 section. It is associated with fine facies (Fm). It consists of sub-centimeter layers of sand from coarse to fine with different structures, massive or parallel laminated, and rarely with ripples on the top. These are sandy

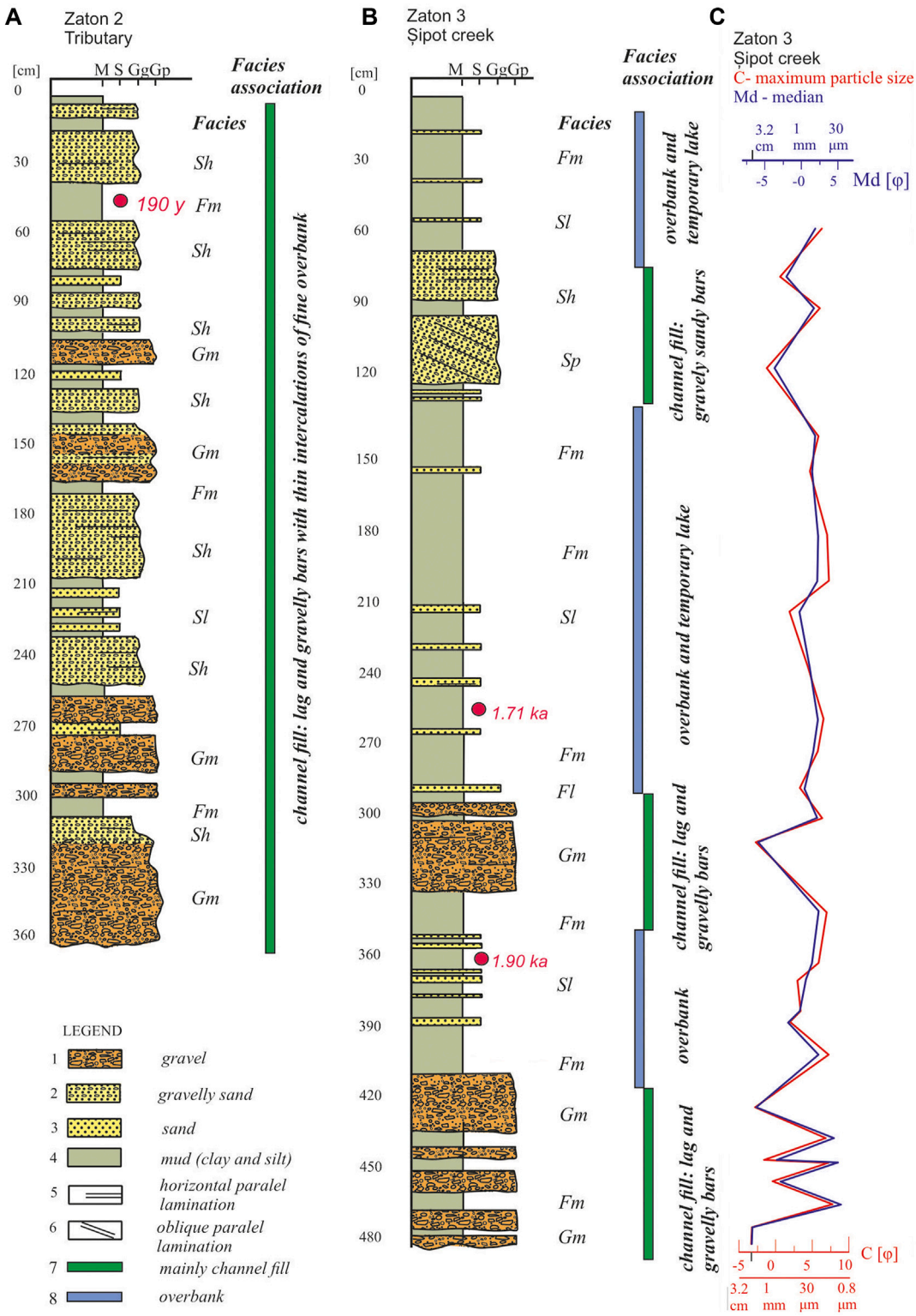

FIGURE 3 | Sedimentological logs of Zăton Lake. **(A)** Zaton2 (see **Figure 1E** for location). **(B)** Zaton3. **(C)** The distribution graph of depth and the granulometric parameters C (maximum particle size) and median (Md). The grain size categories on the top of logs: M–mudstone, S–sand, Gg–gravel (granules: 2–4 mm), and Gp–gravel (pebbles: 4–64 mm). The facies codes on the right side of the log are described in the text: Gm, Sh, Sp, Fl, and Fm.

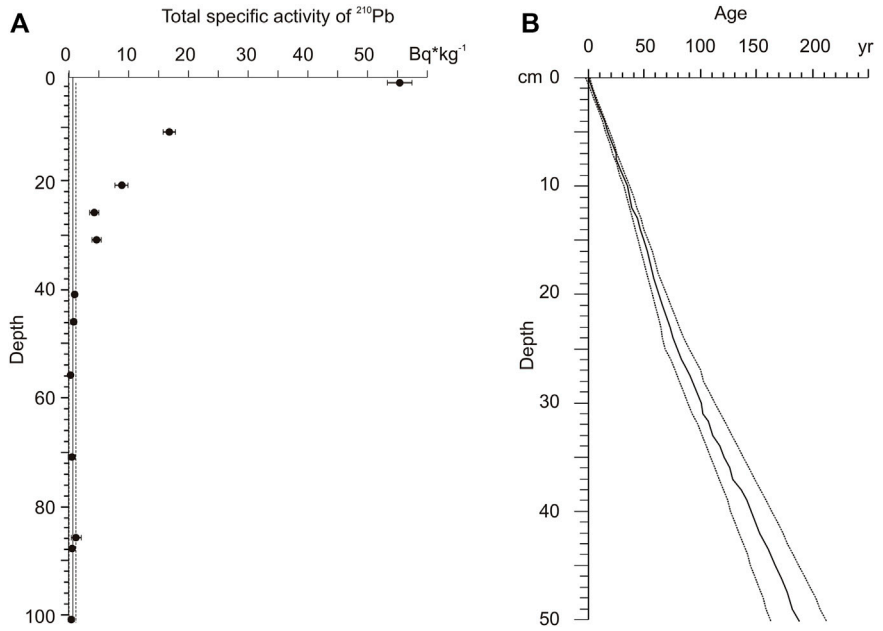

FIGURE 4 | (A) Total specific activity of 210 Pb in sediments of Zaton2; the solid line is a calculated value of supported 210 Pb. **(B)** Age-depth model (solid line) with the 2SD confidence band (dashed lines) for the Zaton2 sediment sequence based on ^{210}Pb dating.

sheets in the overbank or alluvial plain deposits formed during floods (Miall, 1985). Massive silty mud or mud (Fm) is a facies that dominates the middle part of the Zaton3 section. It is composed of clays and silt with a massive structure. The layers are usually thick in centimeters but sometimes may exceed 10 cm. The facies suggest suspension settling processes on the alluvial plain during occasional floods.

The described facies can be associated in two categories. Association I consists of coarser facies (Gm, Sh, and Sp). It constitutes the main part of the Zaton2 profile and the lower part of the Zaton3 section. It is interpreted in terms of gravelly and sandy bars of river channels. Association II consists of the fine facies (Fm and Sl). The association dominates the middle and upper sectors of the Zaton3. It suggests flooding and overflow processes and suspension settling during lake stages (**Supplementary Figure S2**).

Sedimentary Evolution and Depositional Conditions

From both macroscopic geomorphological observations and analyses, it is clear that in the history of sediment filling of the Zăton depression, the fluvial phases alternated with lacustrine phases. Thus, periods of accumulation alternated with periods of erosion, and for the last 4 m analyzed in the vicinity of the top, next to the Zaton3 section, fluvial facies, canals, ridges (overbank), and finer lake facies were identified (**Figure 3**). The control factors must have been the climatic and hydrological regime, the position, and the width of the cave system siphons.

The GPR survey (**Supplementary Figure S3**) proved to be a helpful tool for characterizing the spatial distribution of the depositional elements, their geometry, and their bounding surface within the vadose zone. The high conductivity saturated zone of the sediment filling of the lake acted as a shield for the radar waves; therefore, the features below the vadose zone could not be detected due to the high attenuation of the signal.

The high amplitude reflectors, which can be vaguely observed also below the saturated zone, are present on the radargram between X.T. = 0 m and X.T. = 25 m in the southeastern part of the profile and between X.T. = 80 m and X.T. = 100 m in the northwestern part of the profile, having a concave-up shape, and can be associated with buried channels filling depositional elements. These high amplitude reflectors bound packages of parallel or oblique reflectors having low lateral continuity, which may be associated with different cycles of the channel filling. The middle part of the radargram shows reflectors having a low inclination and moderate amplitude. We can remark the alternation in the depth of continuous reflectors with reflectors having poor lateral continuity. The latter is being faded by the presence of other reflectors and may be associated with finer overbank, alluvial, or lacustrine facies, characterized by low angle cross-stratification alternation of gravel to fine grain, thus highlighting the alternation of fluvial phases with lacustrine phases.

Age Control of the Sections

Zaton2

The total specific activity of ^{210}Pb ranged from 54.8+/−1.2 Bq kg-1 at the sediment surface to 0.14 +/− 0.28 Bq kg-1 at 56 cm (**Figure 4A**). The calculated activity of supported ^{210}Pb was 0.30+/−0.25 Bq kg-1, and the supported lead level was reached at 40 cm. The age-depth model (**Figure 4B**) showed that the uppermost 50 cm of the sediment sequence was deposited during the last 190 years.

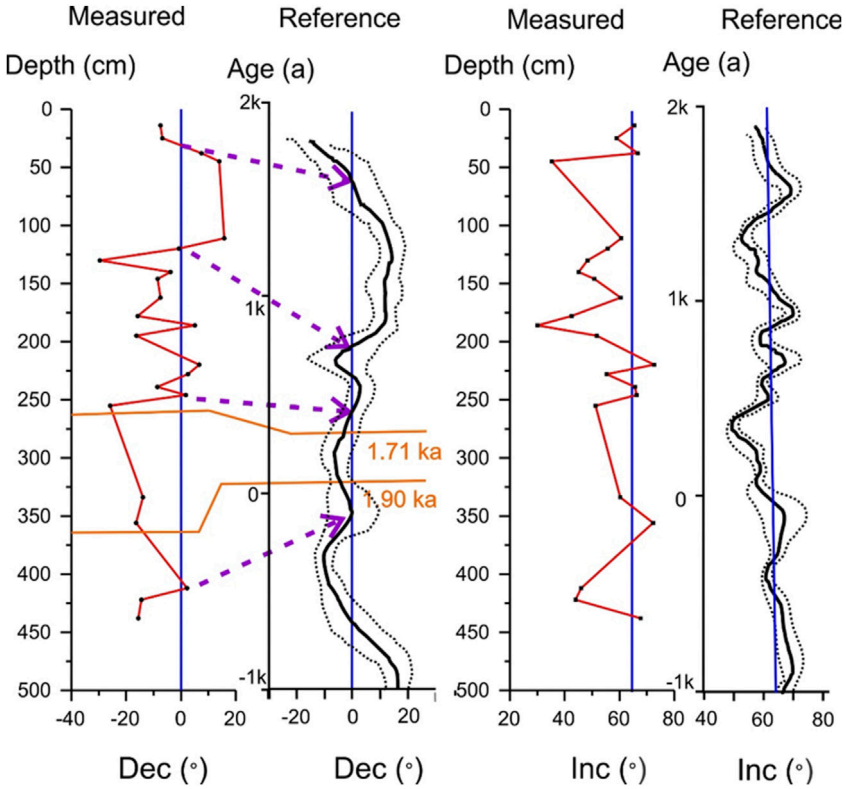

FIGURE 5 | Paleomagnetic dating of sediments in the Zaton3 section using the correlation of the measured declinations and inclinations (Dec; Inc.; red lines) with the reference paleosecular variation curve for Bulgaria (Kovacheva et al., 2014) based on the Bayesian approach (black line = reference curve; dotted lines = confidence limits). Blue lines mark expected declination and inclination based on the geocentric axial dipole hypothesis. OSL ages are marked with orange lines. Dotted purple lines mark suggested correlation points.

Zaton3

For further information on the age of the sediments, we used a paleomagnetic record (**Figure 5**). We have obtained two reliable OSL ages at a depth of 265 cm (1.71 ± 0.17 ka) and 360 cm (1.90 ± 0.20 ka).

Paleomagnetic Dating

The characteristic paleomagnetic directions at the sampling site are presented in **Figure 5**, separately for declination and inclination. The typical demagnetization results are presented in **Supplementary Figure S4**. These data were compared for paleomagnetic dating with the paleosecular variation curve from Bulgaria (Kovacheva et al., 2014), the nearest regional reference curve (~300 km south of the study site). Comparing the measured inclination and the expected declination, it is evident that the measured inclination is shallower than the expected inclination based both on the reference curve and the geocentric axial dipole hypothesis. Such inclination shallowing can happen during sediment deposition related to factors such as particle shape, viscosity, pH, and current shear or during compaction of sediments (Li and Kodana, 2016). Due to this inclination shallowing, we mainly used the declination values to date the sediments. Assuming quasi-continuous sedimentation produced by seasonal flooding episodes, we have identified similar oscillations on the measured and reference declination curves. The correlation of inflection points around zero declination between these two curves is marked with dotted arrows in **Figure 5**. Such correspondence agrees with the two available OSL ages. Since the sampling density was not uniform along the section due to the presence of coarse sediments, this time model must be regarded as a crude one. Based on this preliminary time model, we estimated that the age of the sediments is between the present and ~ 2.2 ka for the sampled section.

Fossil Oribatid Mites

The Zaton2 section had 136 individuals belonging to 40 species (**Supplementary Table S1**), with only three species having more than 10 individuals (**Table 1**). Two layers were richer in individuals, located in the lower part of the section with *Zygoribatula exarata* as the most abundant species. Along with the profile, the layers with fossils were cyclically intercalated with layers without fossils (**Supplementary Table S1**).

The Zaton3 section had 742 individuals belonging to 89 species of oribatid mites, with 23 species represented by more than 10 individuals (**Table 2**; **Supplementary Table S2**; **Figure 6**). Two principal successions of layers in the section were especially rich in fauna, between 116 and 200 cm and between 290 and 439 cm in depth. *Tectocepheus velatus*, a cosmopolitan and eurytopic species,

TABLE 1 | Identified Oribatida in the Zaton2 section (**Supplementary Table S1**) for species with more than 10 individuals; most abundant depths are vertically marked in gray. Color legend: yellow = dry/xerophile, dark blue = halotolerant, and light blue = open area.

SPECIES / DEPTH (CM)	0-20	52-60	60-70	70-80	135-136	220-225	240-241	256-265	274-278	295-323	TOTAL
Punctoribates hexagonus	2	1	1	1		3		4			*12*
Punctoribates punctum	1			1	1	2	1	2	2	2	*12*
Zygoribatula exarata	1		1			7		4	4	4	*21*
Zygoribatula undulata						10		1			*11*
TOTAL	*4*	*1*	*2*	*2*	*1*	*22*	*1*	*11*	*6*	*6*	

TABLE 2 | Identified Oribatida in the Zaton3 section (**Supplementary Table S2**) for species with more than 10 individuals; most abundant depths are vertically marked in gray. Color legend: dark green = forest, light green = shrub, light red = eurytopic, yellow = dry/xerophilic, dark blue = halotolerant, light blue = open area, and white = nonspecific.

SPECIES / DEPTH (CM)	ZATON3												
	54-68	69-74	116-185	186-200	201-202	290-340	341-380	381-412	413-439	440-470	471-503	504-543	TOTAL
Berniniella bicarinata						3	7	3				1	14
Berniniella inornata				5		5							10
Dissorhina ornata				2	1	2	8	18	10	1			33
Graptoppia foveolata						11	1	3	1				16
Liebstadia pannonica				2		7	11	12	3				35
Micreremus gracilior				5		8	7	10	3			1	25
Microppia minus	2	2	29	1	2	13	5	10	5				60
Oppiella nova			25	5		13	14	19	10	2			79
Oppiella propinqua			2			3		3	2	2			12
Oxyoppia europaea			5	5		2	4		1				17
Peloptulus phaenotus			1				1	1	3			1	7
Protoribates monodactylus				1		3	1		4			1	10
Punctoribates hexagonus						5	13	7	5	4	1	18	53
Punctoribates punctum			5	18	1	2	1	4	1	1			33
Quadroppia hammerae				1		1	6	2					10
Ramusella elliptica				3		1		5	2	2		1	14
Ramusella furcata						3	1	3	1			1	9
Rhinoppia loksai			3	1	1	1		5					11
Rhinoppia obsoleta						2	3	5	3			2	15
Scheloribates laevigatus							2		4			2	8
Scutovertex sculptus			1	1			1	3	4		1		11
Suctobelbella arcana				1		5		3	1				10
Tectocepheus minor							3	4	2	3			12
Tectocepheus velatus			37	11	2	29	39	36	16	5		7	182
Zygoribatula exarata				2		4	14	12	2			3	37
Zygoribatula glabra							8	3	3	4		1	19
TOTAL	*2*	*2*	*108*	*64*	*7*	*123*	*150*	*171*	*86*	*24*	*2*	*39*	*742*

*There were 15 species common for both profiles (**Supplementary Table S1**).*

was the most abundant species, with 182 individuals in the entire section. In abundance was also *Microppia minus*, a forest generalist present in most of the section, *Opiella nova*, eurytopic, and *Punctoribates hexagonus*, living in moist habitats and which was only found in the lower half of the section.

Some of the levels in the Zaton3 section were very poor in fossils, that is, the upper part down to 75 cm, a fine clay layer at −200 cm, and a layer between 470 and 500 cm in depth. The section was dominated by eurytopes, a species with large ecological spectra, while their dominance increased drastically in its upper part. At depths of ~190 cm, 450 cm, and 520 cm, the dominance of species characteristic for open areas and of those halotolerant was visible. Forest and shrub species were mainly below −290 cm, with the highest representation at ~450 cm depth.

Zaton2 is contemporaneous with the upper part of Zaton3 (**Figure 7**). From the ecological point of view, most of the species in Zaton2 are in the lower part of the section (between 220 and 265 in depth) and are represented by xerophytic or open area species (**Figure 7**). Above −220 cm, in the upper section, very few species are characteristic for open areas. In the lower part of Zaton3 (between 300 and 450 cm in depth), eurytopic species are abundant, with species characteristics for grassland and open areas and forest and shrub species. In the middle part of the profile (between 116 and 200 cm in depth), the forest species became less abundant, with a reduction of xerophilous and dry habitat species. Eurytopic species became dominant at this depth. The upper part of the section (0–75 cm in depth) is almost depleted of mites, with only three species represented in a very low number, *Micreremus brevipes*,

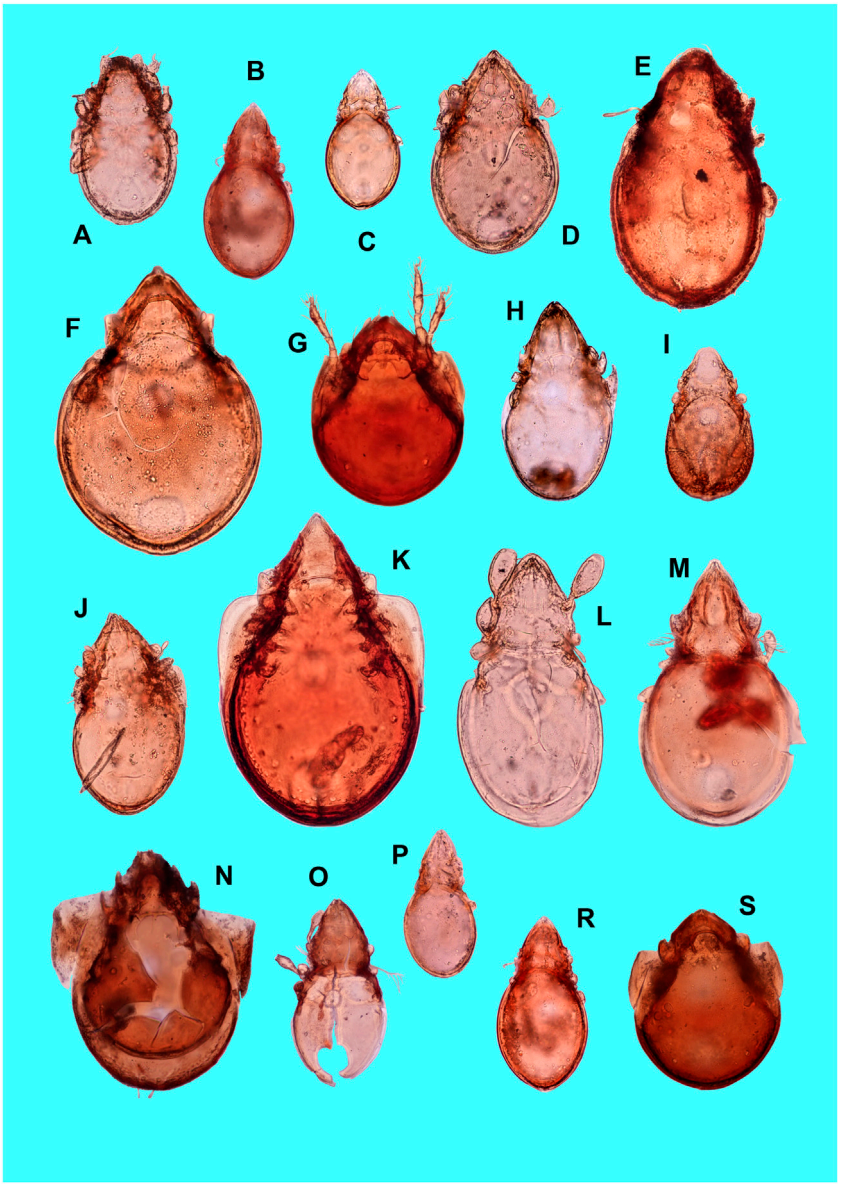

FIGURE 6 | Some of the identified oribatid fossils in Zăton Lake sediments. **(A)** *Tectocepheus velatus;* **(B)** *Oppiella nova;* **(C)** *Dissorhina ornata;* **(D)** *Zygoribatula exarata;* **(E)** *Scutovertex minutus;* **(F)** *Zygoribatula undulata;* **(G)** *Punctoribates hexagonus;* **(H)** *Protoribates monodactylus;* **(I)** *Micreremus brevipes;* **(J)** *Liebstadia pannonica;* **(K)** *Scheloribates laevigatus;* **(L)** *Eueremaeus* sp.; **(M)** *Ctenobelba* sp.; **(N)** *Peloptulus phaenotus;* **(O)** *Ramusella insculpta;* **(P)** *Confinoppia confinis;* **(R)** *Oppiella uliginosa;* **(S)** *Punctoribates punctum.*

Microppia minus (forest generalist), and *Phauloppia* sp. (soil inhabitant) species.

DISCUSSION

Sedimentary Environment Changes in the Last 2,200 Years

The facies and grain size analysis suggested a variability of the sediment characteristics from the median section, Zaton3, dominated by fine sediments of alluvial plain (facies association II) and secondary by channel fill and gravelly bars (facies association I) toward the marginal section, Zaton2, dominated by the coarse channel fill of the tributary systems alternating with the fine sediments of the alluvial plain of the main Șipot Creek (**Supplementary Figures S1, S2**). The tractive and suspension processes could also be interrupted by mass flows forming alluvial cones from the torrential tributary systems, which are reflected in the Gm facies and lack the internal structure, especially in the marginal sectors. Throughout the last 2,200 years, during which the last 4.5 m of the sedimentary filling of the Zăton basin was

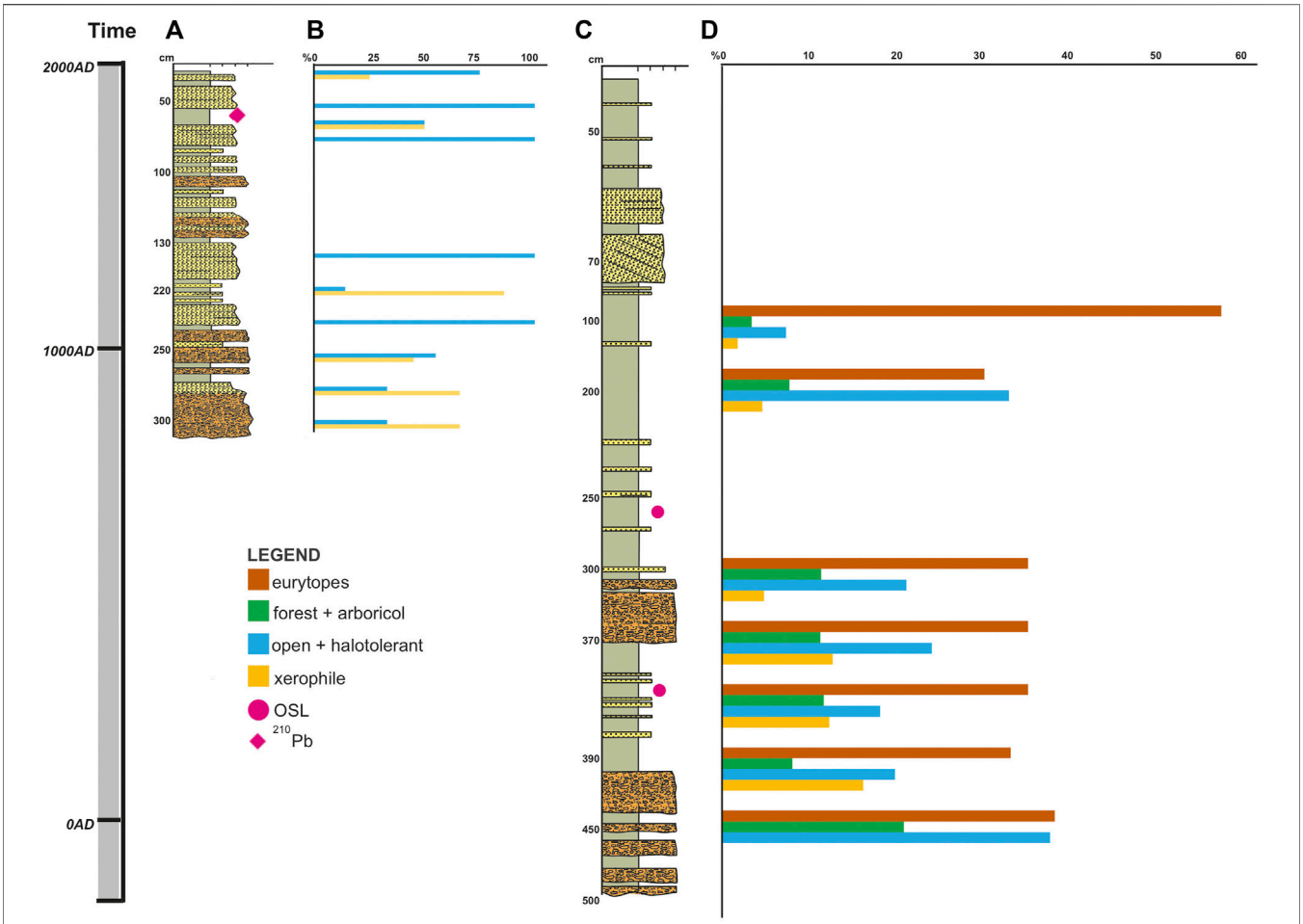

FIGURE 7 | Age and the corresponding sedimentary profiles **(A,C)** in Zăton Lake with the distribution of oribatid mites (only species with more than 10 individuals) in Zaton2 **(B)** and Zaton3 **(D)** according to their environmental requirements.

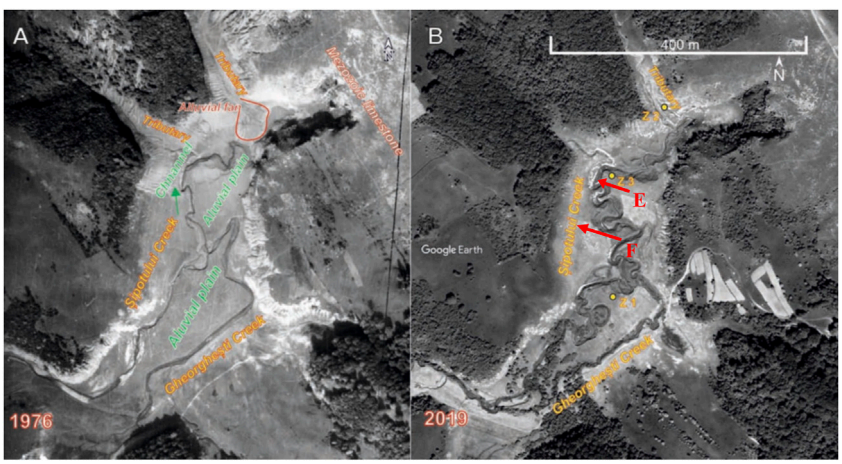

FIGURE 8 | Aerial images of the Zăton Basin taken in 1976 **(A)**; source: The Emil Racovita Institute of Speleology archive); and in 2019 **(B)**; source: Google Earth). It shows a variable morphology through time from a relatively straight fluvial style in 1976 to a meandering style in 2019. The difference in the forest cover around the lake from 1976 to 2019 should be noted, with a slight increase more recently.

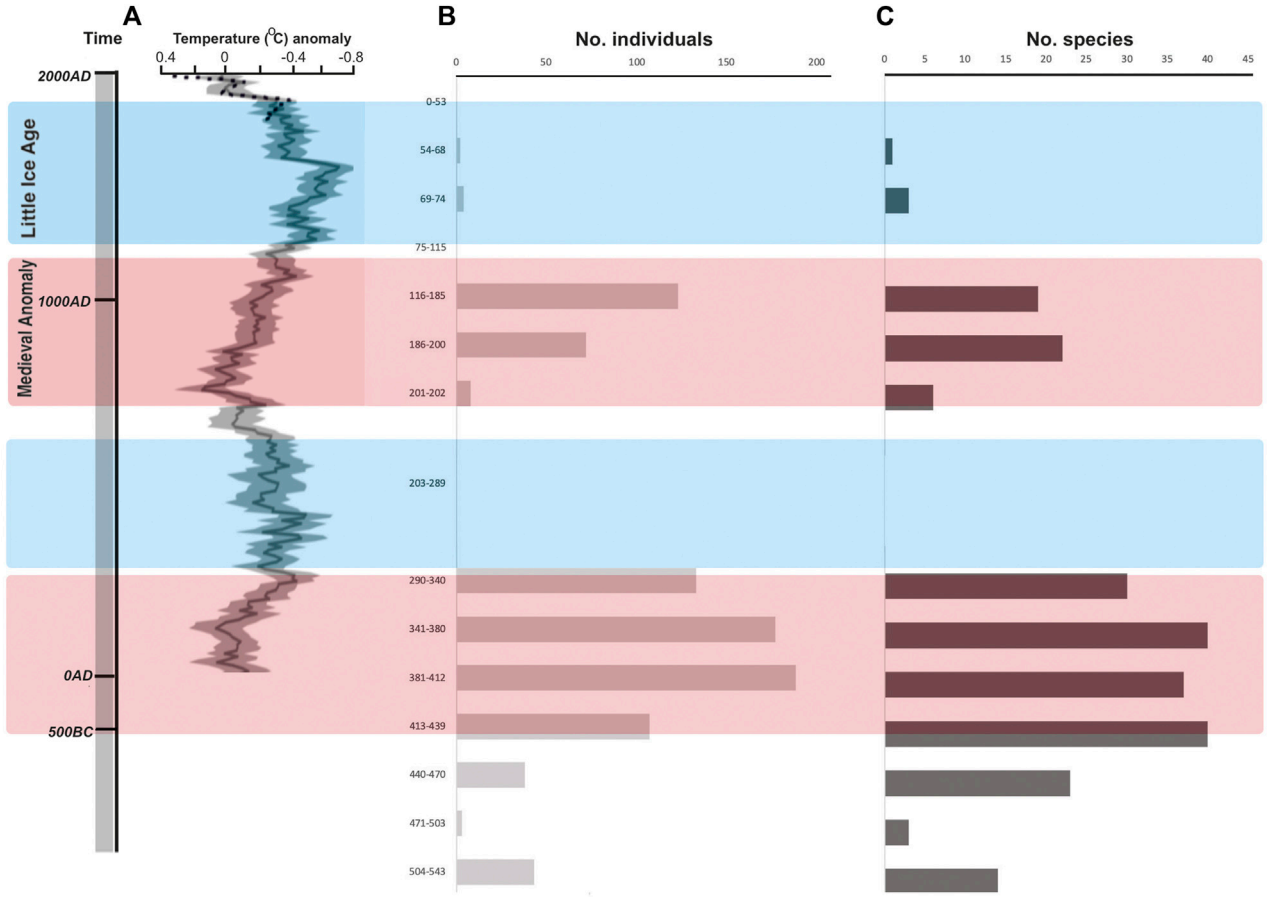

FIGURE 9 | Distribution of the oribatid mites' abundances **(B)** and diversity **(C)** in the Zaton3 profile and the corresponding temperature anomaly **(A)** from PAGES 2k Consortium, 2013). Warmer (red) and colder (blue) periods alternate along time.

TABLE 3 | Tentative correlation of historical time events and paleoenvironment during the last 2,200 years (Wikipedia, 2021) in the Zăton Lake area, as inferred from fossil oribatids and sediment data. Blue = colder periods; red = warmer periods.

Sediment age	~594B.C.- ~ 864A.D.		~ 864A.D. - ~1629A.D.		~1629A.D.-present
Depth of age interval (cm)	412-118		118-31		31-0
Periods	1	2	3	4	5
Profile depth (cm)	290-470	200-280	115-200	53-75	0-50
Climatic events in Europe (Age BC/AD)	Roman Warm Period (250BC-200AD)	Colder period (around 250AD)	Medieval Warm Period (950-1250AD)	Little Ice Age (1300-1870AD)	Modern Warm Period (1870-present)
Dominant Oribatid species ecology	Abundant and biodiverse eurytopic, open areas, forest species	No abundant or well represented species	Eurytopic species	Poor fauna	No abundant or well represented species
Environment around the lake	Humid, with temporary (seasonal) water in the lake, with swampy areas, surrounded by forests and shrubs	Open areas with some shrubs alternating with long periods of permanent water in the lake	Disturbed environment, some shrubs and trees	Some trees/shrubs and open areas	Open areas, agricultural fields, some trees and shrubs
Historical events in the area	Probably sparse and scarce human settlements	Probably sparse and scarce human settlements	Probably sparse and scarce settlements	Establishment of larger human settlements	2,425 people in the village around the lake (data from 2011)

accumulated, the periods of channel fill bars accumulation alternated with periods of sedimentation of fine facies, overbank, or lake. These changes could have been possible due to the change of sedimentation regime in this type of basin. The periods of total flooding and drying have led to the alternation of the accumulative and erosional processes. Even though the flood periods are dicyclic, the number of flood days per year must also be variable. Other control factors are the drainage system and the communication with the cave where the stream flows. The position of the siphon and the drainage capacity controlled the accumulation and erosion processes and the style of the fluvial systems. If, at present, the streams are meandering (**Figure 8B**), in 1976, the basin included two streams with a relatively linear flow (**Figure 8A**). As it appears recorded on the columns shown in **Figure 3**, this sedimentation style has certainly worked since the beginning of the filling history of the basin. All these factors of the hydrodynamic regime and sedimentation regime must have been affected by the vegetation around the lake and the Oribatida mites' communities.

Paleoenvironmental Inferences

The two analyzed sections were different in abundance and in the diversity of Oribatida. Zaton2, which covered the last ~ 600 years, was generally poor in species, and its abundances were from zero (in nine layers) to very low (with only three layers with more than five specimens). The sediment accumulation in this profile is evidence of changes in the lake surroundings, with increased soil erosion in the last six centuries. The Zaton2 profile is characterized by the cyclical alternation of layers with few species and no fauna. The layers without fauna in Zaton2 are those with higher granulometry and those resulting from the cyclic soil erosion of the adjacent slope. Zaton2 is similar in environmental information to the upper part of Zaton3.

The Zaton3 section covers more than the last 2,200 years and shows a change from a mixture of eurytopic, forest, and grassland with open areas in the lower part to dominant eurytopic species in the middle part of the profile and almost lack species in the upper, most recent part of the section. The increased abundance and diversity for oribatid mites in the Zaton3 section are associated with warmer periods in the last 2,200 years (**Figure 9**). Colder periods are scarce in species and have a very low number of individuals, except for the colder period around 250 A.D., with no species. Another exception is the Modern Warm Period (1870 A.D.—present), when no fossils could be extracted. The correspondent upper layers of Zaton2 contained a mixture of a low number of halotolerant, open space, and xerophilic species (*Punctoribates hexagonus*, *P. punctum*, and *Zygoribatula exarata*) and a new species with no known ecology (*Ramusella* cf. *sengbushi*).

The lower part of the profile has particular species often found in soils with salinization, probably due to the presence of fine sediments with high capillarity overflown by water in spring and then drying on hot summer sunny weather, much similar to the dynamic of the lake in the present. However, the species association in the lower part of Zaton3 suggested a more humid environment with more water in the system, perhaps even swampy areas. Eurytopic species dominance in the middle part of the profile indicated a change from the lower part of the section surrounded by trees to a more open landscape that is less humid, maybe with some shrublands and individual trees, but indeed not a period with larger forested areas. The almost depleted fauna layers correspond to colder periods, except for the upper part of the section (**Figure 9**). A scarcity of species in the upper, more recent part of the section resembles the colder periods more and can be explained by the alteration of the forest cover, which at present is only maintained in small areas with planted trees. For the Zaton3 profile, the thickest layer with no oribatid fossils was around 250 A.D. with a colder climate and possibly more extended periods of water accumulation in the lake, as suggested by the fine sediments, especially the mixture of clay and silt.

Thus, five periods could be identified in the evolution of the lake environments from sediment granulometry and facies, together with Oribatida mites' communities (**Table 3**). These periods can be related to the area's less or more dense human presence:

1. ~250 B.C.–~ 200 A.D. Neolithic and Bronze Age sites in the area (data from the National Archeologic Repertoire) attest to human settlements in the region even before the deposition of the studied sediments in the lake. The Roman occupation that lasted in the region between 96 B.C. and 275 A.D. has left no archeological trace. However, if human settlements were established around the lake before and during the Roman occupation, they were probably formed from small or temporary populations with less impact on the area. Oribatida species were abundant and specific for a mixture of forest and open areas in this period of warmer climate. We found a different age limit for the historically established climatic events when considering the Oribatid fauna in Zaton3. For example, the Roman Warm Period in the Zăton basin started earlier than ~250 B.C. and extended to earlier than ~250 A.D., which is in contrast to the attributed limits to this climatic period, 250 B.C.–400 A.D. (Cambell et al., 1998).
2. Around 250 A.D. A strong signal of colder weather was observed in our data, with significant deposition of sediments and almost no oribatids. Loehle (2007) also mentioned this climatic anomaly from 18 multi-proxy long series in different regions on Earth.
3. ~950 A.D.–~1250 A.D. Human settlements were probably present, but we have no archeological data on the occupation in the area. The effects of a change in the environment are already attested by almost exclusively eurytopic species, characteristic of disturbed environments with some shrubs and trees, corresponding to the Medieval Warm Period.
4. ~1300 A.D.–~1870 A.D. The cold period called the "Little Ice Age" in Europe is observed in the scarcity of oribatids in the lake sediments, with taxa characteristic for a mixture of trees, shrubs, and open areas, much more like the landscape in the present (**Figure 2**). A more significant human population in the area can be traced back to 1766 and 1792, the foundation dates of two wooden churches (now historical monuments). Local information also mentions a former wooden church

dating back to the 14th century. These are time landmarks for more organized human settlements and agricultural practices in the very proximity of Zăton Lake. Alterations of the forest cover were probably contemporaneous with the need for more land for agricultural purposes in a generally rocky and dry karstic area. The Little Ice Age also appeared differently in our study on Zaton2. It started around 1300 but ended sooner, in the 17th century, not during the 15th–19th centuries, as in other parts of Europe. However, such differences can be caused by a poor age control for the two analyzed profiles.

5. ~1870 A.D.–present. The modern period has a warmer climate, and one would expect a relatively abundant oribatid fauna as in other warm periods of the last millennia. We did not expect high diversity of taxa but at least many specimens due to a favorable climate and better chances of preservation of fossils of such young ages. On the contrary, we obtained no abundant or diversified oribatid representatives. The growing human population has, even more, impacted the already installed degradation of the initial environment around the lake in the last two centuries, with intense use of the land around the lake and in the region. More substantial anthropogenic impacts in the last 100–150 years were also documented for other northern, northeastern, and northwestern Romanian lake sediments or peat bogs (Feurdean et al., 2013, 2015; Haliuc et al., 2019, 2020).

CONCLUSION

Climate has an essential role in lakes' water availability and evolution, especially for temporary lakes such as Zăton, whose evolution depends on the precipitation amount and duration. However, vegetation, especially forests, can play an essential role in water availability, protection from desiccation, and buffering the impact of climate. For Zăton Lake, this natural cycle was interrupted by establishing human settlements around the lake, the forest cutting in the region, and the use of land for agriculture and cattle. Soil erosion is also enhanced due to reduced vegetation on the lake slopes, especially the northern, steeper slopes. The Zaton2 profile, formed in the last 600 years, might have resulted from forests cut around the lake during the Little Ice Age combined with establishing more significant human settlements in the area, beginning with the 14–18th century. Most probably, forest cuttings were more intense at the beginning of the human occupation, and disturbances continue to be strong at present with more populations in the area (2,425 in the village around the lake in 2011, with more than double the populations in the area after the WWII), whose living is partly based on agriculture.

Temporary lakes, such as Zăton Lake, can be a good model for paleoenvironmental studies, where natural and anthropic processes can drastically influence the shape, annual dynamics, and sediment deposition. Zăton Lake has become an important site for paleoenvironmental reconstruction covering the last 2,200 years, a period poorly documented for the Romanian Carpathians. As a biological proxy, Oribatida mites have proven once again to be a good indicator of past environments and indirectly assess the human presence in a relationship or decoupled from the rhythmic climate changes. Minor differences in the past climate at local levels are of utmost importance to understand regional climatic influences and can be used to model future regional impacts for the sustainable use of local natural resources.

DATA AVAILABILITY STATEMENT

The original contributions presented in the study are included in the article/**Supplementary Material**, further inquiries can be directed to the corresponding author.

AUTHOR CONTRIBUTIONS

OM and SC designed the research. OM, CP, R-DR, MK, IM, AP, and MR collected the field data. LM made the identification of oribatid mites. CP made the paleomagnetic analyses. R-DR made the sedimentologic analysis. MG and HH made the ^{210}Pb analysis. RO made the resistivity measurements. MK and IM made the maps, and OM, LM, CP, R-DR, and SC wrote the first draft. All authors corrected and approved the final version.

FUNDING

The Ministry of Research, Innovation and Digitization grant, CNCS/CCCDI – UEFISCDI, project no. 2/2019 (DARKFOOD), within PNCDI III and the EEA Financial Mechanism 2014-2021 under the project contract no. 3/2019 (KARSTHIVES 2) financially supported the different teams for the analyses and result interpretation.

ACKNOWLEDGMENTS

We are grateful to Mihai Terente, Daniel Vereș, and Marius Vlaicu for the help with sampling, Alida Gabor for the OSL dates, and Ioana Meleg for the sorting of the sediments in the laboratory; all these activities were financially supported by the KARSTHIVES Project—"Climate archives in karst". We acknowledge the reviewers for improving the clarity of the manuscript.

SUPPLEMENTARY MATERIAL

The Supplementary Material for this article can be found online at: https://www.frontiersin.org/articles/10.3389/feart.2022.856685/full#supplementary-material

REFERENCES

Appleby, P. G. (2001). "Chronostratigraphic Techniques in Recent Sediments,". *Tracking Environmental Changes Using Lake Sediments: Basin Analysis, Coring, and Chronological Techniques*. Editors W. M. Last and J. P. Smol (Dordrecht: Kluwer Academic Publishers), 1, 171–203. doi:10.1007/0-306-47669-X_9

Arnaud, F., Révillon, S., Debret, M., Revel, M., Chapron, E., Jacob, J., et al. (2012). Lake Bourget Regional Erosion Patterns Reconstruction Reveals Holocene NW European Alps Soil Evolution and Paleohydrology. *Quat. Sci. Rev.* 51, 81–92. doi:10.1016/j.quascirev.2012.07.025

Battarbee, R. W., Anderson, N. J., Bennion, H., and Simpson, G. L. (2012). Combining Limnological and Palaeolimnological Data to Disentangle the Effects of Nutrient Pollution and Climate Change on lake Ecosystems: Problems and Potential. *Freshw. Biol.* 57, 2091–2106. doi:10.1111/j.1365-2427.2012.02860.x

Behan-Pelletier, V. M. (1999). Oribatid Mite Biodiversity in Agroecosystems: Role for Bioindication. *Agric. Ecosyst. Environ.* 74, 411–423. doi:10.1016/s0167-8809(99)00046-8

Behan-Pelletier, V., and Newton, G. (1999). Linking Soil Biodiversity and Ecosystem Function: The Taxonomic Dilemma. *BioScience* 49 (2), 149–153. doi:10.2307/1313540

Bennion, H., Battarbee, R. W., Sayer, C. D., Simpson, G. L., and Davidson, T. A. (2010). Defining Reference Conditions and Restoration Targets for lake Ecosystems Using Palaeolimnology: a Synthesis. *J. Paleolimnol* 45, 533–544. doi:10.1007/s10933-010-9419-3

Bennion, H., Carvalho, L., Sayer, C. D., Simpson, G. L., and Wischnewski, J. (2012). Identifying from Recent Sediment Records the Effects of Nutrients and Climate on Diatom Dynamics in Loch Leven. *Freshw. Biol.* 57, 2015–2029. doi:10.1111/j.1365-2427.2011.02651.x

Borrelli, P., Robinson, D. A., Fleischer, L. R., Lugato, E., Ballabio, C., Alewell, C., et al. (2017). An Assessment of the Global Impact of 21st century Land Use Change on Soil Erosion. *Nat. Commun.* 8, 2013. doi:10.1038/s41467-017-02142-7

Bortolotti, L. E., St. Louis, V. L. V. L., Vinebrooke, R. D., and Wolfe, A. P. (2016). Net Ecosystem Production and Carbon Greenhouse Gas Fluxes in Three Prairie Wetlands. *Ecosystems* 19, 411–425. doi:10.1007/s10021-015-9942-1

Cambell, I. D., Campbell, C., Apps, M. J., Rutter, N. W., and Bush, A. B. G. (1998). Late Holocene Similar to 1500 Yr Climatic Periodicities and Their Implications. *Geology* 26, 471–473.

Catalán, Núria, N., von Schiller, Daniel, D., Marcé, Rafael, R., Koschorreck, Matthias, M., Gomez-Gener, Lluís, L., and Obrador, Biel, B. (2014). Carbon Dioxide Efflux during the Flooding Phase of Temporary Ponds. *Limnetica* 33, 349–360. doi:10.23818/limn.33.27

Chadima, M., and Hrouda, F. (2006). Remasoft 3.0 - a User-Friendly Paleomagnetic Data Browser and Analyzer. *Travaux Géophysiques* XXVII, 20–21.

Cleveland, W. S., and Devlin, S. J. (1988). Locally Weighted Regression: An Approach to Regression Analysis by Local Fitting. *J. Am. Stat. Assoc.* 83, 596–610. doi:10.1080/01621459.1988.10478639

Coetzee, L., and Brink, J. S. (2003). Fossil Oribatid Mites (Acari, Oribatida) from the Florisbad Quaternary Deposits, South Africa. *Quat. Res.* 59, 246–254. doi:10.1016/s0033-5894(02)00024-8

Daily, W., and Lytle, J. (1983). Geophysical Tomography. *J. Geomagn. Geoelec* 35, 423–442. doi:10.5636/jgg.35.423

Dubois, N., Saulnier-Talbot, É., Mills, K., Gell, P., Battarbee, R., Bennion, H., et al. (2018). First Human Impacts and Responses of Aquatic Systems: A Review of Palaeolimnological Records from Around the World. *Anthropocene Rev.* 5 (1), 28–68. doi:10.1177/2053019617740365

Elias, S. A. (1994). *Quaternary Insects and Their Environments*. Washington D. C.: Smithsonian Institution Press, 284.

Erdmann, G., Otte, V., Langel, R., Scheu, S., and Maraun, M. (2007). The Trophic Structure of Bark-Living Oribatid Mite Communities Analysed with Stable Isotopes (15N, 13C) Indicates strong Niche Differentiation. *Exp. Appl. Acarol* 41, 1–10. doi:10.1007/s10493-007-9060-7

Erickson, J. M. (1988). "Fossil Oribatid Mites as Tools for Quaternary Paleoecologists: Preservation Quality, Quantities, and Taphonomy," in *Late Pleistocene and Early Holocene Paleoecology and Archaeology of the Eastern Great Lakes Region*. Editors R. S. Laub, N. G. Miller, and D. W. Steadman (New York: Bulletin of the Buffalo Society of Natural Sciences), 33, 207–226.

Erickson, J. M., Platt, R. B., Jr., and Jennings, D. H. (2003). Holocene Fossil Oribatid Mite Biofacies as Proxies of Palaeohabitat at the Hiscock Site, Byron, New York. *Bull. Buffalo Soc. Nat. Sci.* 37, 176–189.

Erickson, J. M., and Platt, R. B. (2007). "Oribatid Mites," in *Encyclopedia of Quaternary Science*. Editor S. A. Elias (Oxford: Elsevier), 1547–1566. doi:10.1016/b0-44-452747-8/00290-8

Feurdean, A., Galka, M., Kuske, E., Tantau, I., Lamentowicz, M., Florescu, G., et al. (2015). Last Millennium Hydro-Climate Variability in Central-Eastern Europe (Northern Carpathians, Romania). *The Holocene* 25, 1179–1192. doi:10.1177/0959683615580197

Feurdean, A., Liakka, J., Vannière, B., Marinova, E., Hutchinson, S. M., Mosburgger, V., et al. (2013). 12,000-Years of Fire Regime Drivers in the Lowlands of Transylvania (Central-Eastern Europe): a Data-Model Approach. *Quat. Sci. Rev.* 81, 48–61. doi:10.1016/j.quascirev.2013.09.014

Fick, S. E., and Hijmans, R. J. (2017). WorldClim 2: New 1-km Spatial Resolution Climate Surfaces for Global Land Areas. *Int. J. Climatol* 37, 4302–4315. doi:10.1002/joc.5086

Fountain, M. T., and Hopkin, S. P. (2001). Continuous Monitoring of *Folsomia candida* (Insecta: Collembola) in a Metal Exposure Test. *Ecotoxicology Environ. Saf.* 48, 275–286. doi:10.1006/eesa.2000.2007

Goran, C. (1978). Le Karst du plateau du Mehedinți. I. Partie nord. *Travaux de L'institut de Spéologie "E. Racovitza"* XVII, 165–183.

Haliuc, A., Buczkó, K., Hutchinson, S. M., Ács, É., Magyari, E. K., Korponai, J., et al. (2020). Climate and Land-Use as the Main Drivers of Recent Environmental Change in a Mid-altitude mountain lake, Romanian Carpathians. *PLoS ONE* 15 (10), e0239209. doi:10.1371/journal.pone.0239209

Haliuc, A., Feurdean, A., Mîndrescu, M., FrantiucHutchinson, A. S. M., and Hutchinson, S. M. (2019). Impacts of forest Loss in the Eastern Carpathian Mountains: Linking Remote Sensing and Sediment Changes in a Mid-altitude Catchment (Red Lake, Romania). *Reg. Environ. Change* 19, 461–475. doi:10.1007/s10113-018-1416-5

Henig-Sever, N., Poliakov, D., and Broza, M. (2001). A Novel Method for Estimation of Wild Fire Intensity Based on Ash Ph and Soil Microarthropod Community. *Pedobiologia* 45, 98–106. doi:10.1078/0031-4056-00072

Jenny, J.-P., Koirala, S., Gregory-Eaves, I., Francus, P., Niemann, C., Ahrens, B., et al. (2019). Human and Climate Global-Scale Imprint on Sediment Transfer during the Holocene. *Proc. Natl. Acad. Sci. U.S.A.* 116, 22972–22976. doi:10.1073/pnas.1908179116

Jeppesen, E., Meerhoff, M., Davidson, T. A., Trolle, D., Sondergaard, M., Lauridsen, T. L., et al. (2014). Climate Change Impacts on Lakes: an Integrated Ecological Perspective Based on a Multi-Faceted Approach, with Special Focus on Shallow Lakes. *J. Limnology* 73, 84–107. doi:10.4081/jlimnol.2014.844

Kirschvink, J. L. (1980). The Least-Squares Line and Plane and the Analysis of Palaeomagnetic Data. *Geophys. J. Int.* 62, 699–718. doi:10.1111/j.1365-246x.1980.tb02601.x

Kostic, B., and Aigner, T. (2007). Sedimentary Architecture and 3D Ground-Penetrating Radar Analysis of Gravelly Meandering River Deposits (Neckar Valley, SW Germany). *Sedimentology* 54, 789–808. doi:10.1111/j.1365-3091.2007.00860.x

Kovacheva, M., Kostadinova-Avramova, M., Jordanova, N., Lanos, P., and Boyadzhiev, Y. (2014). Extended and Revised Archaeomagnetic Database and Secular Variation Curves from Bulgaria for the Last Eight Millennia. *Phys. Earth Planet. Interiors* 236, 79–94. doi:10.1016/j.pepi.2014.07.002

Krivolutsky, D. A., and Druk, A. Y. (1986). Fossil Oribatid Mites. *Annu. Rev. Entomol.* 31, 533–545. doi:10.1146/annurev.en.31.010186.002533

Krivolutsky, D. A., and Sidorchuk, E. A. (2003). Subfossil Oribatid Mites in the Holocene Deposits of the Arkhangel'sk Region. *Doklady Akademii Nauk* 392, 421–425.

Li, Y.-X., and Kodama, K. P. (2016). Detecting and Correcting for Paleomagnetic Inclination Shallowing of Sedimentary Rocks: A Review. *Front. Earth Sci.* 4, 7. doi:10.3389/feart.2016.00007

Lindo, Z., and Visser, S. (2004). Forest Floor Microarthropod Abundance and Oribatid Mite (Acari: Oribatida) Composition Following Partial and clear-cut Harvesting in the Mixed wood Boreal forest. *Can. J. For. Research-Revue Canadienne de Recherche Forestiere* 34, 998–1006. doi:10.1139/x03-284

Loehle, C. (2007). A 2000-Year Global Temperature Reconstruction Based on Non-treering Proxies. *Energ. Environ.* 18, 1049–1058. doi:10.1260/095830507782616797

Loke, M. H., and Barker, R. D. (1995). Least-squares Deconvolution of Apparent Resistivity Pseudosections. *Geophysics* 60, 1682–1690. doi:10.1190/1.1443900

Loke, M. H., and Dahlin, T. (2002). A Comparison of the Gauss-Newton and Quasi-Newton Methods in Resistivity Imaging Inversion. *J. Appl. Geophys.* 49, 149–162. doi:10.1016/s0926-9851(01)00106-9

Longman, J., Veres, D., Finsinger, W., and Ersek, V. (2018). Exceptionally High Levels of lead Pollution in the Balkans from the Early Bronze Age to the Industrial Revolution. *Proc. Natl. Acad. Sci. U S A.* 115, E5661–E5668. doi:10.1073/pnas.1721546115

Longman, J., Ersek, V., Veres, D., and Salzmann, U. (2017). Detrital Events and Hydroclimate Variability in the Romanian Carpathians during the Mid-to-late Holocene. *Quat. Sci. Rev.* 167, 78–95. doi:10.1016/j.quascirev.2017.04.029

Miall, A. D. (1985). Architectural-element Analysis: A New Method of Facies Analysis Applied to Fluvial Deposits. *Earth-Science Rev.* 22, 261–308. doi:10.1016/0012-8252(85)90001-7

Miall, A. D. (1996). *The Geology of Fluvial Deposits: Sedimentary Facies, Basin Analysis and Petroleum Geology*. New York: Springer-Verlag, 582.

Micu, D. M., Dumitrescu, A., Cheval, S., and Birsan, M.-V. (2015). *Climate of the Romanian Carpathians*. Springer-Verlag.

Migliorini, M. (2009). "Oribatid Mite (Arachnida: Oribatida) Coenoses from SW Sardinia,". *Research on the Terrestrial Arthropods of Sardinia*. Editors P. Cerretti, F. Mason, A. Minelli, G. Nardi, and D. Whitmore (Italy: Zootaxa), 2318, 8–37. doi:10.11646/zootaxa.2318.1.4

Migliorini, M., Pigino, G., Caruso, T., Fanciulli, P. P., Leonzio, C., and Bernini, F. (2005). Soil Communities (Acari Oribatida; Hexapoda Collembola) in a clay pigeon Shooting Range. *Pedobiologia* 49, 1–13. doi:10.1016/j.pedobi.2004.06.009

Miko, L. (2016). Oribatid Mites (Acarina: Oribatida) of the Czech Republic. Revised Check–List with a Proposal for Czech Oribatid Nomenclature. *Klapalekiana* 52 (Suppl. l), 1–302.

Moldovan, O. T., Constantin, S., Panaiotu, C., Roban, R. D., Frenzel, P., and Miko, L. (2016). Fossil Invertebrates Records in Cave Sediments and Paleoenvironmental Assessments - a Study of Four Cave Sites from Romanian Carpathians. *Biogeosciences* 13, 483–497. doi:10.5194/bg-13-483-2016

Moldovan, O. T., Mihevc, A., Miko, L., Constantin, S., Meleg, I. N., Petculescu, A., et al. (2011). Invertebrate Fossils from Cave Sediments: a New Proxy for Pre-quaternary Paleoenvironments. *Biogeosciences* 8, 1825–1837. doi:10.5194/bg-8-1825-2011

Montgomery, D. R. (2007). Soil Erosion and Agricultural Sustainability. *Proc. Natl. Acad. Sci. U.S.A.* 104, 13268–13272. doi:10.1073/pnas.0611508104

Morris, E. P., Flecha, S., Figuerola, J., Costas, E., Navarro, G., Ruiz, J., et al. (2013). Contribution of Doñana Wetlands to Carbon Sequestration. *PLoS ONE* 8, e71456. doi:10.1371/journal.pone.0071456

Murray, A. S., and Wintle, A. G. (2003). The Single Aliquot Regenerative Dose Protocol: Potential for Improvements in Reliability. *Radiat. Measurements* 37, 377–381. doi:10.1016/s1350-4487(03)00053-2

PAGES 2k Consortium (2013). Continental-scale Temperature Variability during the Past Two Millennia. *Nat. Geosci.* 6, 339–346. doi:10.1038/ngeo1797

Peters, M., Friedmann, A., Stojakowits, P., and Metzner-Nebelsick, C. (2020). Holocene Vegetation History and Environmental Change in the Lăpuş Mountains, north-west Romania. *Palynology* 44, 441–452. doi:10.1080/01916122.2019.1615567

Renberg, I. (1990). A 12,600 Year Perspective of the Acidification of Lilla Oresjon, Southwest Sweden. *Philosophical Trans. R. Soc. B* 327, 357–361.

Roberts, N., Fyfe, R. M., Woodbridge, J., Gaillard, M.-J., Davis, B. A. S., Kaplan, J. O., et al. (2018). Europe's Lost Forests: a Pollen-Based Synthesis for the Last 11,000 Years. *Sci. Rep.* 8, 716. doi:10.1038/s41598-017-18646-7

Roberts, N., Moreno, A., Valero-Garcés, B. L., Corella, J. P., Jones, M., Allcock, S., et al. (2012). Palaeolimnological Evidence for an East-West Climate See-Saw in the Mediterranean since AD 900. *Glob. Planet. Change* 84-85, 23–34. doi:10.1016/j.gloplacha.2011.11.002

Rose, N. L., Morley, D., Appleby, P. G., Battarbee, R. W., Alliksaar, T., Guilizzoni, P., et al. (2011). Sediment Accumulation Rates in European Lakes since AD 1850: Trends, Reference Conditions and Exceedence. *J. Paleolimnol* 45, 447–468. doi:10.1007/s10933-010-9424-6

Schatz, H. (1983). *U.-Ordn.: Oribatei, Hornmilben. Catalogus Faunae Austriae, Teil IXi.* Wien: Verlag der Österreichischen Akademie der Wissenschafter, 118.

Silvester, P. P., and Ferrari, R. L. (1990). *Finite Elements for Electrical Engineers*. 2nd. ed. Cambridge University Press.

Solhøy, I. W., and Solhøy, T. (2000). The Fossil Oribatid Mite Fauna (Acari: Oribatida) in Late-Glacial and Early-Holocene Sediments in Kråkenes Lake, Western Norway. *J. Paleolimnology* 23, 35–47.

Solhøy, T. (2001). "Oribatid Mites," in *Tracking Environmental Change Using lake Sediments. 4: Zoological Indicators*. Editors J. P. Smol, H. J. B. Birks, and W. M. Last (Dordrecht: Kluwer Academic Publishers), 81–104.

Van Straalen, N. M. (1998). Evaluation of Bioindicator Systems Derived from Soil Arthropod Communities. *Appl. Soil Ecol.* 9, 429–437. doi:10.1016/s0929-1393(98)00101-2

Vincze, I., Orbán, I., Birks, H. H., Pál, I., Finsinger, W., Hubay, K., et al. (2017). Holocene Treeline and Timberline Changes in the South Carpathians (Romania): Climatic and Anthropogenic Drivers on the Southern Slopes of the Retezat Mountains. *The Holocene* 27, 1613–1630. doi:10.1177/0959683617702227

R. G. Walker and N. P. James (Editors) (1992). *Facies Models Response to Sea Level Change*. St. John's, Canada: Geological Association of Canada, 119–142.

Wang, Z., Hoffmann, T., Six, J., Kaplan, J. O., Govers, G., Doetterl, S., et al. (2017). Human-induced Erosion Has Offset One-Third of Carbon Emissions from Land Cover Change. *Nat. Clim Change* 7, 345–349. doi:10.1038/nclimate3263

Weigmann, G. (2006). "Hornmilben (Oribatida)," in *Die Tierwelt Deutschlands*. Editor F. Dahl (Keltern: Goecke and Evers), 76, 1–520.

Weigmann, G., and Kratz, W. (1982). Die deutschen Hornmilbenarten und ihre ökologische Charakteristik. *Zool. Beitr.* 27, 259–489.

Wikipedia (2021). Wikipedia.com. Avilableat: https://en.wikipedia.org/wiki/List_of_periods_and_events_in_climate_history (Accessed on October2021 4.

Williamson, C. E., Dodds, W., Kratz, T. K., and Palmer, M. A. (2008). Lakes and Streams as Sentinels of Environmental Change in Terrestrial and Atmospheric Processes. *Front. Ecol. Environ.* 6, 247–254. doi:10.1890/070140

Wintle, A. G., and Murray, A. S. (2006). A Review of Quartz Optically Stimulated Luminescence Characteristics and Their Relevance in Single-Aliquot Regeneration Dating Protocols. *Radiat. Measurements* 41, 369–391. doi:10.1016/j.radmeas.2005.11.001

Wozniak, T., Bania, G., Moscicki, W., J., and Cwiklik, M. (2018). Electrical Resistivity Tomography (ERT) and Sedimentological Analysis Applies to Investigation of Upper Jurassic Limestones from the Krzeszowice Graben (Krakow Upland, Southern Poland). *Geol. Quaterly* 62, 287–302.

Yogeshwar, P., Hamacher, S., Reçi, H., Hauck, T., Onuzi, K., and Tezkan, B. (2019). Investigating Sedimentological Architecture Using Electrical Resistivity Tomography: A Case Study from the Archaeological Open-Air Site Shën Mitri, Southern Albania. *Pure Appl. Geophys.* 176, 843–856. doi:10.1007/s00024-018-1987-6

Zijderveld, J. D. A. (1967). "A.C. Demagnetization of Rocks: Analysis of Results," in *Methods of Palaeomagnetism*. Editors D. W. Collinson, K. M. Creer, and S. K. Runcorn (Amsterdam: Elsevier), 254–286.

Conflict of Interest: The authors declare that the research was conducted in the absence of any commercial or financial relationships that could be construed as a potential conflict of interest.

frontiers | Frontiers in Earth Science

ORIGINAL RESEARCH
published: 03 May 2022
doi: 10.3389/feart.2022.885586

Influence of Slope Amplification on the Pile Dynamic Behavior Based on the Data Mining Method

Yu Wang, Tong Zheng, Rui Sun, Wenhao Qi and Wanwan Qi*

Key Laboratory of Earthquake Engineering and Engineering Vibration, Institute of Engineering Mechanics, China Earthquake Administration, Key Laboratory of Earthquake Disaster Mitigation, Ministry of Emergency Management, Harbin, China

In this article, a centrifuge shaking table model test of anchored stabilizing piles for strengthening landslides was established, and the dynamic response characteristics of the pile–anchor–slope under earthquake action were analyzed. On this basis, combined with the fuzzy gray relational analysis and the rank-sum ratio method, the correlation between the amplification of the acceleration response of the heterogenous slope and the dynamic response of the support structure was explored. Based on the obtained results, relevant suggestions for engineering design were proposed. The results showed that the seismic amplification of the complex soil–rock slope reinforced by the pile–anchor structure was not uniform and the amplification coefficient had strong variability. Among them, the amplification coefficient of the slope, dynamic earth pressure, and dynamic bending moment of the pile near the connection of the pile–anchor cable continued to increase; the correlation between the seismic amplification and the seismic behavior of the pile–anchor structure is different at different positions of the slope. The measurement points with a higher comprehensive ranking of correlation are mainly concentrated in the pile–anchor connection, the middle of the slope, and the high-angle soil–rock interface. It is related to the geometric characteristics of the model and the high seismic amplification of the slope; for the pile–anchor connection part and the high-angle soil–rock structure surface of the slope, the shock absorption measures and grouting strength of the anchor cable's anchoring section should be considered in the engineering design.

Keywords: centrifuge shaking table test, anchored stabilizing pile, fuzzy gray relational grade, rank sum ratio method, data mining

OPEN ACCESS

Edited by:
Chong Xu,
Ministry of Emergency Management, China

Reviewed by:
Rajeswari J. S,
National Institute of Technology, Andhra Pradesh, India
Yazdan Shams Maleki,
Kermanshah University of Technology, Iran
Pengpeng Ni,
Sun Yat-sen University, China

****Correspondence:***
Tong Zheng
zhengt0928@163.com

Specialty section:
This article was submitted to Geohazards and Georisks, a section of the journal Frontiers in Earth Science

Received: *28 February 2022*
Accepted: *04 April 2022*
Published: *03 May 2022*

Citation:
Wang Y, Zheng T, Sun R, Qi W and Qi W (2022) Influence of Slope Amplification on the Pile Dynamic Behavior Based on the Data Mining Method. Front. Earth Sci. 10:885586. doi: 10.3389/feart.2022.885586

1 INTRODUCTION

Strong earthquake action and complex geological conditions inevitably lead to a large number of earthquake landslides. Landslides induced by large earthquakes have a strong disaster-causing capacity. In the early 21st century alone, tens of thousands of people have been killed and billions of dollars have been lost (Huang and Li, 2009; Halder et al., 2021; and Hu H. Q et al., 2021). Therefore, utilizing reinforcement technologies to improve the stability of slopes in seismically active areas has become one of the popular research topics in the field of geological disaster prevention (Liu et al., 2021; Chen et al., 2022).

As a new reinforcement technology, anchored stabilizing piles can effectively improve slope stability and thus have been applied to treat large or super large landslides in many

countries (Wang, 1998; Zhao, et al., 2017). The Wenchuan earthquake damage investigation found that the slope reinforced with pre-stressed anchored stabilizing piles was not damaged when the fortification intensity of the structure was exceeded and has good seismic resistance (Zhou et al., 2010). So far, the quasi-static method has been adopted in the seismic design of anchored stabilizing piles, which lacks a recognized and reasonable method system and ignores the influence of the seismic dynamic effect. Due to the complex stress system of the structure, the action mechanism of the anchor cable and the dynamic interaction of pile–anchor–soil mass are still unclear. The seismic response law of the anchored stabilizing pile is to reveal the seismic mechanism and failure mode of the anchored stabilizing pile, the dynamic interaction law of the pile–anchor–slope mass, and establish a scientific foundation for the seismic design method. Therefore, the research on the dynamic response of anchored stabilizing piles has an important theoretical value.

Field measurement and physical model tests are the most reliable methods to study the mechanical properties of anchored stabilizing piles. Recently, a series of 1-g large-scale shaking table tests have been conducted to analyze the mechanical characteristics of anchored stabilizing piles and slope deformation (Ma et al., 2019; Hu M. M et al., 2021). However, these tests can only qualitatively reveal the seismic response law of the anchor–pile structures because the 1-g shaking table test cannot simulate the actual stress–strain relationship in the field (Garala and Madabhushi, 2019). Especially in tests related to slope stability, the influence of the slope self-weight is significant. Meanwhile, the nonlinear change in the *in situ* modulus and the modulus with a strain in the soil has a strong impact on soil–structure interaction (Finn et al., 1986). This can also affect the deformation and displacement of the slope, thus making the dynamic behavior of retaining structures unreliable. In contrast, the centrifuge test can simulate real gravity through the centrifuge force formed by high-speed rotation. Therefore, this technology can effectively reflect the stress field of the prototype and has been widely applied to many fields (Zelikson et al., 1983; Ghosh and Madabhushi, 2007). Unfortunately, only a few studies have used this technology to analyze the seismic performance of anchored stabilizing piles. Zheng et al. (2016) conducted a centrifuge shaking table test to discuss the seismic response characteristics of a slope reinforced by anchored stabilizing piles and determined the distribution of soil pressure and the bending moment of the pile and its variation laws with different input ground motions. Huang et al. (2020) used a silica gel model instead of soil to examine the seismic stress characteristics and ultimate failure mode of the pile–anchor structures when the slope continued to slide along the circular arc sliding surface. In addition, the theoretical calculation model is also one of the reference methods to explore the pile–soil interaction. Ni et al. (2017) proposed the deflection model of the pile under transverse load and deduced the distribution mode of surrounding soil displacement and earth pressure.

The existing tests based on a 1-g shaking table or the centrifuge shaking table mainly focused on the seismic capacity of the retaining structure but ignored the influence of the slope response on the structures. Recent studies have demonstrated that the propagation of a ground motion in nonuniform slopes is very complex and can significantly affect the mechanical behavior of structures (Veletsos and Younan, 1997; Gazetas et al., 2004; Psarropoulos et al., 2005). This may cause the actual response of the project to not meet the expectations and has been confirmed in many earthquake investigations (Zhang et al., 2012; Liu et al., 2016). Therefore, it is necessary to study the correlation between the seismic response of the slope and the seismic behavior of the anchored stabilizing piles.

The methods of analyzing data relevance generally include mathematical statistics, machine learning, and gray relational analysis. However, there are some problems in mathematical statistics, such as regression analysis, analysis of variance, and principal component analysis. This method does not apply to the dynamic response model test results with a complex and no obvious probability distribution form. With the development of computers, machine learning has been gradually introduced into the field of geotechnical engineering and has played an important role in many directions (Ni et al., 2018; Ni and Mangalathu, 2018; Ni et al., 2020). However, due to limited data of the centrifugal shaking table test of anchored stabilizing piles, this method has not been applied. Fortunately, gray relational analysis solves this problem well. This method is also applicable to the number of samples and whether the samples are regular (Deng, 2002).

In this study, centrifuge shaking table tests of reinforcing an accumulation landslide with anchored stabilizing piles are conducted. Based on the test results, the correlation between the slope seismic response and pile mechanical parameters was discussed using fuzzy gray relational analysis (*FGRA*). In addition, combined with the rank-sum ratio (*RSR*) method, the influence classification of the amplification effect of different slope positions was further divided to give targeted suggestions for engineering design and reinforcement. The results may provide a reference for the optimal design of anchored stabilizing piles.

2 CENTRIFUGE SHAKING TABLE TEST

The test model adopted the large-scale geotechnical centrifuge physical simulation system of Zhejiang University, including the ZJU400 geotechnical centrifuge, electro-hydraulic servo shaking table, and rigid wall model box. The reliability of this test system has been verified many times (Sun et al., 2020; Yan et al., 2020). The relevant design parameters of the ZJU400 centrifuge and its shaking table are referred to in some previous studies (Zheng et al., 2016).

It is worth noting that because the model box belongs to finite boundary conditions during dynamic tests such as the seismic loading test, the input ground motion will be reflected when it propagates to the boundary of the model box, resulting in data distortion. Some scholars have developed a layered shear model box which effectively eliminates the reflection of the ground motion boundary under its small shear resistance, but this model box has little effect on the model with large stiffness. Therefore, after comprehensively considering the test model and

TABLE 1 | Similarity scale of the test model.

Parameter	Physical quantity	Symbol	Similarity scale (model/prototype)
Geometric dimension	Length	L	1/50
	Area	A	$1/50^2$
	Volume	V	$1/50^3$
	Displacement	u	1/50
Mechanical property	Axial force	F	$1/50^2$
	Bending moment	M	$1/50^3$
	Stress	σ	1
	Strain	ε	1
Dynamic characteristic	Time (dynamic)	t	1/50
	Peak acceleration	A_{max}	50
	Speed	v	50
	Frequency	f	50

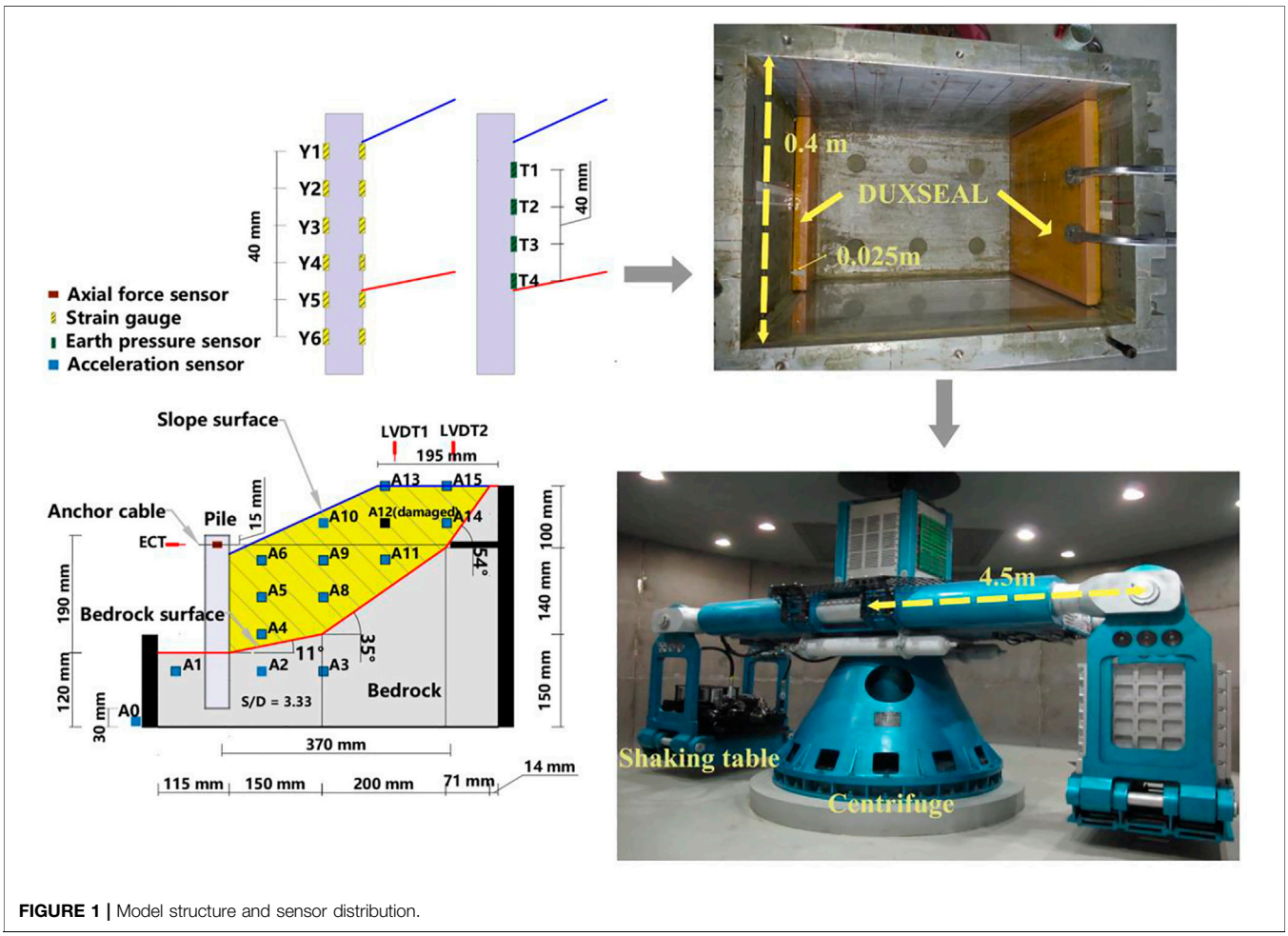

FIGURE 1 | Model structure and sensor distribution.

test equipment in this study, we decided to adopt the fixed-wall rigid model box bearing model. In addition, to avoid the influence of possible boundary effects brought by the rigid model box on the test results, we used DUXSEAL to absorb the ground motion transmitted to the boundary. This method draws on previous related studies (Heron et al., 2015; Cilinger and Madabhushi, 2011). In this research, the absorbing material with a thickness of 25 mm was used. In addition, vaseline was applied on the left and right sides of the model box in the vertical loading direction to reduce the friction between the geotechnical model and the box.

Although the research purpose of this study is not to evaluate the seismic capacity of specific projects, the establishment of the test model has been referred to the anchored stabilizing pile reinforcement project found by Liu et al. (2016) so that the research results can be used as a reference in the design of other similar projects. The centrifuge acceleration of the test was set to

TABLE 2 | Model material parameters.

Position		Model	Prototype
Stabilizing pile	Cantilever length (m)	0.19	9.5
	Embedded length (m)	0.09	4.5
	Bending stiffness (GPa*m^4)	30.44	30
	Material	Rectangular section aluminum alloy pipe (Section 30 × 40 mm)	Reinforced concrete (Section 1.5 × 2 m)
Anchor cable	Prestress (kN)	0.049	122.5
Slide mass	Density (g/cm^3)	1.829	1.829
	Moisture content (%)	18	18
	Internal friction angle (°)	16.14	16.14
	Cohesion (kPa)	58.70	58.70
	Material	Remolded soil	Silty clay
Bedrock	Internal friction angle (°)	40.5	—
	Cohesion (kPa)	257	—
	Material	Cement soil	Mudstone

50 g, and the scaling laws are given in **Table 1**. The selection of the centrifugal similarity scale is referred to in previous related studies (Yan et al., 2020). The geometric dimensions and sensor positions of the test model are shown in **Figure 1**. A variety of sensors were used to obtain the test records of different parameters, including earth pressure sensors (0–1 MPa, 1 %FS), bending moment strain gages (2000 microstrain, 0.1%), axial force sensors (Zheng et al., 2016), micro acceleration sensors (0–50 g, ≤5%), and displacement sensors (±20 mm, 0.03%FS). All types of sensors were calibrated before the test and connected with the automatic acquisition equipment of the centrifuge during the test.

The sliding mass and bedrock were simulated by the remolded prototype slope Xigeda soil and cement soil (silty clay: cement: quartz sand: water = 1: 0.55: 1: 0.25). To obtain the total shear strength parameters (cohesion c and internal friction angle φ) of the simulated material, the failure strength of specimens under different confining pressures was obtained by the unconsolidated undrained triaxial test; then, the Mohr circle and shear strength envelop of the sample were drawn according to the Mohr–Coulomb criterion, and the relevant parameters were obtained. The shear strength parameters of the sliding surface were obtained through the quick shear test in which the cohesion and internal friction angle of the soil rock contact surface is 3.58 kPa and 14.7,° respectively. Other parameters are shown in **Table 2**. It is worth noting that in this test, the bedrock only plays the role of support, so it does not involve problems similar to the prototype. The selection of material strength is referred to in some previous studies (Zheng et al., 2016).

The model pile and anchor cable are simulated by five hollow aluminum alloy pipes with a wall thickness of 2.5 mm and a steel strand with a diameter of 1 mm. The ratio of pile spacing to pile width is S/D = 3.33. The dimensions of the reinforced structure, such as length of the pile, length of the anchor cable, and anchorage position, are shown in **Figure 1**.

Model preparation was conducted in a rigid model box. First, the slope contour was drawn inside the model box, the pile position was designed in advance, and the model pile was fixed. The slope was formed through dynamic compaction and slope cutting. In the process, the model pile was constantly examined to see if it deviated from the predesigned pile position. In the bedrock forming process, the anchor cable was embedded. When the model was accomplished, the box was installed on the shaking table.

TABLE 3 | Ground motion loading scheme.

Loading stage	Input ground motion intensity/g	Loading type
EQ1	0.1	Continuous loading
EQ2	0.2	Continuous loading
EQ3	0.3	Continuous loading
EQ4	0.3	Cumulative loading
EQ5	0.4	Continuous loading
EQ6	0.4	Cumulative loading
EQ7	0.4	Cumulative loading

The input ground motion adopted the Qingxi bedrock wave of the Wenchuan earthquake provided by Liu et al. (2013). According to the ground motion loading scheme presented in **Table 3**, the maximum amplitude range of the input ground motion in seven stages (i.e., EQ1–EQ7) was between 0.1 and 0.4 g. Not only the increase in the seismic intensity at the 0.1-g interval adopted in most studies was considered but also the same intensity (EQ4, EQ6, and EQ7) was set in three stages. As an example, the acceleration time history and Fourier spectrum of A0 at EQ1, with a PGA = 0.118 g, are shown in **Figure 2**. It is worth noting that the cumulative loading and continuous loading mentioned here only refer to whether the input ground motion peak value is the same as that of the previous stage and does not refer to different loading methods. Its purpose is mainly to enrich the variation of ground motion.

3 TEST RESULTS

3.1 Displacement

The displacement and settlements of the pile head and slope at each event are presented in **Figure 3**, where it can be seen that the displacement of the pile head is positive in the direction away from the slope, while the settlement of the slope is positive in the downward direction. The settlement and displacement here refer to the dynamic peak value in the response stage and not the

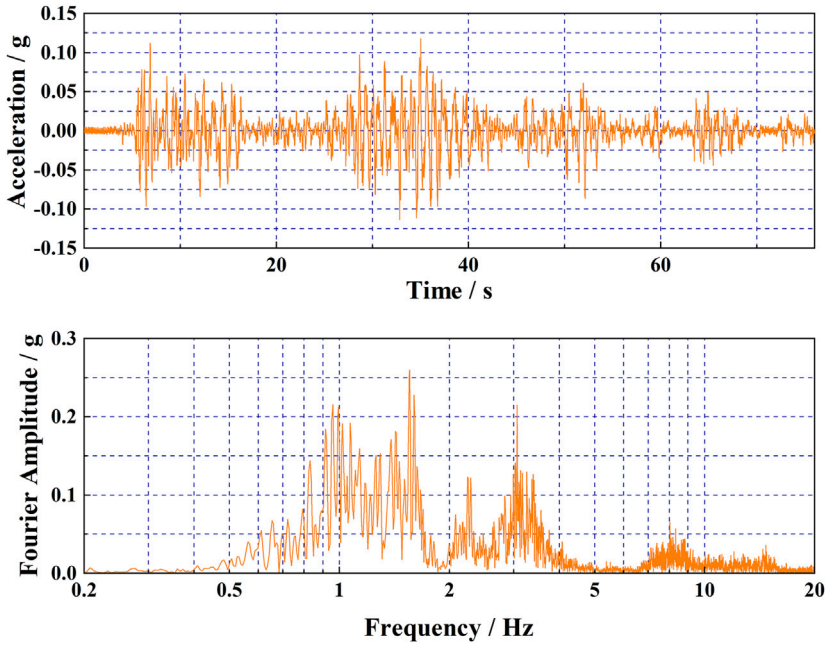

FIGURE 2 | Acceleration time history and Fourier spectrum of A0 during EQ1.

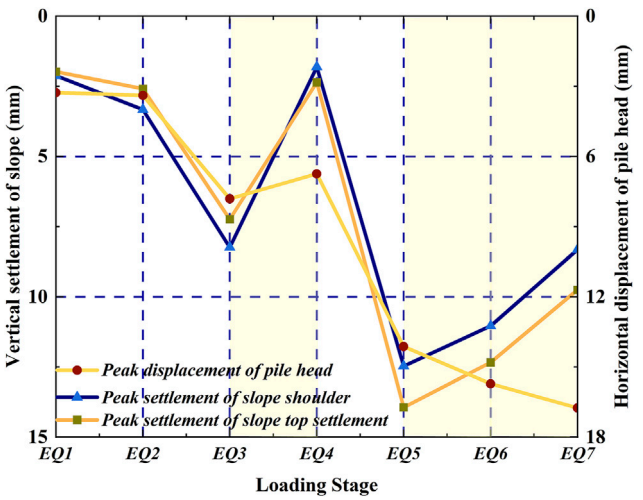

FIGURE 3 | Model displacement and settlement results.

cumulative value. In the whole process, the periodic displacements of the top and the shoulder of the slope show a similar movement trend. When the earthquake intensity increased, the settlement of the slope also increased, but when the intensity was unchanged, the settlement decreased. One possible reason for this change is considered to be that the ground motion of the previous stage makes the slope material more compact, thereby reducing the peak dynamic settlement (displacement) in the next adjacent stage of the same input strength. The slope settlement in the loading growth stage is much larger than that in the adjacent stable stage. Even for EQ6 and EQ7 with high strength, the settlement deformation decreases gradually. It should be stated that the test results in this study are displayed after being converted to the prototype size.

Before EQ5, the variation trend of the pile head's horizontal displacement with seismic intensity is the same as that of the slope settlement. However, during multiple high-intensity earthquakes (EQ5–EQ7), the pile head displacement continued to increase, even when there is only a small increase. It is worth noting that the first high-intensity earthquake EQ5 causes a more obvious settlement of the slope than earthquakes EQ1–3. Although the subsequent settlement decreased, the settlement is still larger than that of the medium- and low-intensity earthquakes. This also makes the pile body tilt out to resist slope sliding, resulting in a continuous increase in the pile head displacement.

3.2 Slope Amplification

Acceleration measuring points are divided into three groups according to their spatial position, as shown in **Figure 4A**: Group A (GA) includes three measuring points, which are located behind the pile, representing the upper, middle, and lower parts of the cantilever section of the pile body. Measuring points A4 and A6 are close to the soil rock contact surface and anchor cable, respectively. Group B (GB) comprises measuring points on the slope surface and slope top, where the amplification effect is obvious. Group C (GC) includes the measuring point A9 which is located at the center of the slope and measuring points A8, A11, and A14 which are near the bedrock surface.

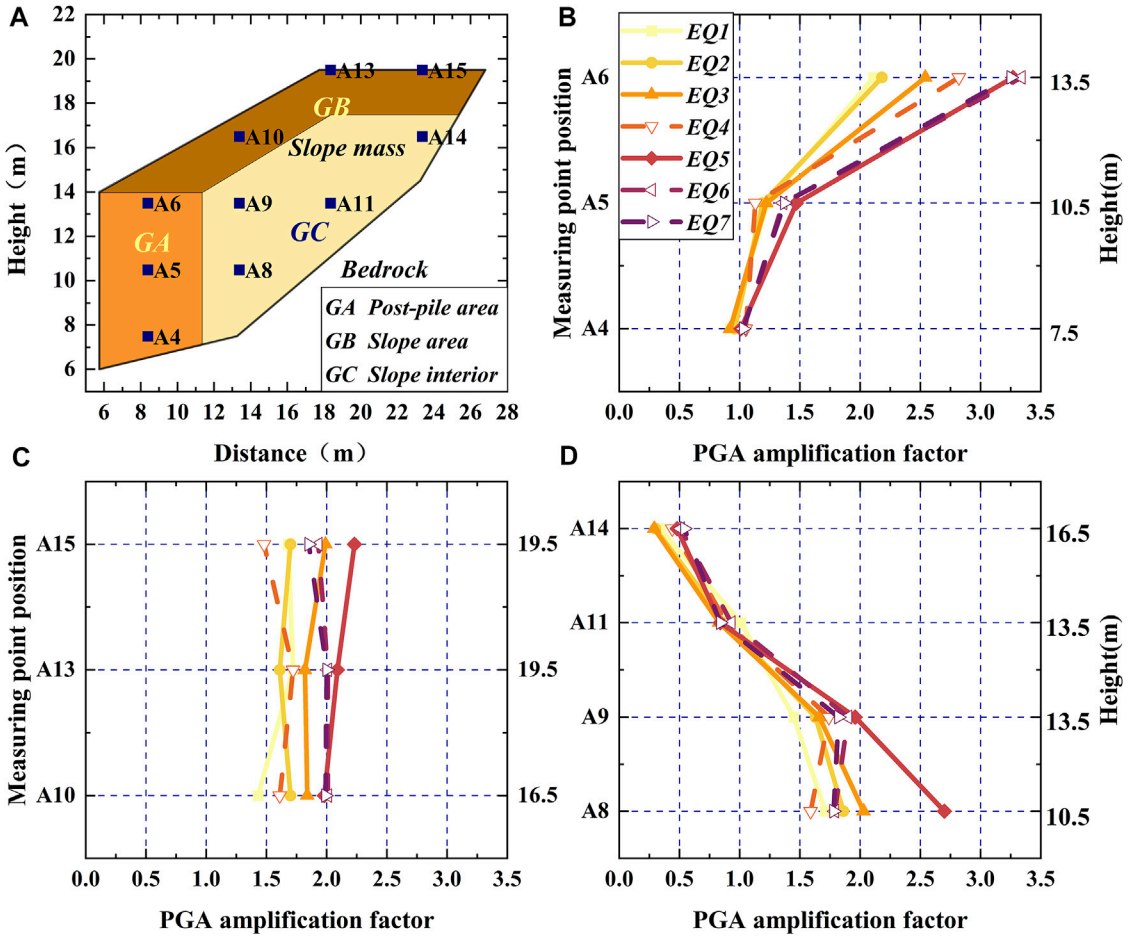

FIGURE 4 | PGA amplification factor results: **(A)** Grouping of acceleration measuring points; **(B)** the results of GA; **(C)** the results of GB; and **(D)** the results of GC.

The variation curve of the amplification factor of GA with elevation is presented in **Figure 4B**, where it can be seen that the peak ground acceleration (PGA) amplification factor shows a significant elevation amplification effect, which increases with the elevation. With the change in the input ground motion intensity, the change in each measuring point shows different trends. The amplification factor of the measuring points increases with the earthquake intensity but decreases slightly under a high-grade earthquake with the same intensity. The amplification factor of A6 is the largest, especially under high-intensity earthquakes, when it can reach more than 3.0. This is due to the topographic effect, site conditions, and dynamic interaction of the structure and slope.

As shown in **Figure 4C**, the amplification factor of measuring points in GB also increases with the earthquake intensity but decreases in varying degrees under subsequent earthquakes with the same intensity. The amplification factors of this group are concentrated between 1.25 and 2.25, showing an obvious topographic amplification effect. This is because the measuring points of GB are found near the free surface of the slope surface. The magnification effect becomes more pronounced as the distance from special terrains such as slope corners decreases.

In contrast to general expectations, the acceleration amplification factor of the measuring point on the slope in GC does not increase with the elevation, as shown in **Figure 4D**. This phenomenon could be attributed to the influence of the slope structure on seismic wave propagation. The reflection and refraction, including the surface and bedrock surface, and the phase difference of the seismic waves during the wave propagation could reduce the acceleration amplification effect to a certain extent. Similar phenomena have been noted by Bouckovalas and Papadimitriou, 2005.

In general, different from the homogenous slope amplification, the slope with a complex soil–rock interface strengthened by a pile–anchor structure is very uneven, and the amplification factor shows strong variability. This means that a quasi-static method may have a higher risk in the seismic design of slopes similar to the model considered in this study because the nonuniformity of the ground motion distribution is not considered (Seed and Whiteman, 1970).

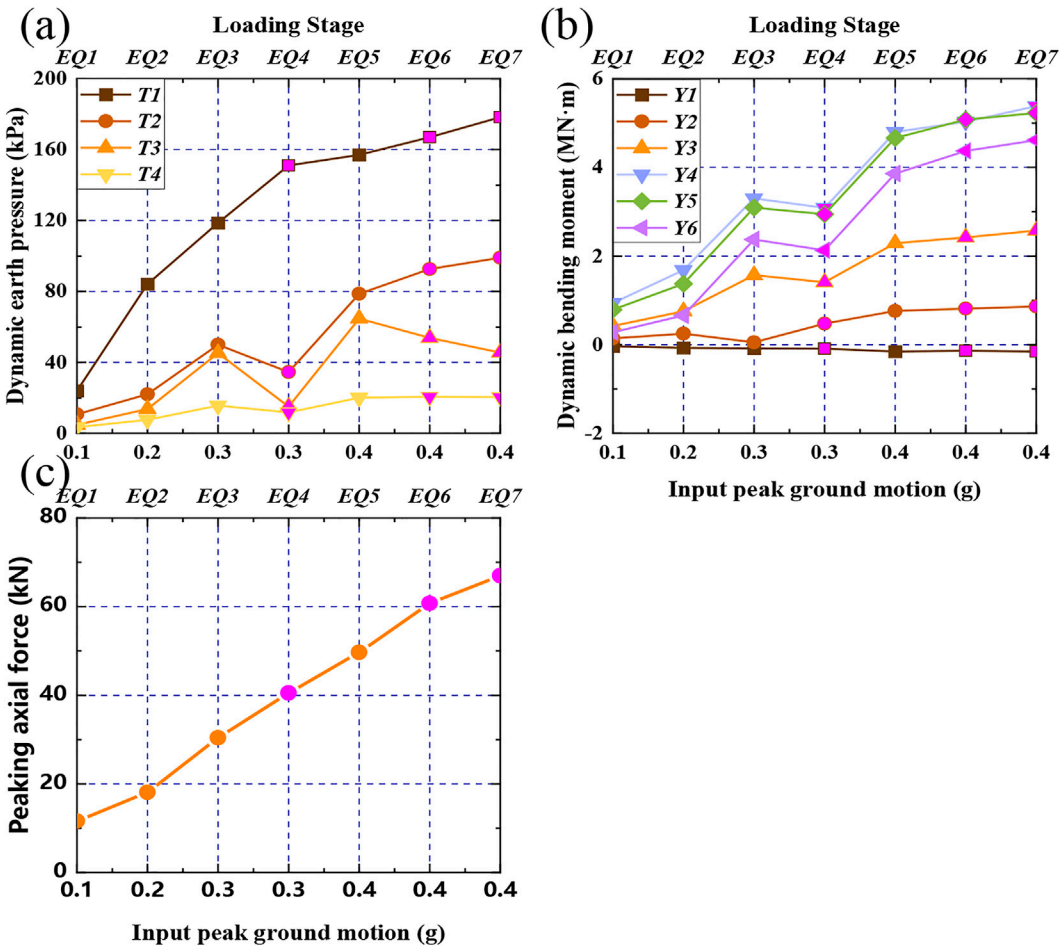

FIGURE 5 | Variation curve of the peak value of pile dynamic behavior with input ground motion intensity: **(A)** The peak dynamic earth pressure of the pile; **(B)** The peak dynamic bending moment of the pile; **(C)** The peak axial force of the anchor cable.

3.3 Structure Response

3.3.1 Dynamic Earth Pressure

The peak value variation of the pile with the earthquake intensities is shown in **Figure 5A**, where it can be seen that dynamic earth pressure increased with the elevation. T1 near the anchor cable is the largest, and T4 near the bedrock surface is the smallest. With the change in the earthquake intensity, the change law of different measuring points is different. T1 continued to increase, even under the high-strength processes EQ5–EQ7, which could be related to the pile–soil compression caused by anchor cable traction. For other measuring points, at medium and low intensities, the dynamic earth pressure increases and decreases under continuous action of the same intensity. This trend is consistent with the dynamic settlement of the slope. Under large earthquakes (EQ5–EQ7) with a PGA of 0.4 g, the dynamic earth pressure of T2 continues to increase, while that of T3 and T4 either decreases or remains unchanged. This indicates that the pile–soil compression caused by the anchor cable traction decreased with the elevation, but it significantly affected the stress on the upper part of the pile at a high seismic intensity.

3.3.2 Dynamic Bending Moment

The variation curve of the pile dynamic bending moment with seismic intensity is shown in **Figure 5B**. In this study, the bending moment is positive when the pile body is pulled on the side of the slope. Except for Y1, which has a negative bending moment, the other measuring points have positive bending moments. The dynamic bending moment first increased and then decreased from the pile top to the end, and Y4 reached the maximum in the middle of the pile. The negative bending moment near the anchor cable indicates that the tension of the anchor cable makes the pile deform inward. The variations of different measuring points with the earthquake intensity can be divided into two categories: Y1, where variations continued to increase and are not sensitive to the seismic intensity changes, and the category that included all other measuring points, where variations increase when the earthquake intensity changes but decrease when the earthquake intensity is unchanged.

3.3 3 Anchor Force

The peak axial force of the anchor cable obtained under different seismic events is shown in **Figure 5C**. Regardless

TABLE 4 | Example sequence of the fuzzy correlation degree.

Sequence	Test no.						
	1	2	3	4	5	6	7
$X_1(k)$	1	2	2.5	2.5	3	5	6
$Y_1(k)$	1	1.8	2.3	2.4	2.8	4.8	5.8
$Y_2(k)$	1	2.17	2.5	2.1	3	4.1	5.8

of the seismic intensity being increased or staying unchanged, the peak axial force of the anchor cable always increases and is not sensitive to the input ground motion loading mode. This trend may affect the behavior of the piles near the anchor cable so that the dynamic earth pressure and dynamic bending moment near the anchor cable have similar changing trends.

4 DATA MINING METHODS

The centrifuge model test results show that there may be some fuzzy correlations between the seismic response of the slope and the behavior of the pile–anchor structure. This ambiguous correlation can be used for data mining by using the gray relational analysis (GRA). Compared with other data mining methods, the gray relational analysis method is equally applicable to the size of the sample and regularity of the sample. Therefore, it is suitable for the analysis and evaluation of a slope under an earthquake, which is limited, complex, and highly uncertain.

4.1 Gray Relational Analysis

GRA is an integral part of the gray system theory. Compared with Pearson's correlation coefficient, maximum mutual information coefficient (MIC), and other evaluation methods with high requirements for data linearity or sample number, the main advantage of GRA is that it can be used in the case of limited data to determine the correlation between various change and reference factors. The correlation is expressed in gray relational grade, and the greater the gray relational grade is, the better the correlation is. The essence of this method is to explore the correlation between different factors by comparing the similarity of the curves. The specific calculation method is as follows (Deng, 2002):

Let the reference sequence be $X_i = \{x_i(k)|k = 1, 2, \ldots, n\}$ and the comparison sequence be $Y_j = \{y_j(k)|k = 1, 2, \ldots, n\}$, where $i = (1, 2, \ldots, t)$ and $j = (1, 2, \ldots, m)$. Then, the gray relational coefficient of $x_i(k)$ to $y_j(k)$ is given by

$$\xi_{ij}(k) = \frac{\Delta_{min} + \theta\Delta_{max}}{\Delta_{ij}(k) + \theta\Delta_{max}} \tag{1}$$

where $\Delta_{min} = min_j min_k |x_i(k) - y_j(k)|$; $\Delta_{max} = max_j max_k |x_i(k) - y_j(k)|$; $\Delta_{ij}(k) = |x_i(k) - y_j(k)|$; θ is the identification coefficient, and $\theta \in (0, 1)$, and usually used as 0.5.

The gray relational grade can be obtained by averaging the gray relational coefficient, which can be expressed as follows:

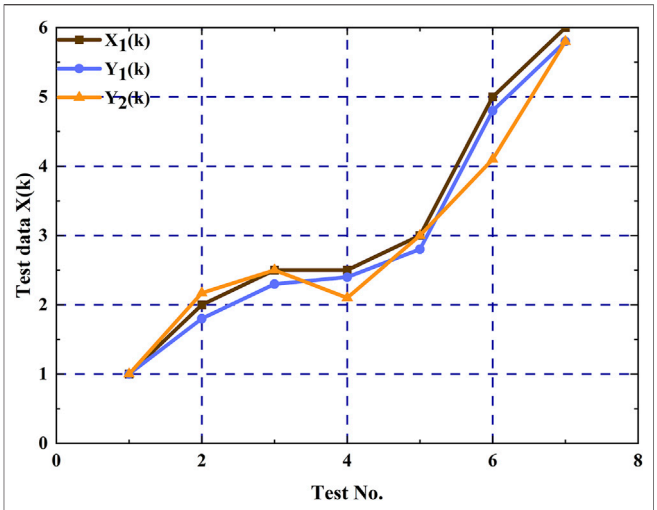

FIGURE 6 | Comparison chart of the variation trend of example sequences.

$$\lambda_{ij} = \frac{1}{n}\sum_{k=1}^{n} \zeta_{ij}(k) \tag{2}$$

4.2 Identification Coefficient Optimization

In **Eq. 1**, the identification coefficient is usually determined subjectively, and there has been no general solution to the resolution coefficient, which greatly affects the correlation degree value and ranking results, so it is not applicable to most cases. To address this problem, this study further processes data using many improved methods (Xu and Xu, 2011; James et al., 2013; Gao et al., 2018; Ren et al., 2020), which are explained in the following section.

In practical problems, the dimension and order of magnitude of the reference and comparison sequences are usually different, and their effects on the mechanical characteristics of the support structure are also different, which requires further analysis. The usual approach is to normalize data using positive, negative, and other types of normalization. However, such an approach can significantly change the original characteristics of the curve, and the data considered in this study cannot adopt the evaluation criteria of "the larger, the better" or "the smaller, the better." Therefore, the initial value processing method was adopted for comprehensive consideration, which was given by Gao et al., (2018)

$$x_i'(k) = \frac{x_i(k)}{x_i(1)} \tag{3}$$

According to **Eq. 1**, the identification coefficient θ actually acts as a weight of Δ_{max}. Therefore, to consider the integrity of the correlation degree fully, namely, to not only consider the correlation between the correlation degree coefficient and $x_i(k)$ and $y_j(k)$ but also the influence of other factors, the identification coefficient was determined by the following method (Su et al., 2012):

$$\Delta_s = \frac{1}{mn}\sum_{j=1}^{m}\sum_{k=1}^{n}\left|x_i^{'}(k) - y_j^{'}(k)\right| \tag{4}$$

where m and n denote the number of comparison sequences and the amount of sequence capacity, respectively.

When $\eta = \frac{\Delta_s}{\Delta_{\max}}$, the value range of the identification coefficient is $\theta' \in [\eta,\ 2\eta]$. In addition, according to different situations, the resolution coefficient should also meet the following two conditions:

$$\eta \le \theta \le 1.5\eta\ (\Delta_{max} > 3\Delta_s). \tag{5}$$

$$1.5\eta \le \theta \le 2\eta\ (\Delta_{max} \le 3\Delta_s). \tag{6}$$

At this point, $\Delta_{\min}^{'} = \min_k \min_j\{x_i^{'}(k) - y_j^{'}(k)\}$ and $\Delta_{\max}^{'} = \max_k \max_j\{x_i^{'}(k) - y_j^{'}(k)\}$. The advantage of determining the identification coefficient in this way is that when the difference at a certain point is large (i.e., the correlation of other values is strong), the identification coefficient will obtain a smaller value to strengthen the integrity of the gray relational grade and avoid inaccurate calculation results in extreme cases.

4.3 Gray Relational Grade Optimization

The traditional gray average correlation degree calculation method considers that the sum of gray relational coefficients remains unchanged, ignoring the fact that local similarity is the premise of overall similarity, which can lead to wrong conclusions. The data in **Table 4** are taken as examples and drawn in **Figure 6**. For sequences X_1, Y_1, and Y_2, it can be seen that the development trends of Y_1 are much closer to those of X_1 than of Y_2. However, the gray relational grade of the two is 0.7542 and 0.7544, respectively, indicating the opposite result from the figure and is unreasonable. Therefore, this study selects the gray Euclidean relational grade (Yang et al., 2011) for calculation, which is given by

$$\lambda_{ij}^{'} = 1 - d_{ij} = 1 - \frac{1}{\sqrt{n}}\sqrt{\sum_{k=1}^{n}\left(1 - \xi_{ij}(k)\right)^2} \tag{7}$$

where d_{ij} is the Euclidian distance and $\lambda_{ij}^{'}$ is the fuzzy gray relational grade between sequences $X_i^{'}$ and $Y_j^{'}$. Using the improved correlation degree calculation method, it can be inferred that $\lambda_{11}^{'} = 0.731 > \lambda_{12}^{'} = 0.6545$.

4.4 Comprehensive Discrimination Based on the RSR Method

The gray relational grades of the reference and comparison sequences can be obtained through the fuzzy gray relational grade analysis, however, when the reference sequence changes, the ranking of the gray relational grade may be different and not conducive to comprehensively judging the correlation of the system factors. Fortunately, the rank-sum ratio (*RSR*) method can effectively carry out a comprehensive discrimination for complex sorting.

The *RSR* method (Wang et al., 2015) performs an overall ranking based on the dimensionless statistics of 0–1 obtained from the average value of the rank sum of the corresponding comparison sequence under each index. In the experiment, the rank of the same comparison sequence is taken under each relevant reference sequence; the method of summing and taking the average value was used to observe the impact of a group of comparison sequences on the whole. In this way, the problem that the fuzzy gray relational grade had too many results when dealing with the ranking and evaluation of multiple comparison sequences and multiple reference sequences of a whole, which made obtaining the overall view difficult, was solved. In addition, because the gray relational grade only had practical significance in relative comparison and sorting, the disadvantage of losing a certain amount of the original data in the calculation process of the *RSR* method has also been addressed. The calculation formula of the *RSR* value is as follows:

$$RSR_j = \frac{\sum_{i=1}^{t} R_{\mathrm{ij}}}{m \times t} \tag{8}$$

where j is the number of evaluated units (or the j_{th} comparison sequence); i is the number of evaluation indicators (or the i_{th} reference sequence); and R_{ij} is the rank of the j_{th} comparison sequence under the i_{th} reference sequence. In particular, the higher the *RSR* value is, the higher the ranking is.

5 RESULT ANALYSIS

According to the types of seismic response parameters of the pile–slope-anchor system, the pile head seismic peak displacement (PPERD), peak dynamic bending moment (Y1–Y6), peak dynamic earth pressure (T1–T4), and peak axial force (PC) of the anchor cable are determined as a reference sequence, and the comparison sequence is designated as the PGA amplification factor of the measuring points at different positions, as presented in **Table 5**. The sample size of each sequence is 7 due to the test events. It is worth noting that the formulation rules of the comparison sequence made the correlation ranking associated with the spatial position of the measuring points. The gray relational grade is calculated by **Eqs 1–6**. **Figure 7** shows the contour maps at some typical points, while the sorting results of all parameters are given in **Table 6**.

As presented in **Figure 7**, the distribution of the gray relational grades for different reference sequences shows the same trend. In detail, all the calculation results are greater than zero, and the shape of the isolines is crooked. That means the seismic responses at all positions of the slope contribute to the dynamic behavior of the pile, but the correlations are different, which is related to the position of the acceleration measuring point. The measuring points with a higher comprehensive ranking of correlation are A6, A10, A14, A9, and A8. Among the measuring points, A6 has the largest gray relational grade. It is located where the interaction of slope, vertical free surface, and pile–anchor structure is significant and where the amplification factor is significantly high and abnormal. The peak dynamic earth pressure of the pile near A6 is the largest, and the peak dynamic bending moment shows a reversal from positive to negative. A8–A10 were located in the middle of the slope, and the amplification factors of the

TABLE 5 | Summary of the fuzzy gray relational analysis sequences.

	Simplified spelling	Meaning
Reference sequence	PPERD	Peak displacement of the pile head under a seismic event
	Y1–Y6	Peak value of the dynamic bending moment under a seismic event
	T1–T4	Peak value of the dynamic earth pressure under a seismic event
	PC	Peak value of the anchor cable axial force under a seismic event
Contrast sequence	A4–A15	PGA amplification factor of a measuring point

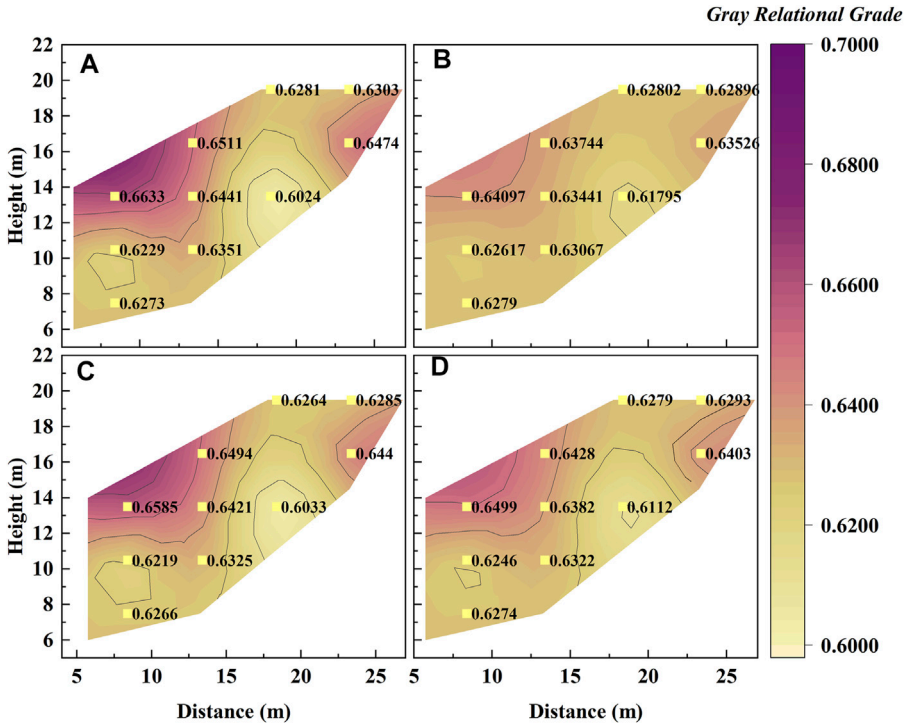

FIGURE 7 | Contour map of the gray relational grades at some typical measuring points: **(A)** The results of PPERD; **(B)** The results of T1; **(C)** The results of Y1; **(D)** The results of PC.

TABLE 6 | Results of gray relational sorting.

No.	PPERD	PC	T1	T2	T3	T4	Y1	Y2	Y3	Y4	Y5	Y6
1	A6	A6	A6	A6	A6	A6	A6	A6	A6	A6	A6	A6
2	A10	A10	A10	A10	A10	A10	A10	A14	A10	A10	A10	A10
3	A14	A14	A14	A14	A14	A14	A14	A10	A14	A14	A14	A14
4	A9	A9	A9	A9	A9	A9	A9	A9	A9	A9	A9	A9
5	A8	A8	A8	A8	A8	A8	A8	A4	A8	A8	A8	A8
6	A15	A15	A15	A15	A15	A15	A15	A8	A15	A15	A15	A15
7	A13	A13	A13	A13	A13	A13	A4	A13	A13	A13	A13	A13
8	A4	A4	A4	A4	A4	A4	A13	A15	A4	A4	A4	A4
9	A5	A5	A5	A5	A5	A5	A5	A5	A5	A5	A5	A5
10	A11	A11	A11	A11	A11	A11	A11	A11	A11	A11	A11	A11

three points are greater than those of the surrounding points, especially when the earthquake intensity increased. During the test, obvious cracks between the slope and the bedrock were observed near A14, which could be attributed to the large contact angle. The other measuring points in the ranking have no special phenomenon on the ground motion parameters and slope failure.

From the model test results, it is not difficult to find that the slope acceleration amplification varied nonlinearly, while it can be divided into three categories according to the maximum,

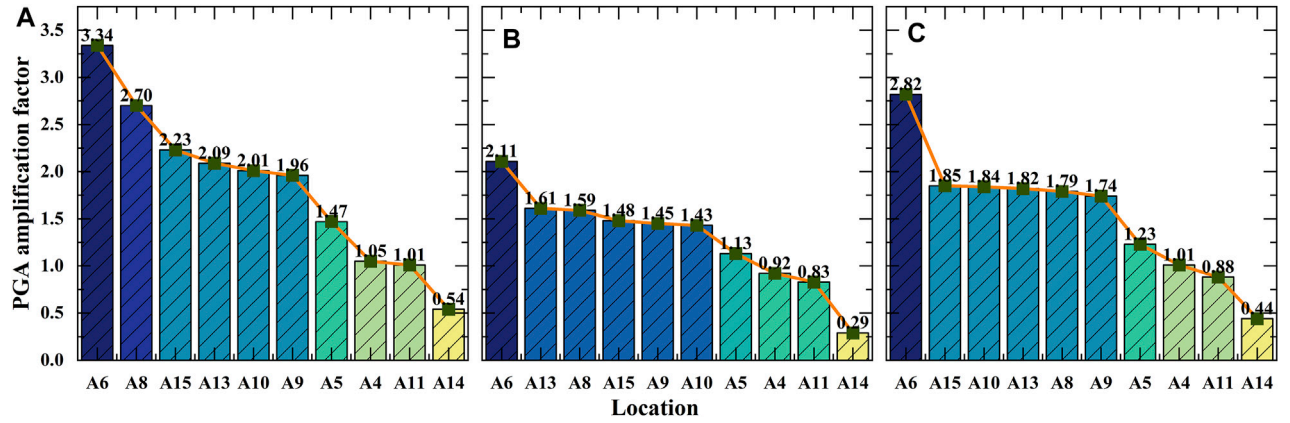

FIGURE 8 | PGA amplification factor ordering: **(A–B–C)** in the figure is the ranking result of the maximum value, minimum value, and median value of the PGA amplification factor.

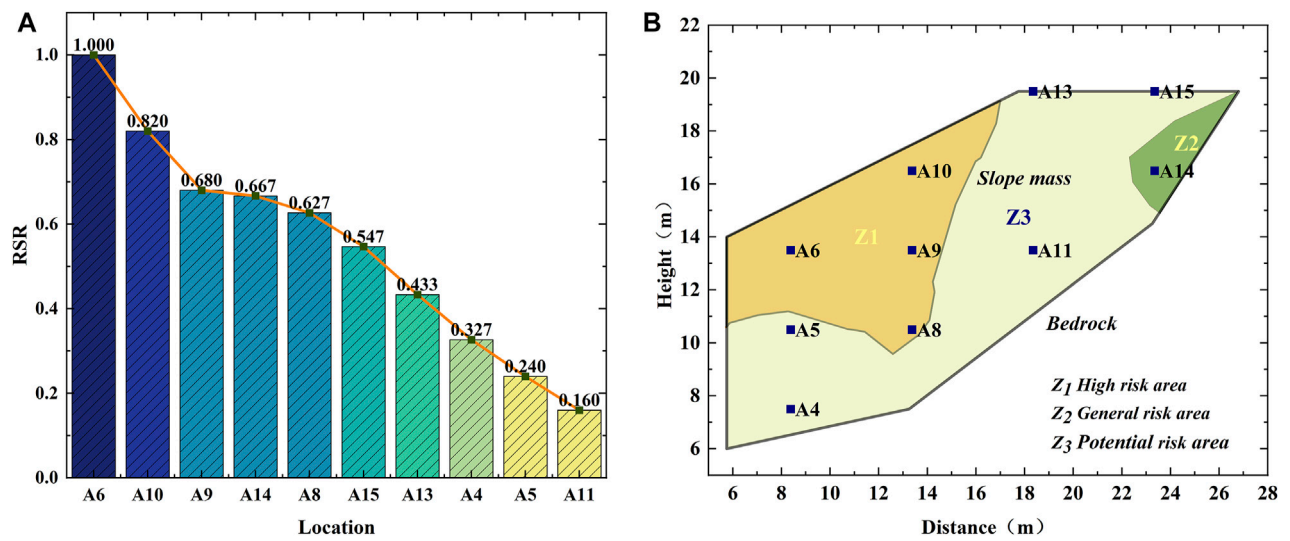

FIGURE 9 | Comprehensive evaluation results: **(A)** *RSR* ranking histogram **(B)** Slope risk zoning map.

minimum, and median values. The three types of results are shown in **Figure 8** as descending orders and can be considered the most dangerous, safest, and relatively moderate seismic action experienced by the slope, respectively. It can be seen that about 60%–70% of the PGA amplification factor obtained by deploying the measuring points is greater than the minimum amplification factor of 1.2, which has been specified in Eurocode 8 (CEN European Committee for standardization, 2003). This indicates that the actual slope seismic response has exceeded the provisions of the specification, which would affect engineering safety. If the seismic design is fully considered according to the maximum acceleration amplification factor, the engineering economy may be unacceptable. Therefore, to comprehensively evaluate the influence of slope amplification on the pile–anchor–slope reinforcement system, the ranking results of the gray relational grade and the classification results of slope acceleration amplification factor should be considered together during the *RSR* assessment, and the result is shown in **Figure 9A**.

Figure 9A shows that the high correlation is related to the high amplification factor and the distance from the measuring point to the pile, which conforms to St. Venant's principle. In the *RSR* ranking, A6 and A8–A10 are in the top five, indicating that the high acceleration response inside the slope has a significant contribution to the dynamic behavior of the pile–anchor structure. Except the aforementioned measuring points, A14 ranked fourth, and the large inclination of the bedrock surface near this point is not conducive to the stability of the slope. Although A4 and A5 are close to the pile, the amplification factors are just 1.13–1.47 and 0.92–1.05, respectively. In addition, although the amplification on the slope crest has a limited

effect on the reinforced structure, it may influence the structures built on the slope top which has been confirmed by Brennan and Madabhushi (2009).

The *RSR* ranking results also show that some positions inside the slope need special consideration in seismic design, rather than assuming that the slope is subjected to the consistent seismic force based on the quasi-static method. According to the acceleration amplification effect and *RSR* ranking result, the slope can be divided into three risk areas, as shown in **Figure 9B**. The high-risk and potential-risk areas denoted areas where the *RSR* value is higher than 0.6. The former is the area where the acceleration is significantly amplified, while the latter is related to the slope instability caused by the geometric parameters of the bedrock surface. It may be one of the more possible strategies to add shock absorption materials to high-risk areas with abnormal acceleration amplification. Some 1-g shaker test results suggest that additional shock-absorbing material is a possible treatment (Ma et al., 2019; Pai and Wu, 2021). This can not only eliminate the occurrence of unknown factors to a certain extent but also reduce economic waste. For the potential-risk areas, it is necessary to ensure that the grouting strength of the embedded section of the anchor cable meets the design standard to prevent the anchor cable from being pulled out from the bedrock.

6 CONCLUSION

To study the correlation between slope amplification and the seismic behavior of the pile, a centrifugal shaking table test was established considering the effect of different seismic intensities, and the slope amplification factor and pile mechanical parameter data of the pile–anchor–slope reinforcement system were obtained. On this basis, combined with the fuzzy gray relational analysis and the rank-sum ratio method, the correlation between the amplification of the acceleration response of the heterogenous slope and the dynamic response of the support structure was explored. Based on the obtained results, relevant suggestions for engineering design were put forward. The main conclusions and suggestions are summarized as follows:

1) The acceleration amplification of the slope body is uneven, the amplification of the pile–anchor cable connection is the largest, and the high-angle soil–rock interface is the smallest. The variation law is consistent, and it increases or decreases with the change of the input ground motion intensity. Slope amplification inhomogeneity may cause actual earthquake damage not to meet the design expectations of the quasi-static method.
2) The peak value of the peak dynamic earth pressure of the pile increases with the increase of the relative elevation and the soil mass is squeezed by the pile-anchor joint, resulting in the largest dynamic earth pressure near the top of the pile, and the smallest T4 near the bedrock surface; the peak dynamic bending moment of the pile is negative near the top of the pile, gradually becomes positive as the elevation decreases, reaches the maximum value near the bedrock surface, and then gradually decreases; except for the continuous increase of the dynamic soil pressure, dynamic bending moment, and peak axial force at the pile–anchor connection, the other measurement points increase when the input ground motion intensity increases but decrease when the input ground motion intensity remains the same.
3) The comprehensive ranking of the *FGRA-RSR* method shows that the magnification of different positions has different effects on the seismic force of the pile. The positions of the top 50% of the ranking are located in the pile–anchor connection part, the middle of the slope, and the high-angle soil–rock interface. Most of these locations have high soil magnification or have obvious geometric features. Therefore, it is necessary to consider the shock absorption measures of the pile–anchor cable connection and ensure the grouting strength of the anchor cable anchoring section in the actual design.

The research in this article still has some limitations. This mainly focuses on the lack of more available engineering cases and model test data. Undoubtedly, more cases will make the ranking results of the comprehensive evaluation more convincing and can provide more valuable suggestions for engineering practice. Unfortunately, there are, indeed, some objective difficulties. In the follow-up, it may be considered to obtain data in more cases using numerical simulation after calibration based on model tests (Ni et al., 2018; Ni and Mangalathu, 2018; Ni et al., 2020).

DATA AVAILABILITY STATEMENT

The datasets presented in this article are not readily available because they are used only with the consent of the corresponding author of this article. Requests to access the datasets should be directed to ZT, zhengt0928@163.com.

AUTHOR CONTRIBUTIONS

YW handled most of the work of the article. TZ is the main contributor to guide the revision of the article. Other authors also contributed some suggestions to the article.

FUNDING

This work was supported by the Scientific Research Fund of Institute of Engineering Mechanics, China Earthquake Administration (Grant Nos 2018B04; 2020B03), the National Natural Science Foundation of China (Grant Nos 51808515; 41874067), the Natural Science Foundation of Heilongjiang Province (Grant No. LH2020E020), and the Hebei Natural Science Foundation of China (Grant No. E2020201017).

REFERENCES

Bouckovalas, G. D., and Papadimitriou, A. G. (2005). Numerical Evaluation of Slope Topography Effects on Seismic Ground Motion. *Soil Dyn. Earthquake Eng.* 25, 547–558. doi:10.1016/j.soildyn.2004.11.008

Brennan, A. J., and Madabhushi, S. P. G. (2009). Amplification of Seismic Accelerations at Slope Crests. *Can. Geotech. J.* 46, 585–594. doi:10.1139/t09-006

CEN European Committee for Standardization (2003). *Design Provisions for Earthquake Resistance of Structures - Part 5: Foundations, Retaining Structures and Geotechnical aspectsEurocode 8 ENV 1998-5*. Brussels: CEN European Committee for Standardization.

Chen, G. F., Zhang, G. D., Guo, F., Wang, L., Zhan, Q. H., and Huang, X. H. (2022). New Arm-stretching-type Anti-slide Pile Design and Verification. *Front. Earth Sci.* 10. Article 846616. doi:10.3389/feart.2022.846616

Cilinger, U., and Madabhushi, S. P. G. (2011). Effect of Depth on Seismic Response of Circular Tunnels. *Can. Geotechnical J.* 48, 117–127.

Deng, J. L. (2002). *Gray Theory Basis*. Wuhan: Huazhong University of Science & technology Press.

Finn, W. D. L., Ledbetter, R. H., and Beratan, L. L. (1986). Seismic Soil-Structure Interaction: Analysis and Centrifuge Model Studies. *Nucl. Eng. Des.* 94, 53–66. doi:10.1016/0029-5493(86)90153-6

Gao, C.-l., Li, S.-c., Wang, J., Li, L.-p., and Lin, P. (2018). The Risk Assessment of Tunnels Based on Grey Correlation and Entropy Weight Method. *Geotech Geol. Eng.* 36, 1621–1631. doi:10.1007/s10706-017-0415-5

Garala, T. K., and Madabhushi, G. S. P. (2019). Seismic Behaviour of Soft clay and its Influence on the Response of Friction Pile Foundations. *Bull. Earthquake Eng.* 17, 1919–1939. doi:10.1007/s10518-018-0508-4

Gazetas, G., Psarropoulos, P. N., Anastasopoulos, I., and Gerolymos, N. (2004). Seismic Behaviour of Flexible Retaining Systems Subjected to Short-Duration Moderately strong Excitation. *Soil Dyn. Earthquake Eng.* 24, 537–550. doi:10.1016/j.soildyn.2004.02.005

Ghosh, B., and Madabhushi, S. P. G. (2007). Centrifuge Modelling of Seismic Soil Structure Interaction Effects. *Nucl. Eng. Des.* 237 (8), 887–896. doi:10.1016/j.nucengdes.2006.09.027

Halder, L., Dutta, S. C., Sharma, R. P., and Bhattacharya, S. (2021). Lessons Learnt from post-earthquake Damage Study of Northeast India and Nepal during Last Ten Years: 2021 Assam Earthquake, 2020 Mizoram Earthquake, 2017 Ambasa Earthquake, 2016 Manipur Earthquake, 2015 Nepal Earthquake, and 2011 Sikkim Earthquake. *Soil Dyn. Earthquake Eng.* 151. Article ID 106990. doi:10.1016/j.soildyn.2021.106990

Heron, C. M., Haigh, S. K., and Madabhushi, S. P. G. (2015). A New Macro-Element Model Encapsulating the Dynamic Moment-Rotation Behaviour of Raft Foundations. *Géotechnique* 65, 442–451. doi:10.1680/geot.sip.15.p.020

Hu, H. Q., Huang, Y., Xiong, M., and Zhao, L. Y. (2021). Investigation of Seismic Behavior of Slope Reinforced by Anchored Pile Structures Using Shaking Table Tests. *Soil Dyn. Earthquake Eng.* 150. Article ID 106900. doi:10.1016/j.soildyn.2021.106900

Hu, M. M., Wu, Z. H., Reicherter, K., Ali, S., Huang, X. L., and Zuo, J. M. (2021). A Historical Earthquake-Induced Landslide Damming Event at the Qiaojia Reach of the Jinsha River, SE Tibetan Plateau: Implication for the Seismic Hazard of the Xiaojiang Fault. *Front. Earth Sci.* 9. Article ID 649543. doi:10.3389/feart.2021.649543

Huang, R. Q., and Li, W. L. (2009). Analysis of the Geo-Hazards Triggered by the 12 May 2008 Wenchuan Earthquake, China. *Bull. Eng. Geol. Environ.* 68, 363–371. doi:10.1007/s10064-009-0207-0

Huang, Y., Xu, X., Liu, J. J., and Mao, W. W. (2020). Centrifuge Modeling of Seismic Response and Failure Mode of a Slope Reinforced by a Pile-Anchor Structure. *Soil Dyn. Earthquake Eng.* 131. Article ID 106037. doi:10.1016/j.soildyn.2020.106037

James, N., Liu, K., and Hu, Y. X. (2013). Application of Feature-Weighted Support Vector Regression Using gray Relational Grade to Stock price Forecasting. *Neural Comput. Appl.* 22 (Suppl. 1), S143–S152.

Liu, H., Bo, J., Li, P., Qi, W., and Zhang, Y. (2016). Site Amplification Effects as an Explanation for the Intensity Anomaly in the Hanyuan Town during the Wenchuan M W 7.9 Earthquake. *Earthq. Eng. Eng. Vib.* 15, 435–444. doi:10.1007/s11803-016-0334-0

Liu, H. S., Yang, J. B., Bo, J. S., and Liu, Y. (2013). Bedrock Ground Motion Input to High-Intensity Abnormality Area in Hanyuan County Town during Wenchuan Ms 8.0 Earthquake. *J. Earthquake Eng. Eng. Vibration* 33 (2), 27–36.

Liu, X. L., Yan, J. K., T, B., and Liu, L. (2021). Evaluation of Micropiles with Different Configuration Settings for Landslide Stabilization Based on Large-Scale Experimental Testing. *Front. Earth Sci.* 9. Article 693639. doi:10.3389/feart.2021.693639

Liu, X. L., Zhang, Z. M., and Zhou, D. P. (2004). Improved Calculation Method of Prestressed Anchor cable Anti Slide Pile. *Chin. J. Rock Mech. Eng.* 23 (15), 2568–2572. (in Chinese).

Ma, N., Wu, H., Ma, H., Wu, X., and Wang, G. (2019). Examining Dynamic Soil Pressures and the Effectiveness of Different Pile Structures inside Reinforced Slopes Using Shaking Table Tests. *Soil Dyn. Earthquake Eng.* 116, 293–303. doi:10.1016/j.soildyn.2018.10.005

Ni, P., and Mangalathu, S. (2018). Fragility Analysis of gray Iron Pipelines Subjected to Tunneling Induced Ground Settlement. *Tunnelling Underground Space Tech.* 76, 133–144. doi:10.1016/j.tust.2018.03.014

Ni, P., Mangalathu, S., and Liu, K. (2020). Enhanced Fragility Analysis of Buried Pipelines through Lasso Regression. *Acta Geotech.* 15, 471–487. doi:10.1007/s11440-018-0719-5

Ni, P., Mangalathu, S., and Yi, Y. (2018). Fragility Analysis of Continuous Pipelines Subjected to Transverse Permanent Ground Deformation. *Soils and Foundations* 58, 1400–1413. doi:10.1016/j.sandf.2018.08.002

Ni, P. P., Song, L. H., Mei, G. X., and Zhao, Y. L. (2017). On Predicting Displacement-dependent Earth Pressure for Laterally Loaded Piles. *Soil and Foundations* 58 (1), 85–96.

Pai, L. F., and Wu, H. G. (2021). Shaking Table Test of Comparison and Optimization of Seismic Performance of Slope Reinforcement with Multi-Anchor Piles. *Soil Dyn. Earthquake Eng.* 145. Article ID 106737. doi:10.1016/j.soildyn.2021.106737

Psarropoulos, P. N., Klonaris, G., and Gazetas, G. (2005). Seismic Earth Pressures on Rigid and Flexible Retaining walls. *Soil Dyn. Earthquake Eng.* 25, 795–809. doi:10.1016/j.soildyn.2004.11.020

Ren, S. J., Wang, C. P., and Xiao, Y. (2020). Thermal Properties of Coal during Low Temperature Oxidation Using a gray Relational Method. *Fuel* 260. Article ID 116287. doi:10.1016/j.fuel.2019.116287

Seed, H. B., and Whiteman, R. V. (1970). "Design of Earth Retaining Structures for Dynamic Load,"in *Lateral Stresses in the Ground and Design of Earth Retaining Structures*. ASCE, 103–147.s

Su, Y. H., Luo, Z. D., and Li, X. (2012). Gray Relational Analysis Method for Cut-And-Fill Roadbed Slope Stability Based on Uniform experiment. *Rock Soil Mech.* 33 (8), 2259–2264.

Sun, Z., Kong, L., Guo, A., and Alam, M. (2020). Centrifuge Model Test and Numerical Interpretation of Seismic Responses of a Partially Submerged deposit Slope. *J. Rock Mech. Geotechnical Eng.* 12, 381–394. doi:10.1016/j.jrmge.2019.06.012

Veletsos, A. S., and Younan, A. H. (1997). Dynamic Response of Cantilever Retaining Walls. *J. Geotechnical Geoenvironmental Eng.* 123 (2), 161–172. doi:10.1061/(asce)1090-0241(1997)123:2(161)

Wang, G. X. (1998). Present Situation of Landslide Control Engineering Measures at home and Abroad. *Chin. J. Geol. Hazard Control.* 9 (1), 1–9. (in Chinese).

Wang, Z., Dang, S., Xing, Y., Li, Q., and Yan, H. (2015). Applying Rank Sum Ratio (RSR) to the Evaluation of Feeding Practices Behaviors, and its Associations with Infant Health Risk in Rural Lhasa, Tibet. *Ijerph* 12 (12), 15173–15181. doi:10.3390/ijerph121214976

Xu, J., and Xu, Y. (2011). Grey Correlation-Hierarchical Analysis for Metro-Caused Settlement. *Environ. Earth Sci.* 64, 1249–1256. doi:10.1007/s12665-011-0940-0

Yan, K. M., He, J. S., and Cheng, Q. G. (2020). A Centrifuge Experimental Investigation on the Seismic Response of Group-Pile Foundation in a Slope with an Inclined Weak Intercalated Layer. *Soil Dyn. Earthquake Eng.* 130. Article ID 105961. doi:10.1016/j.soildyn.2019.105961

Yang, L. B., Gao, Y. Y., and Ling, W. X. (2011). *Principle and Application of Fuzzy Mathematics*. Guangzhou: South China University of Technology Press.

Zelikson, A., Leguay, P., and Pascal, C. (1983). Centrifugal Model Analysis of Pile and Raft Foundations Subject to Earthquakes. *Int. J. Soil Dyn. Earthquake Eng.* 2 (4), 222–227. doi:10.1016/0261-7277(83)90039-6

Zhang, J., Qu, H., Liao, Y., and Ma, Y. (2012). Seismic Damage of Earth Structures of Road Engineering in the 2008 Wenchuan Earthquake. *Environ. Earth Sci.* 65, 987–993. doi:10.1007/s12665-011-1519-5

Zhao, B., Wang, Y. S., Wang, Y., Shen, T., and Zhai, Y. C. (2017). Retaining Mechanism and Structural Characteristics of H Type Anti-slide Pile (hTP Pile) and Experience with its Engineering Application. *Eng. Geology.* 222, 29–37.

Zheng, T., Liu, H. S., Yuan, X. M., and Qi, W. H. (2016). Experimental Study on Seismic Response of Anti-slide Piles with Anchor Cables by Centrifuge Shaking Table. *Chin. J. Rock Mech. Eng.* 35 (11), 2276–2286.

Zhou, D. P., Zhang, J. J., and Tang, Y. (2010). Seismic Damage Analysis of Road Slope in Wenchuan Earthquake. *Chin. J. Rock Mech. Eng.* 29 (3), 565–576. (in Chinese).

Conflict of Interest: The authors declare that the research was conducted in the absence of any commercial or financial relationships that could be construed as a potential conflict of interest.

frontiers | Frontiers in Earth Science

ORIGINAL RESEARCH
published: 19 May 2022
doi: 10.3389/feart.2022.908899

Late Quaternary Activity: Kouma Fault

Weimin He, Leihua Wei, Shuya Xu, Senlin Wan, Jie Yang and Mingjun Liu*

Geophysical Exploration Center, China Earthquake Administration, Zhengzhou, China

The Kouma Fault, located at the northern foot of the Mangshan Mountain in Luoyang City, Henan Province, China, is an active fault newly discovered in the field seismic geological survey. The Kouma Fault is a normal fault that is approximately 30 km in length, near the east-west strike, and the north dip. The study on the nature of the Quaternary activity of the Kouma Fault is of great significance to the potential seismic source zone division, urban and rural land planning, site selection for major projects, the assessment and prevention of earthquake disaster risk. Through a series of seismic geological surveys, 12 fault outcrops were discovered, which were all distributed on the slopes of the loess gullies. The Kouma Fault cuts loess, clay, sand, and gravel. The fault planes and scratch can be seen clearly. The filling in the fault zone is dominated by clay, loess, and pebbles, among others. When the width of the fault zone is smaller (10–30 cm), most clay in the zone is laminated in occurrence. The laminated surface is almost parallel to the fault plane and the long axis direction of pebbles in the fault zone is almost parallel to the fault plane. When the width of the fault zone is greater (for instance, 1.6 m), the clay and loess in the fault zone are massive. The composite drilling geological section and trench reveal two paleoseismic events of the Kouma Fault, the paleoseismic event I occurred at the fault in the Middle Pleistocene; the paleoseismic event II occurred at the fault in the later period of the Late Pleistocene, and the vertical offset of the upper Pleistocene bottom boundary is 13.57 m. Based on the OSL age data in the fault G1 outcrop of the fault and TC1 and TC2 trenches, the latest activity age of the Kouma Fault may be defined within the range of (38.84 ± 4.69) to (40.90 ± 4.45) kaB.P. The latest active age of the Kouma fault is the late of Late Pleistocene. The average vertical slip rate of the fault during the Late Pleistocene has been 0.11 mm/a.

Keywords: active fault, trenching, composite drilling geological section, OSL, loess, Mangshan Mountain, Kouma fault

OPEN ACCESS

Edited by:
Hanchao Jiang,
China Earthquake Administration, China

Reviewed by:
Lichun Chen,
Guilin University of Technology, China
Ma Yinsheng,
Chinese Academy of Geologi-cal Sciences (CAGS), China
Mingjian Liang,
Independent researcher, China

****Correspondence:***
Weimin He
wmhe65@163.com

Specialty section:
This article was submitted to Structural Geology and Tectonics, a section of the journal Frontiers in Earth Science

Received: *31 March 2022*
Accepted: *02 May 2022*
Published: *19 May 2022*

Citation:
He W, Wei L, Xu S, Wan S, Yang J and Liu M (2022) Late Quaternary Activity: Kouma Fault. Front. Earth Sci. 10:908899. doi: 10.3389/feart.2022.908899

1 INTRODUCTION

The Kouma Fault is a newly discovered and named active fault by the seismic and geological survey works conducted in recent years, located at the northern foot of the Mang Mountain in Luoyang, Henan, China, and adjacent to the Yellow River in the northern direction (He, 2022). The Western Henan where the Kouma Fault is located features dense cities and towns, large populations, and a prosperous economy. The local people have high demands on their safety and prevention against earthquake disaster risks. It is of great significance for the division of potential hypocenters in Western Henan, urban and rural land planning, siting of significant projects, and evaluation, prevention, and control of earthquake disaster risks to research on the Late Quaternary activity of the Kouma Fault. The seismic and geological survey, trenching, drilling, and radiometric dating are substantial means to research on the fault activity, and abundant achievements have been obtained

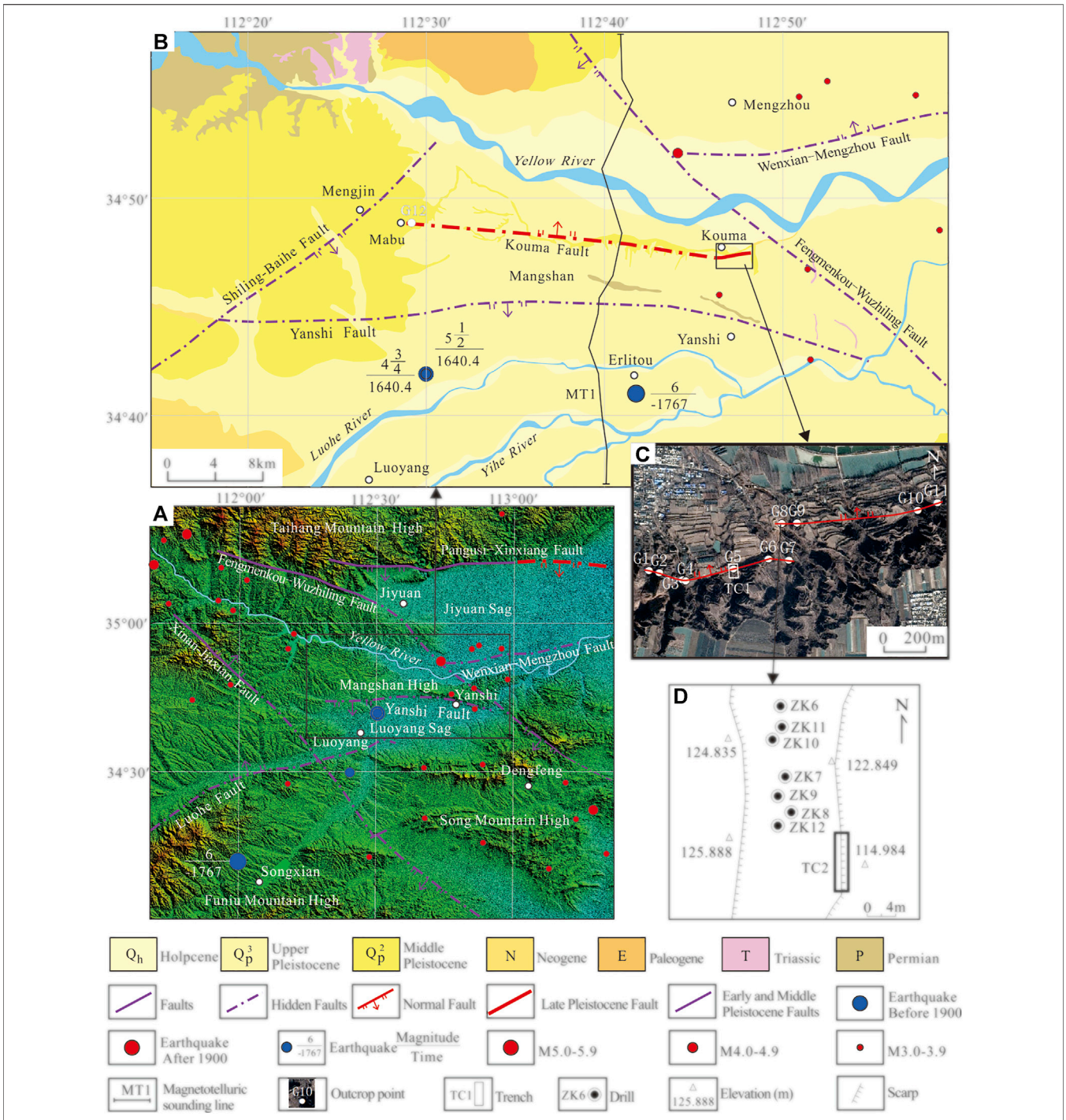

FIGURE 1 | The seismic and geological map of the study area. **(A)** Distribution map of main faults and earthquakes in study area. **(B)** The seismic and geological map of Kouma rigion. **(C)** The location map of fault outcrop points and trench. **(D)** The location map of trench and drills.

(Jiang et al., 2000; Ran et al., 2014a; Ran et al., 2014b; Ran et al., 2018; Wang et al., 2015; Min et al., 2016; Sun et al., 2016; Cao et al., 2018; Li et al., 2019). Some scholars (Wang et al., 2004; Pan et al., 2005; Bi et al., 2018; Ran et al., 2018; Li et al., 2020; Luo et al., 2020; Ma et al., 2020; Yu et al., 2020; Chang et al., 2021; Ha et al., 2021; Li et al., 2021; Liu et al., 2021; Lu et al., 2022; Shi et al., 2022) have established the loess-paleosol series of the Mang Mountain through research on loess and paleomagnetic test data of the mountain. Some scholars have obtained the occurrence of the Kouma Fault at the buried position (He, 2022), but the activity of the Kouma Fault is not demonstrated. Based on the seismic and geological survey, trenching, drilling, and radiometric dating,

among others, this study carries out comprehensive research on the Late Quaternary activity of the Kouma Fault, providing scientific evidence for earthquake prevention and disaster reduction in this region.

2 GEOLOGICAL SETTING

Kouma fault is surrounded by the Jiyuan sag on the north and Mangshan mountain on the south (**Figures 1A,B**). The south of Mangshan mountain is Luoyang sag. In the study area, the major Quaternary faults includ Xinan-Jiaxian fault, Fengmenkou-Wuzhiling fault, Luohe fault, Pangusi-Xinxiange fault, Yanshi fault, and Wenxian-Mengzhou fault. Among them, the Xinan-Jiaxian fault, the Fengmenkou-Wuzhiling fault, the Luohe fault, the Yanshi fault, the Pangusi-Xinxiange fault, and the Wenxian-Mengzhou fault are the early and middle Pleistocene faults. In addition, the last active times of the Pangusi-Xinxiang fault are the early and middle Pleistocene in the western section, the late Pleistocene in the middle section, and the early and middle Pleistocene in the eastern section (outside the figure) respectively. The Yanshi fault belongs to one of the northern marginal faults of the Luoyang sag.

The Kouma Fault is located in the western part of the Henan Province, China, which ranges from the Mabu Village, Mengjin County in the west to the Kouma Village, Mengjin County in the east. The Kouma Fault is a normal fault, with a strike of almost west-east, and a dip of the north (**Figure 1B**). The length of the Kouma Fault is calculated based on the distance from the outcrop of the fault at the most western end to that at the most eastern end, namely, and is approximately 30 km.

The Kouma fault is one of the southwest marginal faults of the Jiyuan sag, which is an inherited subsidence basin in the Mesozoic and Cenozoic, with a subsidence range of 6,000–9,000 m. The subsidence rate of Jiyuan sag has weakened since the Neogene and formed a tilted basin rising in the north and falling in the south, with the corresponding deposit thickness is 200–400 m.

The maximum historical earthquake in the study area is the 1767 B.C Yanshi Earthquake, which had a magnitude of 6 (**Figures 1A,B**).

3 MATERIAL AND METHODS

Using the method of seismic and geological survey, 12 fault outcrops (**Figures 1A,B**) have been found in the Kouma Fault through the seismic and geological survey, all of which are located on the slope of the loess gully. There are 11 outcrops (G1–G11) in the southeastern part of the Kouma Village, and there is one outcrop (G12) at the eastern part of the Mabu Village. Among them, the fault plane in some fault outcrops occurs in the valleys and steep cliffs, and those in other fault outcrops are covered by slope deposits that have to be exposed by manual excavation. The Kouma Fault cuts loess, clay, sand, and gravel. The fault planes and scratch can be seen clearly. From a top view, the Kouma fault is hidden in Malan loess. The typical fault outcrops are introduced hereunder.

The G5 and G8 outcrops of the fault with the existence of the Late Pleistocene loess (Malan Loess) were selected to carry out trenching work, and the numbers of the trenches are TC1 and TC2 (**Figures 1C,D**), respectively. After the excavation of every trench and leveling-down treatment of the trench wall, we hung the square grid line with a side length of 1 m on the surface of the trench wall, then carried out the measurement, geological record, photography, and age sampling and testing, and then carried out comprehensive research. The OSL age was tested at Key Laboratory of Crustal Dynamics, Institute of Crustal Dynamics, CEA, and the ESR age was tested at Measurement and Testing department of China Institute of Atomic Energy.

In TC1 and TC2 trenches, the equivalent stratum in the footwall (hanging wall) of the fault has not been revealed. The drilling survey was carried out on the hanging wall of the TC2 trench, and seven holes were drilled with a depth of 21–42 m (**Figure 1D**) to obtain the vertical fault throw and slip rate of the fault.

In order to detect the deep structure of the Kouma fault, a 48.36 km magnetotelluric sounding line named MT1, was arranged across the Kouma fault and Mangshan Mountain (**Figure 1B**). The V8 networked multi-function electrical instrument of Phoenix geophysical company of Canada was used for field data acquisition, and 14 broadband magnetotelluric sounding points were completed, of which 2 are inspection points. The collected frequency range is 320–0.000137 hz. Five electromagnetic field components of Ex, Ey, Hx, Hy, and Hz were collected on the magnetotelluric sounding points.

4 RESULTS

4.1 Seismic and Geological Survey

The typical fault outcrop points discovered through seismic and geological survey are introduced as follows.

4.1.1 G1 Outcrop of Fault

As shown in **Figures 2A–C**, the footwall (hanging wall) stratum revealed by the G1 outcrop of fault is almost consistent with the loess-paleosol series of the Mang Mountain (Wang et al., 2004). Among them, the U4 paleosol stratum is S11; the U11 loess stratum is L8, and the paleomagnetism B/M boundary located at the bottom of L8; the U16 paleosol stratum is S5; the U23 loess stratum is L2, where the age data of 1 OSL is (74.75 ± 8.79) ka.

The surface of the hanging wall (footwall) of the fault is the U13 loess stratum, where the age data of 1 OSL is (95.13 ± 10.67) ka (**Figure 2A**; **Table 1**). Subject to the offset impact of the fault, there are some missing points for the U22 paleosol stratum of the hanging wall of the fault located adjacent to the fault; the thickness of the U21 paleosol stratum varies greatly, and the paleosol stratum is up-warping towards the near-fault direction in terms of spatial distribution (**Figures 2A,B**).

The fault revealed by the G1 outcrop is a normal fault, and the fault plane and fault zone are clear (**Figures 2A–C**). The width at the middle-upper part of the fault is within the range of 2–8 cm, and the width at the lower part may reach 30 cm. The filling in the

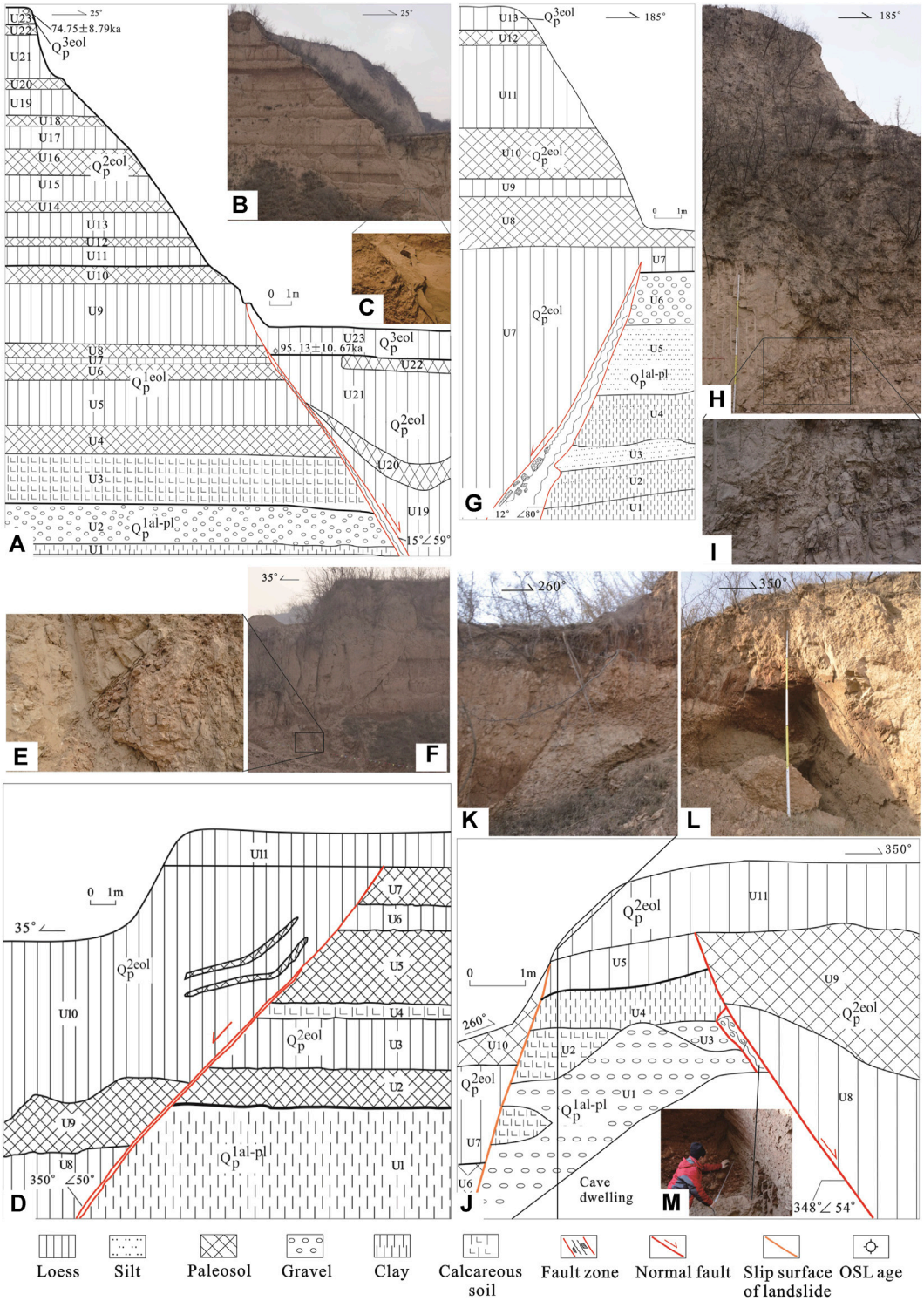

FIGURE 2 | The photographs and explanation of the typical outcrops of Kouma Fault. **(A)** The geological profile of G1 outcrop. **(B)** The panoramic photographs of G1. **(C)** The photographs of fault zone of G1 outcrop. **(D)** The geological profile of G2 outcrop. **(E)** The photographs of fault zone of G2 outcrop. **(F)** The panoramic photographs of G2. **(G)**The eological profile of G3 outcrop. **(H)** The panoramic photographs of G3. **(I)** The photographs of fault zone of G3 outcrop. **(J)** The geological profile of G6 outcrop. **(K)** The photographs on the left of G6. **(L)** The photographs on the middle and right of G6. **(M)** The photographs of fault zone of G6 outcrop.

TABLE 1 | OSL dating results of the Kouma Fault.

Sampling Site	Laboratory Number	Testing Method	U (μg/g)	Th (μg/g)	K (%)	Water Content (%)	Environmental Dose Rate (Gy/Ka)	Equivalent Dose (Gy)	Age (Ka)
G1	19-OSL-250	SMAR	2.27	11.20	1.75	3.78	3.81 ± 0.28	284.43 ± 25.81	74.75 ± 8.79
G1	19-OSL-251	SMAR	2.21	11.60	1.79	5.14	3.79 ± 0.28	360.63 ± 30.43	95.13 ± 10.67
TC1	18-OSL-182	SMAR	2.34	10.00	1.95	2.39	4.02 ± 0.31	178.67 ± 13.71	44.49 ± 4.81
TC1	18-OSL-182r	SMAR	2.34	10.00	1.95	2.39	4.02 ± 0.31	162.07 ± 8.22	40.36 ± 3.70
TC1	18-OSL-183	SMAR	2.35	10.20	1.93	1.97	4.04 ± 0.31	156.86 ± 14.64	38.84 ± 4.69
TC1	19-OSL-242	SMAR	2.01	11.50	1.87	6.55	3.65 ± 0.27	292.62 ± 30.62	80.22 ± 10.32
TC1	19-OSL-243	SMAR	2.08	10.90	1.62	5.89	3.40 ± 0.25	233.38 ± 19.07	68.59 ± 7.60
TC1	19-OSL-244	SMAR	2.36	11.40	1.84	1.26	4.01 ± 0.31	257.12 ± 18.93	64.19 ± 6.90
TC2	18-OSL-178	SMAR	2.26	10.10	1.96	2.68	3.85 ± 0.30	161.73 ± 7.37	42.06 ± 3.83
TC2	18-OSL-178r	SMAR	2.26	10.10	1.96	2.68	3.85 ± 0.30	168.58 ± 9.42	43.84 ± 4.24
TC2	18-OSL-180	SMAR	2.36	10.90	2.02	2.49	4.10 ± 0.32	228.11 ± 24.72	55.63 ± 7.42
TC2	18-OSL-181	SMAR	2.33	11.00	2.01	3.74	4.03 ± 0.31	215.87 ± 16.89	53.55 ± 5.86
TC2	19-OSL-246	SMAR	2.61	10.80	1.81	5.01	3.78 ± 0.28	304.34 ± 22.67	80.51 ± 8.56
TC2	19-OSL-247	SMAR	2.10	8.75	1.63	4.41	3.27 ± 0.25	222.53 ± 18.98	68.15 ± 7.82
TC2	19-OSL-248	SMAR	2.54	10.80	1.81	1.44	3.99 ± 0.31	163.3 ± 12.44	40.90 ± 4.45

fault zone is dominated by the grayish-yellow and yellowish-brown loess, which is massive. The latest stratum offset by the fault is the loess at the U23 stratum, and the overlying stratum is lacking above the fault up-break point.

At the G1 outcrop of the fault, the measured occurrence of the fault plane is 15°∠59°.

4.1.2 G2 Outcrop of Fault

As shown in **Figure 2D**, the footwall stratum of the fault revealed by the G2 outcrop of the fault is the Lower Pleistocene Series clay stratum, and the Middle Pleistocene Series paleosol stratum and loess stratum. The hanging wall stratum of the fault is the Middle Pleistocene Series paleosol stratum and loess stratum. Among them, the thickness of the U9 paleosol stratum varies greatly; there are two pieces of paleosol belts in the U10 loess stratum, the upper part of which is spread approximately in parallel with the fault plane, and the lower part of which has less inclination. The spatial spread shape of the paleosol belt in the U10 loess stratum is related to the offset activity of the fault.

The fault revealed by the G2 outcrop fault is a normal fault, and the fault plane and fault zone are clear (**Figures 2D–F**). The width of the fault zone is within the range of 10–20 cm. The fault zone becomes convergent upwards and narrows down, and then pinches out at the bottom of the U11 loess stratum of the Middle Pleistocene Series. The filling of the fault zone is dominated by red clay and yellowish-brown loess, which are laminated in occurrence. The laminated surface is distributed almost in parallel with the fault plane.

The G2 outcrop reveals that the latest active age of the fault is the Middle Pleistocene. At the G2 outcrop of the fault, the measured occurrence of the fault plane is 350°∠50°.

4.1.3 G3 Outcrop of Fault

As shown in **Figure 2G**, the footwall stratum of the fault revealed by the G3 outcrop of fault is the clay, silty-sand, and pebble stratum of the Lower Pleistocene Series. The hanging wall stratum of the fault is the Middle Pleistocene Series paleosol stratum and loess stratum.

The fault revealed by the G3 outcrop is a normal fault, and the fault plane and fault zone are clear (**Figures 2G–I**). The width of the lower part of the fault zone is 1.6 m and the fault zone becomes convergent upwards and narrows down. Subject to the blocking effect of slope surface deposits at the upper part of the fault outcrop, the location of the fault up-breakpoint is relatively fuzzy. According to the preliminary judgment, the fault up-breakpoint will pinch out upwards on top of the U7 loess stratum of the Middle Pleistocene Series. The filling in the fault zone is dominated by the grayish-yellow, which is massive; it contains the purple-red clay mass, whose surface is developed with the grayish-black ferromanganese thin film. It contains a few pebbles with good roundness and also contains the grayish-white calcium mass, grayish-yellow, and grayish-green silty sand mass.

The G3 outcrop reveals that the latest active age of the fault is the Middle Pleistocene. At the G3 outcrop of the fault, the measured occurrence of the fault plane is 12°∠80°.

Therefore, the G3 outcrop of fault is covered by the slope surface deposits of loess valleys, which are exposed by manual excavation only.

4.1.4 G6 Outcrop of the Fault

As shown in **Figure 2J**, the footwall stratum of the fault revealed by the G6 outcrop of fault is pebble, calcium soil, clay, paleosol, and loess clay stratum of the Lower Pleistocene Series. The hanging wall stratum of the fault is the Middle Pleistocene Series paleosol stratum and loess stratum.

The fault revealed by the G6 outcrop is a normal fault, and the fault plane and fault zone are clear (**Figures 2J–M**). The width of the upper part of the fault zone is 20 cm, and the fault zone pinches out upwards at the bottom of the U11 loess stratum of the

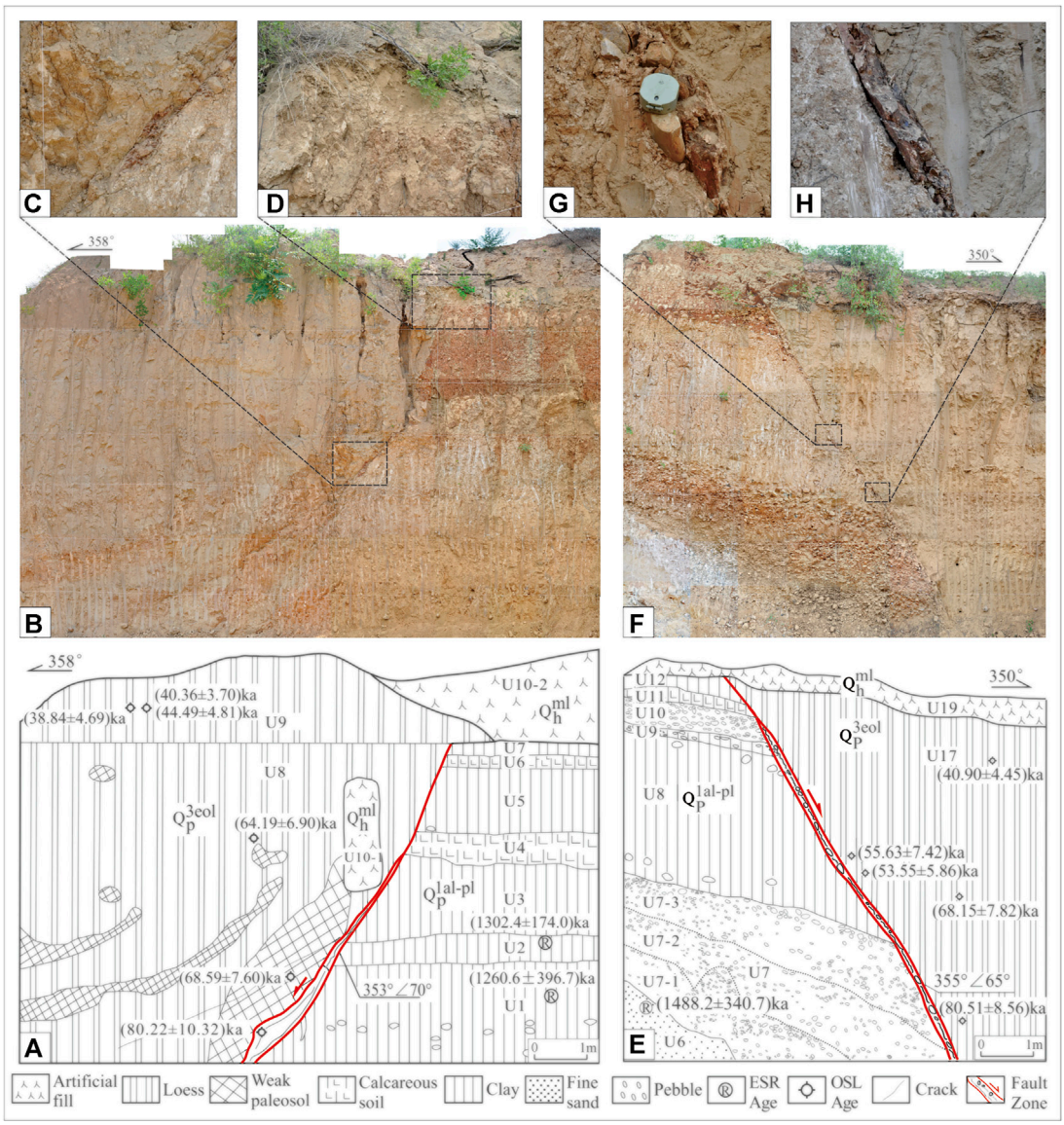

FIGURE 3 | The photographs and explanation of TC1 Trench (Left) and TC2 Trench (Right) of Kouma Fault. **(A)** The geological profile of TC1 trench. **(B)** The splicing photograph of TC1 trench. **(C)** The photograph of fault zone of TC1 trench. **(D)** The photograph of up-break point of TC1 trench. **(E)** The geological profile of TC2 trench. **(F)** The splicing photograph of TC2 trench. **(G)** The photograph of fault zone of TC2 trench. **(H)** The photograph of fault zone of TC2 trench.

Middle Pleistocene Series. The filling in the fault zone is dominated by the brownish red loess, which is massive but includes a few pebbles. The upper fault plane is brownish-red, and the striations of the fault are clear and longitudinal.

The G6 outcrop reveals that the latest active age of the fault is the Middle Pleistocene. At the G6 outcrop of the fault, the measured occurrence of the fault plane is 348°∠54°.

Notably, a landslide exists on the left side of the G6 outcrop of the fault (**Figure 2K**), and the landslide body consists of the U6 paleosol stratum, the U7 loess stratum, and the U10 paleosol stratum. Seemingly, this landslide looks like a normal fault, which is prone to cause misjudgment. The landslide body is located at the slope of the loess valley, namely, the free face, and the sliding surface of the landslide is almost in parallel with the slope surface of the loess valley.

4.2 Trenching

4.2.1 TC1 Trench

The TC1 trench is 11 m long and 6.4–8.8 m high (deep). See **Figure 3A** for the geological section of the trench wall and **Figure 3B** for the splicing photos of the trench wall. See **Table 2** for the main strata revealed by the TC1 trench, **Table 1** for OSL age data, and **Table 3** for ESR age data.

In the U8 stratum of the hanging wall, the grain size of weak paleosol mass ranges from 1 to 3 cm (smaller ones) to 30–40 cm (larger ones), and they are distributed in the grayish-yellow loess

TABLE 2 | Main strata revealed by TC1 trench.

Number of Stratum	Lithology	Geological Description	Geological Age and Origin Type	Location of Stratum
U1	Clay	It is yellowish brown, and contains the grayish white caliche nodules and grayish black ferromanganese nodules, and a few pebbles distributed in the shape of scattered beads (the mother rock is purple-red sandy rock) with the particle size of 3–8 cm, in the ellipsoidal shape, and with its surface being enveloped by the white grayish white calcium content; the soil texture is hard. A ESR sample age: (1,260.6 ± 396.7) ka	Q_p^{1al-pl}	Footwall stratum of the fault
U2	Clay	It is yellowish brown, and contains the grayish white caliche nodules and a few grayish black ferromanganese spots; the soil texture is hard. A ESR sample age: (1,302.4 ± 174.0) ka	Q_p^{1al-pl}	
U3	Clay	It is light grayish white and contains a great number of grayish white caliche nodules; the soil texture is hard	Q_p^{1al-pl}	
U4	Calcium soil	It is grayish white, and has the square structure, and the vertical fissure is developed; the soil texture is hard	Q_p^{1al-pl}	
U5	Clay	It is brownish red, and has the square structure, grayish black ferromanganese thin film and a few caliche nodules, and the pebbles with the grain size of 10–15 cm are occasionally found; the soil texture is hard	Q_p^{1al-pl}	
U6	Calcium soil	It is grayish white, and has the short square-cylinder-shaped structure, and the vertical fissure is developed; the soil texture is hard	Q_p^{1al-pl}	
U7	Clay	It is brownish red, and has the square structure, grayish black ferromanganese thin film and a few caliche nodules; the soil texture is hard	Q_p^{1al-pl}	
U8	Loess	It is grayish yellow, and contains a few white snail shells and a few caliche nodules. It contains the light reddish brown weak paleosol masses or belts. Two OSL samples age: (64.19 ± 6.90) and (68.59 ± 7.60) ka	Q_p^{3eol}	Hanging wall stratum of the fault
U9	Loess	It is grayish yellow, and contains a few white snail shells and a few caliche nodules. Three OSL samples age: (38.84 ± 4.69), (44.49 ± 4.81), and (40.36 ± 3.70) ka	Q_p^{3eol}	Hanging wall stratum of the fault
U10-1	Artificial fill	It is dominated by the grayish yellow loess, which is the artificially deposited soil. The greenish gray tiles may be found at bottom, the soil texture is loose, and the large pore may be found	Q_h^{ml}	Overlying stratum of the fault
U10-2	Artificial fill	It is dominated by the grayish yellow loess, which is the artificially deposited soil on the surface. The tree roots may be found, and the soil texture is loose. It is piled up by manual excavation	Q_h^{ml}	Overlying stratum of the fault

in the shape of scattered beads, and the weak paleosol belt is spread approximately in parallel with the fault plane; alternatively, its lower end is arc-shaped, extends northwards, and gradually levels off (**Figure 3A**); the spatial distribution characteristics of the weak paleosol mass or belt are caused by the offset of the fault.

The fault revealed by the TC1 trench is a normal fault, with a clear fault plane and fault zone (**Figures 3A–D**). The fault zone is generally wide at the bottom and narrow at the top, becomes convergent upwards, and then narrows down on top of the U8 loess stratum (**Figures 3B,D**), meaning the upper breakpoint of the fault is located on top of the U8 loess stratum. The overlying stratum of the up-breakpoint is the U9 loess stratum. The ages of three OSL samples are (38.84 ± 4.69), (44.49 ± 4.81), (40.36 ± 3.70) ka, respectively (**Figure 3A**; **Tables 1**, **2**). The latest active age of the fault is the late of Late Pleistocene revealed by TC1 trench. The width of the middle-up part of the fault zone is within the range of 5–10 cm. The filling is dominated by clay, which is reddish-brown, and laminated in occurrence. The laminated surface of the filling is distributed almost in parallel with the fault plane (**Figures 3B,C**). The striations on the fault plane are clear and almost vertical to the strike line of the fault plane. The

TABLE 3 | ESR dating results of the kouma Fault.

Sampling Site	Sample Serial Number	Annual dose (Gy·ka^{-1})	Paleo dose (Gy)	Age (ka)
TC1	KM-TC1-ESR-01	2.89	3,645 ± 1,147	1,260.6 ± 396.7
TC1	KM-TC1-ESR-02	3.41	4,447 ± 594	1,302.4 ± 174.0
TC2	KM-TC2-ESR-01	2.65	3,940 ± 902	1,488.2 ± 340.7
ZK11	KM-ZK11-ESR-03	3.55	3,588 ± 806	1,011.9 ± 227.3
ZK11	KM-ZK11-ESR-04	3.19	4,262 ± 725	1,337.7 ± 227.6

TABLE 4 | Main Strata Revealed byTC2 Trench.

Number of Stratum	Lithology	Geological Description	Geological Age and Origin Type	Location of Stratum
U6	Fine sand	It is off-white and contains the grayish white calcium mass and clay mass; the sand texture is loose. A ESR sample age: (1,488.2 ± 340.7) ka	Q_p^{1al-pl}	Footwall stratum of the fault
U7-1	Pebble	The pebble surface is enveloped by the grayish white calcium, most of pebbles have the grain size of 3–5 cm, a few of pebbles have the grain size of 10–15 cm; the mother rock is dominated by the greenish gray sandstone and a few mother rocks are purple-red sandstone, and they have good roundness and ellipsoidal shape; the filling is dominated by the light gray silty sands and is rich in calcium content; the local semi-cementation is found	Q_p^{1al-pl}	
U7-2	Pebble	Most of pebbles have the grain size of 2–4 cm, a few of pebbles have the grain size of 10–20 cm, and they have good roundness and ellipsoidal shape; the mother rock is dominated by the greenish gray sandstone; the filling is dominated by the reddish brown clay and contains the gray medium-fine sand and a few calcium masses; it is dense	Q_p^{1al-pl}	
U7-3	Pebble	The pebble surface is enveloped by the white calcium, most of pebbles have the grain size of 2–5 cm, a few of pebbles have the grain size of 10–20 cm, and they have good roundness and ellipsoidal shape; the mother rock is dominated by the greenish gray sandstone; the filling is dominated by the reddish brown clay and contains the calcium content; it is dense	Q_p^{1al-pl}	
U8	Clay	It is grayish yellow, and the grayish white calcium content is high. It contains a few pebbles (with the grain size of 10–15 cm), they have good roundness and ellipsoidal shape, and they are scattered at top and bottom of the stratum	Q_p^{1al-pl}	
U9	Clay	It is brownish red and contains the grayish white caliche nodules; the soil texture is hard. It contains the pebbles (with the grain size of 10–20 cm), and they have good roundness and ellipsoidal shape	Q_p^{1al-pl}	
U10	Pebble	The pebbles have the grain size of 10–15 cm, and they have good roundness and ellipsoidal shape; the filling is dominated by the reddish brown clay and it is dense	Q_p^{1al-pl}	
U11	Calcium soil	It is grayish white, and has the square structure, and the vertical fissure is developed; the soil texture is hard	Q_p^{1al-pl}	
U12	Clay	It is brownish red and contains a few pebbles (with the grain size of 4–6 cm) and grayish black ferromanganese thin film, and has the square structure and the vertical fissure is developed; the soil texture is hard	Q_p^{1al-pl}	
U17	Loess	It is grayish yellow, and contains a few white snail shells and a few caliche nodules. Five ESR samples age: (40.90 ± 4.45), (55.63 ± 7.42), (53.55 ± 5.86), (68.15 ± 7.82), and (80.51 ± 8.56) ka	Q_p^{3eol}	Hanging wall stratum of the fault
U19	Artificial fill	It is dominated by the grayish yellow loess and reddish brown clay, and the ash pit is locally found, which is the artificial soil deposited on surface. The tree roots may be found, and the soil texture is loose	Q_h^{ml}	Overlying stratum of the fault

medium laminated clay of the fault zone is mainly developed by the clay in the hanging wall of the fault (footwall) during the offset process. The filling at the lower part of the fault zone is dominated by the loess, which is grayish-yellow and 40 cm wide (thick). It contains white caliche nodules and a brownish-red clay mass. The loess in the lower part of the fault zone is loess in the hanging wall (footwall) of the fault zone that is residual in the new fault zone during the offsetting process. The age of the loess OSL sample in the fault zone is (80.22 ± 10.32) ka, but it does not indicate the offsetting age of the fault. The main cause is that the loess at this location is not fully exposed during the offsetting process.

At the TC1 trench, the measured occurrence of the fault plane is 353°∠70°.

4.2.2 TC2 Trench

The TC2 trench is 8 m long and 8.0–8.6 m high (deep). See **Figure 3E** for the geological section of the trench wall and **Figure 3F** for the splicing photos of the trench wall. See **Table 4** for the main strata revealed by the TC2 trench.

It should be noted that: 1) the U7 stratum consists of the U7-1 stratum, U7-2 stratum, and U7-3 stratum. 2) There is a path on top of the TC2 trench, and a scarp at the height of 2.6–3.4 m above the road surface is located on the western side of the path (**Figure 1D**), which reveals the U18 loess stratum (**Figure 4**).

The fault revealed by the TC2 trench is a normal fault, and the fault plane and fault zone are clear (**Figures 3E–H**). The fault zone is generally wide at the bottom and narrow at the top, becomes convergent upwards and then narrows down on top of the U17 loess stratum (**Figures 3E,F**), that is, the overlying stratum of the upper breakpoint of the fault is the U18 loess stratum. The ages of two OSL samples are (42.06 ± 3.83) and (43.84 ± 4.24)ka, respectively (**Figure 4**; **Tables 1**, **5**). The latest active age of the fault is the late of Late Pleistocene revealed by TC2 trench. The width of the fault zone is within the range of

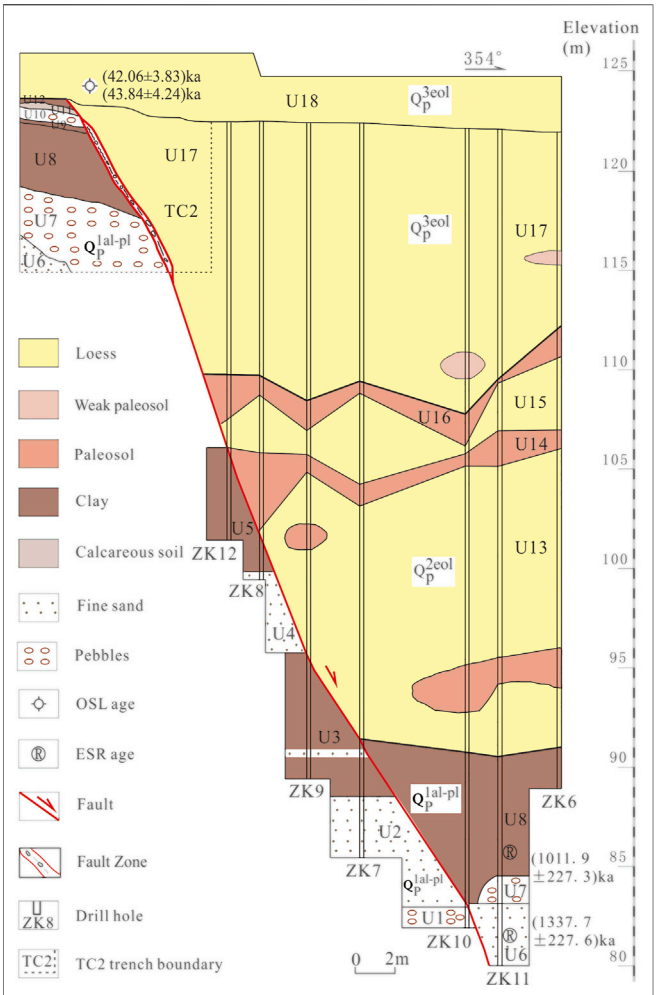

FIGURE 4 | The comprehensive interpretation map of trench and composite drilling geological section.

10–20 cm. The filling is dominated by clay, which is reddish-brown and dark-brown in color, and laminated in occurrence. The laminated surface of the filling is distributed almost in parallel with the fault plane (**Figure 3H**); the medium laminated clay of the fault zone is mainly developed by the clay in the hanging wall of the fault (footwall) during the offset process. The local filling is of pebble (with a grain size of 10–15 cm), and the long axis of the pebble is almost in parallel with the fault plane (**Figure 3G**). The fault zone contains the white calcium mass and laminated clay inclusive of grayish-black ferrimanganic content; the striations on the fault plane are clear and almost vertical to the strike line of the fault plane.

At the TC2 trench, the measured occurrence of the fault plane is 355°∠65°.

4.3 Drilling Survey

The obtained combined composite drilling geological section, the TC2 trench profile sketch, and the geological profile of the scarp on the western side of path on top of the TC2 trench (**Figure 1D**) were drawn together, as shown in **Figure 4**. The main strata revealed by the combined drilling geological profile are shown in **Table 5**.

As shown in **Figure 4**, the top interfaces of the U1 pebble stratum (in borehole ZK10), the U3 clay stratum (in boreholes ZK7 and ZK9), and the U5 clay stratum (in boreholes ZK8 and ZK12) are fault planes. On the top and bottom of the fault plane, the lithologic characteristics of the stratum in a borehole may vary greatly. The fault plane occurrence revealed by the drilling has a good consistency with that revealed by the TC2 trench (He, 2022).

The stratum surface of the hanging wall of the faults such as the U10 paleosol stratum, U11 loess stratum, and U12 paleosol stratum revealed by drilling are uneven; the paleosol mass and weak paleosol mass exist in the loess stratum. These phenomena are related to fault activity.

In terms of the ESR age data, the ESR age [(1,337.7 ± 227.6) ka] for the U6 fine sand stratum of the hanging wall of the fault revealed by drilling is closer to that [(1,488.2 ± 340.7) ka] for the U6 fine sand of the footwall of the fault revealed by TC2 trench. Through the comparison and analysis conducted in combination with the lithologic characteristics of the stratum, it is found that the U6 fine sand stratum, U7 pebble stratum, and U8 clay stratum of the hanging wall of the fault revealed by drilling (**Figure 4**; **Table 5**) are the equivalent strata (strata of the same age) with the U6 fine sand stratum, U7 pebble stratum and U8 clay (**Figure 3E**, **Figure 4**, **Table 4**) stratum of the footwall of the fault revealed by drilling, respectively.

According to the measurement of the composite drilling geological section and the TC2 trench, the elevation difference of the top interface of the U8 clay stratum (bottom interface of the U13 loess stratum) is 29.02 m, and the elevation difference of the bottom surface of the U17 loess stratum is 13.57 m.

4.4 Magnetotelluric Sounding

Non-linear Conjugate Gradient Inversion was used to process the magnetotelluric sounding data and the magnetotelluric two-dimensional electrical interpretation map was obtained (**Figure 5**). In the upper part of the profile with a depth of 5 km, the apparent resistivity value directly below Mangshan is significantly higher than that of Luoyang sag and Jiyuan sag on both sides. The Yanshi fault interpreted between Mangshan and Luoyang sag, is regarded as a normal fault apparent dipping to the south. Between Mangshan and Jiyuan sag, a fault can also be interpreted, named the Kouma fault, it is a normal fault with an apparent dip to the north. Mangshan is a bulge relative to Luoyang sag and Jiyuan sag. Mangshan is a bulge relative to Luoyang sag and Jiyuan sag, which form a horst structure.

5 DISCUSSION

5.1 Evidence of Kouma Fault

According to the seismic and geological survey, 12 Quaternary outcrops were discovered along the Kouma fault (**Figures 1B,C**, **2**). From the perspective of landform, there seems to be a loess landslide sliding northward (towards the Yellow River) at the

north edge of Mangshan Mountain in the southeast of Kouma village, however, through the investigation of all the Loess gullies developed in the north-south direction (some with a depth of 96 m), there is no sliding surface of landslide sliding in the north direction with steep upper part and gentle lower part. In addition, landslides sliding eastward (towards the gully) have also been discovered in the loess slopes on both sides of the Loess Gully (**Figures 2J,K**).

The composite drilling geological section located in the hanging wall of the Kouma fault also indicates the existence of the fault (**Figure 4**).

Magnetotelluric sounding MT1 section also reflects the existence of faults on the northern edge of Mangshan Mountain (**Figure 5C**).

Certainly, further work is needed on the research of Kouma fault, such as shallow seismic exploration and drilling.

5.2 Activity Analysis of the Kouma Fault

Through the above works such as trenching, drilling, and radiometric dating, among others, the composite drilling geological section and the TC2 trench reveal two paleoseismic events of the Kouma Fault (**Figure 6**).

Event I: In the Middle Pleistocene, the paleoseismic events occurred at the fault, and both the hanging wall and the footwall of the fault are the Middle Pleistocene stratum and the Lower Pleistocene stratum (**Figure 6A**). After the Middle Pleistocene stratum of the fault footwall was completely eroded, it accumulated the eolian loess of the Late Pleistocene (**Figure 6B**). In Event I, the vertical fault throw for the bottom interface of the Middle Pleistocene (the bottom interface of the U13 loess stratum in **Figure 4**) is 15.45 m.

Event II: In the later period of the Late Pleistocene, the paleoseismic events occurred to the fault again, which offset

TABLE 5 | Main strata revealed by drilling.

Number of Stratum	Lithology	Geological Description	Geological Age and Origin Type	Location of Stratum
U1	Pebble	The pebbles have the grain size of 10 cm, and they have good roundness and ellipsoidal shape; the mother rock is dominated by the quartz sandstone; the filling is dominated by the light yellow clay and contains the purple-red silty sands, blackish gray coarse sands and grayish white calcium content	Q_p^{1al-pl}	Footwall stratum of the fault
U2	Fine sand	It is brownish yellow and grayish yellow, and the calcium content is high	Q_p^{1al-pl}	
U3	Clay	It is light reddish brown and brown, and interlayered with the thin sand stratum, and also contains the grayish black ferromanganese mass, grayish white calcium mass and grayish green spot. The soil texture is hard, and the section is smooth and has the oily luster	Q_p^{1al-pl}	
U4	Fine sand	It is grayish white, and the calcium content is high	Q_p^{1al-pl}	
U5	Clay	It is light reddish brown and reddish brown, and contains the grayish white caliche nodules; it contains grayish green spots and grayish black ferromanganese thin films; the soil texture is hard, and the section is smooth and has the oily luster	Q_p^{1al-pl}	
U6	Fine sand	It is off-white and contains the grayish white calcium mass, and the clay content is high. A ESR sample age: (1,337.7 ± 227.6) ka	Q_p^{1al-pl}	Hanging wall stratum of the fault
U7	Pebble	The pebbles have the grain size of 5–10 cm, they have good roundness and ellipsoidal shape, the mother rock is dominated by the greenish gray sandstone, and the filing is the light reddish brown clay and gray fine sands, and contains the grayish white calcium content	Q_p^{1al-pl}	
U8	Clay	It is grayish yellow, and contains the grayish white caliche nodules and the caliche nodules are locally rich; the soil texture is hard, and the section is smooth and has the oily luster. A ESR sample age: (1,011.9 ± 227.3)ka	Q_p^{1al-pl}	
U13	Loess	It is yellowish brown and contains a few grayish black ferromanganese spots and a few grayish white caliche nodules with the grain size of about 2–8 cm, the reddish brown paleosol masses are interlayered	Q_p^{2al-pl}	
U14	Paleosol	It is brownish red, and contains a few grayish white caliche nodules, the grayish white calcium plinthitic stratum is locally developed, and it contains the grayish black ferromanganese spots; the soil texture is hard and the section is smooth	Q_p^{2al-pl}	
U15	Loess	It is brownish yellow, and contains the grayish white caliche nodules, the calcium is locally enriched, and the grain size of caliche nodule is within the range of 3–6 cm	Q_p^{2al-pl}	
U16	Paleosol	It is brownish red, and contains the grayish white caliche nodules and a few grayish black ferromanganese spots; the soil texture is hard and the section is smooth	Q_p^{2al-pl}	
U17	Loess	It is grayish yellow, and contains a few caliche nodules and a few white snail shells. It contains the light reddish brown weak paleosol masses	Q_p^{3eol}	
U18	Loess	It is grayish yellow, and contains a few white snail shells and a few caliche nodules. Two ESR samples age: (42.06 ± 3.83) and (43.84 ± 4.24) ka	Q_p^{3eol}	Overlying stratum of the fault

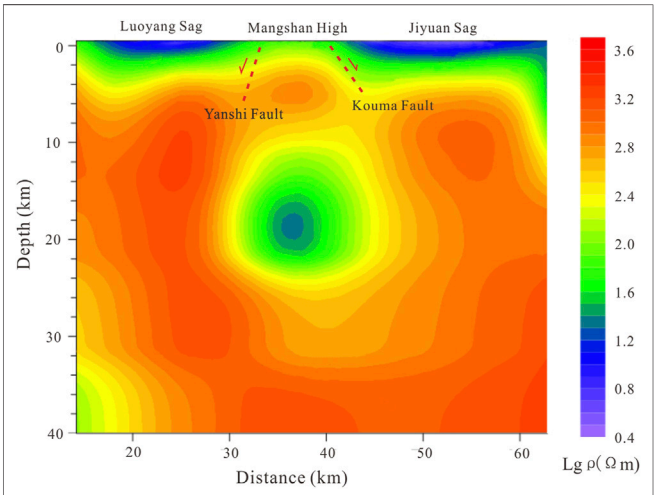

FIGURE 5 | The magnetotelluric two-dimensional electrical interpretation map.

the loess stratum of the Late Pleistocene (**Figure 6C**). After the fault scarp was completely eroded, it continued to accept the loess deposits of the Late Pleistocene (**Figure 6D**). Afterward, no further activity occurred to the fault. Subject to the effects of the loess slope erosion and human activities (for instance farming and road building), the present microgeomorphic landscape has been developed.

The faults zone revealed by TC2 trench is very clear (**Figures 3E,F**). The long axis of pebbles within the fault zone is basically parallel to the fault plane (**Figure 3G**), and the thin-layer clay is basically distributed parallel to the fault plane (**Figure 3H**). The fault zone is well preserved, it indicate that the time of fault dislocation (Paleoseismic event II) is the same as that of U17 loess sliding and covering the fault zone. The lithology and sedimentary age are completely different between U17 loess in the hanging wall of the fault and U7 pebble, U8 clay, U9 clay, U10 pebble, U11 calcareous soil, and U12 in the footwall of the fault (**Figures 3E,F** and **Figure 4**). In **Figure 4**, the weak paleosol mass in U17 layer could also be related to Paleoseismic event II. Paleoseismic event II is also revealed by TC1 trench and G1 fault outcrop.

It may be considered that paleoseismic events II have been revealed by the G1 outcrop of fault, TC1, and TC2 trenches, in view of the difference in sampling locations of OSL samples and the data errors of radiometric dating.

In the G1 outcrop of fault, the OSL sample age (74.75 ± 8.79) ka B.P in the latest offset, the U23 loess stratum can be used as the upper limit age data of the paleoseismic events II. In trial TC1 trench, the OSL sample age (64.19 ± 6.90) ka B.P in the latest U8 loess stratum offset by the fault may be used as the upper limit age data of the paleoseismic events II; the OSL sample age (38.84 ± 4.69) ka B.P, (40.36 ± 3.70) ka B.P and (44.49 ± 4.81) ka B.P in the overlying U9 loess stratum of the fault may be used as the lower limit age data of the paleoseismic events II. In trial TC2 trench, the OSL sample age (40.90 ± 4.45) ka B.P in the latest U17 loess stratum offset by the fault may be used as the upper limit age data of the paleoseismic events II; the OSL sample age (42.06 ± 3.83) and (43.84 ± 4.24) kaB.P in the overlying U18 loess stratum of the fault may be used as the lower limit age data of the paleoseismic events II. Based on these age data, the time of the paleoseismic events II may be defined within the range of (38.84 ± 4.69) to (40.90 ± 4.45) kaB.P (**Figure 7**). The latest active age of the Kouma fault is the late of Late Pleistocene.

In Paleoseismic event II, the vertical fault throw for the bottom interface of the Upper Pleistocene (the bottom interface of the U17 loess stratum in **Figure 4**) is 13.57 m, and the average vertical slip rate of the fault during the Late Pleistocene has been 0.11 mm/a.

5.3 The 1767 B.C. Yanshi Earthquake

The 1767 B.C. Yanshi earthquake had a magnitude of 6. According to "Historical strong earthquake catalog in China" (Department of earthquake disaster prevention, CEA, 1995), the 1767 B.C. Yanshi earthquake occurred in the southwest of Yanshi, Henan Province, with the epicenter (34.2°N, 112.0°E) near Song county (**Figure 1A**). Through the subsequent verification, Dong Ruishu (Dong et al., 2010) believes that the epicenter of the 1767 B.C. Yanshi earthquake is located at the Erlitou cultural site (the capital site of Xia Dynasty) in the south of Yanshi (**Figure 1B**).

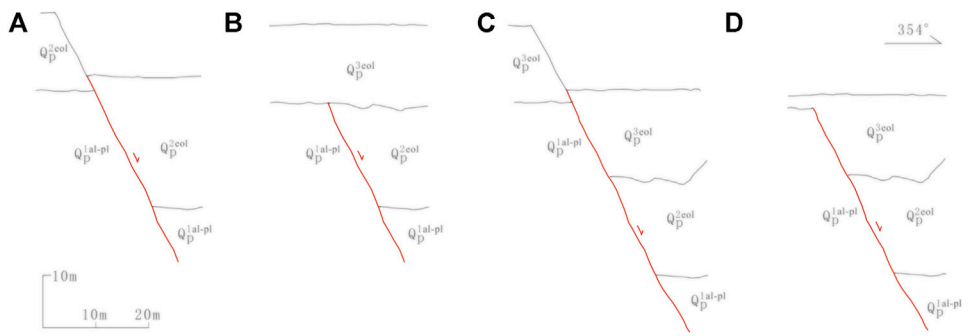

FIGURE 6 | (A) Schematic diagram of paleoseismic eventI. **(B)** Schematic diagram between paleoseismic eventI and paleoseismic eventII. **(C)** Schematic diagram of paleoseismic eventII. **(D)** Schematic diagram of present geological profile.

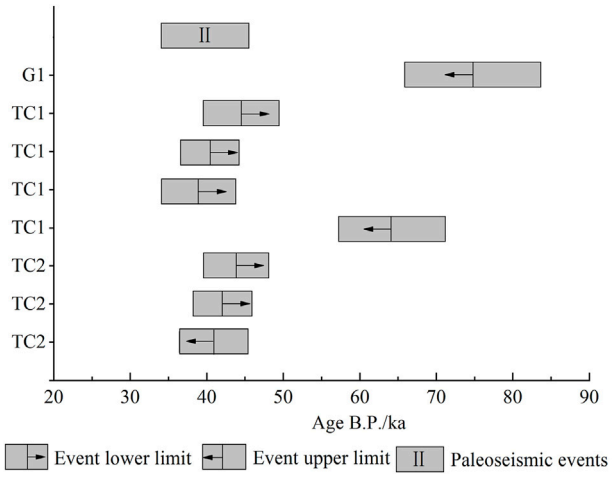

FIGURE 7 | The progessive constrained paleoseismic event in Kouma Fault.

The author considers that the seismotectonics of the 1767 B.C. Yanshi earthquake could related to the Kouma fault.

6 CONCLUSION AND SUGGESTIONS

(1) The Kouma Fault is a normal fault, with a dip of the north, a strike of almost east-west, and a length of approximately 30 km. As shown by the results obtained through the seismic and geological survey, trenching, drilling, radiometric dating, and comprehensive analysis—the paleoseismic events occurred at the fault in the Middle Pleistocene (event I); the paleoseismic events occurred at the fault again in the later period of the Late Pleistocene (event II). Based on the OSL age data in the G1 outcrop of the fault and the TC1 and TC2 trenches, the latest activity age of the Kouma Fault may be defined within the range of (38.84 ± 4.69) to (40.90 ± 4.45) kaB.P. The latest active age of the Kouma fault is the late of Late Pleistocene. The vertical fault throw for the bottom interface of the Upper Pleistocene (the bottom interface of the U13 loess stratum) of the Kouma Fault is 13.57 m, and the average vertical slip rate of the fault during the Late Pleistocene has been 0.11 mm/a.

(2) The filling in the fault zone of the Kouma Fault is dominated by clay, loess, and pebble, among others. When the width of the fault zone is smaller (10–30 cm), most clay in the fault zone is laminated in occurrence. The laminated surface is almost in parallel with the fault plane, and the long axis direction of pebbles in the fault zone is almost parallel to the fault plane. When the width of the fault zone is greater (for instance, 1.6 m), the clay and loess are massive.

(3) In the loess valley region, some outcrops of the fault are covered by slope deposits; the sliding surfaces of landslides on some loess valley side slopes are very similar to the sliding surfaces of the fault. They shall be carefully identified during the field geological survey process.

(4) Geological data is inadequate for the middle and deep part of the Kouma Fault, and it is recommended to carry out further research with shallow and deep seismic explorations, and to conduct the Kouma Fault seismic hazard evaluation based on those results.

DATA AVAILABILITY STATEMENT

The original contributions presented in the study are included in the article/Supplementary Material, further inquiries can be directed to the corresponding author.

AUTHOR CONTRIBUTIONS

WH is responsible for the overall implementation and writing papers. LW responsible for Seismic and Geological Survey and data analysis. SX responsible for geological graph drawing and paper finishing work. SW and JY participate in field operation drilling. ML has carried on the theory of technical guidance to the whole paper.

FUNDING

This study was supported by Spark Program of Earthquake Sciences (No. XH19060) and National Natural Science Foundation of China (No. 41704058).

ACKNOWLEDGMENTS

We are particularly grateful to Professor from Institute of Geology, CEA, China earthquake disaster prevention center and National institute of natural hazards, China for their helpful field guidance. We are also extremely grateful to Institute of Crustal Dynamics, CEA, and China Institute of Atomic Energy for their age test work.

REFERENCES

Bi, H., Zheng, W., Ge, W., Zhang, P., Zeng, J., and Yu, J. (2018). Constraining the Distribution of Vertical Slip on the South Heli Shan Fault (Northeastern Tibet) from High-Resolution Topographic Data. *J. Geophys. Res. Solid Earth* 123, 2484–2501. doi:10.1002/2017jb014901

Cao, Y., Ran, Y., Xu, H., Li, Y., Ma, X., Liang, M., et al. (2018). Holocene Activity of the Anqiu-Juxian Fault on the Jiangsu Segment of the Tanlu Fault Zone and its Tectonics Implication. *Chin. J. Geophys.* 61 (7), 2828–2844. (In Chinese with English abstract). doi:10.6038/cjg2018L0111

Chang, Z., Chang, H., Li, J., Mao, Z., and Zang, Y. (2021). Holocene Activity and Paleoearthquakes of the Weixi-Qiaohou Fault. *Seismol. Geol.* 43 (4),

881–898. (In Chinese with English abstract). doi:10.3969/j.issn.0253-4967.2021.04.009

Department of earthquake disaster prevention, CEA (1995). *Historical Strong Earthquake Catalog in China*. Beijing: Seismological Press. (In Chinese).

Dong, R., Yu, H., and Pan, B. (2010). Re-check of the 1767 B.C. Yanshi Earthquake, Henan Province. *Technol. Earthq. Disaster Prev.* 5 (4), 493–499. (In Chinese with English abstract). doi:10.3969/j.issn.1673-5722.2010.04.012

Ha, G., Ren, Z., Liu, J., Li, Z., Li, Z., Min, W., et al. (2021). New Discovery of Xiariha Fault Zone Around Dulan Area, Qinghai Province and its Tectonic Implications. *Seismol. Geol.* 43 (3), 614–629. (In Chinese with English abstract). doi:10.3969/j.issn.0253-4967.2021.03.009

He, W. (2022). Three-Point Method for Calculation of the Occurrence of Buried Active. *Fault* 46 (01), 36–47. (In Chinese with English abstract). doi:10.16539/j.ddgzyckx.2020.06.015

Jiang, W., Hou, Z., and Xiao, Z. (2000). Study on Paleoearthquakes of Qixinzhuang Trench at the XIadian Fault, Beijing Plain. *Seismol. Geol.* 22 (4), 413. (In Chinese with English abstract). doi:10.3969/j.issn.0253-4967.2000.04.010

Li, K., Xu, X., Wei, L., Wang, Q., and Shu, P. (2019). Evidence of Long Recurrence Times and Low Slip Rate along the 1668 Tancheng Earthquake Fault. *Chin. Sci. Bull.* 64 (11), 1168–1178. (In Chinese with English abstract). doi:10.1360/N972018-00961

Li, Z., Li, Y., Zhou, B., Zhu, G., liu, B., and Wu, J. (2021). New Insight on the Holocene Activity of the Eastern Marginal Fault of Daxing Uplift, Beijing Plain. *Seismol. Geol.* 43 (6), 1671–1681. (In Chinese with English abstract). doi:10.3969/j.issn.0253-4967.2021.06.018

Li, Z., Ren, Z., Liu, J., Ha, G., Li, Z., Wang, B., et al. (2020). New Discovery of Reshui-Taostuo River Fault in Dulan, Qinghai Province and its Implications. *Seismol. Geol.* 42 (1), 18–32. (In Chinese with English abstract). doi:10.3969/j.issn.0253-4967.2020.01.002

Liu, X., Yuan, D., Yao, Y., and Zou, X. (2021). Paleoearthquake Characteristics in Dunhuang Segment of the Sanweishan Fault. *Seismol. Geol.* 43 (6), 1398–1411. (In Chinese with English abstract). doi:10.3969/j.issn.0253-4967.2021.06.004

Lu, L., Zhou, Y., Zhang, P., and Cheng, X. (2022). Modelling Fault Scarp Degradation to Determine Earthquake History on the Muztagh Ata and Tahman Faults in the Chinese Pamir. *Front. Earth Sci.* 10 (9), 838866. doi:10.3389/feart.2022.838866

Luo, X., li, C., Ren, G., Li, X., Ma, Z., and Dong, J. (2020). The Late Quaternary Activity Features and Slip Rate of the Yanggao-Tianzhen Fault. *Seismol. Geol.* 42 (2), 399–413. (In Chinese with English abstract). doi:10.3969/j.issn.0253-4967.2020.02.010

Ma, J., Zhou, B., Wang, M., and An, L. (2020). Geological and Geomorphic Evidences for the Holocene Activity of the Nw Zheduotang Branch within the Xianshuihe Fault System. *Seismol. Geol.* 42 (5), 1021–1038. (In Chinese with English abstract). doi:10.3969/j.issn.0253-4967.2020.05.001

Min, W., Liu, Y., Chen, T., Shu, P., and Yu, Z. (2016). The Quantative Study on Activity of Dengdengshan-Chijiaciwo Faults Since Late Quaternary. *Seismol. Geol.* 38 (03), 503–522. (In Chinese with English abstract). doi:10.3969/j.issn.0253-4967.2016.03.002

Pan, B., Wang, J., Gao, H., Guan, Q., Wang, Y., Su, H., et al. (2005). Paleomagnetic Age of the Highest Terrace of the Yellow River in Kouma, Henan Province and its Indication to the Age of the Connection of the Yellow River. *Chin. Sci. Bull.* 50 (3), 255–261. (In Chinese). doi:10.1360/03wd0290

Ran, Y., Li, Y., Du, P., Chen, L., and Wang, H. (2014a). Key Techniques and Several Cases Analysis in Paleoseismic Studies in Mainland China(3):Rupture Characteristics, Environment Impact and Paleoseismic Indicators on Normal Faults. *Seismol. Geol.* 36 (02), 287–301. (In Chinese with English abstract). doi:10.3969/j.issn.0253-4976.2014.02.001

Ran, Y., Wang, H., Chen, L., Chen, W., Liang, M., and Xu, X. (2018). Late-Quaternary Fault Activity of the Longmen Shan Fault Zone-Evidence from Paleoseismic Trenching. *Chin. J. Geophys.* 61 (5), 1938–1948. (In Chinese with English abstract). doi:10.6038/cjg2018M0251

Ran, Y., Wang, H., Yang, H., and Xu, L. (2014b). Key Techniques and Several Cases Analysis in Paleoseismic Studies in Mainland China(4):Sampling and Event Analysis of Paleoseismic Dating Methods. *Seismol. Geol.* 36 (04), 939–955. (In Chinese with English abstract). doi:10.3969/j.issn.0253-4967.2014.04.001

Shi, F., He, H., Liu, Y., Wei, Z., and Sun, H. (2022). Active Tectonics of the Nantinghe Fault in Southeastern Tibetan Plateau and its Implications for Continental Collision. *Front. Earth Sci.* 9 (21), 818225. doi:10.3389/feart.2021.818225

Sun, H., He, H., Wei, Z., and Gao, W. (2016). The Quantative Study on Activity of Dengdengshan-Chijiaciwo Faults Since Late Quaternary. *Seismol. Geol.* 38 (03), 503–522. (In Chinese with English abstract). doi:10.3969/j.issn.0253-4967.2016.03.002

Wang, S., Jiang, F., Wu, X., Tian, G., Zhang, Z., Liu, A., et al. (2004). Loess Stratigraphy of Mangling in Henan Province. *J. Geomechanics* 7 (4), 309–314. (In Chinese with English abstract). doi:10.3969/j.issn.1006-6616.2001.04.004

Wang, Z., Wang, L., Xu, H., Ge, F., Yang, C., and Li, J. (2015). Geometric Feature and Latest Activities of the North Segment of the Anqiu-Juxian Fault. *Seismol. Geol.* 37 (1), 176–191. (In Chinese with English abstract). doi:10.3969/j.issn.0253-4967.2015.01.014

Yu, Z., Pan, H., Shen, J., Li, J., Zhang, M., and Dai, X. (2020). The Activity Features of Xiadian Fault Zone Revealed by Rongjiabao Trench and its Probabilistic Seismic Hazard Evaluation. *Seismol. Geol.* 42 (3), 688–702. (In Chinese with English abstract). doi:10.3969/j.issn.0253-4967.2020.03.010

Conflict of Interest: The authors declare that the research was conducted in the absence of any commercial or financial relationships that could be construed as a potential conflict of interest.

frontiers | Frontiers in Earth Science

TYPE Original Research
PUBLISHED 10 August 2022
DOI 10.3389/feart.2022.927102

OPEN ACCESS

EDITED BY
Chong Xu,
Ministry of Emergency Management, China

REVIEWED BY
Yuandong Huang,
Ministry of Emergency Management, China
Ionut Cristi Nicu,
Norwegian Institute for Cultural Heritage Research, Norway
Xiangli He,
Ministry of Emergency Management, China
Matebie Meten,
Addis Ababa Science and Technology University, Ethiopia
Sajid Ali,
RWTH Aachen University, Germany

*CORRESPONDENCE
Zhang Jianqiang,
zhangjq@imde.ac.cn

SPECIALTY SECTION
This article was submitted to Geohazards and Georisks, a section of the journal Frontiers in Earth Science

RECEIVED 23 April 2022
ACCEPTED 04 July 2022
PUBLISHED 10 August 2022

CITATION
Jianqiang Z, Yonggang G, Yong L, Qiang Z, Yuhong J, Huayong C and Xiaoqing C (2022), Zonation-based landslide hazard assessment using artificial neural networks in the China-Pakistan Economic Corridor.
Front. Earth Sci. 10:927102.
doi: 10.3389/feart.2022.927102

Zonation-based landslide hazard assessment using artificial neural networks in the China-Pakistan Economic Corridor

Zhang Jianqiang*, Ge Yonggang, Li Yong, Zou Qiang, Jiang Yuhong, Chen Huayong and Chen Xiaoqing

Key Laboratory of Mountain Hazards and Earth Surface Processes, Institute of Mountain Hazards and Environment, Chinese Academy of Sciences, Chengdu, China

Distribution of landslide is controlled by various causative factors that have different impacts on the occurrence of landslide in different regions. Using one single model to build the hazard assessment is not enough to fully reflect the spatial differences of landslide controlling factors especially for large area. Landslide hazard assessment based on zonation was therefore proposed in this study with an attempt to take effective measures to address this problem. The China–Pakistan Economic Corridor was taken as the study area where landslide hazard assessment was carried out. Based on the features of geological structure, topography, and climate, the study area was divided into three zones. The controlling factors were further analyzed by the geographical detectors method. It was found that the main controlling factors for landslides in these three zones were related to the site's topography (altitude, slope gradient, and relief amplitude), land use, and distance to an earthquake epicenter. Furthermore, different factors for landslide hazard assessment were selected based on the result of a controlling factor analysis. An artificial neural network model was employed to build the hazard assessment models, and hazard assessment maps were generated. Validations were conducted, showing that the accuracy of hazard assessment maps by zones was higher than that by the whole study area, despite there was no significant difference during the modeling process.

KEYWORDS

China–Pakistan Economic Corridor, landslide, controlling factor, hazard assessment, artificial neural networks

Introduction

The China–Pakistan Economic Corridor (CPEC) is an important geographical linkage that strengthens the transportation, energy, and communication between China and Pakistan. Due to special geological, geomorphic, and climatic conditions, geo-hazards are frequent and widely distributed along the corridor, causing disasters to major infrastructure establishments and projects. For example, the Karakoram Highway (KKH) constructed between 1966 and 1979 was often broken due to highly frequent geo-hazards until 2007. On 8 October 2005, a 7.6 magnitude earthquake in Northern Kashmir triggered a large number of landslides which caused damages to the KKH (Sato et al., 2007; Aydan et al., 2009). Subsequently, in 2010, a huge landslide occurred in Attabad village and formed a large landslide lake, disrupting the traffic for 5 years (NDMA, 2010). Therefore, it is necessary to carry out landslide hazard assessment for this area.

Landslide hazard assessment at the regional scale was carried out for CPEC in this research. These regional-scale landslide hazard assessment methods include expert experience method (Ercanoglu et al., 2008; Thiery et al., 2014), statistical analysis (Lee and Min, 2001; Demir, 2018; Barella et al., 2019), and physical-based model (van Beek and van Asch, 2004; Xie et al., 2004; Rana and Babu, 2022). In recent years, data mining and machine learning methods, such as artificial neural network (ANN) (Yilmaz, 2009; Liu, 2010), logistic regression models (Xu et al., 2013; Meten et al., 2015; Zhang et al., 2019a), and support vector machine (SVM) (Su et al., 2015; Zhang et al., 2019b) were widely used to assess landslide hazard and showed satisfactory results in practice.

There are already plethora of studies on earthquake and rainfall-triggered landslide inventories, as well as related landslide risk and hazard assessments, that have been carried out in the region, mainly in Pakistan (Dunning et al., 2007; Khattak et al., 2010; Ahmed and Rogers, 2015; Basharat et al., 2016; Khan et al., 2019; Imtiaz et al., 2022). In recent years, landslide-oriented research has been extended to the entire CPEC, especially for landslides along the KKH (Bacha et al., 2018; Rashid et al., 2020; Chang et al., 2021; Hussain et al., 2021; Maqsoom et al., 2022; Su et al., 2021). Hazard and risk assessments of some large-sized landslides were also carried out in this area, such as the Attabad landslide (Chen et al., 2017), where landslide dam breach and its hazards to the KKH project construction site downstream was discussed.

Generally, landslide hazard assessment only builds one model for one area. However, for a regional scale of landslide hazard assessment, the characteristics of landslide and causative factors can be spatially different due to the large size of the study area. One hazard model is thus not able to represent the situation of landslides. In the case of CPEC, for example, landslides are widely distributed in the northern high mountains including the Hindu Kush Mountains, the Himalayas, and the Karakoram Mountains. These regions are characterized by complex geological structures, steep terrains, and intense glacier activities. In addition, landslides also occur in the Sulaiman Mountains, Central Barhui Range, Kirthar Range, and Central Makran Range in the west and southwest of CPEC. However, these landslides are small due to gentle slopes and low precipitation. Hence, the study area was first divided into different zones to account different environmental background factors and distribution of landslide. Then landslide hazard assessment models were built for each zone. In doing so, the accuracy of the regional-scale landslide hazard assessment of this study was improved.

Study area

Spanning two countries, the study area of CPEC starts from Kashgar in Xinjiang Uygur Autonomous Region of China in the north and reaches Gwadar in Pakistan in the south. It is adjacent to Afghanistan to the west and India to the East. With an area of as large as 1.06 million square kilometers (Figure 1), CEPC has a large area with a wide north–south span with different environmental and landslide characteristics.

Geological structure

CPEC passes through the western edge of the Tibetan Plateau and is located at the junction of the Western Himalayan and Pamir syntaxes, which is one of the most tectonically active regions worldwide (Kumar et al., 2013). The main active faults of CPEC include the Kashir River Fault, Tashikurgan Fault, Karakorum Fault, Main Himalayan Thrust (MHT), and Pamir Frontal Thrust. The structural deformation is mainly concentrated in the Karakoram strike-slip fault zone and the Tashikurgan Fault (Martin, 2017).

Geomorphology

The landform type of CPEC from north to south include Kashgar Plain, northern high mountain area, western low mountain area, Baluchistan Plateau, Potwar Plateau, and Indus Plain (Yang and Liu, 2005). The northern high mountain area covers the Karakoram Range and Himalayan and Hindu Kush ranges, with K2 and Nanga Parbat, two mountain peaks of higher than 8000 m located in this region. The Baluchistan Plateau, located in the western part of the corridor, is mainly composed of north–south parallel ranges with an average altitude above 3000 m, and the plateau is at an altitude between 500 and 2000 m. The Potwar Plateau is bounded by Hazara Mountain and Pirpanjai Mountain in the north; Salt range in the south; and Indus River and its tributary Jelum River in the west and east, respectively. The area of the

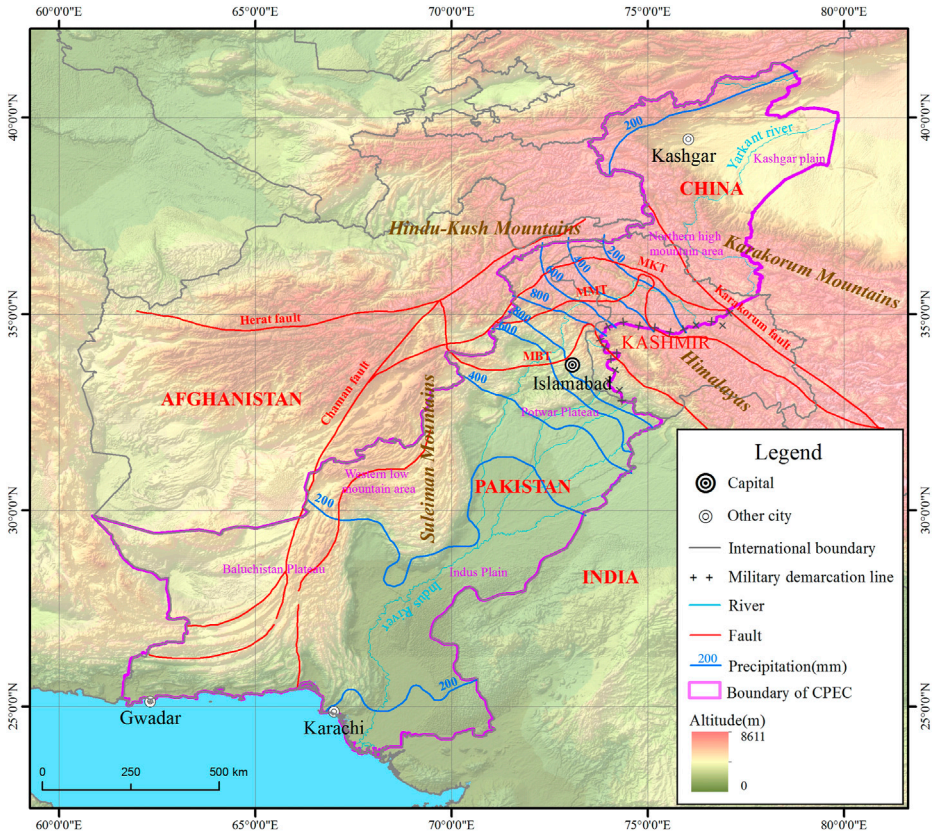

FIGURE 1
Location of the study area.

Potwar Plateau is 4,350 km^2 and the altitude is around 500 m (Xu et al., 1982; Miller and Craig, 1996).

Climate

The climate of CPEC is affected by the interaction of Westerly and Southwest monsoons. Most of the area has an arid and semiarid climate, except the western coast where the climate is tropical monsoon. Annual precipitation increases first and then decreases from south to north. The maximum annual precipitation is exceeding 1200 mm and the minimum rainfall is less than 100 mm (Yu et al., 2021).

Data source and methodology

Data source

Causative factors

Based on the distribution and characteristics of landslides in this region, causative factors (e.g., topography, geology, and land use) and triggering factors (e.g., earthquake and rainfall) were considered for the landslide hazard assessment in this study. Altitude, slope gradient, slope aspect, relief amplitude, distance to fault, distance to epicenter, and annual precipitation were selected as alternative landslide hazard assessing factors.

Topographic factors including slope gradient, slope aspect, and relief amplitude were calculated based on SRTM DEM, with spatial resolution of 30 m. Fault data of CPEC were obtained from the Geological Map of North Pakistan and Adjacent Areas of Northern Ladakh and Western Tibet with a scale of 1:650,000 (Searle and Asif Khan, 1997; Yaseen et al., 2021), based on which the distance to fault was calculated. The average annual precipitation was calculated on historical monthly weather data from year 2010 to 2018 by WorldClim with resolution of 2.5 min (Harris et al., 2014). The historical seismic data of CPEC were obtained from the USGS Earthquake Disaster Project, including epicenter location, magnitude, and occurrence time of earthquakes with magnitude above three since 1960, based on which distance to epicenter was calculated. Land use data were obtained from global land use data of Tsinghua University in 2017 with resolution of 10 m (Gong et al., 2019). All these factors were rasterized with a grid size of 0.5 × 0.5 km.

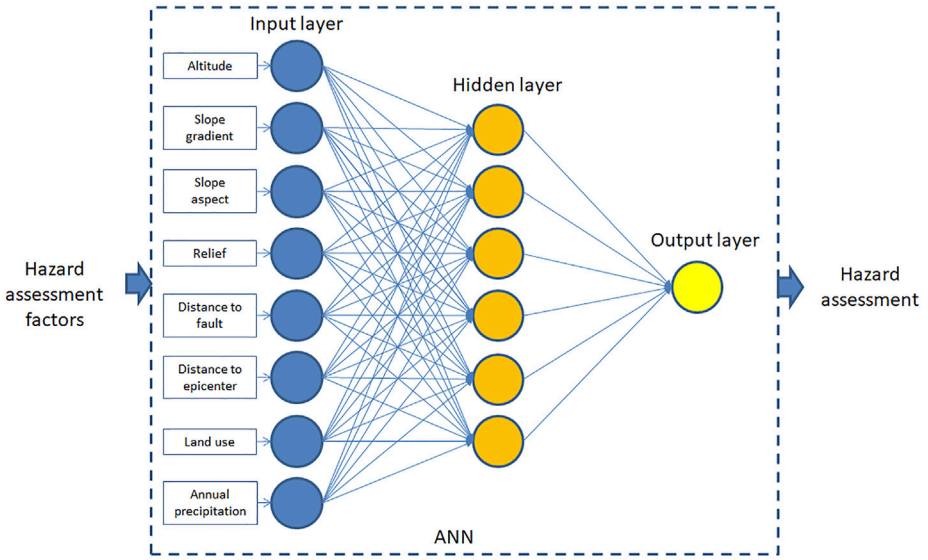

FIGURE 2
Artificial neural networks and landslide hazards assessment.

Landslide inventory

A dataset including 2045 rockfalls and landsides that occurred from 1970 to 2020 was utilized in this research (Yi et al., 2021). Landslide inventory mapping was supported by the project of "Comprehensive Investigation and Assessment of Natural Disasters along the China–Pakistan Economic Corridor". High resolution images from Google Earth were utilized to identify the location and boundary of landslide by the artificial interpretation method in the study area, and then a field investigation was conducted along the Karakoram Highway (KKH) in 2019 to validate the landslide data and obtain more information including landslide triggers, volumes, height differences, and so forth.

Methodology

Geographical detectors method

The geographical detectors method (Wang et al., 2010) was employed to detect the controlling factors for landslides in different regions. Geographical detectors are a set of statistical methods utilized to detect the spatial heterogeneity of geographical phenomena and find the driving forces. The geographical detectors method is based on the assumption that if an independent variable has an important influence on a dependent variable, the spatial distribution of the independent variable and the dependent variable should be similar. In this study, the differentiation and factor detection were utilized to detect the spatial differentiation of dependent variable Y (numbers for landslide), so as to probe how strong the influence of independent variable X (causative factors for landslide) on Y, which was measured by q value with the equation:

$$q = 1 - \frac{\sum_{h=1}^{L} N_h \sigma_h^2}{N\sigma^2} = 1 - \frac{SSW}{SST}, \quad (1)$$

$$SSW = \sum_{h=1}^{L} N_h \sigma_h^2, \quad (2)$$

$$SST = N\sigma^2. \quad (3)$$

In this equation, h = 1...; L is the classification or partition of variable Y or factor X; N_h and N are the number of classification and the number of units in the study area, respectively; σ_h^2 and σ^2 are the variances of h and Y value, respectively; and SSW and SST are Within Sum of Squares and Total Sum of Squares, respectively. The range of q value is (0, 1), and the larger q value is, the more obvious the spatial differentiation of Y will be, otherwise weaker. The q value of one indicates that factor X completely controls the spatial distribution of Y, while the q value of 0 indicates that factor X has no influence on Y.

Artificial neural networks

Artificial neural networks (ANN) have also been utilized for landslide hazard assessment (Figure 2). The artificial neural network model is based on the principle of multilayer perceptron, which is composed of three layers of neurons: input layer, hidden layer, and output layer. Neurons are the basic components of neural networks, and the connection between neurons is realized by synaptic weights w_{ij}. Generally,

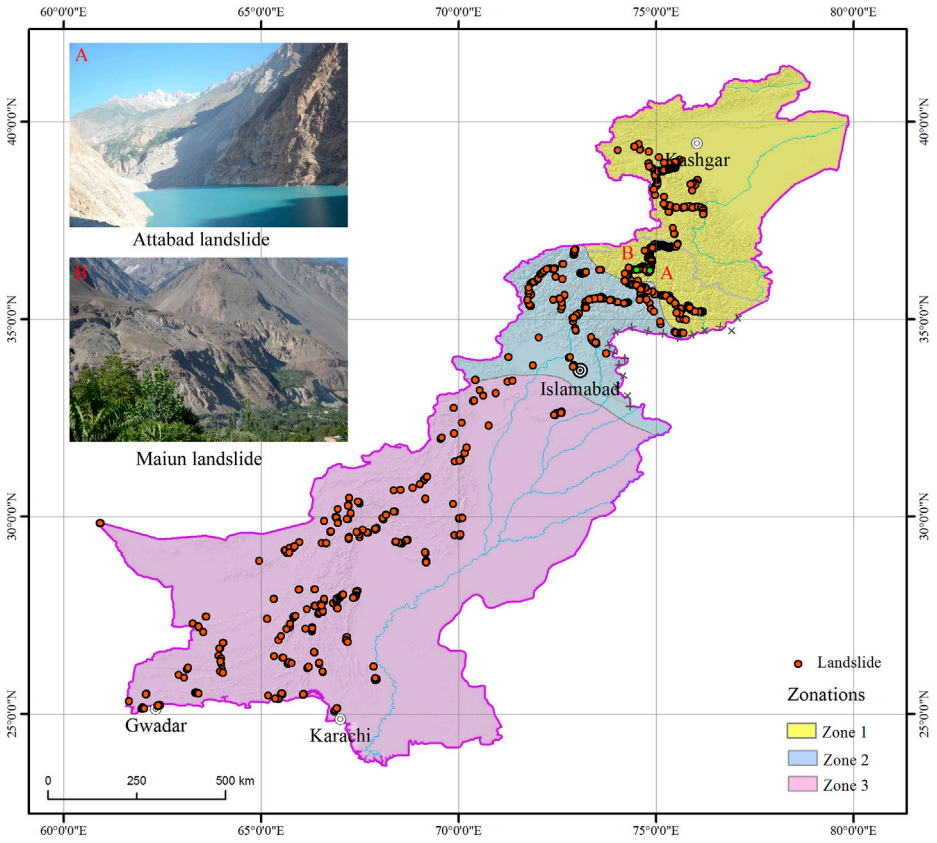

FIGURE 3
Zonation in CPEC [**(A)** Attabad landslide with coordinates of N 36°18′48.66", E 74°49′6.43"; **(B)** Maiun landslide with coordinates of N 36°14′34.71", E 74°25′11.98"].

TABLE 1 Zonation of CPEC.

Zonation	Area (10^3km^2)	Topography	Precipitation	Geology	Landslide
Zone 1	228.72	Karakoram mountains	Less than 200 mm	Karakoram Fault	764
Zone 2	117.17	Hindu Kush and the Himalayas	200–1600 mm	Main Boundary Thrust	417
Zone 3	712.19	Sulaiman Mountains ACT, Central Barhui Range, Kirthar Range, and Central Makran Range	Less than 500 mm	Chaman Fault Zhob Valley Thrust	864

the greater the value of w_{ij}, the higher contribution given by the factor. A positive value of w_{ij} indicates that the factor is positively correlated with the hazard assessment result, otherwise negatively.

In this study, an open-source GIS-integrated tool, r.landslide was used to carry out the hazard assessment based on the ANN model in the GIS software named Geographic Resources Analysis Support System (GRASS) (Bragagnolo et al., 2020; GRASS Development Team, 2017). The tool was written in Python language and works on the ANN model and landslide database. The sigmoid activation function, defined in Eq. 4, was used in r.landslide to depict a balance between linear and non-linear behaviors.

$$f(x) = \frac{1}{1 + e^{-\beta x}}. \quad (4)$$

In this equation, x refers to the input value of the intermediate or output layer neuron after weight-bearing by the synaptic weights; β is the slope parameter; and sigmoid functions with different slopes are obtained by assigning varied β values.

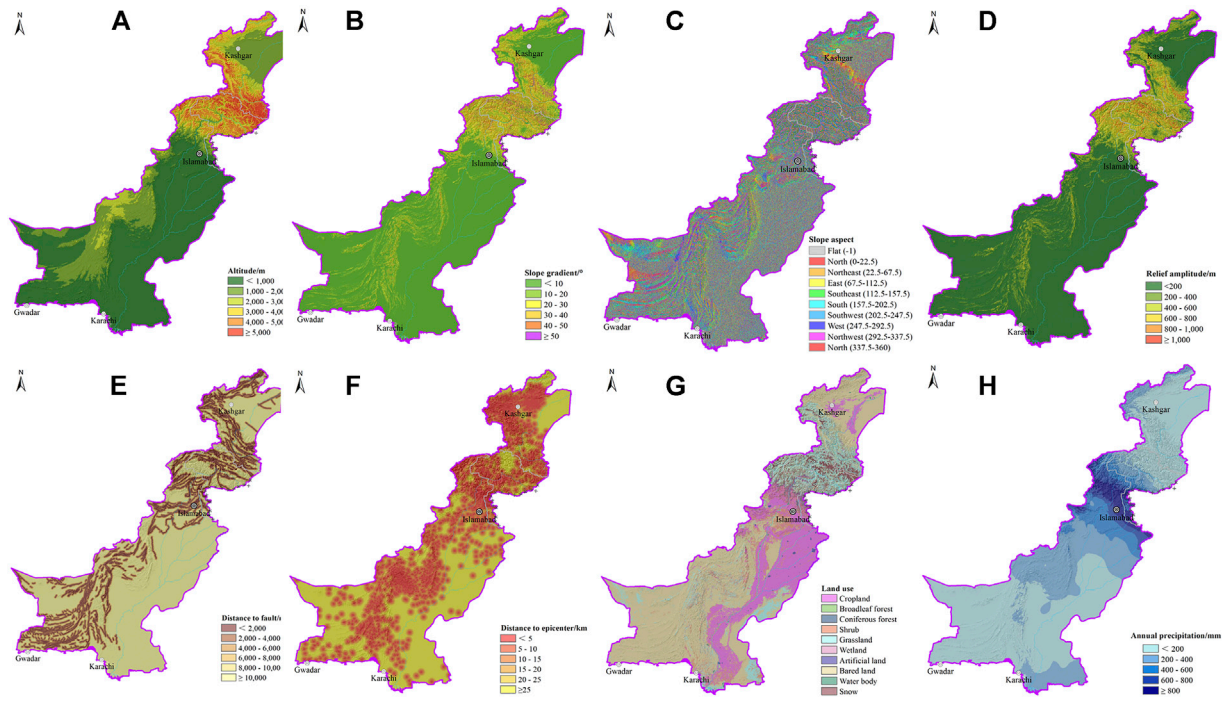

FIGURE 4
Landslide hazard assessment factors of CPEC [**(A)** altitude; **(B)** slope gradient; **(C)** slope aspect; **(D)** relief amplitude; **(E)** distance to fault; **(F)** distance to epicenter; **(G)** land use; and **(H)** annual precipitation].

Training of ANNs was performed by using the back-propagation algorithm, which the weight is calculated by evaluating the error between the response value obtained by propagation and the known true value (Haykin, 1999). During the training process, each sample is given a corresponding output value O, which is compared with the reference value O_D. T stands for the transpose, which defines the error function by Eq. 5:

$$E = -\frac{1}{2}(O_D - O)^T (O_D - O). \quad (5)$$

Moreover, Δwij is the increment of synaptic wij, and it is calculated by Eq. 6:

$$\Delta w_{ij} = -\alpha \frac{\partial E}{\partial w_{ij}}, \quad (6)$$

where α is the learning rate which controls the adjustment strength related to the synaptic weights. The objective of the back-propagation algorithm is to adjust the synapse weights so that the error function E is minimized during the training process.

Integrated natural zonation

An integrated natural zonation was carried out based on mountain ranges, main fault systems, and precipitation in this research. The study area was divided into three zones (Figure 3; Table 1). Zone 1 is located in the northernmost of CPEC, where the topography is mainly dominated by the Karakoram Mountains with an annual precipitation less than 200 mm. The Main Karakoram Thrust and Main Mantle Thrust are the main fault systems in this area. In Zone 2, the mountains include the Hindu Kush and the Himalayas, and the main fault is the Main Boundary Thrust. This region has the highest annul precipitation between 200 and 1600 mm. Zone 3 covers the southern part of CPEC, with the Sulaiman Mountains, Central Barhui Range, Kirthar Range, and Central Makran Range located in this region. The main faults in this zone are the Chaman Fault and Zhob Valley Thrust (ZVT). The annual rainfall in this region is less than 500 mm. The quantities of landslides are counted by zones. From the landslide inventory, 37.4, 20.4, and 42.3% landslides fall in Zone 1, Zone 2, and Zone 3, respectively.

Controlling factors of landslide distribution

Causative factors

Landslide causative factors are chosen as the parameters of the hazard assessment model. At present, there is no unified

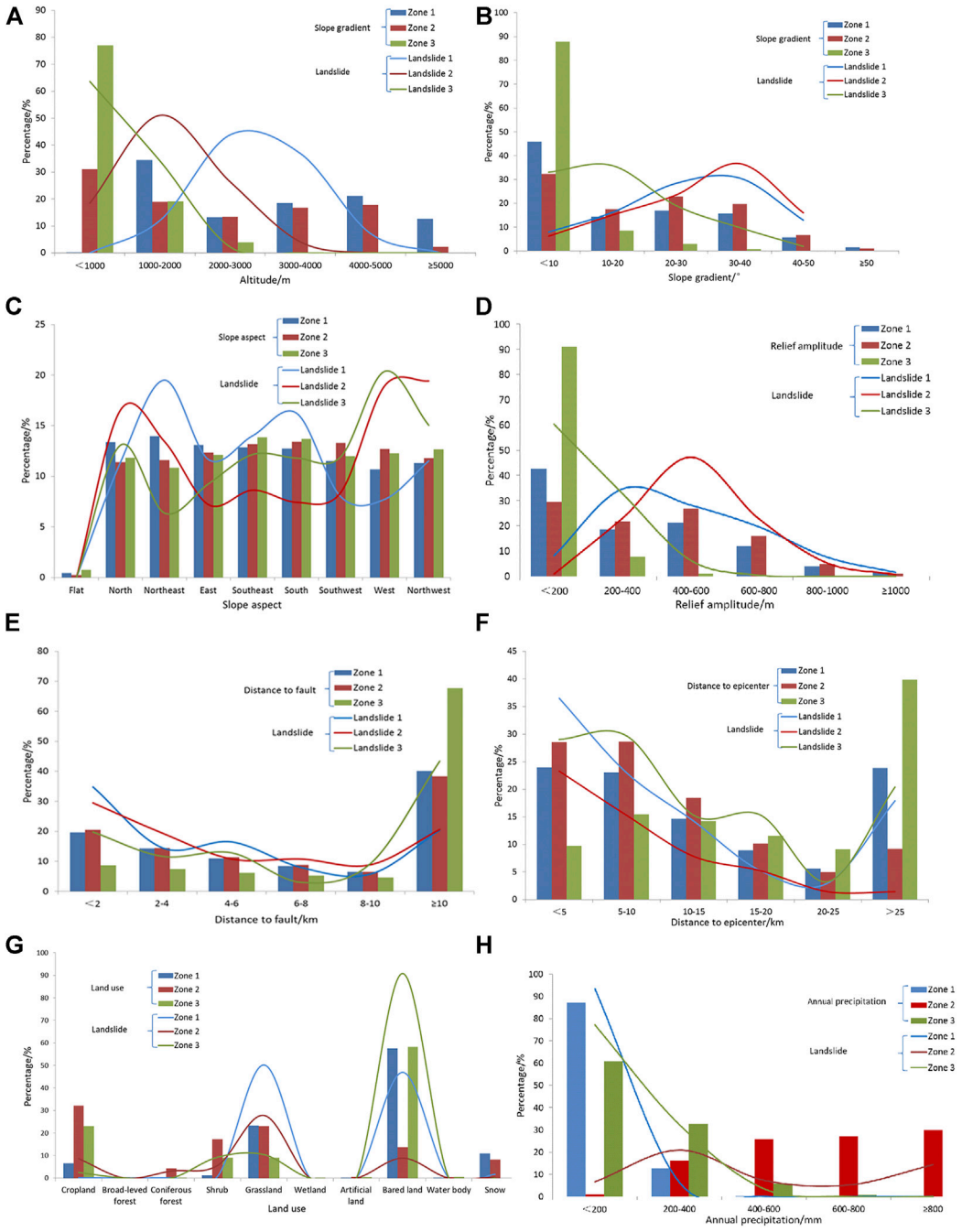

FIGURE 5
Classification of different factors and distribution of landslides in each zone [**(A)** altitude; **(B)** slope gradient; **(C)** slope aspect; **(D)** relief amplitude; **(E)** distance to fault; **(F)** distance to epicenter; **(G)** land use; and **(H)** annual precipitation).

causative factor system for landslide hazard assessment. Mostly, researchers select landslide causative factors through field investigation and characteristics analysis of landslide distribution in the study area. In this study, landslide triggering conditions and environmental background conditions are considered. Precipitation and earthquake were mainly considered as the triggering conditions, and geology, topography, and land cover were considered as the environmental background conditions. Finally, a total of eight factors were selected as landslide causative factors.

Classifications were carried out on eight causative factors: altitude (x_1), slope gradient (x_2), slope aspect (x_3), relief

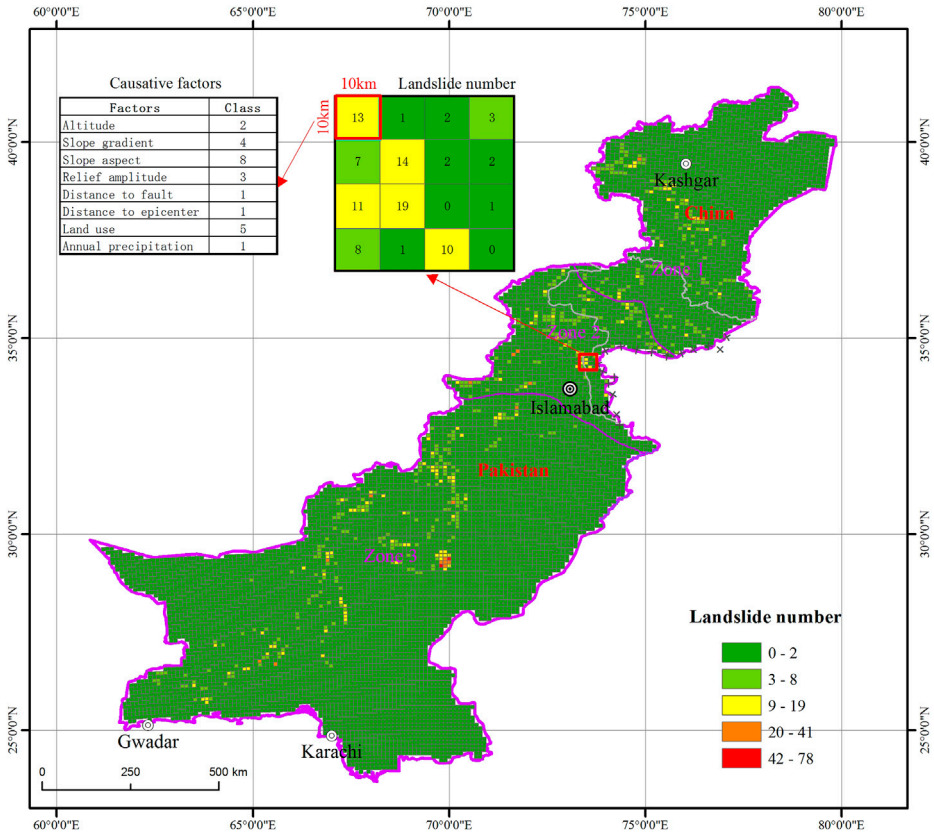

FIGURE 6
Controlling factors analysis by geographical detectors.

TABLE 2 Landslide controlling factors in different zones.

No.	Zone 1		Zone 2		Zone 3		All zones	
	Factors	q value	Factors	q value	Factors	q value	Factors	q value
1	Altitude	0.088	Altitude	0.049	Distance to epicenter	0.021	Altitude	0.026
2	Slope gradient	0.049	Relief amplitude	0.035	Relief amplitude	0.018	Relief amplitude	0.025
3	Land use	0.041	Slope gradient	0.033	Altitude	0.014	Slope gradient	0.022
4	Relief amplitude	0.043	Annual precipitation	0.015	Slope gradient	0.012	Distance to epicenter	0.021
5	Distance to fault	0.028	Distance to fault	0.013	Annual precipitation	0.011	Distance to fault	0.014
6	Distance to epicenter	0.020	Land use	0.012	Land use	0.008	Annual precipitation	0.012
7	Slope aspect	0.007	Distance to epicenter	0.007	Distance to fault	0.008	Land use	0.011
8	Annual precipitation	0.002	Slope aspect	0.005	Slope aspect	0.007	Slope aspect	0.007

amplitude (x_4), distance to fault (x_5), distance to epicenter (x_6), land use type (x_7), and annual precipitation (x_8) (Figure 4). In specific, the altitude was classified into six classes by an interval of 1000m; and the slope gradient was classified into six classes by an interval of 10°.

According to the statistics of the area for each factor classification and landside quantities, it can be seen that the environmental conditions and distribution of landslides are different in three zones. In terms of altitude factor (Figure 5A), in Zone 1, there is a large area with the altitude

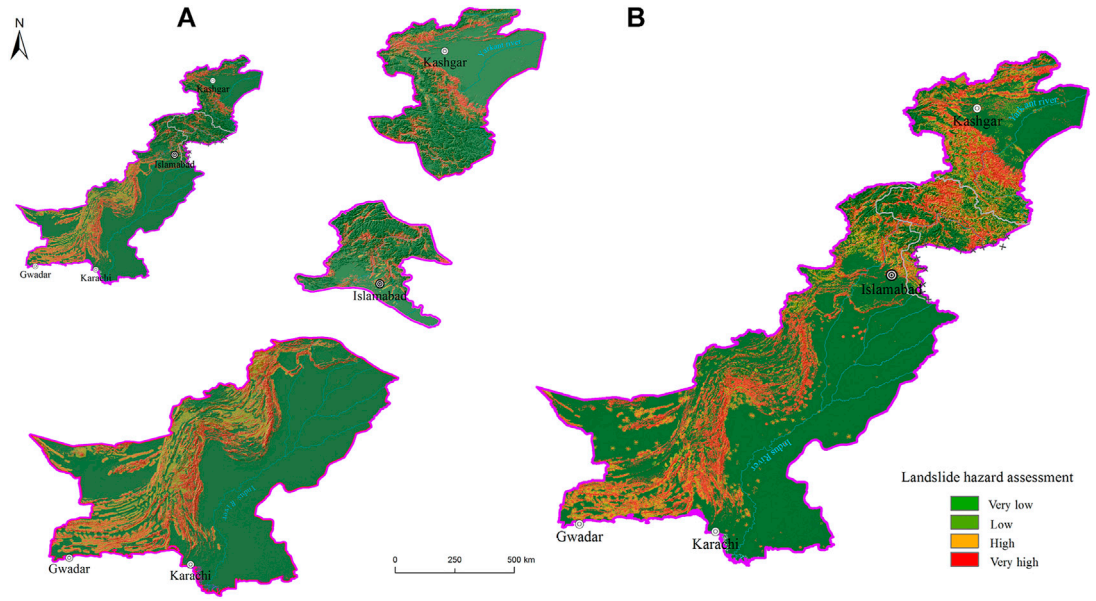

FIGURE 7
Landslide hazard assessment maps [**(A)** landslide hazard assessment map by zones; **(B)** landslide hazard assessment map of the whole region].

between 1000 and 2000 m. The altitude in Zone 2 is mostly below 5000 m. The altitude of Zone 3 is mostly below 3000 m, and the proportion of the area with an altitude less than 1000 m is especially high, accounting for almost 80%. There are also significant differences for the distribution of landslides. In Zone 1, landslides are most distributed in the area with an altitude of 2000–3000 m, while in Zone 2, landslides are mostly distributed in the altitude of 1,000–2000 m. In Zone 3, landslides are mainly distributed in the area with an elevation less than 1000 m.

Slope gradient is considered as one of the most significant factors for landslide. If the slope gradient is larger than the natural angle of repose of the substrate, landslide may occur when there is no enough cohesion (Kamp et al., 2008). Proportions of slope gradient divisions are consistent in Zone 1 and 2, but different in Zone 3. The distribution of landslides also shows the same tendency. In Zone 1 and 2, more landslides are distributed in the area with a slope gradient of 30°–40°, while in Zone 3, more landslides tend to be distributed in areas with a slope gradient of 10°–20°(Figure 5B). The proportions of slope aspect in different classes are highly consistent in each zone, but the proportions of landslides distributed in slope aspect divisions are different in three zones (Figure 5C).

The relief amplitude factor represents the gravitational potential energy of the slope. The greater relief amplitude value is, the greater the gravitational potential energy of the slope will be, which may cause higher susceptibility and large scales of landslides. Proportions of relief amplitude are similar in Zone 1 and Zone 2, but there is a big difference in Zone 3, where the proportion of relief amplitude with a value less than 200 is particularly high. The correlation between landslides and relief amplitude is explained as, there are large numbers of landslides distributed in the area with relief amplitude of 400–600 m in Zone 2, more landslides distributed in the area with relief amplitude of 200–400 m in Zone 1, but in Zone 3 most landslides are distributed in the area with relief amplitude of less than 200 m (Figure 5D).

The distance to faults, whether area proportion or landslide quantity, are consistent in the three zones (Figure 5E). The distance to an earthquake epicenter reflects the influence of the earthquake, and the proportion of the earthquake-affected areas in Zone 2 is higher.

Earthquake is one significant trigger for landslides. Earthquake with big magnitude can cause a large number of co-seismic landslides, and it can also destroy the stability of slope and lead more sliding after the shake. Historical earthquake epicenters were concentrated in north–west of CPEC in China, North high mountain area and western low mountain area in Pakistan.

Generally, the quantity of landslides shows a gradual decreasing trend against the distance from the earthquake (Figure 5F). Since land use types of bare land and grassland cover large areas in CPEC, therefore more landslides are distributed in the area of these land use type (Figure 5G). Finally, annual precipitation is low in Zone 1 and Zone 3. Hence, the effect of annual precipitation on landslides is not significant in both zones. However, the number of landslides is increased in Zone 2 as a result of the zone's higher annual precipitation (Figure 5H).

TABLE 3 Landslide hazard assessment maps validation.

ANN models	Zones	Validation samples	Correct samples	Accuracy (%)
Zone 1	Zone 1	153	134	87.6
	Zone 2	83	80	96.4
	Zone 3	173	105	60.7
Zone 2	Zone 1	153	142	92.8
	Zone 2	83	75	90.4
	Zone 3	173	165	95.3
Zone 3	Zone 1	153	87	56.8
	Zone 2	83	60	72.3
	Zone 3	173	148	85.6
By 3 models	Whole	409	357	87.3
By 1 model	Whole	409	345	84.4

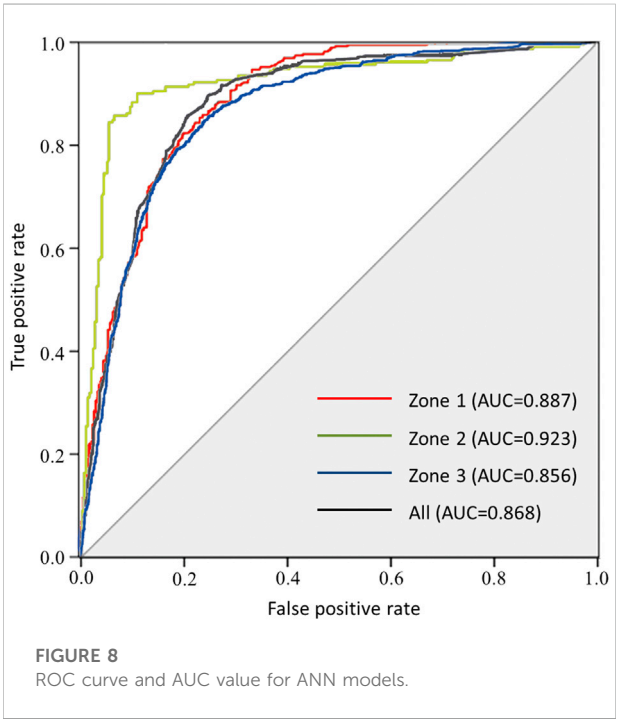

FIGURE 8
ROC curve and AUC value for ANN models.

Controlling factor analysis

The landslide controlling factor was defined as the most significant causative factors, which affect the distribution of landslides at the regional scale. The landslide controlling factor analysis was carried out based on landslide inventory and causative factors. First, the study area was divided into small units by the size of 10 × 10 km (Figure 6). Then the number of landslides was counted in each unit of the eight causative factors that are associated with landslide occurrence. Finally, the q value was calculated by geographical detectors, and the main controlling factors were analyzed for landslide in each zone.

Results showed that the controlling factors are different in each zone (Table 2). Topographical factors including altitude, slope gradient, and relief amplitude are controlling factors in Zone 1, especially for the altitude factor. In addition, land use factor also plays a significant role on the distribution of landslides. The q values for all these four factors are larger than 0.04. In Zone 2, altitude is also the most significant factor for landslide, followed by relief amplitude and slope gradient. But the q values of these three factors are smaller than in Zone 1. Large differences for controlling factors are showed in Zone 3, where the distance to the epicenter is the most significant factor, which means earthquake affects strongly on the occurrence and distribution of landslide in this region. Other main controlling factors are topographical factors including relief amplitude, altitude, and slope gradient in Zone 3. But all the q values in this region are smaller than either Zone 1 or Zone 2. When it comes to the entire study area, topographical factors including altitude, relief amplitude, and slope gradient are the top controlling factors for landslide, followed by the distance to the epicenter.

Landslide hazard assessment

Hazard assessment

Landslide hazard assessment was conducted for each zone. In order to make a contrast, landslide hazard assessment in the whole study area was also carried out.

Based on the analysis of main controlling factors, the top six factors ranked by q values were selected as the hazard assessment factors in different zones. Altitude, slope gradient, land use, relief amplitude, distance to fault, and distance to epicenter were selected for Zone 1; altitude, relief amplitude, slope gradient,

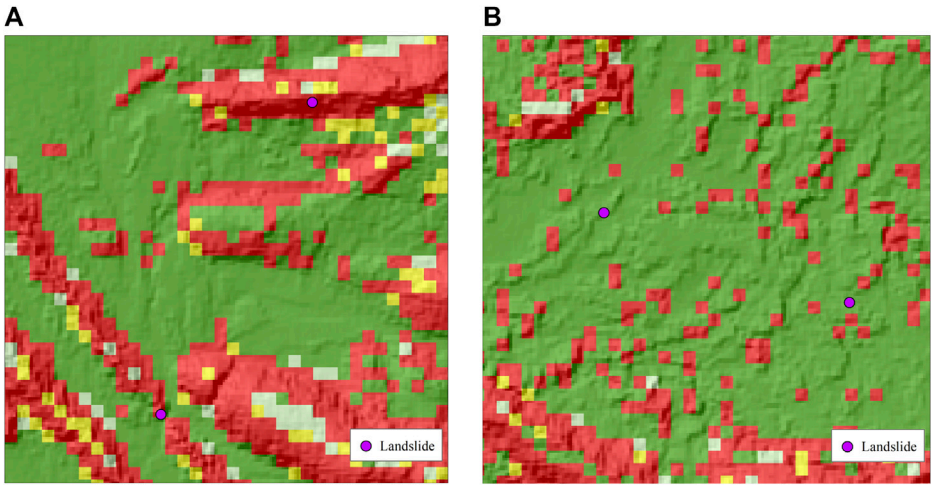

FIGURE 9
Validation landslide samples [**(A)** correctly assessed landslide; **(B)** wrongly assessed landslide].

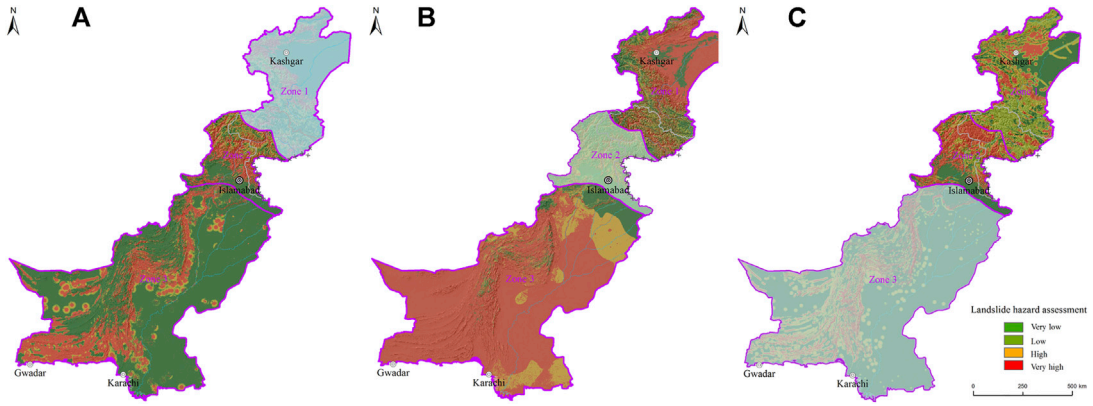

FIGURE 10
Landslide hazard maps base on different models [**(A)** landslide hazard model built in Zone 1 applied in the whole region; **(B)** landslide hazard model built in Zone 2 applied in the whole region; and **(C)** landslide hazard model built in Zone 3 applied in the whole region].

annual precipitation, distance to fault, and land use were selected for Zone 2; and distance to epicenter, altitude, relief amplitude, slope gradient, annual precipitation, and land use were selected for Zone 3. For the whole study area, altitude, relief amplitude, slope gradient, distance to epicenter, distance to fault, and annual precipitation were selected as the hazard assessment factors.

The artificial neural network is defined as a supervised classification model that determines part of landslide samples that need to be selected to train and build the hazard model. In this study, the landslide inventory was divided into two parts in each zone. In addition, 80% of landslides were selected randomly for building the model, and the other 20% samples were taken for validation. The hazard assessment models of landslides were modeled by using the artificial neural network method based on r.slope. Proportions of the dataset for the training, validation, and test of the ANN were 70, 15, and 15%, respectively. A three-layer neural network was used to train the data. The input layer had six neurons, the hidden layer had 14 neurons, and the number of iterations was 200.

Finally, landslide hazard assessment maps were generated by the hazard assessment models for the three zones as well as the whole region (Figure 7). The value of hazard assessment map ranged from 0 to 1, and it was classified into four classes by the intervals of 0–0.25, 0.25–0.5, 0.5–0.75, and 0.75–1. The hazard levels were defined as very low, low, high, and very high. Areas of very high and high landslide hazard levels in three zones were

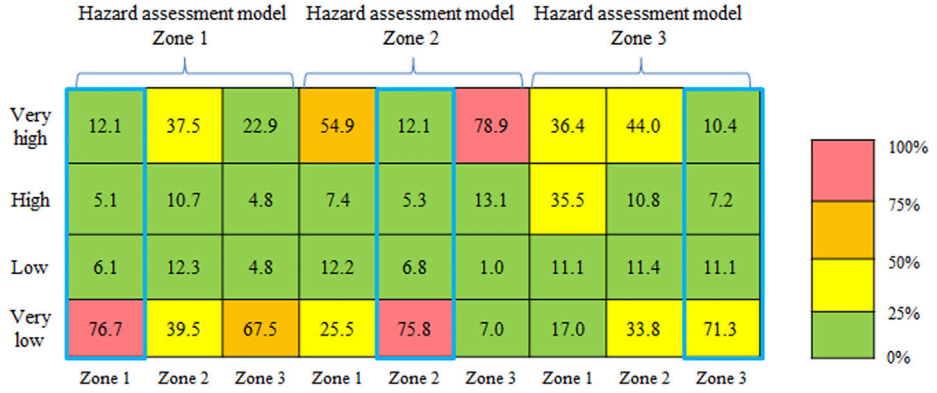

FIGURE 11
Proportion of landslide hazard levels in different zones.

very similar, accounting for 17.2, 17.4, and 17.6%, respectively. But for the hazard assessment map by the whole region, the proportion of very high and high landslide hazard levels reaches 23.6%. Obvious differences could be recognized between two assessment maps, especially in Zone 3. Areas near the earthquake epicenters showed very high or high landslide hazard level.

Landslide hazard assessment model validation

The receiver operating characteristic (ROC) curve was utilized to validate the landslide hazard assessment models for three zones and the whole region, and the area under curve (AUC) value was calculated for each curve to compare the accuracy of each model quantitatively (Figure 8). The result shows that all the AUC values were greater than 0.5, indicating that all these models were effective. A larger AUC value indicates a higher accuracy of the model. The AUC values of landslides for three zones and the whole region were very similar.

Validation of landslide hazard assessment maps

By using the 20% samples of landslides not involved in the model construction, the proportion of hazards located in different hazard zone levels was counted to validate the hazard assessment results. If more landslide samples are located in high and very high hazard level region, it means that the hazard assessment map has a higher accuracy (Table 3).

Comparing the accuracy level of landslide hazard assessment maps in three zones and the whole region, some phenomena were found: 1) the accuracy of hazard assessment by zone was higher than that of the whole region. Accuracies of hazard assessment in three zones were 87.6, 90.4, and 85.6% respectively, and average accuracy in the whole region could reach 87.3%, but the accuracy for the whole region by one landslide hazard model was only 84.4%. 2) Compared with Zone 1 and 2, the accuracy of hazard maps for Zone 3 was relatively low.

The validation of the landslide hazard assessment map of Zone 3 showed the lowest accuracy (Figure 9). Not as same as high mountains and deep valleys in Zone 1 and Zone 2, the topography in Zone 3 is much gentler. Misevaluated landslides are mostly located in the front edge of the slope area or on the sides of the gullies. Due to low precision of topographic factors, especially slope gradient, relief amplitude, the micro-geomorphology and characteristics of these areas could not be described precisely. Therefore, the landslide hazard could not be incorrectly assessed in these areas. In addition, the area of Zone 3 is the largest during three zones, and the landslide quantity is also the largest one. Hence, the effect on landslide by causative factors on landslide may vary in different areas of this zone.

Results analysis

The landslide hazard assessment models were applied to different zones to analyze the applicability for each model (Figures 10, 11). Landslide hazard model built in Zone 1 was applied to Zone 2 and Zone 3. The landslide hazard map shows that the proportion of very high hazard zones in these two zones were much larger than in Zone 1, reaching more than three times and nearly two times, respectively. By using the landslide hazard model built in Zone 2 to Zone 1 and Zone 3, the proportion of very high hazard area in Zone 1 and Zone 3 exceeded 50% due to the influence of precipitation, which was in fact inconsistent with the situation of landslide activities. The landslide hazard model

built in Zone 3 was applied to Zone 1 and Zone 2, and the proportion of very high hazard area was 36.4 and 44.0%, respectively, which was also much higher than the proportion of very high hazard in Zone 3.

The accuracy level of landslide hazard assessment result was compared by using landslide validation samples (Table 3). The landslide hazard assessment model built in Zone 1 had a very high accuracy in Zone 2, while a very low accuracy in Zone 3. The landslide hazard assessment model built in Zone 2 had a very high accuracy in both Zone 1 and 3. However, it was due to the extremely large proportion of a very high hazard level area in Zone 1 and 3, the high accuracy in both zones was of no practical significance. The landslide hazard assessment model built in Zone 3 had a low accuracy in both Zone 1 and Zone 2.

Therefore, it suggests that the landslide hazard model should be built within the subzones of a study area, which suits for specific environmental backgrounds of landslides in the region. If the model is applied to other regions, especially for the places that have significant differences from the modeling region, it could lead to decreased landslide evaluation accuracy, and even erroneous results.

Conclusion

From this research, the following conclusions were drawn.

1) The controlling factors for landslides vary in different area of CPEC. Considering diverse features of geological, topography, and precipitation, the study area was divided into three zones. Geographical detectors were utilized to analyze the controlling factors for landslides in different zones. Landslide controlling factors were very similar in Zone 1 and Zone 2. Topographical features including altitude, slope gradient, and relief amplitude influenced the occurrence of landslides significantly. In addition, the land use type played an important role in Zone 1 rather than in Zone 2. In Zone 3, the distance to epicenter was the most significant factor, which was different with Zone 1 and Zone 2.
2) Landslide hazard assessments were carried out by using the ANN method in three zones and the whole region based on 80% random landslide samples. The ROC curve was utilized to validate the accuracy of hazard assessment modeling. All AUC values of ROC curve were similar and greater than 0.5, which indicated that all these models were valid. The accuracy of landslide hazard maps of all three zones and the whole region was validated by the 20% samples not involved in the modeling. Results show that the accuracy level of landslide hazard assessment maps by zones was higher than by the whole region. Therefore, hazard assessment by subzones is a more advantageous approach than that of the whole region.
3) Landslide hazard model built by ANN within the subzones has a high accuracy. However, if it is applied to other regions, especially for the places that have significantly different environmental backgrounds from the modeling region, it could lead to lower accuracy, even bringing erroneous results.
4) In addition to landslides, CPEC suffers from multiple natural hazards, such as mudslides, avalanches, and glacial lake outburst floods (GLOF). It is particularly important to carry out a comprehensive multi-hazard assessment on top of the single-hazard assessment. First, it is especially crucial to clarify the relationship between different types of hazards. For example, Cees van Westen et al. (2014) analyzed the interrelationships between different types of mountain hazards, which are broadly summarized into three types: 1) different types of mountain hazards induced by the same trigger; 2) one hazard provides development conditions for another hazard to occur; and 3) hazard chains or cascading hazards, in which one hazard causes another. Second, the different types of mountain hazards determine that the units for their evaluation cannot simply use uniform-sized pixel cells. Some scholars have proposed the concept of slope units as the basic unit for multi-hazard assessment. Susceptibility and risk of different types of hazards could then be carried out for each slope unit (Alvioli et al., 2016; Lombardo et al., 2020). This method can also be applied to regional scale studies such as CPEC, which may be useful for integrated multi-hazard assessments.

Data availability statement

The datasets presented in this study can be found in online repositories. The names of the repository/repositories and accession number(s) can be found at: http://www.csdata.org/p/634/.

Author contributions

ZJ in charge of landslide hazard modeling and paper writing; GY made the zonation and analyzed the controlling factors of landslide; LY optimized the methodology and improved the manuscript; ZQ, JY, and CH carried out the landslide field investigation; and CX designed the methodology of the research.

Funding

This research was supported by the Special Foundation for National Science and Technology Basic Research Program of China: Comprehensive Investigation and Assessment of Natural Disasters along the China–Pakistan Economic Corridor, Topic 6: Integrated Assessment and Data Sharing Platform for Natural

Disasters (2018FY100506), and the International Science & Technology Cooperation Program of China (2018YFE0100100).

Conflict of interest

The authors declare that the research was conducted in the absence of any commercial or financial relationships that could be construed as a potential conflict of interest.

Publisher's note

All claims expressed in this article are solely those of the authors and do not necessarily represent those of their affiliated organizations, or those of the publisher, the editors, and the reviewers. Any product that may be evaluated in this article, or claim that may be made by its manufacturer, is not guaranteed or endorsed by the publisher.

References

Ahmed, M. F., and Rogers, J. D. (2015). Regional level landslide inventory maps of the Shyok River watershed, Northern Pakistan. *Bull. Eng. Geol. Environ.* 75, 563–574. doi:10.1007/s10064-015-0773-2

Alvioli, M., Marchesini, I., Reichenbach, P., Rossi, M., Ardizzone, F., Fiorucci, F., et al. (2016). Automatic delineation of geomorphological slope units with <tt> r.slopeunits v1.0</tt> and their optimization for landslide susceptibility modeling. *Geosci. Model. Dev.* 9, 3975–3991. doi:10.5194/gmd-9-3975-2016

Aydan, Ö., Ohta, Y., and Hamada, M. (2009). Geotechnical evaluation of slope and ground failures during the 8 October 2005 Muzaffarabad earthquake, Pakistan. *J. Seismol.* 13, 399–413. doi:10.1007/s10950-008-9146-7

Bacha, A. S., Shafique, M., and van der Werff, H. (2018). Landslide inventory and susceptibility modelling using geospatial tools, in Hunza-Nagar valley, northern Pakistan. *J. Mt. Sci.* 15, 1354–1370. doi:10.1007/s11629-017-4697-0

Barella, C. F., Sobreira, F. G., and Zêzere, J. L. (2019). A comparative analysis of statistical landslide susceptibility mapping in the southeast region of Minas Gerais state, Brazil. *Bull. Eng. Geol. Environ.* 78, 3205–3221. doi:10.1007/s10064-018-1341-3

Basharat, M., Shah, H. R., and Hameed, N. (2016). Landslide susceptibility mapping using GIS and weighted overlay method: A case study from NW Himalayas, Pakistan. *Arab. J. Geosci.* 9, 292. doi:10.1007/s12517-016-2308-y

Bragagnolo, L., da Silva, R. V., and Grzybowski, J. M. V. (2020). Landslide susceptibility mapping with r.landslide: A free open-source GIS-integrated tool based on artificial neural networks. *Environ. Model. Softw.* 123, 104565. doi:10.1016/j.envsoft.2019.104565

Chang, M., Cui, P., Dou, X., and Su, F. (2021). Quantitative risk assessment of landslides over the China-Pakistan economic corridor. *Int. J. Disaster Risk Reduct.* 63, 102441. doi:10.1016/j.ijdrr.2021.102441

Chen, X., Cui, P., You, Y., Cheng, Z., Khan, A., Ye, C., et al. (2017). Dam-break risk analysis of the Attabad landslide dam in Pakistan and emergency countermeasures. *Landslides* 14, 675–683. doi:10.1007/s10346-016-0721-7

Demir, G. (2018). Landslide susceptibility mapping by using statistical analysis in the North Anatolian Fault Zone (NAFZ) on the northern part of Suşehri Town, Turkey. *Nat. Hazards (Dordr).* 92, 133–154. doi:10.1007/s11069-018-3195-1

Dunning, S. A., Mitchell, W. A., Rosser, N. J., and Petley, D. N. (2007). The Hattian Bala rock avalanche and associated landslides triggered by the Kashmir Earthquake of 8 October 2005. *Eng. Geol.* 93, 130–144. doi:10.1016/j.enggeo.2007.07.003

Ercanoglu, M., Kasmer, O., and Temiz, N. (2008). Adaptation and comparison of expert opinion to analytical hierarchy process for landslide susceptibility mapping. *Bull. Eng. Geol. Environ.* 67 (4), 565–578. doi:10.1007/s10064-008-0170-1

Gong, P., Liu, H., Zhang, M., Li, C., Wang, J., Huang, H., et al. (2019). Stable classification with limited sample: Transferring a 30-m resolution sample set collected in 2015 to mapping 10-m resolution global land cover in 2017. *Sci. Bull.* 64 (6), 370–373. doi:10.1016/j.scib.2019.03.002

GRASS Development Team (2017). *Geographic resources analysis support system (GRASS GIS) software*. version 7.2. Beaverton: Open Source Geospatial Foundation. URL: http://grass.osgeo.org.

Harris, I., Jones, P. D., Osborn, T. J., and Lister, D. H. (2014). Updated high-resolution grids of monthly climatic observations - the CRU TS3.10 Dataset. *Int. J. Climatol.* 34, 623–642. doi:10.1002/joc.3711

Haykin, S. (1999). Editor second ed. (New Jersey: Prentice-Hall), 897.*Neural networks: A comprehensive foundation.*

Hussain, M. L., Shafique, M., Bacha, A. S., Chen, X. q., and Chen, H. y. (2021). Landslide inventory and susceptibility assessment using multiple statistical approaches along the Karakoram highway, northern Pakistan. *J. Mt. Sci.* 18 (3), 583–598. doi:10.1007/s11629-020-6145-9

Imtiaz, I., Umar, M., Latif, M., Ahmed, R., and Azam, M. (2022). Landslide susceptibility mapping: Improvements in variable weights estimation through machine learning algorithms—a case study of upper Indus River basin, Pakistan. *Environ. Earth Sci.* 81, 112. doi:10.1007/s12665-022-10233-y

Kamp, U., Growley, B. J., Khattak, G. A., and Owen, L. A. (2008). GIS-based landslide susceptibility mapping for the 2005 Kashmir earthquake region. *Geomorphology* 101 (4), 631–642. doi:10.1016/j.geomorph.2008.03.003

Khan, H., Shafique, M., Khan, M. A., Bacha, M. A., Shah, S. U., and Calligaris, C. (2019). Landslide susceptibility assessment using Frequency Ratio, a case study of northern Pakistan. *Egypt. J. Remote Sens. Space Sci.* 22 (1), 11–24. doi:10.1016/j.ejrs.2018.03.004

Khattak, G. A., Owen, L. A., Kamp, U., and Harp, E. L. (2010). Evolution of earthquake-triggered landslides in the Kashmir Himalaya, northern Pakistan. *Geomorphology* 115, 102–108. doi:10.1016/j.geomorph.2009.09.035

Kumar, M. R., Mishra, D. C., and Singh, B. (2013). Lithosphere, crust and basement ridges across ganga and Indus basins and seismicity along the himalayan front, India and western fold belt, Pakistan. *J. Asian Earth Sci.* 75, 126–140. doi:10.1016/j.jseaes.2013.07.004

Lee, S., and Min, K. (2001). Statistical analysis of landslide susceptibility at Yongin, Korea. *Environ. Geol.* 40 (9), 1095–1113. doi:10.1007/s002540100310

Liu, Y. L. (2010). Application of logistic regression and artificial neural networks in spatial assessment of landslide hazards. *Hydrogeology Eng. Geol.* 37 (5), 92–96.

Lombardo, L., Tanyas, H., and Nicu, I. C. (2020). Spatial modeling of multi-hazard threat to cultural heritage sites. *Eng. Geol.* Geology277, 105776. doi:10.1016/j.enggeo.2020.105776

Maqsoom, A., Aslam, B., Khalil, U., Kazmi, Z. A., Azam, S., Mehmood, T., et al. (2022). Landslide susceptibility mapping along the China Pakistan Economic Corridor (CPEC) route using multi-criteria decision-making method. *Model. Earth Syst. Environ.* 8, 1519–1533. doi:10.1007/s40808-021-01226-0

Martin, A. J. (2017). A review of Himalayan stratigraphy, magmatism, and structure. *Gondwana Res.* 49, 42–80. doi:10.1016/j.gr.2017.04.031

Meten, M., Bhandary, N. P., and Yatabe, R. (2015). GIS-Based frequency ratio and logistic regression modelling for landslide susceptibility mapping of debre sina area in Central Ethiopia. *J. Mt. Sci.* 12 (6), 1355–1372. doi:10.1007/s11629-015-3464-3

Miller, D. J., and Craig, S. R. (1996). *Rangelands and pastoral development in the Hindu kush-himalayas: Proceedings of a regional experts' meeting*. Kathmandu: ICIMOD. doi:10.53055/ICIMOD.267

NDMA(National Disaster Management Authority Pakistan) (2010). NDMA newsletter. Available at: https://cms.ndma.gov.pk/storage/app/public/publications/October2020/tzYh8Fgm2dpYjhjAqSdp.pdf.1#2.

Rana, H., and Babu, G. L. S. (2022). Regional back analysis of landslide events using TRIGRS model and rainfall threshold: An approach to estimate landslide hazard for kodagu, India. *Bull. Eng. Geol. Environ.* 81, 160. doi:10.1007/s10064-022-02660-9

Rashid, B., Iqbal, J., and Su, L. (2020). Landslide susceptibility analysis of Karakoram highway using analytical hierarchy process and scoops 3D. *J. Mt. Sci.* 17 (7), 1596–1612. doi:10.1007/s11629-018-5195-8

Sato, H. P., Hasegawa, H., Fujiwara, S., Tobita, M., Koarai, M., Une, H., et al. (2007). Interpretation of landslide distribution triggered by the 2005 Northern Pakistan earthquake using SPOT 5 imagery. *Landslides* 4, 113–122. doi:10.1007/s10346-006-0069-5

Searle, M. P., and Asif Khan, M. (1997). *Geological map of North Pakistan and adjacent areas of northern Ladakh and western Tibet*. Hague: Shell International Exploration and Production.

Su, C., Wang, L., Wang, X., Huang, Z., and Zhang, X. (2015). Mapping of rainfall-induced landslide susceptibility in Wencheng, China, using support vector machine. *Nat. Hazards (Dordr).* 76, 1759–1779. doi:10.1007/s11069-014-1562-0

Su, X., Zhang, Y., Meng, X., Yue, D. x., Ma, J. h., Guo, F. y., et al. (2021). Landslide mapping and analysis along the China-Pakistan Karakoram Highway based on SBAS-InSAR detection in 2017. *J. Mt. Sci.* 18, 2540–2564. doi:10.1007/s11629-021-6686-6

Thiery, Y., Maquaire, O., and Fressard, M. (2014). Application of expert rules in indirect approaches for landslide susceptibility assessment. *Landslides* 11, 411–424. doi:10.1007/s10346-013-0390-8

van Beek, L., and van Asch, T. (2004). Regional assessment of the effects of land-use change on landslide hazard by means of physically based modelling. *Nat. Hazards* 31, 289–304. doi:10.1023/B:NHAZ.0000020267.39691.39

van Westen, C., Kappes, M. S., Luna, B. Q., Frigerio, S., Glade, T., and Malet, J. P. (2014). "Medium-scale multi-hazard risk assessment of gravitational processes," in *Mountain risks: From prediction to management and governance. Advances in natural and technological hazards research*. Editors T. Van Asch, J. Corominas, S. Greiving, J. P. Malet, and S. Sterlacchini (Dordrecht: Springer), Vol. 34. doi:10.1007/978-94-007-6769-0_7

Wang, J., Li, X., Christakos, G., Liao, Y., Zhang, T., Gu, X., et al. (2010). Geographical detectors-based health risk assessment and its application in the neural tube defects study of the heshun region, China. *Int. J. Geogr. Inf. Sci.* 24 (1-2), 107–127. doi:10.1080/13658810802443457

Xie, M., Esaki, T., and Zhou, G. (2004). GIS-based probabilistic mapping of landslide hazard using a three-dimensional deterministic model. *Nat. Hazards* 33, 265–282. doi:10.1023/B:NHAZ.0000037036.01850.0d

Xu, C., Xu, X., Dai, F., Wu, Z., He, H., Shi, F., et al. (2013). Application of an incomplete landslide inventory, logistic regression model and its validation for landslide susceptibility mapping related to the May 12, 2008 Wenchuan earthquake of China. *Nat. Hazards (Dordr).* 68, 883–900. doi:10.1007/s11069-013-0661-7

Xu, S., Li, J., and Ai, N. (1982). Studies of the structural landforms of the Potwar plateau, Pakistan. *Sci. Geogr. Sin.* 2 (2), 125–134.

Yang, C., and Liu, C. (2005). *Guide to the world states*. Beijing: Social Sciences Academic Press.

Yaseen, M., Shahab, M., Ahmad, Z., Khan, R., Shah, S. F. A., and Naseem, A. A. (2021). Insights into the structure and surface geology of balanced and retrodeformed geological cross sections from the Nizampur basin, Khyber Pakhtunkhwa, Pakistan. *J. Pet. Explor. Prod. Technol.* 11, 2561–2571. doi:10.1007/s13202-021-01180-8

Yi, X., Shang, Y., Shao, P., and Meng, H. (2021). A dataset of spatial distributions and attributes of typical rockfalls and landslides in the China-Pakistan Economic Corridor from 1970 to 2020. *China Sci. Data* 6 (4). doi:10.11922/11-6035.csd.2021.0057.zh

Yilmaz, I. (2009). A case study from Koyulhisar (Sivas-Turkey) for landslide susceptibility mapping by artificial neural networks. *Bull. Eng. Geol. Environ.* 68, 297–306. doi:10.1007/s10064-009-0185-2

Yu, Z., Yu, X., and Yang, F. (2021). Spatio-temporal characteristics of climate change in China-Pakistan Economic Corridor from 1980 to 2019. *Arid Zone Res.* 38 (3), 695–703. doi:10.13866/j.azr.2021.03.11

Zhang, J., van Westen, C. J., Tanyas, H., Mavrouli, O., Ge, Y., Bajrachary, S., et al. (2019a). How size and trigger matter: Analyzing rainfall- and earthquake-triggered landslide inventories and their causal relation in the koshi river basin, central himalaya. *Nat. Hazards Earth Syst. Sci.* 19, 1789–1805. doi:10.5194/nhess-19-1789-2019

Zhang, T., Han, L., Zhang, H., Zhao, Y. h., Li, X. a., and Zhao, L. (2019b). GIS-based landslide susceptibility mapping using hybrid integration approaches of fractal dimension with index of entropy and support vector machine. *J. Mt. Sci.* 16, 1275–1288. doi:10.1007/s11629-018-5337-z

Frontiers in Earth Science

Investigates the processes operating within the major spheres of our planet

Advances our understanding across the earth sciences, providing a theoretical background for better use of our planet's resources and equipping us to face major environmental challenges.

Discover the latest Research Topics

See more →

Frontiers

Avenue du Tribunal-Fédéral 34
1005 Lausanne, Switzerland
frontiersin.org

Contact us

+41 (0)21 510 17 00
frontiersin.org/about/contact